VOL 11
ISSUE 3
May 2026

eMetN METEOR JOURNAL

eJournal for meteor observers www.emetn.net

Composite image of the Milky Way taken at the Hakos Observatory in Namibia by the author in July 2011. The photo was taken with a Canon 40D, a Canon EF 15 mm F 2.8 lens mounted on an AstroTrac tracking mount. Three Capricornids and two Southern delta-Aquariids can be seen (Author Koen Miskotte).

ISSN 3041 - 4261

Contents

Meteoroid orbit shower identification method and its application in meteor shower case studies

Paul Roggemans[1], **Denis Vida**[2,3], **Damir Šegon**[4,5] **and James M. Scott**[6]

[1] **Pijnboomstraat 25, 2800 Mechelen, Belgium**
paul.roggemans@gmail.com

[2] **Department of Physics and Astronomy, University of Western Ontario, Richmond Street, London, N6A 3K7, Ontario, Canada**

[3] **Institute for Earth and Space Exploration, University of Western Ontario, Perth Drive, London, N6A 5B8, Ontario, Canada**
denis.vida@gmail.com

[4] **Astronomical Society Istra Pula, Park Monte Zaro 2, 52100 Pula, Croatia**

[5] **Višnjan Observatory, Istarska 5, 52463 Višnjan, Croatia**

[6] **Department of Geoscience, Aarhus University, Høegh-Guldbergs Gade 2. DK-8000 Aarhus C, Denmark**
jscott@geo.au.dk

This article explains the procedure used by the Global Meteor Network to identify meteor showers using meteoroid orbits. Frequently used astronomical terms are explained for people unfamiliar with these terms. The practical application of this method is described with a case study on a newly discovered shower, M2025-Y1, which appears as an outburst caused by an unknown dust trail related to the parent body comet 12P/Pons-Brooks and the December kappa-Draconids.

1 Introduction

Although the first scientific meteor observations started in the early 19th century, meteor showers were known to radiate from a common point in the sky for many centuries. Ordinary people who witnessed meteor storms described it as if stars moved creating a tunnel effect. Major meteor showers were informally named according to the constellation from where the meteors seemed to radiate from, e.g. the Perseids from Perseus in August, the Leonids from Leo in November. This reminds us of the Quadrantids in January, which is from the obsolete constellation Quadrans Muralis defined by the French astronomer Jérôme Lalande in 1795. In 1922, this constellation was removed by the International Astronomical Union (IAU) when the official modern constellations were defined.

For major showers the identification can be done on sight during their maximum activity. However, there are many hundreds of dust trails crossing the Earth orbit which produce only weak activity hidden within the overall sporadic activity. Even major showers are hard to distinguish from sporadic activity when their number of meteors is statistically irrelevant before and after their maximum.

19th century astronomers developed visual observing techniques to plot meteors on star maps or on a star globe, tracing the trail seen at the sky backwards to reveal the radiant - the point in the night sky from where it was supposed to come. This backwards projection of meteor trails on star maps in gnomonic projection remained popular among amateur meteor observers in the 20th century. However, the presence of the sporadic background radiants and the effect of small-number statistics made it somewhat like gambling about the possible radiant association. More about the history and different meteor observing techniques can be found in the "Handbook for meteor observers" (Rendtel, 2020).

Meteors that belong to a meteor shower can be distinguished by their orbits since all particles within a meteoroid stream are spread along a common orbit (*Figure 1*). Since low light camera networks became affordable to the amateur community, large numbers of meteoroid orbit data have been collected. The properties determined for these meteoroid orbits offer a reliable alternative for meteor shower identifications.

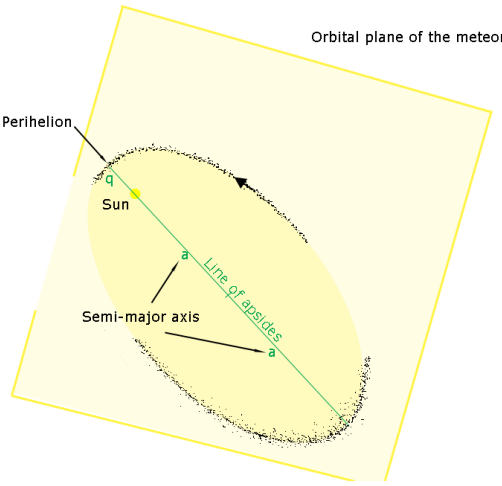

Figure 1 – Schematic presentation of a meteoroid stream with particles dispersed along an elliptic shaped orbit.

2 The orbital elements

For meteoroid orbits we use five parameters that describe the shape, size and orientation of the meteoroid orbit. These parameters are known as the Keplerian elements, with the semi-major axis a, eccentricity e, inclination i, longitude of the ascending node Ω and argument of periapsis (perihelion) ω. The orbital elements are basic geometry using references like the ecliptic plane and the vernal equinox (see *Figure 2*).

The shape of the meteoroid orbit is an ellipse with the Sun in one of its foci. The perihelion is the position where the orbit is at its smallest distance from the Sun. The aphelion is the position at the largest distance from the Sun. The perihelion distance q is the distance of the perihelion point to the Sun, expressed in Astronomical Units with 1 Astronomical Unit = the average distance between the Earth and the Sun.

Semi-major axis a is half the distance between the perihelion and the aphelion, expressed in Astronomical Units.

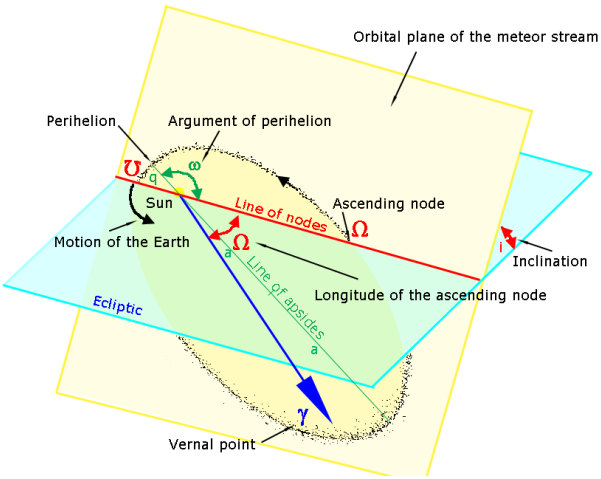

Figure 2 – Schematic presentation of a meteoroid stream with orbital elements in the ecliptic plane and the orbital plane of the meteoroid stream.

The other elements are measured in the ecliptic plane, which is the plane of the orbit of Earth around the Sun, and in the meteoroid orbit plane. The Vernal or Spring equinox is the position of the Earth where the Sun is crossing the Earth's equator from South to North. The line of nodes is the intersection of the orbital plane of the meteoroid stream with the ecliptic plane.

The longitude of the ascending node Ω is the angle from the ascending node of the orbit to the direction of the Vernal equinox.

Argument of perihelion (periapsis) ω gives the orientation in the orbital plane, as the angle measured from the ascending node to the perihelion. The longitude of perihelion Π is defined as the sum of Ω and ω.

Inclination i is the vertical tilt of the orbital plane to the ecliptic, measured at the ascending node. Inclinations from 90° to 180° are called retrograde orbits.

The eccentricity e defines the shape of the ellipse. A perfect circle has $e = 0$, $e < 1$ is an ellipse, $e > 1$ is a hyperbolic orbit, and $e = 1$ is a parabola. Some simple equations allow to compute some of the orbital parameters based on a few known parameters, like the semi-major axis a derived from the perihelion distance q and eccentricity e, or the aphelion distance Q derived from semi-major axis a and eccentricity e:

$$a = \frac{q}{(1-e)}$$

$$Q = a(1+e)$$

3 Ecliptic versus equatorial coordinates

In astronomy books, the positions of stars, nebula and other objects, including meteor shower radiants, are given in equatorial coordinates in Right Ascension and Declination with the Celestial Equator as reference plane. It is easy to find positions at the sky with a classic star atlas or to operate a telescope as these coordinates are aligned with the rotation of the Earth. To study objects like planets, minor bodies and meteoroid streams in our Solar System it is more convenient to use Ecliptic coordinates with the Ecliptic or Earth's orbital plane as reference plane. The difference between the two coordinate systems is in the reference planes and their poles, tilted by about 23.5°. Equatorial coordinates can be converted into ecliptic coordinates by a simple coordinate transformation. More detailed information on coordinate transformation and celestial mechanics can be found in the work "Astronomical Algorithms" by Jean Meeus (1998), which is available for free download[1].

Instead of using calendar dates to define time we use the Solar Longitude, which is a measure of the position of the Earth in its orbit around the Sun, with the vernal equinox at Solar Longitude zero. The Solar Longitude corresponds to how far the Earth has moved in its orbit since the equinox, avoiding leap years and other calendar imperfections. This way meteor shower activity always falls on the same Solar Longitude, which is not the case with calendar dates. The Solar Longitude is noted with the symbol $\lambda_\odot$. The activity period of each meteor shower is listed in Solar Longitude in the IAU-MDC Working List of Meteor Showers[2]. A handy online tool to convert dates into Solar Longitude and vice versa can be found online[3]. How to compute Solar Longitudes can be found in Steyaert (1991).

[1] https://www.scribd.com/document/444162160/Jean-Meeus-Astronomical-algorithms-1998-pdf

[2] https://www.ta3.sk/IAUC22DB/MDC2022/Roje/roje_lista.php?corobic_roje=0&sort_roje=0

[3] https://kikimoreau.shinyapps.io/SollongCalc/

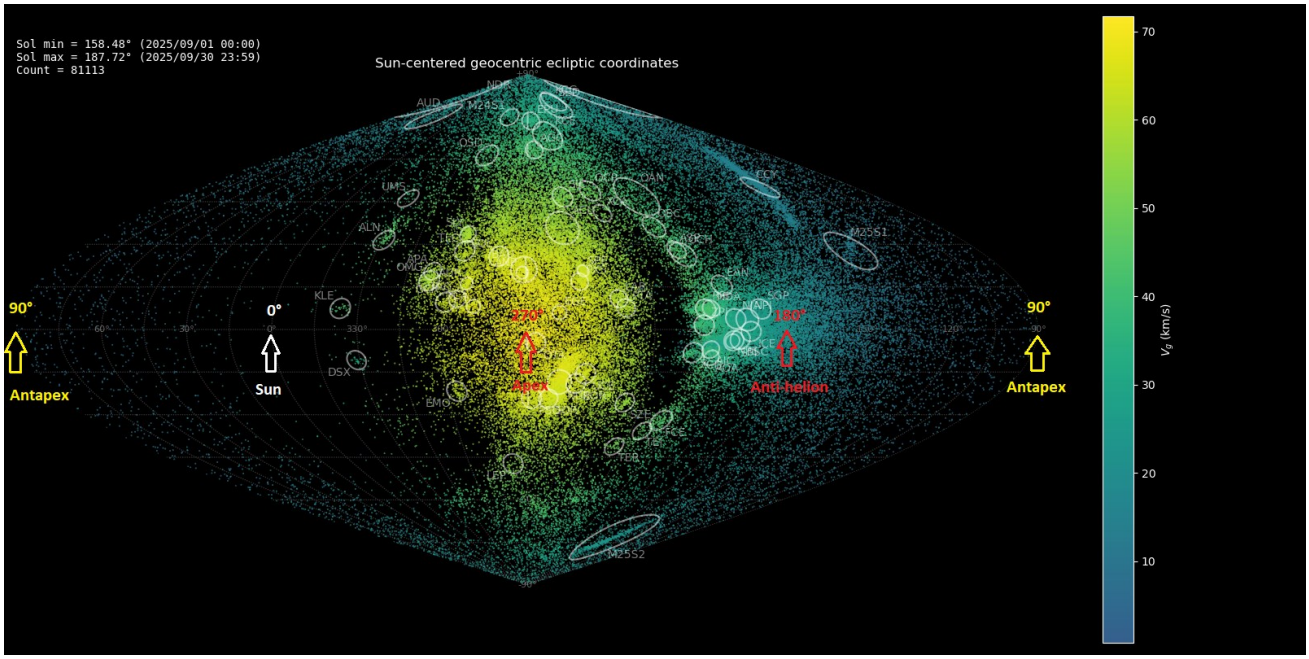

Figure 3 – GMN radiants for September 2025 plotted in Sun-centered Ecliptic Geocentric coordinates (SCE).

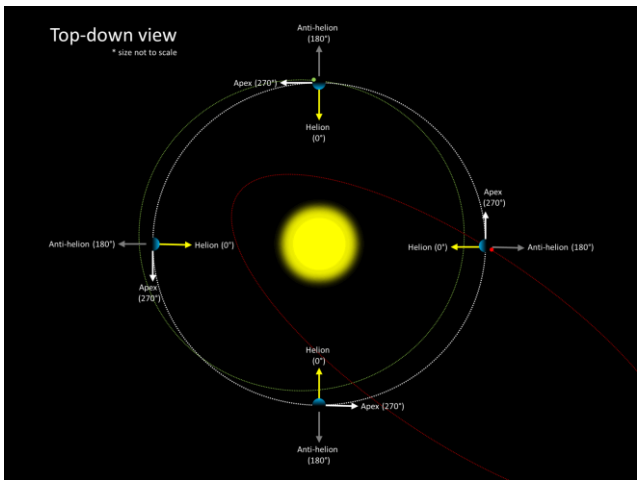

Figure 4 – Illustration of the Sun-centered ecliptic coordinate system with the Earth moving on its orbit in the direction of the Apex. (Credit GMN).

In meteor astronomy we use Sun-centered Ecliptic Geocentric coordinates (SCE), from the perspective of the Earth (geocentric), as opposed to the Sun (heliocentric). The Sun-centered part means that the coordinates are adjusted so that the Sun is always in the same place, at 0° in SCE longitude (*Figure 4*). The Sun-centered Geocentric Ecliptic Longitude is obtained by subtracting the Solar Longitude from the Geocentric Ecliptic Longitude and noted as $\lambda_g - \lambda_\odot$.

The best way to describe these coordinates is that they show the Earth's "windshield", knowing that the average orbital speed of the Earth around the Sun is approximately 29.78 km/s. *Figure 3* shows the radiant distribution in Sun-centered Ecliptic Geocentric coordinates. The middle of the plot is the Earth's apex – it's direction of motion around the Sun. The reason why meteor speeds here are the highest is because we hit them head-on. 90° to the left is the Sun, and 90° to the right is the anti-helion direction. At 180° is our "back" and we see fewer meteors there because they have to catch up with the Earth so their apparent speeds are very slow.

This coordinate system is helpful because there is less radiant drift since the rotation of the Earth around the Sun is compensated. Most meteor shower radiants appear as fixed activity sources in *Figure 3*. Only a few radiants appear as elongated activity sources like the chi-Cygnids (CCY) where the radiant drift in Sun-centered Ecliptic Geocentric coordinates is caused by gradual changes in the meteoroid stream orbit orientation during Earth's transit.

Most meteors are sporadics because they cannot be associated with any known meteoroid stream. GMN data has about 28% of meteors identified as belonging to meteor showers. These activities appear at the sky as a cluster of radiant points when the Earth crosses a trail of meteoroids moving around the Sun along a cometary or asteroidal orbit. Depending on the density of the dust concentration the number of shower meteors and related radiant points may be very distinct. Earth also intersects meteoroid streams at their outer edges where particles are irregularly and thinly distributed. Perceiving the presence of such activity embedded in the rich sporadic background is a matter of distinguishing between statistically relevant and spurious radiant concentrations.

4 Orbit data selection

Working with large datasets of millions of meteoroid orbits is rather slow and therefore we select only the orbits recorded during the activity period of a meteor shower.

As a first step all orbit data is selected during the expected activity period of the shower using the Solar Longitude. The limits of meteor shower activity are uncertain and can change with time. Therefore, adding one or two degrees in

Solar Longitude to detect possible earlier or later activity than previously known can be useful. Solar Longitude makes it easy to combine data from different years. In some cases, the shower activity is studied for a specific year.

All available orbits are selected within the chosen range of time including both sporadic and shower meteoroid orbits. This is necessary to compare the shower activity to the sporadic background activity and to make specific distributions of orbital elements versus each other to evaluate the occurrence of orbit concentrations.

During the transit of the Earth through a meteoroid stream, the orientation of the Earth orbit relative to the direction of the meteoroid stream changes, resulting in a drift per day of the shower radiant at the sky. This motion of the Earth on its orbit can be compensated by using the Sun-centered ecliptic coordinates. All these coordinates are geocentric, relative to the Earth, including the Sun-centered coordinates and should not be confused with heliocentric coordinates, which are relative to the Sun.

To search for a possible concentration of orbits we need a reference orbit as a starting point for an iterative procedure to locate the best fitting mean orbit. To find such a start reference, we use the radiant position of the shower in Sun-centered geocentric ecliptic coordinates to select only those meteors that have their radiant within an estimated range in radiant position and velocity interval. The radiant position and size can be estimated from the radiant density maps[4]. The velocity can be approached as the median velocity of this sample. This selection of meteors and their orbits consists mainly of shower meteors including a limited number of sporadics. The mean orbit for this selection is then computed using the method of Jopet et al. (2006). The resulting mean orbit serves as a first approach to find the best fitting mean orbit for all orbits that fit within a well-defined range of similarity.

5 Orbit discrimination criteria

We use the so-called similarity or discrimination or D-criteria to accept or to reject the identification of a shower meteoroid orbit. D-criteria are trying to put a number on how different two orbits are. $D = 0$ means the orbits are the same. The problem here is that using Keplerian orbital elements is tricky. The similarity criteria consider the distance between some of the orbital elements combined with the angle between the orbital planes. They're trying to find a physically meaningful way to weight the differences, so that's why we have different versions. The first numeric discrimination criterion was proposed by Southworth and Hawkins (1963), referred to as D_{SH}. Later Drummond (1981) introduced a slightly different criterion, referred as D_D. Jopek (1993) proposed another version D_J, based on the former criteria. We can apply all three criteria combined. Index p represents the reference orbit, index m the tested meteor orbit:

First, we determine the sign Γ, –1 or +1, as:

$$\Gamma = \begin{cases} +1, & |\Omega_p - \Omega_m| \le 180^o \\ -1, & |\Omega_p - \Omega_m| > 180^o \end{cases}$$

Then we calculate ψ, the angle between the two orbital planes from:

$$\psi = \arccos\left[\cos i_p \cos i_m + \sin i_p \sin i_m \cos(\Omega_p - \Omega_m)\right]$$

Next, we calculate Π, the angle between the perihelion points:

$$\Pi = \omega_p - \omega_m + 2\Gamma \arcsin\left(\cos\frac{i_p + i_m}{2} \sin\frac{\Omega_p - \Omega_m}{2} \sec\frac{\psi}{2}\right)$$

λ is the ecliptic longitude of the perihelion, with

$$\lambda = \Omega + \arctan(\cos i \tan \omega),$$

where λ has 180° added if $\cos \omega < 0$.

β is the ecliptic latitude of the perihelion, with

$$\beta = \arcsin(\sin i \sin \omega),$$

The angle θ between the two perihelion points on each orbit is given by the equation:

$$\theta = \arccos[\sin\beta_p \sin\beta_m + \cos\beta_p \cos\beta_m \cos(\lambda_p - \lambda_m)]$$

The three different discriminant criteria can now be calculated from the following equations, with D_{SH} for the Southworth Hawkins criterion (1963), D_D for the Drummond criterion (1981) and D_J for the Jopek criterion (1993):

$$D_{SH}^2 = (q_p - q_m)^2 + (e_p - e_m)^2 + \left(2\sin\frac{\psi}{2}\right)^2 + \left(\frac{e_p + e_m}{2} \cdot 2\sin\frac{\Pi}{2}\right)^2,$$

$$D_D^2 = \left(\frac{e_p - e_m}{e_p + e_m}\right)^2 + \left(\frac{q_p - q_m}{q_p + q_m}\right)^2 + \left(\frac{\psi}{180^\circ}\right)^2 + \left(\frac{e_p + e_m}{2}\right)^2 \cdot \left(\frac{\theta}{180^\circ}\right)^2,$$

$$D_J^2 = (e_p - e_m)^2 + \left(\frac{q_p - q_m}{q_p + q_m}\right)^2 + \left(2\sin\frac{\psi}{2}\right)^2 + \left(\frac{e_p + e_m}{2}\right)^2 \cdot \left(2\sin\frac{\Pi}{2}\right)^2.$$

The larger the values of ψ, Π or θ, the bigger the 'distances' between the orbits and the less the probability becomes for an association. Related orbits have values in the order of a few degrees or less. The final values for these similarity criteria are dimensionless numeric values, where 0

[4] https://globalmeteornetwork.org/data/plots/

represents identical orbits. The smaller the D-values the higher the degree of similarity and the better the probability becomes for an association. The D-criteria should be applied with caution. The result is a discriminant, without providing any proof for some physical relationship between the orbits. It is an approach in the sense of best effort and requires careful evaluation as the result highly depends upon the type of orbit.

Most meteor shower analyzers use arbitrary determined upper limits as a 'safe' threshold for the similarity criteria, typically $D_{SH} < 0.25$ for Southworth and Hawkins and $D_D < 0.105$ for Drummond. However, these thresholds are far too optimistic in most cases. Applying these values blindly leads to erroneous and confusing results. The most appropriate thresholds have to be considered on a case-by-case evaluation. A Rayleigh distribution fit on a sample of orbits under investigation helps to estimate the upper limit threshold in most cases. There are other methods to determine the optimal threshold for D-criteria some of which were published by Neslušan et al. (1995) and Rudawska et al. (2015).

Moreover, the D-criteria have specific shortcomings. The Southworth and Hawkins criterion has been criticized for being too dependent on the perihelion distance q. The Drummond criterion is too sensitive for the eccentricity e. The criterion defined by Jopek reduces the above-mentioned dependencies.

The purpose of identifying the best fitting orbit for a meteoroid stream is to eliminate sporadic look-alikes. Inappropriate use of D-criteria thresholds risks to result in a larger number of shower meteors but strongly affected by sporadic contamination. Therefore, we use the D-criteria of Southworth and Hawkins (1963), Drummond (1981) and Jopek (1993) combined. The results are considered in different classes of D-criteria thresholds with different degrees of similarity:

- Minimal: $D_{SH} < 0.25$ & $D_D < 0.105$ & $D_J < 0.25$.
- Poor: $D_{SH} < 0.2$ & $D_D < 0.08$ & $D_J < 0.2$.
- Medium poor: $D_{SH} < 0.15$ & $D_D < 0.06$ & $D_J < 0.15$.
- Medium: $D_{SH} < 0.125$ & $D_D < 0.05$ & $D_J < 0.125$.
- Medium high: $D_{SH} < 0.1$ & $D_D < 0.04$ & $D_J < 0.1$.
- Strong: $D_{SH} < 0.075$ & $D_D < 0.03$ & $D_J < 0.075$.
- Very strong: $D_{SH} < 0.05$ & $D_D < 0.02$ & $D_J < 0.05$.
- Best fit: $D_{SH} < 0.025$ & $D_D < 0.01$ & $D_J < 0.025$.

These classes should allow to compare shower characteristics in function of the reliability of the shower identification. While the poor threshold similarity classes may include sporadic orbits that fit the criteria by pure chance, the stronger the threshold the less the risk for contamination with sporadic orbits.

The reference orbit obtained as described in *Section 4* is used to test against all orbits, regardless of their radiant position, by computing the three D-criteria thresholds for each orbit. Depending upon the type of orbit, the most appropriate D-criteria threshold class is used to select all orbits that fit within these threshold limits. A new mean orbit (Jopek et al., 2006) is computed for this selection which is used to repeat the procedure on a new selection of orbits where possibly sporadic orbits were removed. This iterative procedure stops when the set of selected orbits that fit the mean orbit doesn't change anymore. Depending on the type of orbit the iteration procedure can be repeated for a more restricted class of D-criteria thresholds until it converges on a mean orbit as the best fit. All related meteor shower properties are derived from the mean orbit based on the final selection of shower meteor orbits.

If the initial reference orbit has been poorly determined the iteration can require many steps and skip away from the initial starting reference before the solution converges. In case a spurious activity source with unrelated orbits is investigated, the procedure runs idle unless it encounters another real activity source, if not, the iterations run into an endless loop.

6 Further analyses

The orbital parameters of all the meteors that fit a D-criteria threshold class can be used to make line graphs and diagrams for the entire time interval of activity. Orbital elements and velocity may display changes in function of time, expressed in Solar Longitude $\lambda_\odot$. These changes in orbit orientation during Earth's transit results in a radiant drift in Sun-centered geocentric ecliptic coordinates.

The number of shower meteors relative to the number of non-shower meteors per unit of time can be used as an approximate activity profile for the shower. Different classes of D-criteria thresholds can be combined in such activity plot to compare the selection effect.

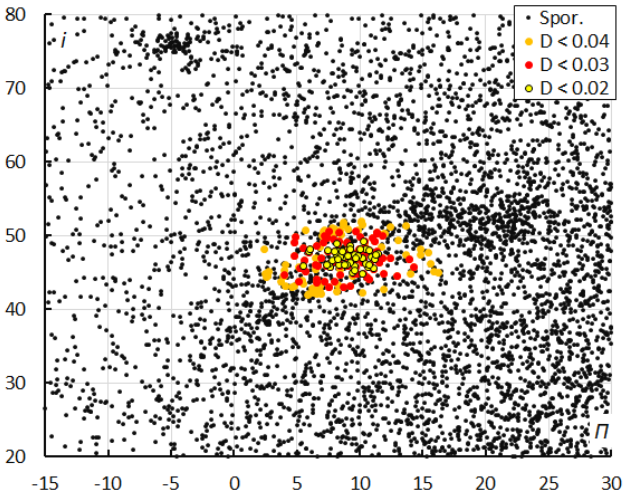

Figure 5 – The diagram of the inclination i against the longitude of perihelion Π color-coded for different classes of D criterion thresholds, for the October epsilon-Carinids in 2023–2025.

Frequently used plots are those of one orbital element versus another orbital element, such as inclination i versus longitude of perihelion Π. An example of the October epsilon-Carinids is given in *Figure 5*. These diagrams visualize the concentration in orbital elements with the non-shower meteors in the background and the investigated

shower meteors color-code for different D-criteria threshold classes.

The type of the meteoroid orbit can be determined by the Tisserand parameter, T_J, with respect to Jupiter:

$$T_J = \frac{a_J}{a_m} + 2\cos i_m \sqrt{\left(\frac{a_m}{a_J} \times (1 - e_m^2)\right)}$$

With a_J = 5.2044 A.U. In an ideal case, the following orbit types can be distinguished:

- $T_J < 0.65$ indicates a Long-period comet type orbit;
- $0.65 < T_J < 2.00$ indicates a Mellish-type shower;
- $2.00 < T_J < 3.50$ indicates a Jupiter family comet type orbit;
- $T_J > 3.50$ indicates an asteroid like type orbit.

In practice, there is a lot of intermixing. E.g. the biggest source of cometary dust in the Solar System is comet Encke, which is on a squarely asteroidal orbit. Further subdivision types have been defined within these classifications, but these main types of orbits are sufficient for the purpose of meteor shower analyses.

Table 1 – Main properties to define a meteor shower.

$\lambda_\odot$ (°)	Solar Longitude at maximum activity.
$\lambda_{\odot b}$ (°)	Solar Longitude at the start of the activity.
$\lambda_{\odot e}$ (°)	Solar Longitude at the end of the activity.
α_g (°)	Geocentric right ascension in the J2000 epoch.
δ_g (°)	Geocentric declination in the J2000 epoch.
$\Delta\alpha_g$ (°)	Radiant drift in Right Ascension.
$\Delta\delta_g$ (°)	Radiant drift in Declination.
v_g (km/s)	Geocentric velocity.
H_b (km)	Begin height of the meteor.
H_e (km)	End height of the meteor.
H_p (km)	Height at which with peak magnitude occurred.
Mag_{Ap}	Average peak mag. normalized at 100 km.
λ_g (°)	Geocentric ecliptic longitude in the J2000 epoch.
λ_g–$\lambda_\odot$(°)	Sun-centered geocentric ecliptic longitude.
β_g (°)	Geocentric ecliptic latitude in the J2000 epoch.
a (A.U.)	Semi-major axis.
q (A.U.)	Perihelion distance.
e	Eccentricity.
i (°)	Inclination.
ω (°)	Argument of perihelion.
Ω (°)	Ascending node.
Π (°)	Longitude of perihelion.
T_j	Tisserand's parameter with respect to Jupiter.
N	Number of meteors used for the mean orbit.

The GMN procedure to identify meteor showers checks if a meteor is within the activity period, with a radiant within a changing radius of association from given coordinates (dispersion changes over time), and has speeds within a given range. The final result identifies a meteor shower with a list of physical parameters that distinguish the activity from other sources (*Table 1*). The meteoroid stream orbit is matched with all known minor bodies in our Solar System to locate any possible parent body.

7 Case study

As an example, we apply the method on a recently discovered meteor shower in Draco (M2025-Y1). This activity was first discovered during the night of December 12–13, 2025, by Belarusian and Ukrainian video camera networks (Harachka, 2026).

However, the likely radiant density maps[5] of the GMN indicates that this activity started earlier and lasted longer than December 12–13, 2025. These maps serve as a first visual verification to estimate the activity duration and radiant location. The maps show a distinct activity from 8 until 15 December 2025, or 256° to 263° in Solar Longitude (*Figures 7 and 8*). Before applying the method for shower identification based on orbits we look at the results obtained by the method based on radiant identification.

7.1 Shower classification based on radiants

The GMN shower association criteria assume that meteors within 1° in Solar Longitude, within 4.9° in radiant in this case, and within 10% in geocentric velocity of a shower reference location are members of that shower. Further details about the shower association are explained in Moorhead et al. (2020). Using these meteor shower selection criteria, 263 meteors have been associated with the M2025-Y1 radiant in 2025, recorded by 414 cameras in Austria, Bosnia-Herzegovina, Belgium, Bulgaria, Canada, Croatia, Czech Republic, Denmark, Germany, Greece, France, Ireland, Italy, Netherlands, Portugal, Russia, Slovenia, South Korea, Spain, Switzerland, Ukraine, United Kingdom and the United States of America.

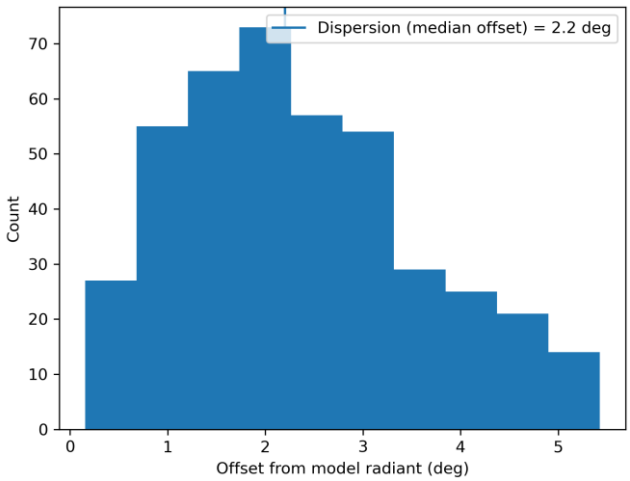

Figure 6 – Dispersion median offset on the radiant position.

[5] https://globalmeteornetwork.org/data/plots/daily/

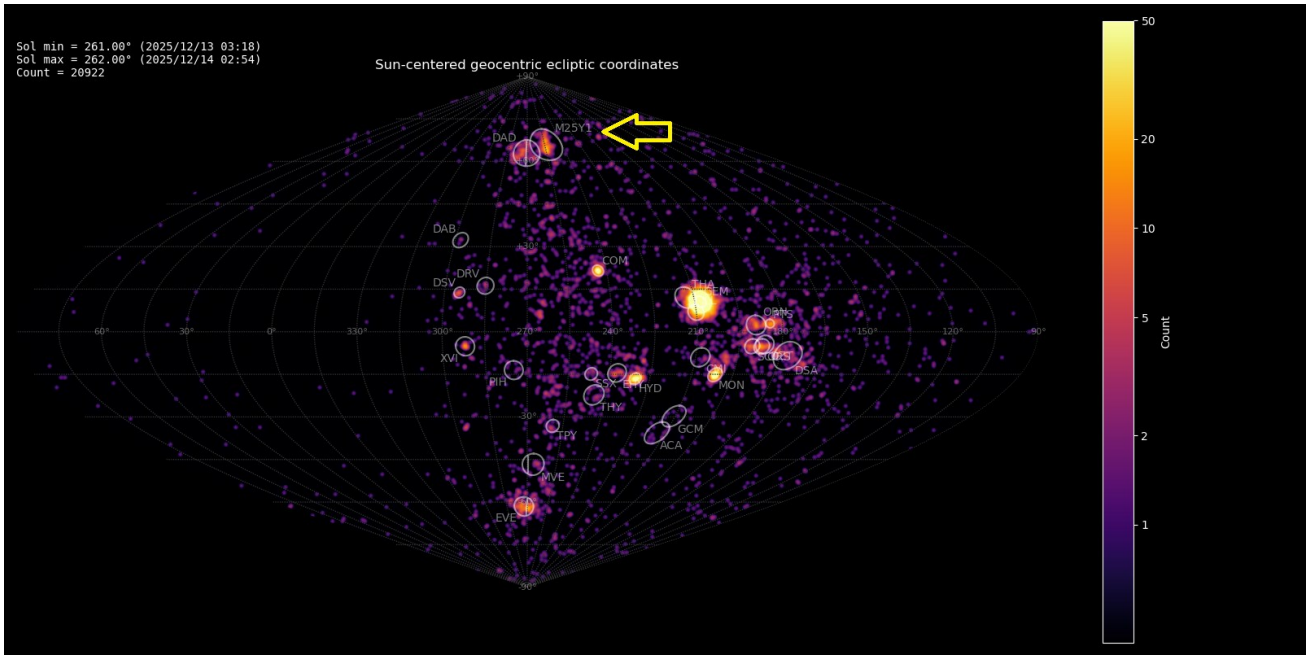

Figure 7 – Radiant density map with 20922 radiants obtained by the Global Meteor Network on 13–14 December, 2025. The position of the M2025-Y1 radiants in Sun-centered geocentric ecliptic coordinates is marked with a yellow arrow.

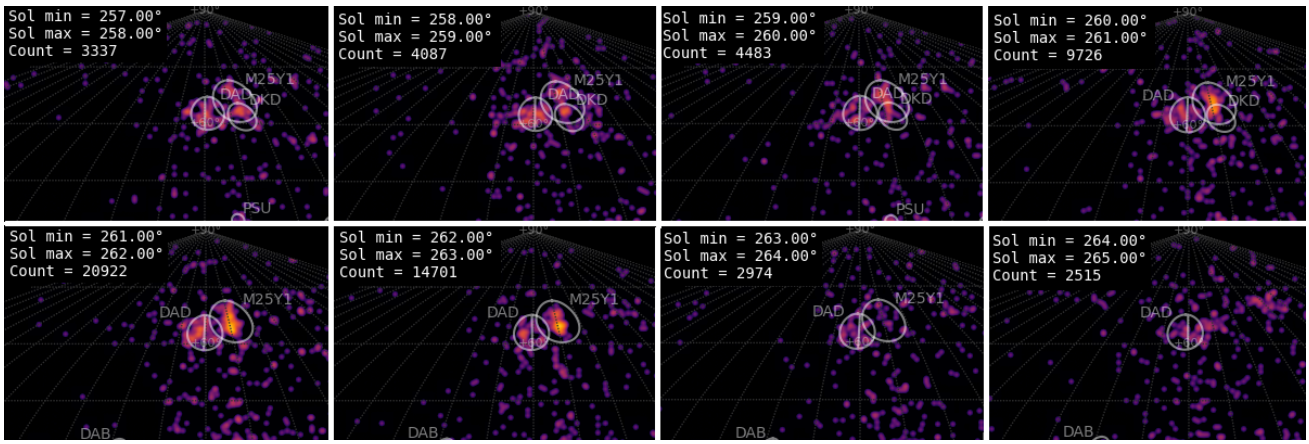

Figure 8 – Radiant density maps for 8–16 December 2025. The shower is labeled M25Y1.

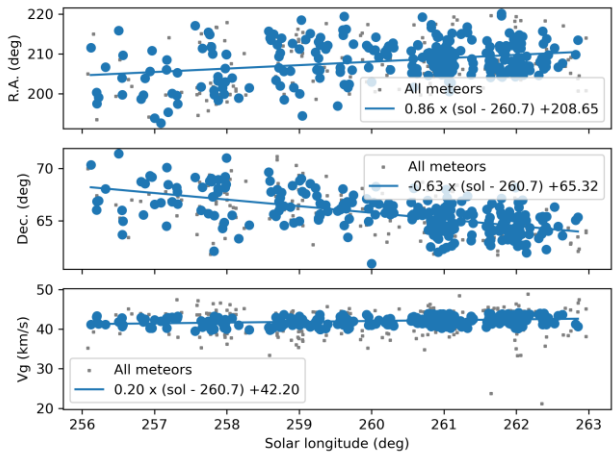

Figure 9 – The radiant drift.

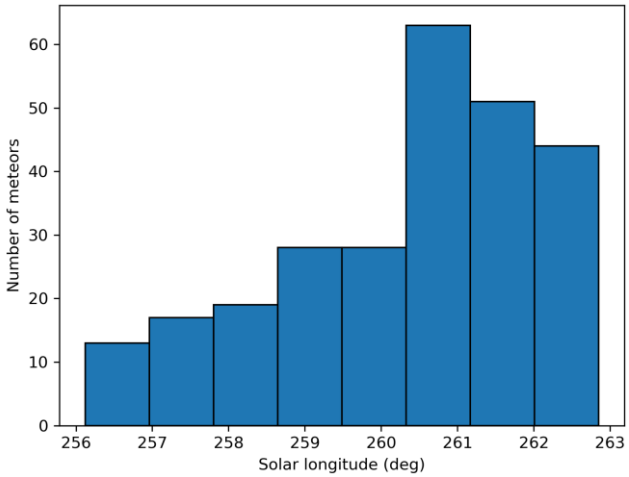

Figure 10 – The uncorrected number of shower meteors recorded per degree in solar longitude.

This first shower identification method allows us to measure the radiant size (*Figure 6*), the radiant drift (*Figure 9*) and the number of M2025-Y1 meteors per degree in Solar Longitude (*Figure 10*).

7.2 Shower classification based on orbits

The first step is to extract all orbit data from the GMN dataset available for the duration of the shower activity in Solar Longitude, 256° to 263°. For the years 2018 to 2025

there are 174427 orbits available within this interval. This selection will serve as a basis for the analysis.

To apply the similarity criteria, we need a first reference orbit to approach the best fitting orbit for M2025-Y1. From the radiant density maps we know the radiant position and the size of the radiant in Sun-centered ecliptic coordinates. We select all meteors that have their radiant within a radiant position roughly estimated from the maps at $\lambda–\lambda_O \sim 252°\pm14°$ and $\beta \sim +66°\pm6$. This sample should include most of the M2025-Y1 meteors. Of the 174427 meteors selected between Solar Longitude 256° and 263°, 1279 have a radiant within these limits. We will use this sample to compute a first mean orbit for M2025-Y1 which will serve as a feed in the iterative procedure to locate orbits that fit within the thresholds of the discrimination criteria. The mean orbit is computed with the method described by Jopek et al (2006) using the Kepler elements q, e, i, Ω and ω. The 1279 selected orbits yield the following mean orbit:

- $q = 0.958261$ AU
- $e = 0.804834$
- $i = 69.93924°$
- $\Omega = 259.4143°$
- $\omega = 196.1131°$

This orbit is used as starting orbit and matched to all 174427 orbits selected between Solar Longitude 256° and 263°. This results in the following numbers of orbits fitting different D-criteria thresholds classes:

- $D_{SH} < 0.250$ & $D_D < 0.105$ & $D_J < 0.250$: 987 (G)
- $D_{SH} < 0.200$ & $D_D < 0.080$ & $D_J < 0.200$: 588 (F)
- $D_{SH} < 0.150$ & $D_D < 0.060$ & $D_J < 0.150$: 266 (E)
- $D_{SH} < 0.125$ & $D_D < 0.050$ & $D_J < 0.125$: 161 (D)
- $D_{SH} < 0.100$ & $D_D < 0.040$ & $D_J < 0.100$: 81 (C)
- $D_{SH} < 0.075$ & $D_D < 0.030$ & $D_J < 0.075$: 33 (B)
- $D_{SH} < 0.050$ & $D_D < 0.020$ & $D_J < 0.050$: 6 (A)
- $D_{SH} < 0.025$ & $D_D < 0.010$ & $D_J < 0.025$: 0 (A+)

These D-criteria do not prove any physical relationship and provide only a parameter that indicates how much two orbits differ. The smaller the value of D, the more similar the orbits are, the larger the value of D, the more difference between the orbit, the less the probability that there is any connection.

Historically, there has been too much confidence in these discrimination criteria and $D_{SH} < 0.250$ was often considered as a safe cutoff to select orbits according to the Southworth and Hawkins D-criterion, or $D_D < 0.105$ for the Drummond criterion. Caution is required as too optimistic cutoff values will include many sporadics that affect, or in some cases ruin, the final solution. The goal is to obtain reliable parameters that are representative for the meteoroid stream. In this perspective, it is better to have less outliers among the meteoroid stream members than to have a result that is contaminated by sporadics. Therefore, we do not use one single criterion but three different combined in order to filter away as many sporadics as possible. The threshold values strongly depend upon the type of orbit. The more sporadic orbits present in the sample used to derive a solution for the investigated meteor shower, the more uncertain the result.

It is recommended not to use the most optimistic cutoff values. The most suitable cutoff values can be derived by try-and-error. If the scatter on the resulting shower orbits is too large, the procedure should be repeated with lower threshold values. In practice it is a matter of experience based upon the type of orbit to pick the right threshold cutoff values. There are different methods to estimate the most relevant cutoff values, such as the Rayleigh fit applied on a set of Discrimination values for a specific criterion like the Drummond criterion for instance (*Figure 11*). In this particular case, the threshold class $D_{SH} < 0.125$ & $D_D < 0.050$ & $D_J < 0.125$ seems most suitable. We use these thresholds to select orbits.

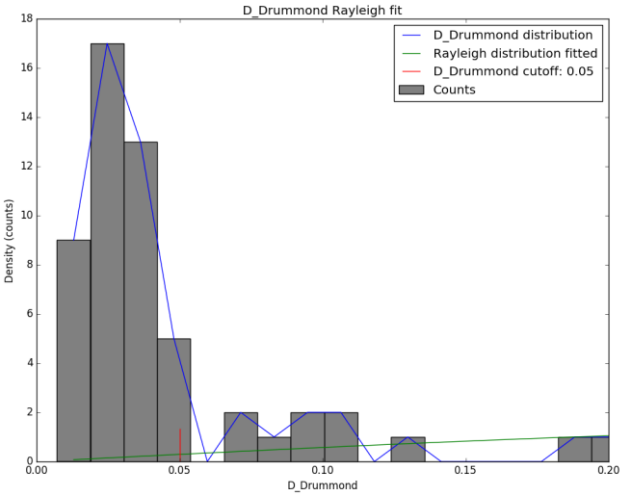

Figure 11 – Rayleigh fit on the Drummond criterion for M2025-Y1, 2025 data.

Table 2 – The Kepler elements for the mean orbit computed at each step in the iteration. The corresponding numbers of orbits that fit the criteria thresholds at each step is listed in *Table 3*.

q	e	i	Ω	ω
0.958261	0.804834	69.93924	259.4143	196.1131
0.963961	0.829654	70.19466	259.7787	196.0776
0.96386	0.856522	70.29293	259.9014	196.0051
0.96374	0.883708	70.50851	260.1155	195.9197
0.963282	0.899591	70.84129	260.0735	196.0455
0.963363	0.907387	71.08345	260.0901	196.0348
0.963446	0.911285	71.19059	260.0956	196.0331
0.963467	0.913492	71.22304	260.0843	196.0079
0.963445	0.914387	71.21668	260.07	196.0104
0.963529	0.91496	71.23434	260.0646	195.986
0.963488	0.91529	71.24994	260.0621	195.9995
0.963484	0.915391	71.26295	260.064	196.0078
0.963484	**0.915391**	**71.26295**	**260.064**	**196.0078**

The 161 orbits that fit this threshold class are selected and a new mean orbit is computed for this selection. This new mean orbit is matched again to the 174427 orbits resulting

in 232 orbits that fit within the selected threshold class (D) (see *Table 3*). A new mean orbit is computed for these 232 orbits, and will be matched with all 174427 orbits. This way an iterative procedure is repeated until the Kepler elements of the obtained mean orbit (*Table 2*) and the number of orbits that fit the threshold class (*Table 3*) and do not change anymore. Then we assume we approached the best representative orbit for the cluster of orbits in our selection.

Table 3 – Evolution of the number of orbits among the sample of 174427 orbits that fit within the different threshold classes for the mean orbit computed at each step in the iteration.

G	*F*	*E*	***D***	*C*	*B*	*A*	*A+*
987	588	266	**161**	81	33	6	0
988	674	376	**232**	140	55	12	0
963	715	481	**357**	208	101	27	0
932	716	521	**416**	296	167	46	4
922	709	529	**423**	319	189	58	6
916	707	526	**424**	318	203	75	9
909	706	521	**425**	320	201	77	6
909	704	519	**428**	324	200	77	6
903	703	517	**428**	327	197	77	8
903	702	517	**430**	326	197	76	8
903	701	514	**429**	327	197	76	8
903	702	513	**429**	328	198	77	8
903	702	513	**429**	328	198	77	8

Table 2 lists the Kepler elements of each mean orbit at each step of the iteration and *Table 3* the corresponding number of orbits that fit within the different threshold classes for these mean orbits for the entire loop of iterations. It is obvious that the starting mean orbit based upon the 1279 meteors that have their radiant within the selected zone included many sporadics and other shower meteors since most of these 1279 meteors don't fit within the threshold values. The number of fitting orbits increases rapidly with each step in the iteration while the cluster of M2025-Y1 orbits is being approached and sporadic orbits being rejected. After twelve steps, 429 orbits fit the threshold class $D_{SH} < 0.125$ & $D_D < 0.050$ & $D_J < 0.125$ and this number (*Table 3*) nor the Kepler elements (*Table 2*) change any further. At this step we conclude that the last mean orbit represents the best fitting solution for the cluster of M2025-Y1 orbits.

The choice of the start orbit for the iteration determines how many steps are needed to approach the best fitting mean orbit. In some cases, it may take only a few steps. If a spurious concentration is searched, the process keeps skipping around. For new activity sources, an estimated radiant area can be used like in the example above. In most cases the GMN orbit data includes a shower association based on known radiant positions. It is possible to derive a mean orbit based upon the GMN shower identification. The GMN orbit dataset has such identification for M2025-Y1 with 370 meteors identified with this new shower in 2025. *Table 4* lists the Kepler elements at each iteration step using the mean orbit for these 370 M2025-Y1 meteors in the dataset in order to find a solution for 2025 data only.

Table 4 – The Kepler elements for the mean orbit computed at each step in the iteration for 2025 data.

q	*e*	*i*	*Ω*	*ω*
0.963691	0.883078	69.97857	260.3954	195.4147
0.964512	0.896789	70.47772	260.4274	195.5483
0.964491	0.901948	70.74938	260.4275	195.5974
0.964493	0.905516	70.89979	260.4216	195.6042
0.964508	0.907729	70.97995	260.4322	195.6119
0.964606	0.908574	70.97657	260.441	195.5711
0.964682	0.909495	70.99641	260.4612	195.5405
0.964698	0.910116	71.01583	260.4589	195.5319
0.9647	0.910762	71.00023	260.4503	195.5205
0.964657	0.911412	70.99261	260.4419	195.5318
0.964657	**0.911412**	**70.99261**	**260.4419**	**195.5318**

Table 5 – Evolution of the number of orbits among the sample of 174427 orbits that fit within the different threshold classes for the mean orbit computed at each step in the iteration for 2025 data.

G	*F*	*E*	***D***	*C*	*B*	*A*	*A+*
434	354	292	**249**	187	101	32	2
425	361	299	**258**	193	118	42	3
425	360	299	**258**	194	124	45	6
421	359	298	**258**	190	123	50	7
423	359	299	**257**	190	122	53	6
422	358	299	**258**	190	120	52	7
424	359	299	**256**	190	119	51	6
424	359	299	**256**	192	119	51	6
424	359	299	**254**	191	118	51	6
424	359	298	**254**	192	117	51	7
424	359	298	**254**	192	117	51	7

For 2025 data, 254 orbits fit the $D_{SH} < 0.125$ & $D_D < 0.050$ & $D_J < 0.125$ threshold values. It is obvious that an outburst occurred in 2025 as previous years had far less M2025-Y1 candidates although that this part of the sky was well covered by GMN in previous years. The number of shower meteors identified using the orbit classification method is much smaller than the 370 M2025-Y1 meteors identified by the radiant classification method.

7.3 Complete example of an in-depth analysis

The two solutions, one for 2025 and one for 2018–2025, make it possible to extract records from the GMN dataset for different threshold classes to make graphics and to compare all meteor shower parameters. In *Table 6*, the results obtained by the orbit identification method, described above, are compared to the result of the radiant based identification method. The plot of the radiant positions in *Figure 12* clearly shows the cluster of M2025-Y1 radiants. Another concentration is visible just south of the M2025-Y1 radiant, the December alpha-Draconids (DAD#334). Right of the M2025-Y1 radiant and partly

mixed with it are the December kappa-Draconids, DKD#336.

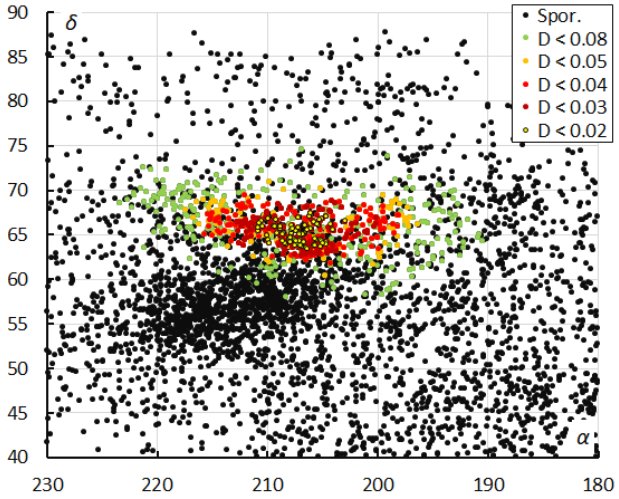

Figure 12 – The radiant distribution during the solar-longitude interval 256° – 263° in equatorial coordinates, color-coded for different threshold values of the combined similarity criteria.

Table 6 – Comparing solutions for M2025-Y1 derived by the radiant based method and the orbit based method for D_{SH} < 0.125 & D_D < 0.050 & D_J < 0.125 for 2025 data, both compared to 2019–2025 data and the December kappa-Draconids, DKD#336 (Jenniskens, 2023).

	Radiant method 2025	Orbit method 2025	Orbit method 2019-25	DKD #336
$\lambda_\odot$ (°)	260.7	260.9	260.6	251.2
$\lambda_{\odot b}$ (°)	256.0	256.2	256.1	244
$\lambda_{\odot e}$ (°)	263.0	262.9	263.0	261
α_g (°)	208.6	207.5	206.7	187.1
δ_g (°)	+65.3	+65.4	+65.5	+69.9
$\Delta\alpha_g$ (°)	+0.86	+0.97	+1.03	+1.05
$\Delta\delta_g$ (°)	–0.63	–0.64	–0.65	–0.50
v_g (km/s)	42.2	42.9	43.0	43.5
H_b (km)	105.0	105.4	105.6	107.7
H_e (km)	94.6	94.5	94.1	93.3
H_p (km)	99.4	99.2	99.2	98.5
Mag_{Ap}	–0.1	–0.25	–0.3	0.0
λ_g (°)	153.93	154.3	153.54	135.6
$\lambda_g - \lambda_\odot$ (°)	253.23	253.2	252.9	244.4
β_g (°)	+65.93	+65.3	+65.1	+61.7
a (A.U.)	8.577	10.9	11.4	9.01
q (A.U.)	0.965	0.965	0.964	0.930
e	0.887	0.911	0.915	0.897
i (°)	70.2	71.0	71.3	72.9
ω (°)	195.4	195.5	196.0	208.2
Ω (°)	260.3	260.4	260.1	251.2
Π (°)	95.8	96.0	96.1	99.7
T_j	1.01	0.87	0.84	0.89
N	263	254	429	1982

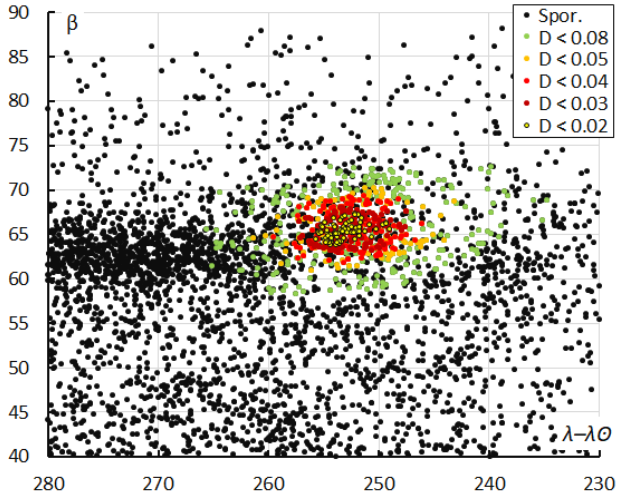

Figure 13 – The radiant distribution during the solar-longitude interval 256° – 263° in Sun-centered geocentric ecliptic coordinates, color-coded for different threshold values of the combined similarity criteria.

The radiant plot in Sun-centered geocentric ecliptic coordinates neutralizes the radiant drift caused by the movement of the Earth on its orbit around the Sun. The large scatter on radiants for D_{SH} < 0.2 & D_D < 0.08 & D_J < 0.2 indicates that these threshold values are too tolerant. *Figure 13* shows a very dense cluster of M2025-Y1 radiants. At left is the concentration of the December alpha-Draconids and at right are December kappa-Draconids radiants. This shower had its maximum nine days before M2025-Y1, but the end of its activity period overlaps with the first days of the M2025-Y1 activity. Several M2025-Y1 orbits had been initially classified as December kappa-Draconids. The meteoroid stream parameters of this shower are added to *Table 6* as these resemble a lot to those of M2025-Y1.

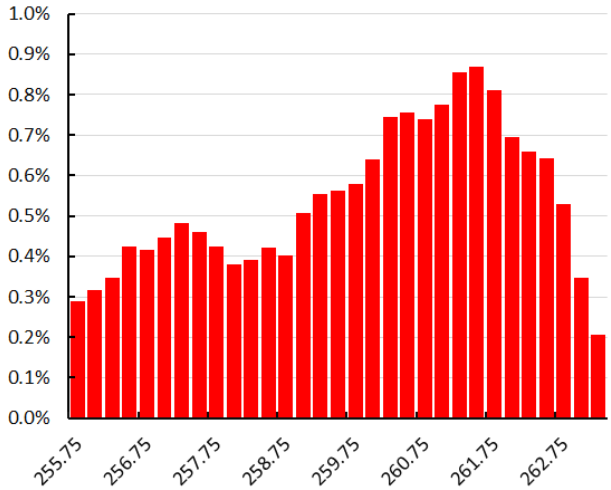

Figure 14 – The percentage of M2025-Y1-meteors relative to the total number of meteors without the Geminids.

The percentage of M2025-Y1 meteors relative to the total number of meteors provides a way to reconstruct an activity profile. As one of the richest meteor showers of the year – the Geminids – had their maximum during this time interval, the Geminids were disregarded. Although the

median value for the Solar Longitude is 260.7°, there is no real peak activity but enhanced activity for about two days.

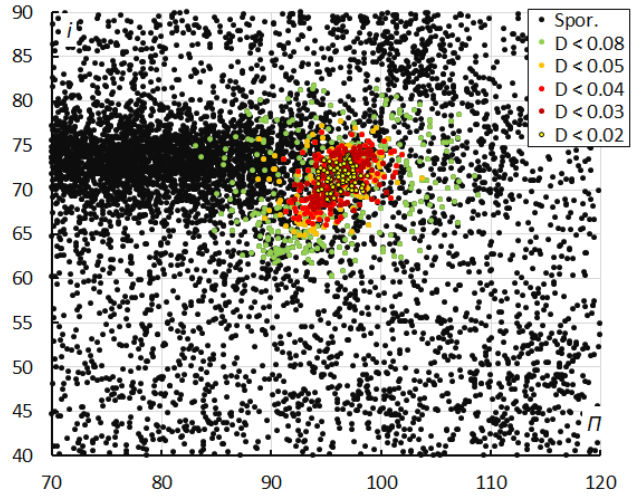

Figure 15 – The diagram of the inclination *i* versus the longitude of perihelion *Π* color-coded for different classes of D-criteria thresholds, for $\lambda_\odot$ between 256° and 263°.

Apart from radiant plots, diagrams with Kepler elements plotted versus each other is a useful way to visualize clusters with similar orbital elements. One of the most suitable combinations is the inclination versus Longitude of Perihelion. In *Figure 15* the M2025-Y1 concentration is very well visible. At the left of it, the December alpha-Draconids. Next to the M2025-Y1 cluster and partially intermixed are the December kappa-Draconids, suggesting that there is a likely relationship between M2025-Y1 and the December kappa-Draconids.

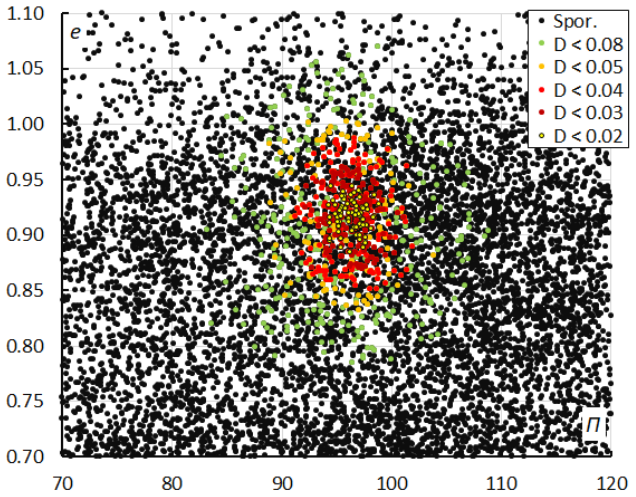

Figure 16 – The diagram of the eccentricity *e* versus the longitude of perihelion *Π* color-coded for different classes of D-criteria thresholds, for $\lambda_\odot$ between 256° and 263°.

Depending on the type of orbits meteoroid streams appear as distinct clusters in these diagrams. Different clusters are visible in *Figures 16 to 19*, caused by different meteor showers such as e-Velids (EVE#746), alpha-Canis Majorids (ACA#394), gamma-Canis Majorids (GCM#395), etc. One particular activity source appears close to the M2025-Y1 or partly mixed in its cluster, the December kappa-Draconids (DKD#336). This suggests a physical connection between M2025-Y1 and the December kappa-Draconids. A sample of December kappa-Draconids has been taken from the 2024 GMN data for comparison.

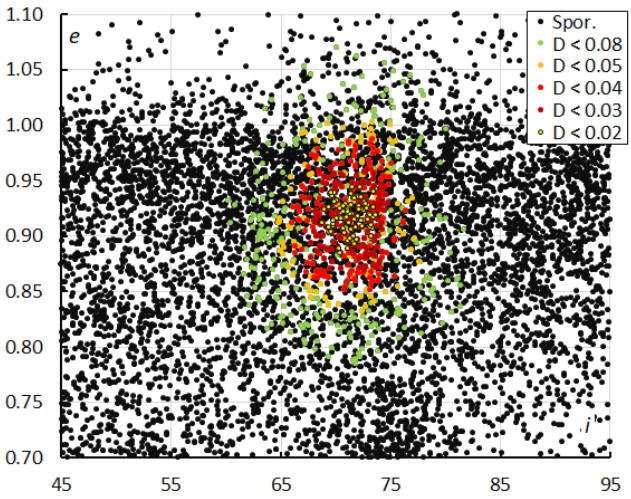

Figure 17 – The diagram of the eccentricity *e* versus the inclination *i* color-coded for different classes of D-criteria thresholds, for $\lambda_\odot$ between 256° and 263°.

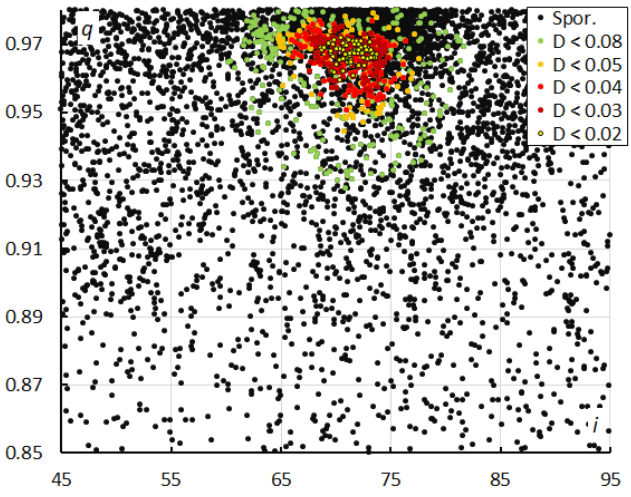

Figure 18 – The diagram of the perihelion distance *q* versus the inclination *i* color-coded for different classes of D-criteria thresholds, for $\lambda_\odot$ between 256° and 263°.

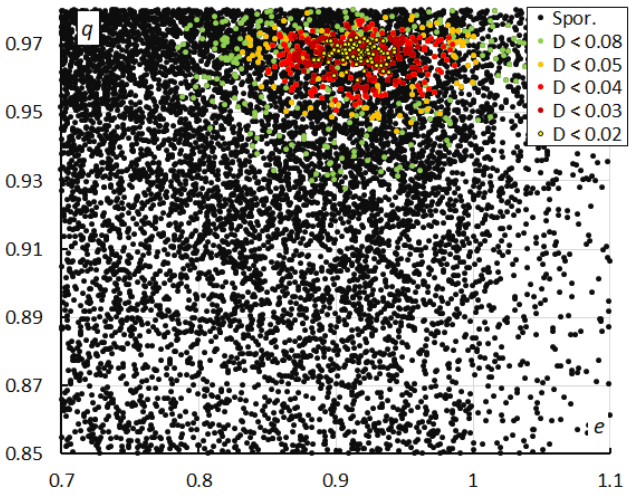

Figure 19 – The diagram of the perihelion distance *q* versus the eccentricity *e* color-coded for different classes of D-criteria thresholds, for $\lambda_\odot$ between 256° and 263°.

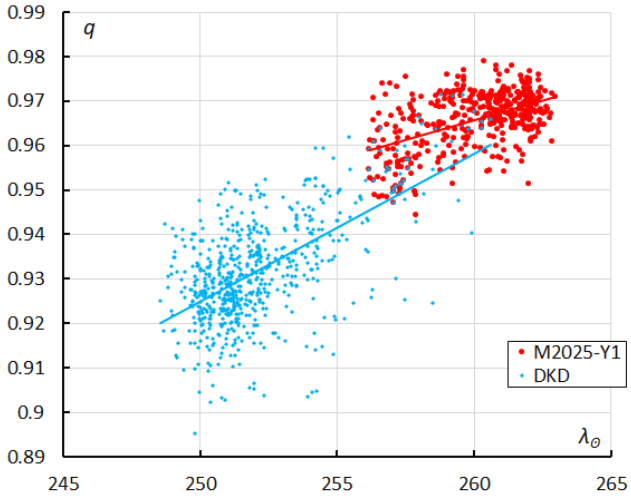

Figure 20 – The evolution of the perihelion distance q in function of the Solar Longitude $\lambda_\odot$ for the M2025-Y1 orbits (2019–2025) and December kappa-Draconids (2024).

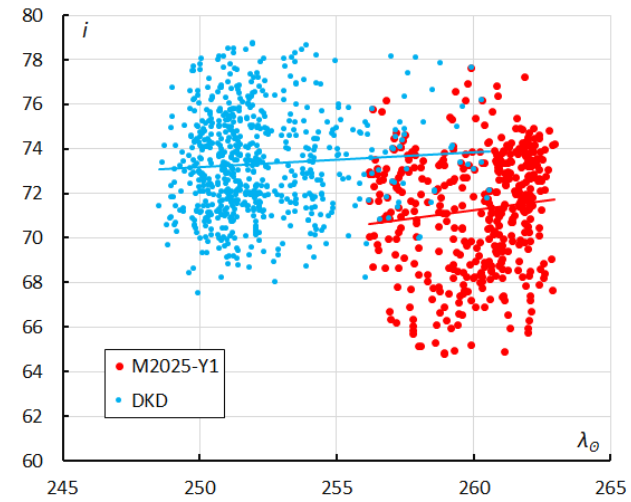

Figure 21 – The evolution of the inclination i in function of the Solar Longitude $\lambda_\odot$ for the M2025-Y1 orbits (2019–2025) and December kappa-Draconids (2024).

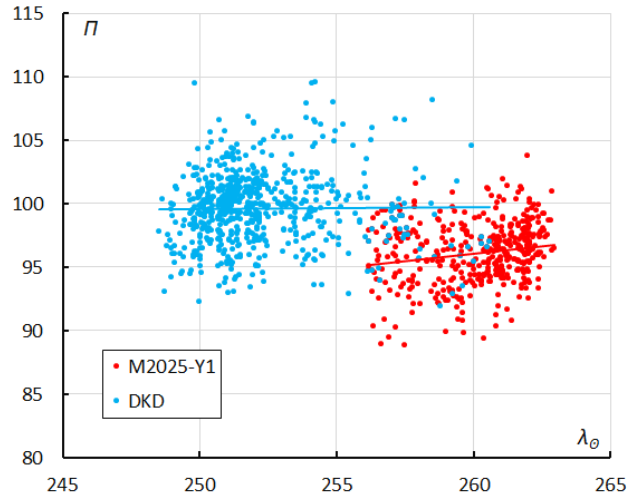

Figure 22 – The evolution of the Longitude of Perihelion Π in function of the Solar Longitude $\lambda_\odot$ for the M2025-Y1 orbits (2019–2025) and December kappa-Draconids (2024).

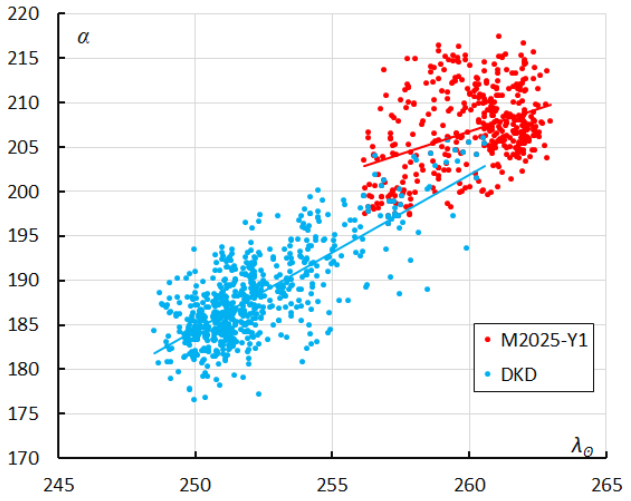

Figure 23 – The radiant drift in Right Ascension α in function of the Solar Longitude $\lambda_\odot$ for the M2025-Y1 orbits (2019–2025) and December kappa-Draconids (2024).

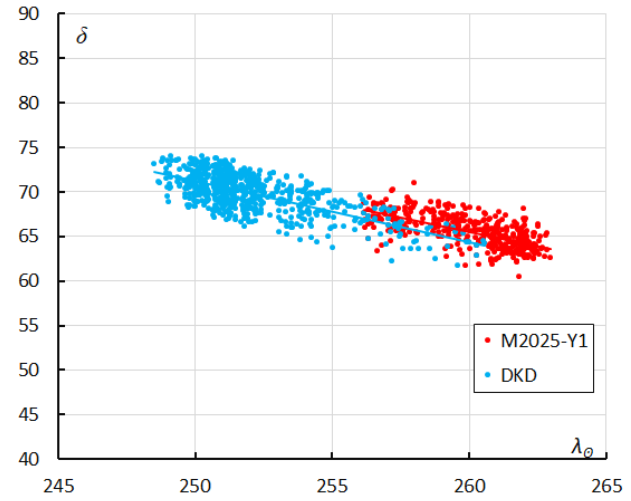

Figure 24 – The radiant drift in Declination δ in function of the Solar Longitude $\lambda_\odot$ for the M2025-Y1 orbits (2019–2025) and December kappa-Draconids (2024).

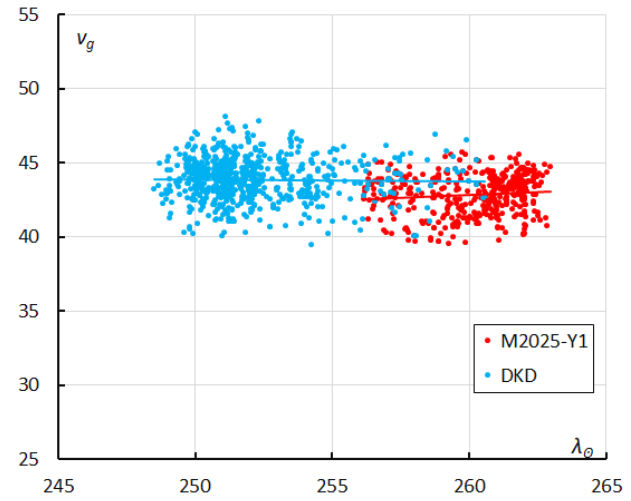

Figure 25 – The geocentric velocity v_g in function of the Solar Longitude $\lambda_\odot$ for the M2025-Y1 orbits (2019–2025) and December kappa-Draconids (2024).

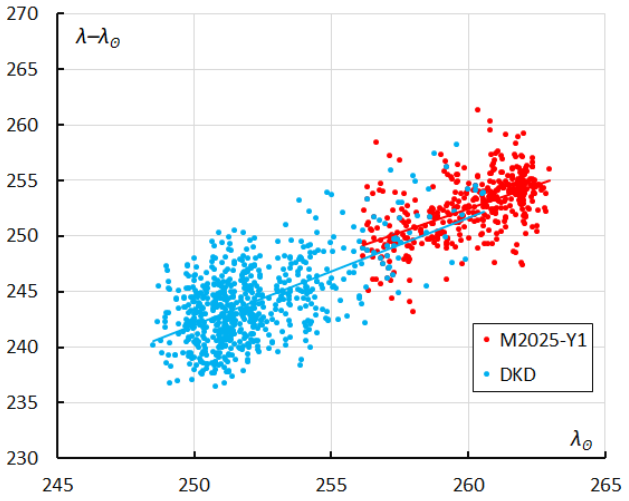

Figure 26 – The Sun-centered geocentric longitude $\lambda–\lambda_\odot$ in function of the Solar Longitude $\lambda_\odot$ for the M2025-Y1 orbits (2019–2025) and December kappa-Draconids (2024).

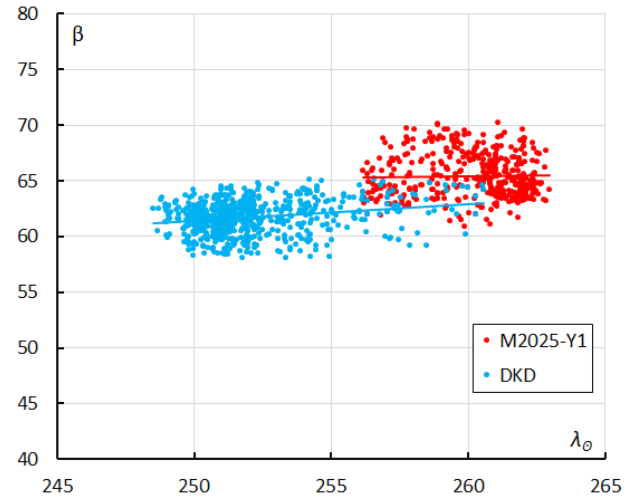

Figure 27 – The geocentric latitude β in function of the Solar Longitude $\lambda_\odot$ for the M2025-Y1 orbits (2019–2025) and December kappa-Draconids (2024).

The distributions for different parameters in function of time ($\lambda_\odot$) show a likely link between M2025-Y1 and the December kappa-Draconids. The perihelion distance q increases during the activity period and where the final days of activity for the DKD ends, M2025-Y1 starts (*Figure 20*). The same for inclination i (*Figure 21*) and Longitude of Perihelion Π (*Figure 22*) with a small offset in position.

The radiant positions in Right Ascension (*Figure 23*) and Declination (*Figure 24*) visualize the radiant drift caused by the movement of the Earth. The radiant drift at the end of the activity of the December kappa-Draconids overlaps with the start of the M2025-Y1 activity and displays a similar trend. The geocentric velocity is comparable (*Figure 25*). The radiant drift in Sun-centered geocentric coordinates is caused by changes in the orientation of the orbital plane during Earth's transit through the meteoroid stream. The December kappa-Draconids and M2025-Y1 align very well in *Figures 26 and 27*.

The Tisserand value relative to Jupiter $T_J = 0.84$ is a Halley-type comet orbit with a subclassification as a Mellish-type shower. This is very close to the value for the December kappa-Draconids which have $T_J = 0.89 \pm 0.52$ (Jenniskens, 2023). Jenniskens associates the December kappa-Draconids with comet 12P/Pons-Brooks.

A search for possible parent bodies for the M2025-Y1 orbit resulted in the ten best matches listed in *Table 7* with comet 12P/Pons-Brooks as most likely candidate, the same parent body of the December kappa-Draconids. The M2025-Y1 orbit fits with the 12P/Pons-Brooks orbit with $D_{SH} = 0.21$ & $D_D = 0.11$ & $D_J = 0.14$, the DKD#336 orbit fits with $D_{SH} = 0.21$ & $D_D = 0.10$ & $D_J = 0.17$. *Figure 28* shows the three highly inclined orbits in space.

Table 7 – Top ten matches of a search for possible parent bodies with $D_D < 0.27$, based upon the mean orbit derived from the radiant classification method.

Name	D_D
12P/Pons-Brooks	0.12
C/1785 A1 (Messier-Mechain)	0.132
8P/Tuttle	0.15
C/1898 L2 (Perrine)	0.228
C/1975 X1 (Sato)	0.231
C/1991 Y1 (Zanotta-Brewington)	0.238
C/2012 V2 (LINEAR)	0.243
C/2012 L2 (LINEAR)	0.248
C/2010 G1 (Boattini)	0.259
(369264) 2009 MS	0.262

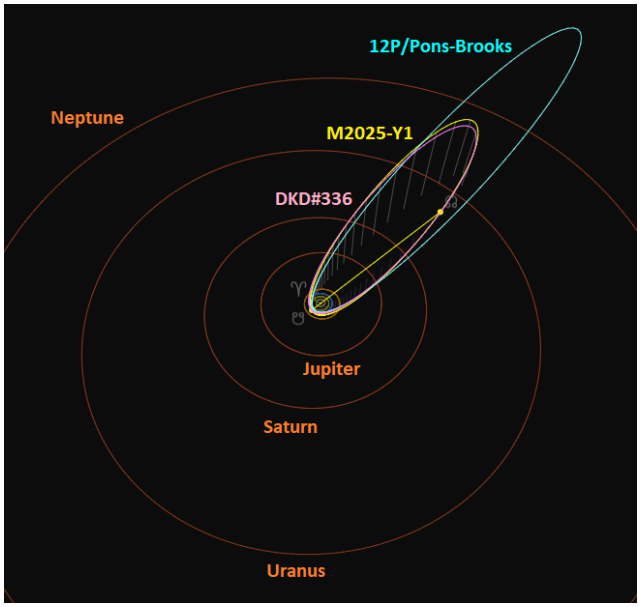

Figure 28 – Comparing the M2025-Y1 solution (yellow) and the December kappa-Draconids (DKD#336) (pink) with the orbit of the most likely parent body 12P/Pons-Brooks (blue). (Plotted with the Orbit visualization app provided by Pető Zsolt).

The DKD#336 orbit intersects the Earth orbit at its descending node shortly before the M2025-Y1 orbit intersects the Earth orbit. The descending node of comet 12P/Pons-Brooks crosses the ecliptic inside the Earth orbit (*Figure 29*). The object is classified as a Near Earth

Asteroid (NEA)[6]. The comet was discovered in July 1812 at Marseilles Observatory by the French astronomer Jean-Louis Pons and was rediscovered by the British-American astronomer William Robert Brooks in 1883, it received the name Pons-Brooks. With its orbital period of 71.491 years, it reoccurred on 20 June 1953. The comet has a nucleus about 34 km in diameter. Older observations were related to this comet in 1385 and 1457. Its most recent perihelion passage took place on April 21, 2024.

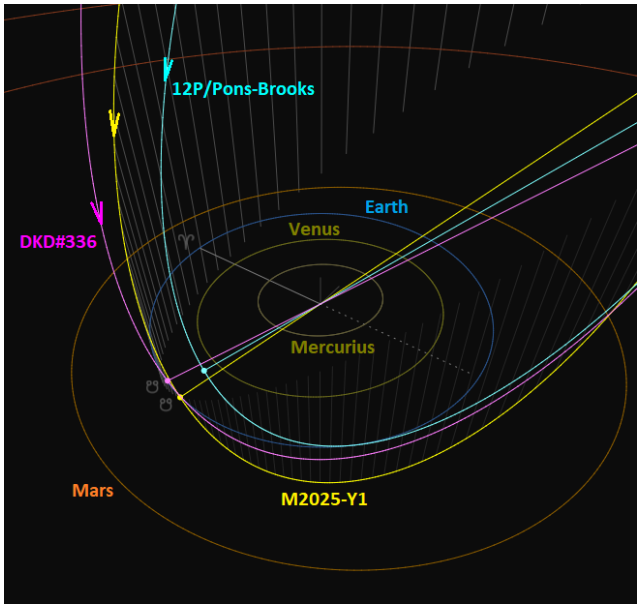

Figure 29 – Comparing the M2025-Y1 solution (yellow) and the December kappa-Draconids (DKD#336) (pink) with the orbit of the most likely parent body 12P/Pons-Brooks (blue), close-up at the inner Solar System. (Plotted with the Orbit visualization app provided by Pető Zsolt).

Belarusian and Ukrainian video meteor networks obtained a spectrum of a M2025-Y1 meteor which belongs to the Fe-poor type. Meteoroids of this type are rich in magnesium and have a normal sodium content, but poor iron content. This is typical for meteoroids with Halley-type orbits (Harachka, 2026). This is different from the spectral type cited by Jenniskens (2023) where December kappa-Draconids are listed as Na poor/free, based on research by Matlovič et al. (2019).

The appearance of a meteor activity outburst, initially considered as a possible new meteor shower, could be linked to the known December kappa-Draconids and the parent object 12P/Pons-Brooks. The outburst occurred after the known end of the activity period of this shower and must have been caused by an unknown dust trail related to the parent body which passed its perihelion in April 2024. In previous years far less possible M2025-Y1 meteors were counted: zero in 2018; two in 2019, three in 2020, nine in 2021, 28 in 2022, 64 in 2023, 71 in 2024 and 252 in 2025. The numbers partially represent the expansion of the GMN network but the outburst in 2025 is clearly the result of an encounter with a dust trail.

8 Conclusion

Meteoroid orbit data offer a completely different gamma of possibilities for meteor shower analyses than what was possible before statistical relevant datasets with meteoroid orbits became available. Amateurs focused their meteor shower analyses on visual observing data for major showers. Minor showers suffered from the uncertainty in radiant determination by single station visual observers and small number statistics. The large numbers of meteoroid orbits obtained by low-light camera networks make it possible to unravel weak activity sources. So far, very few amateurs gained expertise in this field where many discovered but unconfirmed activity sources wait for analyses that can help to document these meteor showers and get them confirmed as established shower in the IAU-MDC Working List of Meteor Showers.

This publication explains the method to identify shower meteors using D-criteria on meteoroid orbits. The method is demonstrated with an analysis of the possible new meteor shower M2025-Y1 that was discovered in December 2025. The ‘new’ meteor shower has the same characteristics as the minor annual shower December kappa-Draconids and appears to have been produced by an unknown dust trail beyond the known activity period of the December kappa-Draconids.

The authors recommend the IAU-MDC to move the entry for M2025-Y1 as a new solution for the December kappa-Draconids. Comet 12P/Pons-Brooks should be listed as parent body.

Acknowledgments

This report is based on the data of the Global Meteor Network (Vida et al., 2020a; 2020b; 2021) which is released under the CC BY 4.0 license[7]. We thank all 927 participants in the Global Meteor Network project for their contribution and perseverance. A list with the names of the volunteers who contribute to GMN has been published in the 2025 annual report (Roggemans et al., 2026). The following 760 cameras contributed to paired meteors used in this study:

AT0004, BA0001, BA0002, BA0003, BA0004, BA0005, BE0001, BE0003, BE0004, BE0005, BE0006, BE0007, BE0008, BE0009, BE000B, BE000C, BE000E, BE000G, BE000H, BE000K, BE000L, BE000M, BE000Q, BE000S, BE000T, BE000U, BE000V, BE000W, BE000X, BE000Y, BE000Z, BE0010, BE0011, BE0013, BE0014, BE0017, BE0018, BE0019, BE001A, BG0001, BG0003, BG0009, BG000A, BG000B, BG000C, BG000F, BG000G, BG000H, BG000J, CA000F, CA000Q, CA000U, CA000V, CA001F, CA001R, CA001X, CA0023, CA002F, CA002K, CA002L, CA002N, CA0031, CA0037, CA003A, CA003B, CA003C, CA003D, CAWEC1, CH0003, CH0004, CH0005, CZ0003, CZ0004, CZ0006, CZ0007, CZ0008, CZ000A, CZ000F, CZ000H, CZ000J, CZ000L, CZ000M, CZ000P, CZ000R, CZ000W, CZ000X, DE0001, DE0002, DE0004, DE0005, DE0006, DE0007, DE0009, DE000B,

[6] https://www.spacereference.org/comet/12p-pons-brooks

[7] https://creativecommons.org/licenses/by/4.0/

DE000G, DE000J, DE000K, DE000M, DE000Q, DE000S, DE000W, DE000X, DE000Y, DE0011, DE0012, DE0013, DE0015, DE0016, DK0001, DK0003, DK0006, DK0009, DK000J, DK000L, DK000M, DK000Q, DK000R, DK000T, ES0001, ES0002, ES0003, ES0004, ES0005, ES0009, ES000D, ES000F, ES000H, ES000Q, ES000T, ES000U, ES000V, ES000X, ES0013, ES0016, ES0019, ES001A, ES001F, FR0003, FR0006, FR000A, FR000F, FR000R, FR000U, FR000X, FR000Y, FR000Z, FR0011, FR0013, FR0014, GR0002, GR0003, GR0004, GR0005, GR0006, GR0007, GR0008, GR0009, HR0001, HR0002, HR0006, HR0007, HR0008, HR000D, HR000J, HR000P, HR000Q, HR000S, HR000U, HR000V, HR000W, HR0010, HR0015, HR001D, HR001E, HR001J, HR001K, HR001M, HR001R, HR001V, HR001X, HR001Z, HR0025, HR0027, HR002D, HR002E, HR002F, HR002G, HR002H, HR002J, HR002K, HR002R, HR002T, HR002V, HR002W, HR002X, HR002Y, HU0002, HU0003, IE0004, IE000G, IE000H, IE000J, IE000M, IL0002, IL0008, IL0009, IL000A, IT0001, IT0004, IT0007, IT0008, IT000A, IT000B, KR0002, KR0004, KR0006, KR0007, KR0009, KR000A, KR000B, KR000C, KR000D, KR000E, KR000F, KR000G, KR000H, KR000J, KR000K, KR000L, KR000M, KR000N, KR000P, KR000Q, KR000R, KR000S, KR000V, KR000Y, KR0010, KR0011, KR0013, KR0014, KR0015, KR0016, KR0017, KR0018, KR0019, KR001A, KR001B, KR001C, KR001E, KR001H, KR001K, KR001L, KR001M, KR001X, KR001Y, KR001Z, KR0020, KR0021, KR0022, KR0023, KR0024, KR0025, KR0026, KR0027, KR0028, KR0029, KR002A, KR002B, KR002C, KR002D, KR002E, KR002F, KR002G, KR002L, KR002M, KR002P, KR002Q, KR002R, KR002S, KR0036, KR0037, KR003A, KR003J, KR003L, KR003M, KR003N, KR003P, KR003Q, KR003R, KR003S, KR003T, KR003U, KR003V, KR003W, KR003X, LU0001, MX000D, NL0001, NL0006, NL0009, NL000A, NL000B, NL000C, NL000D, NL000G, NL000K, NL000M, NL000N, NL000P, NL000Q, NL000R, NL000S, NL000T, NL000U, NL000Z, NL0011, NL0013, NL0014, NL0017, NL0019, NL001E, PT0002, PT0003, RU0001, RU0003, RU0004, RU0008, RU0009, RU000E, RU000F, RU000M, RU000N, RU000Q, RU000T, RU000Y, RU0016, RU0017, RU0018, RU0019, SI0001, SI0002, SI0003, SI0004, SI0005, SI0006, SK0002, SK0003, SK0004, SK0005, SK0006, UA0001, UA0002, UK0001, UK0004, UK0006, UK0008, UK0009, UK000B, UK000D, UK000F, UK000H, UK000J, UK000P, UK000S, UK000T, UK000U, UK000Y, UK000Z, UK001E, UK001H, UK001K, UK001L, UK001M, UK001N, UK001P, UK001Q, UK001R, UK001S, UK001T, UK001U, UK001V, UK001W, UK001Z, UK0021, UK0022, UK0024, UK0025, UK0026, UK0027, UK002F, UK002J, UK002K, UK002L, UK002Q, UK002S, UK002T, UK002W, UK002X, UK002Z, UK0030, UK0031, UK0032, UK0034, UK0035, UK0039, UK003A, UK003B, UK003C, UK003D, UK003E, UK003F, UK003L, UK003N, UK003T, UK003U, UK003V, UK003W, UK003X, UK003Y, UK003Z, UK0041, UK0042, UK0045, UK0049, UK004B, UK004C, UK004D, UK004E, UK004F, UK004G, UK004J, UK004M, UK004N, UK004P, UK004U, UK004V, UK0050, UK0051, UK0055, UK0057, UK005C, UK005E, UK005G, UK005H, UK005J, UK005L, UK005M, UK005N, UK005P, UK005R, UK005S, UK005U, UK005V, UK0061, UK0062, UK0063, UK0066, UK0067, UK006A, UK006B, UK006C, UK006D, UK006G, UK006J, UK006L, UK006P, UK006Q, UK006S, UK006T, UK006U, UK006V, UK006X, UK006Z, UK0070, UK0072, UK0073, UK0074, UK0077, UK0078, UK0079, UK007A, UK007B, UK007C, UK007E, UK007G, UK007H, UK007J, UK007L, UK007N, UK007P, UK007Q, UK007R, UK007U, UK007V, UK007Y, UK007Z, UK0080, UK0081, UK0082, UK0083, UK0084, UK0085, UK0086, UK0087, UK0088, UK0089, UK008A, UK008B, UK008C, UK008D, UK008E, UK008F, UK008G, UK008H, UK008J, UK008Q, UK008R, UK008S, UK008T, UK008U, UK008V, UK008X, UK008Z, UK0090, UK0092, UK0096, UK0098, UK0099, UK009A, UK009C, UK009D, UK009F, UK009G, UK009J, UK009K, UK009L, UK009M, UK009P, UK009Q, UK009R, UK009S, UK009T, UK009U, UK009V, UK009W, UK009X, UK00A0, UK00A1, UK00A2, UK00A3, UK00A4, UK00A5, UK00A6, UK00A7, UK00AA, UK00AB, UK00AD, UK00AE, UK00AF, UK00AG, UK00AJ, UK00AK, UK00AL, UK00AM, UK00AN, UK00AP, UK00AQ, UK00AS, UK00AT, UK00AU, UK00B0, UK00B1, UK00B2, UK00B5, UK00B6, UK00BA, UK00BB, UK00BC, UK00BH, UK00BJ, UK00BK, UK00BL, UK00BN, UK00BQ, UK00BW, UK00C0, UK00C1, UK00C2, UK00C3, UK00C4, UK00C6, UK00C7, UK00C9, UK00CA, UK00CC, UK00CD, UK00CE, UK00CH, UK00CJ, UK00CK, UK00CQ, UK00CS, UK00CT, UK00CU, UK00CV, UK00CZ, UK00D7, UK00D9, UK00DA, UK00DB, UK00DD, UK00DE, UK00DG, UK00DH, UK00DJ, US0001, US0002, US0003, US0004, US0005, US0006, US0007, US0008, US0009, US000A, US000C, US000D, US000E, US000G, US000H, US000J, US000K, US000L, US000M, US000N, US000P, US000R, US000S, US000U, US000V, US0019, US001E, US001G, US001L, US001N, US001P, US001Q, US001R, US001U, US001V, US0020, US0021, US0022, US0023, US0026, US0027, US002A, US002D, US002E, US002J, US002L, US002M, US002N, US002P, US002Q, US002R, US002W, US002X, US002Y, US0030, US0035, US0036, US0037, US0038, US0039, US003G, US003M, US003N, US003P, US003Q, US003R, US003S, US003T, US003Y, US0040, US0043, US0044, US0045, US004B, US004C, US004D, US004J, US004L, US004M, US004N, US004P, US004Q, US0050, US0051, US0054, US0055, US0059, US005A, US005B, US005C, US005E, US005F, US005K, US005W, US005X, US005Y, US005Z, US0061, US0062, US0066, US0067, US0068, US006B, USL002, USL003, USL004, USL005, USL006, USL007, USL008, USL009, USL00A, USL00B, USL00C, USL00D, USL00E, USL00F, USL00G, USL00J, USL00K, USL00L, USL00M, USL00N, USL00P, USL00Q, USL00Y, USL00Z, USL010, USL011, USL012, USL013, USL014, USL015, USL016, USL017, USL019, USL01A, USL01B, USL01C, USL01D, USL01E, USV001, USV002, USV003

References

Drummond J. D. (1981). “A test of comet and meteor shower associations”. *Icarus*, **45**, 545–553.

Harachka Y. (2026). “Possible new meteor shower in Draco (M2025-Y1)”. *eMetN Meteor Journal*, **11**, 52–55.

Jenniskens P. (2023). Atlas of Earth’s meteor showers. Elsevier, Cambridge, United states. ISBN 978-0443-23577-1. Page 795.

Jopek T. J. (1993). “Remarks on the meteor orbital similarity D-criterion”. *Icarus*, **106**, 603–607.

Jopek T. J., Rudawska R. and Pretka-Ziomek H. (2006). “Calculation of the mean orbit of a meteoroid stream”. *Monthly Notices of the Royal Astronomical Society*, **371**, 1367–1372.

Matlovič P., Tóth J., Rudawska R., Kornoš L., and Pisarčíková A. (2019). “Spectral and orbital survey of medium-sized meteoroids”. *Astronomy & Astrophysics*, **629**, id.A71.

Meeus J. (1998). Astronomical Algorithms. Willmann-Bell, Inc. Richmond, Virginia, USA.

Moorhead A. V., Clements T. D., Vida D. (2020). “Realistic gravitational focusing of meteoroid streams”. *Monthly Notices of the Royal Astronomical Society*, **494**, 2982–2994.

Neslušan L., Svoreň J., Porubčan V. (1995). “Procedure of selection of meteors from major streams for determination of mean orbits”. *Earth, Moon, and Planets*, **68**, 427–433.

Rendtel J. (2020). Handbook for meteor observers. IMO, Potsdam, Germany.

Roggemans P., Campbell-Burns P., Kalina M., McIntyre M., Scott J. M., Šegon D., Vida D. (2026). “Global Meteor Network report 2025”. *eMetN Meteor Journal*, **11**, 89–129.

Rudawska R., Matlovič P., Tóth J., Kornoš L. (2015). “Independent identification of meteor showers in EDMOND database”. *Planetary and Space Science*, **118**, 38–47.

Steyaert C. (1991). “Calculating the solar longitude 2000.0”. *WGN Journal of the IMO*, **19**, 31–34.

Southworth R. B. and Hawkins G. S. (1963). “Statistics of meteor streams”. *Smithsonian Contributions to Astrophysics*, **7**, 261–285.

Vida D., Gural P., Brown P., Campbell-Brown M., Wiegert P. (2020a). “Estimating trajectories of meteors: an observational Monte Carlo approach - I. Theory”. *Monthly Notices of the Royal Astronomical Society*, **491**, 2688–2705.

Vida D., Gural P., Brown P., Campbell-Brown M., Wiegert P. (2020b). “Estimating trajectories of meteors: an observational Monte Carlo approach - II. Results”. *Monthly Notices of the Royal Astronomical Society*, **491**, 3996–4011.

Vida D., Šegon D., Gural P. S., Brown P. G., McIntyre M. J. M., Dijkema T. J., Pavletić L., Kukić P., Mazur M. J., Eschman P., Roggemans P., Merlak A., Zubrović D. (2021). “The Global Meteor Network – Methodology and first results”. *Monthly Notices of the Royal Astronomical Society*, **506**, 5046–5074.

New meteor shower in Virgo (M2026-D1)

Damir Šegon[1,2], Denis Vida[3,4], Paul Roggemans[5], James M. Scott[6], Jeff Wood[7]

[1] **Astronomical Society Istra Pula, Park Monte Zaro 2, 52100 Pula, Croatia**

[2] **Višnjan Observatory, Istarska 5, 52463 Višnjan, Croatia**
damir@astro.hr

[3] **Department of Physics and Astronomy, University of Western Ontario, Richmond Street, London, N6A 3K7, Ontario, Canada**

[4] **Institute for Earth and Space Exploration, University of Western Ontario, Perth Drive, London, N6A 5B8, Ontario, Canada**
denis.vida@gmail.com

[5] **Pijnboomstraat 25, 2800 Mechelen, Belgium**

[6] **Department of Geoscience, Aarhus University, Høegh-Guldbergs Gade 2. DK-8000 Aarhus C, Denmark**

[7] **PO Box 162, Willetton, Western Australia 6955, Australia**

A new meteor shower has been detected between the 20th and 26st of February 2026 from a radiant at R.A. = 161.6° and Decl.= +8.9° in the constellation of Virgo, with a geocentric velocity of 27.3 km/s on a Jupiter family comet orbit. The new shower has been included in the IAU-MDC working list of meteor showers with the provisional identification M2026-D1.

1 Introduction

Previously unrecognized meteor activity appeared as a bright spot on the GMN radiant density map of 21–22 February in 2026 (*Figure 1*). A preliminary analysis revealed that the activity had been ongoing for a few days, with the activity having ceased by the 1st of March (*Figure 2*). The shower was detected by 341 cameras from Austria, Australia, Belgium, Bosnia Herzegovina, Canada, Croatia, Czech Republic, France, Greece, Germany, Hungary, Ireland, Italy, Netherlands, New Zealand, Portugal, Slovenia, South Korea, Spain, United Kingdom and the USA.

The radiant is situated in the anti-helion region and difficult to distinguish from the dense sporadic background activity. The new shower has been reported to the IAU-Meteor Data Center (MDC) and got the preliminary designation M2026-D1.

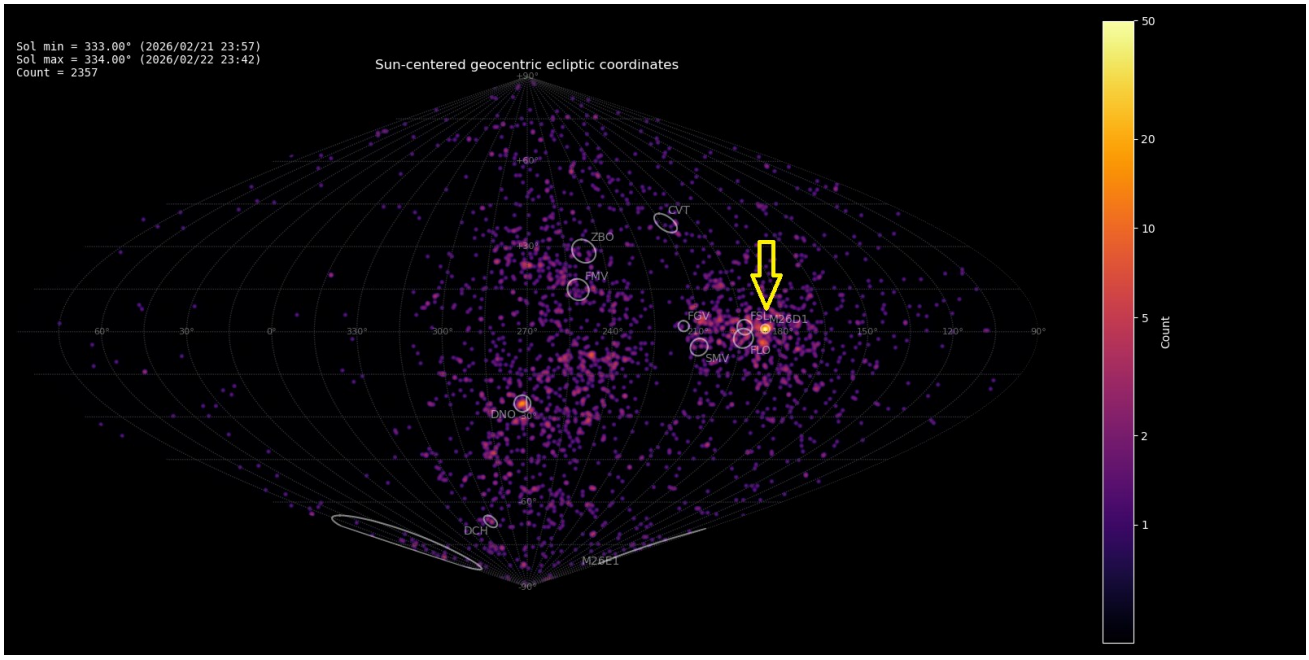

Figure 1 – Radiant density map with 2357 radiants obtained by the Global Meteor Network during 21–22 February, 2026. The position of the M2026-D1 radiant in Sun-centered geocentric ecliptic coordinates is marked with a yellow arrow.

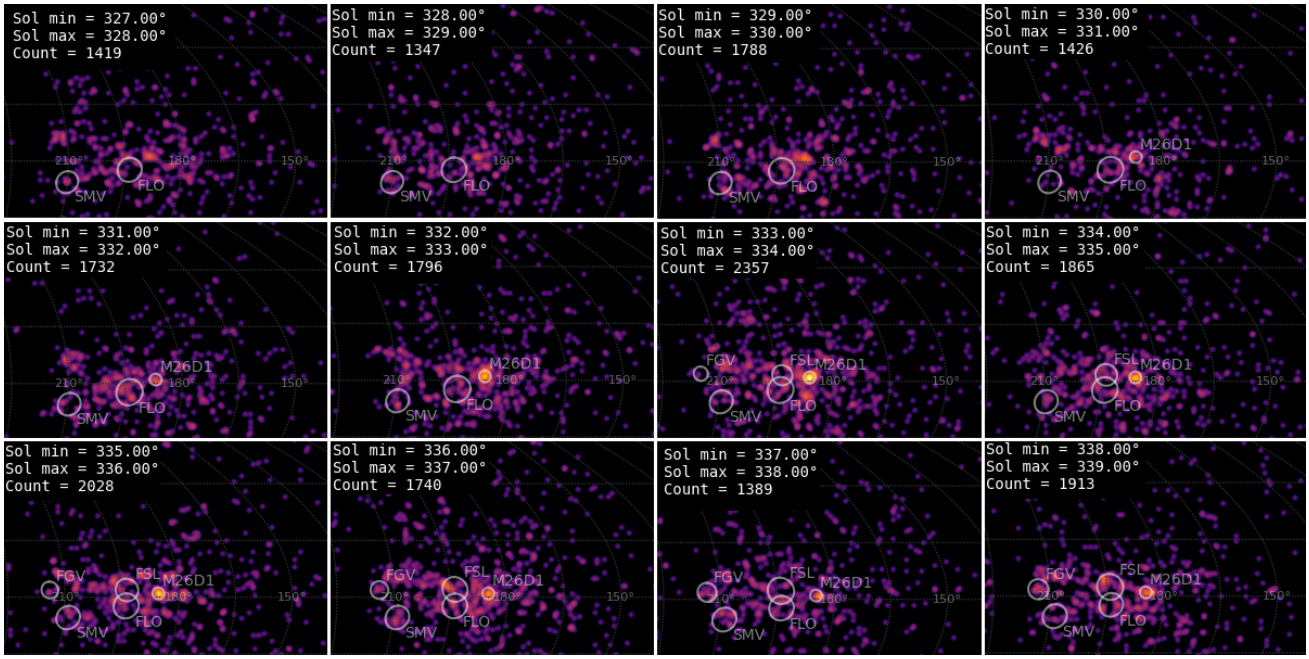

Figure 2 – Changes in the radiant appearance of the M2026-D1 shower during its activity period.

2 Shower classification based on radiants

The GMN shower association criteria assume that meteors within 1° in solar longitude, within 1.2° in radiant in this case, and within 10% in geocentric velocity of a shower reference location are members of that shower.

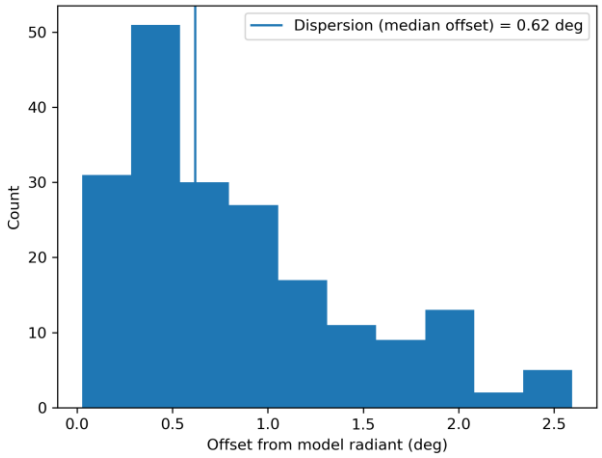

Figure 3 – Dispersion median offset on the radiant position.

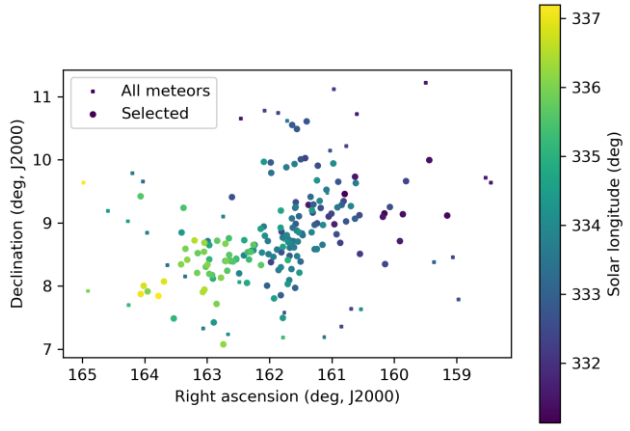

Figure 4 – The radiant distribution during the solar-longitude interval 331° – 337° in equatorial coordinates in 2026.

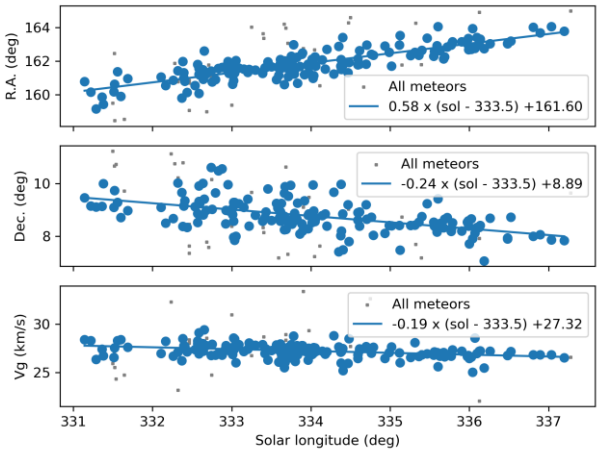

Figure 5 – The radiant drift.

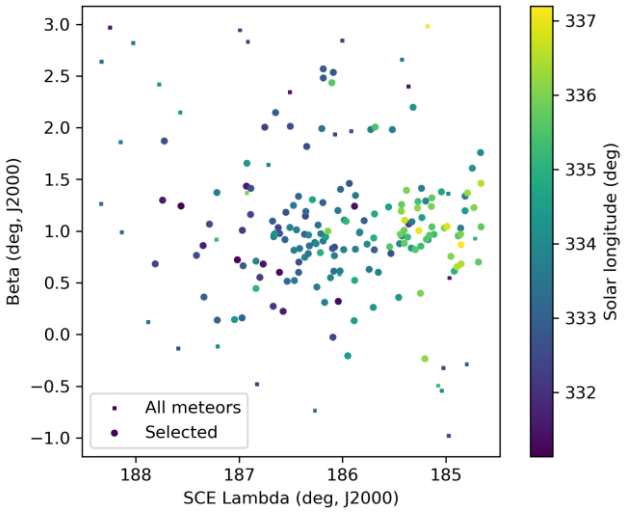

Figure 6 – The radiant distribution during the solar-longitude interval 331° – 337° in Sun centered geocentric ecliptic coordinates.

Further details about the shower association are explained in Moorhead et al. (2020). Using these meteor shower

selection criteria, 160 orbits have been identified as M2026-D1 meteors. The results have been listed in *Table 1*.

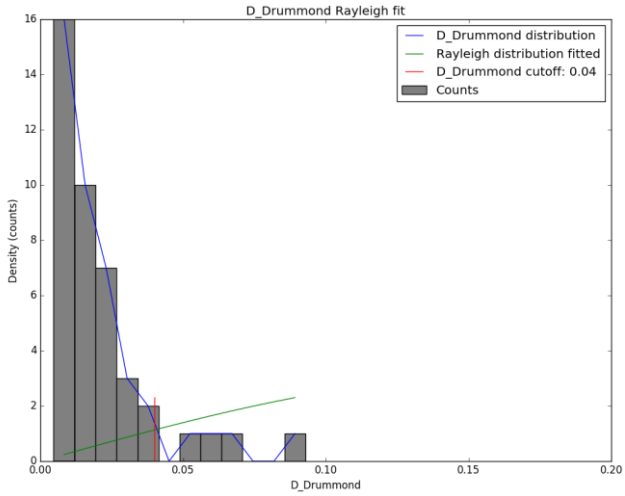

Figure 7 – Rayleigh fit on the Drummond criterion for the 2026 data of M2026-D1.

3 Shower classification based on orbits

A complete independent meteoroid stream search has been applied for confirmation based upon orbit data obtained between Solar Longitude 326.0° and 341.0° during the years 2019 to 2026. 91540 orbits were available within this time interval and a final mean orbit has been computed by the method of Jopek et al. (2006) for the thresholds $D_{SH} < 0.10$ and $D_D < 0.04$ and $D_J < 0.10$ (Southworth and Hawkins, 1963; Drummond, 1981; Jopek, 1993), based upon the Rayleigh fit in *Figure 7*. The results with the mean orbit based upon 562 meteors for 2019–2026 and upon 294 meteors for 2026, have been listed in *Table 1*. The method has been described in a separate publication (Roggemans et al., 2026a).

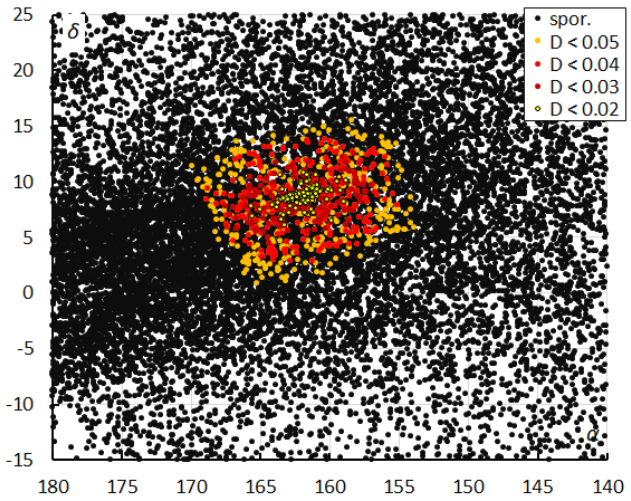

Figure 8 – The radiant distribution during the solar-longitude interval 326° – 341° in equatorial coordinates, color-coded for different threshold values of the combined similarity criteria.

The radiant is located within the anti-helion source, an area of the sky that is densely populated with sporadic radiants. This shower probably did not catch the attention in the past as it couldn't easily be distinguished from the dense sporadic background. The orbit classification method results in a larger scattered radiant than what has been used for the radiant shower classification.

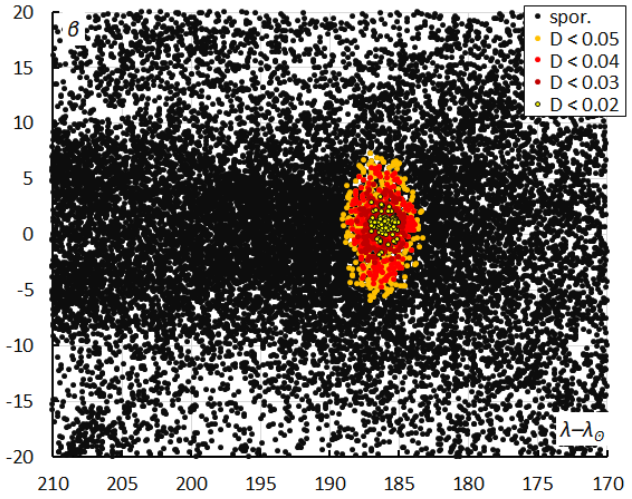

Figure 9 – The radiant distribution during the solar-longitude interval 326° – 341° in Sun-centered geocentric ecliptic coordinates, color-coded for different threshold values of the combined similarity criteria.

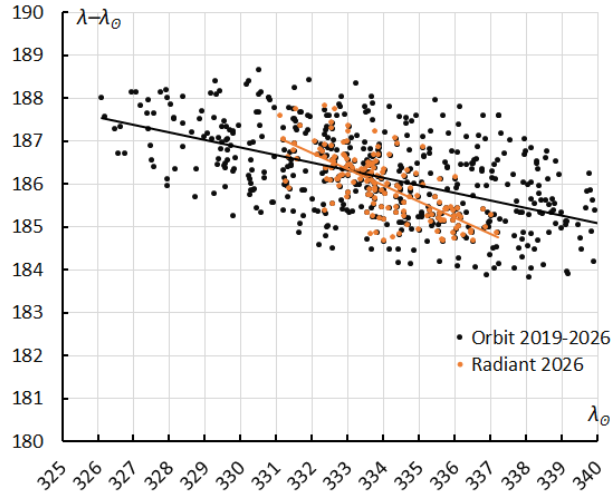

Figure 10 – The Sun-centered geocentric longitude λ–$\lambda_\odot$ in function of the Solar Longitude $\lambda_\odot$ for M2026-D1 based upon orbits (2019–2026) and radiant classification (2026).

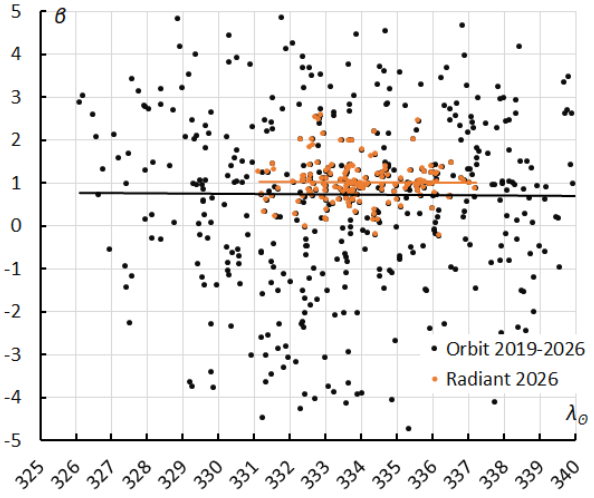

Figure 11 – The Sun-centered geocentric latitude β in function of the Solar Longitude $\lambda_\odot$ for M2026-D1 based upon orbits (2019–2026) and radiant classification (2026).

Both *Figure 8* in Equatorial coordinates and *Figure 9* in Sun-centered ecliptic coordinates show the M2026-D1 radiant embedded in the sporadic background. In Equatorial coordinates the radiant appears elongated due to the radiant drift caused by the movement of the Earth on its orbit. In *Figure 9* the radiant appears more compact because there is only a small drift with $\Delta(\lambda–\lambda_\odot) = –0.38°$/degree in $\lambda_\odot$ due to the change in orbit orientation during Earth's transit (*Figure 10*). The ecliptic latitude β shows no trend (*Figure 11*).

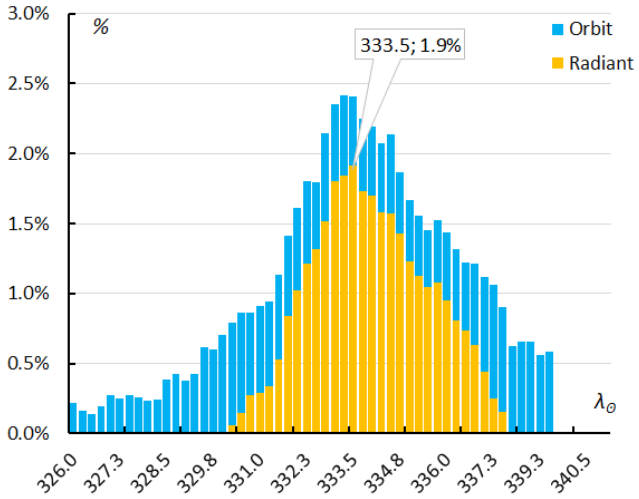

Figure 12 – The percentage of M2026-D1-meteors relative to the total number of meteors, for the radiant method (2026) and the orbit classification method 2026.

The orbit classification method detects a longer activity period than the period assumed for the radiant classification method. Plotting the ratio M2026-D1 meteors/all meteors in *Figure 12*, for time intervals of 2° in Solar Longitude, plotted every 0.25°, results in a skewed profile with a steep incline followed by a slower decline in activity. The orbit method (blue) identified more M2026-D1 candidates than the radiant method (orange).

Both methods identified 304 meteors as M2026-D1 candidates, 150 (49%) of these were identified in common. Ten (3%) meteors were identified by the radiant method but failed to fit the D-criteria thresholds. 144 meteors (47%) were identified by the orbit method, but not by the radiant method. 64 of these meteors had orbits that fit the selection criteria before or after the activity period assumed by the radiant method.

4 Orbit and parent body

This type of low inclination orbit meteoroid stream with its radiant in the anti-helion region is very sensitive to sporadic contamination. Despite the differences in numbers of possible M2026-D1 meteors between both methods, the final mean orbits and shower parameters are in very good agreement, see *Table 1*.

The diagrams with of the Kepler elements versus each other show how the M2026-D1 meteoroid stream is embedded in a very dense cloud of meteoroid orbits. *Figures 13 to 17* show how difficult it is to distinguish between shower meteors and sporadics. There are many low inclination meteors spread along the ecliptic plane so that the diagrams are not very helpful to locate a cluster that stands out of the almost saturated background noise.

Table 1 – Comparing solutions derived by the radiant based method and the orbit based method for $D_{SH} < 0.10$ and $D_D < 0.04$ and $D_J < 0.10$, in 2026 and for the years 2019–2026.

	Radiant method 2026	Orbit method 2026	Orbit method 2019–2026
$\lambda_\odot$ (°)	333.5	333.8	333.8
$\lambda_{\odot b}$ (°)	331.0	326.2	326.1
$\lambda_{\odot e}$ (°)	338.0	340.1	340.8
α_g (°)	161.6	161.7	161.8
δ_g (°)	+8.9	+8.7	+8.6
$\Delta\alpha_g$ (°)	+0.58	+0.74	+0.77
$\Delta\delta_g$ (°)	–0.24	–0.30	–0.31
v_g (km/s)	27.3	27.1	27.0
H_b (km)	98.3	97.8	97.6
H_e (km)	84.7	84.0	83.4
H_p (km)	88.7	88.0	87.6
Mag_{Ap}	+0.2	+0.4	+0.4
λ_g (°)	159.65	159.9	159.9
$\lambda_g - \lambda_\odot$ (°)	186.15	186.0	186.2
β_g (°)	+1.02	+0.9	+0.9
a (A.U.)	2.635	2.560	2.49
q (A.U.)	0.449	0.450	0.449
e	0.830	0.824	0.820
i (°)	1.0	0.8	0.7
ω (°)	281.8	281.8	282.2
Ω (°)	334.0	334.0	333.9
Π (°)	255.8	255.8	256.1
T_j	2.77	2.83	2.88
N	160	294	562

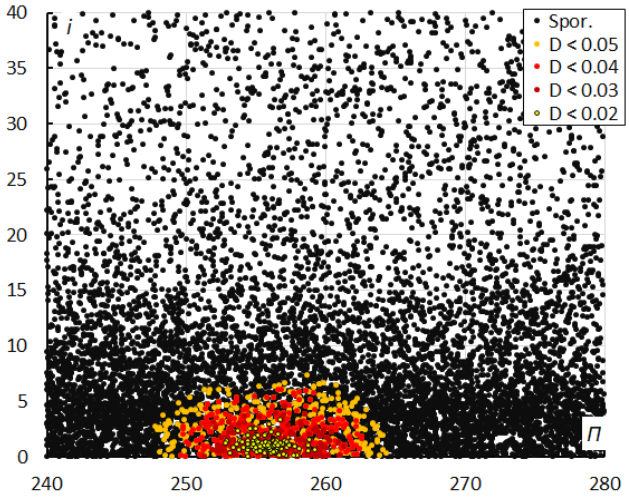

Figure 13 – Inclination i versus the longitude of perihelion Π color-coded for different classes of D-criteria thresholds, for $\lambda_\odot$ between 326° and 341°.

There is a trend in the perihelion distance q during the transit of Earth (*Figure 18*) and in Longitude of Perihelion Π (*Figure 19*) which both increase. The other Kepler elements remain stable during the activity period.

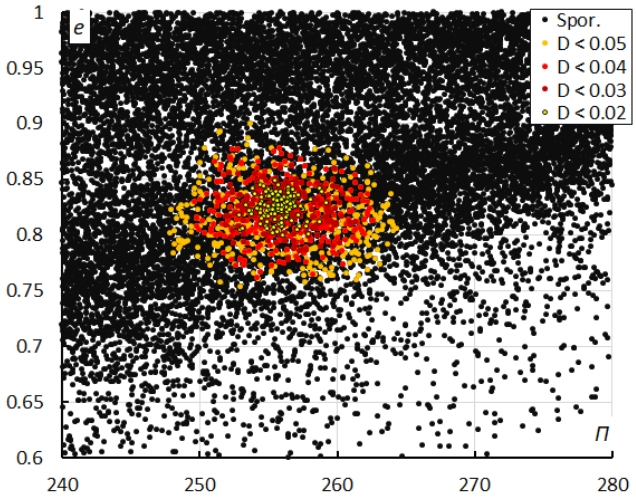

Figure 14 – Eccentricity e versus the longitude of perihelion Π color-coded for different classes of D-criteria thresholds, for $\lambda_\odot$ between 326° and 341°.

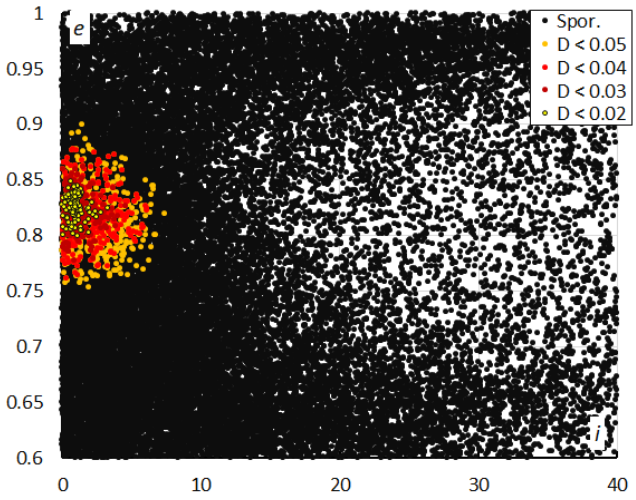

Figure 15 – Eccentricity e versus the inclination i color-coded for different classes of D-criteria thresholds, for $\lambda_\odot$ between 326° and 341°.

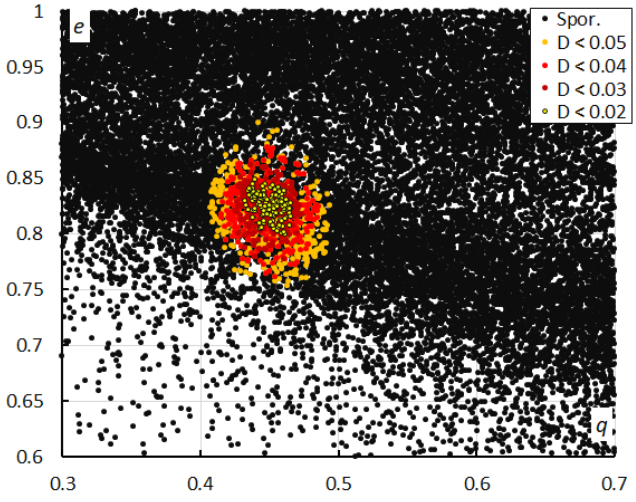

Figure 16 – Eccentricity e versus the perihelion distance q color-coded for different classes of D-criteria thresholds, for $\lambda_\odot$ between 326° and 341°.

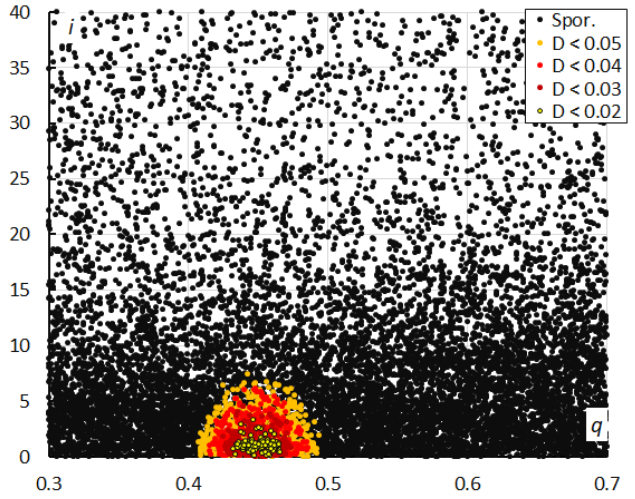

Figure 17 – Inclination i versus the perihelion distance q color-coded for different classes of D-criteria thresholds, for $\lambda_\odot$ between 326° and 341°.

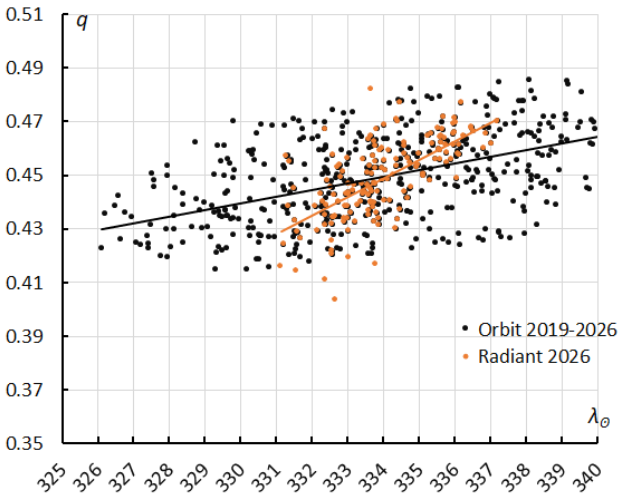

Figure 18 – The evolution of the perihelion distance q in function of the Solar Longitude $\lambda_\odot$ for the M2026-D1 based upon orbits (2019–2026) and radiant classification (2026).

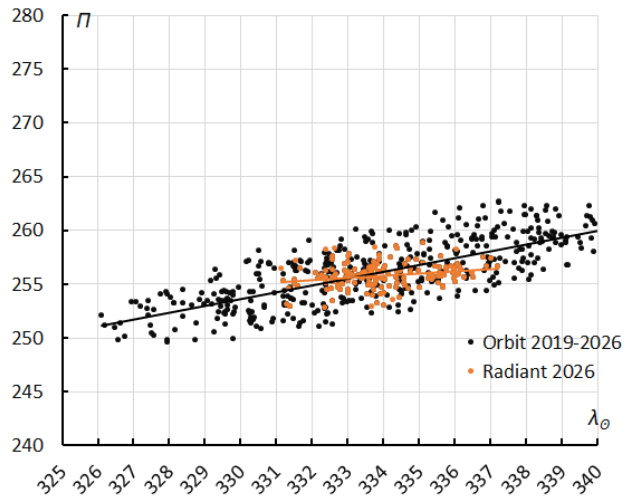

Figure 19 – The evolution of the Longitude of perihelion Π in function of the Solar Longitude $\lambda_\odot$ for the M2026-D1 based upon orbits (2019–2026) and radiant classification (2026).

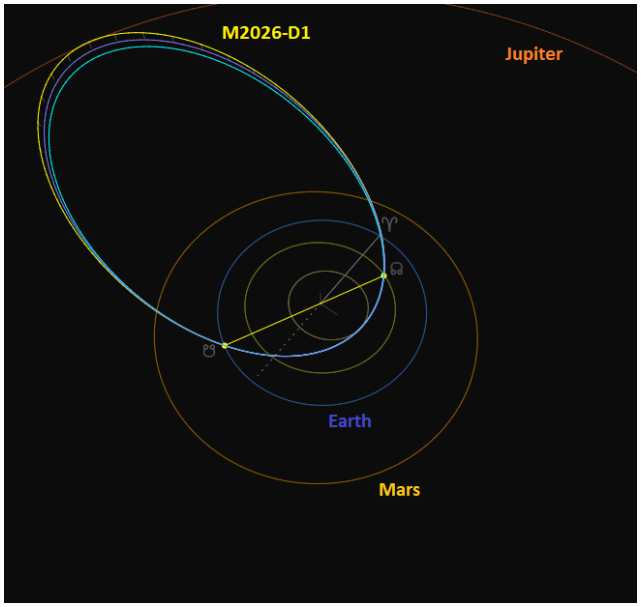

Figure 20 – Comparing the M2026-D1 solution (yellow) obtained by the radiant method with the solutions obtained by the orbit method for 2026 (purple) and 2019–2026 (blue), close-up at the inner Solar System. (Plotted with the Orbit visualization app provided by Pető Zsolt).

The M2026-D1 meteoroid stream has a Jupiter-family comet type orbit with a Tisserand value relative to planet Jupiter of $T_J = 2.77$. The stream is only slightly declined to the ecliptic plane and has its aphelion near the orbit of Jupiter. The stream intersects the Earth orbit at its descending node. The ascending node is slightly inside the orbit of Venus, which may cause a meteor shower on planet Venus. The stream is exposed to gravitational perturbations at close encounters to planets Earth, Jupiter, Mars and Venus. The enhanced activity in 2026 may be related to a dust trail formed by these perturbations. The number of orbits per year reflects the expansion of GMN in its early years but the camera coverage has not changed much since 2023. The number of M2026-D1 meteors in 2026 (*Table 2*) was much higher than in previous years. No trace of this shower could be found in older visual observations.

Table 2 – The number of M2026-D1 orbits with $D_{SH} < 0.10$ and $D_D < 0.04$ and $D_J < 0.10$ per year during the period 2019–2026.

Year	Number of orbits
2019	4
2020	12
2021	35
2022	32
2023	45
2024	32
2025	108
2026	294
Total	562

A search for possible parent bodies resulted in the top ten candidates listed in *Table 3*. Although $D_D < 0.036$ looks like a good degree of similarity between the orbits, this value is at the limit for this type of orbit to exclude pure chance orbit similarity. Numeric integrations of the orbital evolution are required to reconstruct the most likely behavior of the stream and its possible parent bodies.

Table 3 – Top ten matches of a search for possible parent bodies with $D_D < 0.075$, based upon the mean orbit derived from the radiant classification method.

Name	D_D
2024 CA_8	0.036
2013 TR_{135}	0.037
2017 DW_{108}	0.045
2022 SK_{28}	0.055
(199145) 2005 YY_{128}	0.066
(612924) 2005 CL	0.068
D/1766 G_1 (Helfenzrieder)	0.068
2012 DX_{13}	0.069
2019 SO_6	0.070
2024 TH_4	0.070

5 Conclusion

A reliable orbit was established for a newly discovered meteor shower with a radiant in the constellation Virgo that displayed an outburst on 21–22 February 2026. The compact concentration of radiants visible on the daily GMN radiant density plots allowed distinction of the shower from the very dense sporadic background activity at the anti-helion area at the sky. The shower has been added to the IAU-MDC Working List of Meteor Showers with the temporary assignation M2026-D1[8].

Acknowledgments

This report is based on the data of the Global Meteor Network (Vida et al., 2020a; 2020b; 2021) which is released under the CC BY 4.0 license[9]. We thank all 927 participants in the Global Meteor Network project for their contribution and perseverance. A list with the names of the volunteers who contribute to GMN has been published in the 2025 annual report (Roggemans et al., 2026b). The following 767 cameras contributed to paired meteors used in this study:

AT0004, AU0002, AU0003, AU0004, AU0006, AU000A, AU000B, AU000C, AU000D, AU000F, AU000G, AU000J, AU000L, AU000R, AU000S, AU000U, AU000V, AU000W, AU000X, AU000Y, AU000Z, AU0010, AU001A, AU001B, AU001C, AU001D, AU001E, AU001F, AU001K, AU001L, AU001N, AU001P, AU001Q, AU001R, AU001S, AU001U, AU001V, AU001W, AU001X, AU001Y, AU001Z, AU0029, AU002A, AU002B, AU002D, AU0030,

[8] https://www.ta3.sk/IAUC22DB/MDC2022/Roje/pojedynczy_obiekt.php?lporz=02611&kodstrumienia=01254

[9] https://creativecommons.org/licenses/by/4.0/

AU003E, AU003H, AU003J, AU0042, AU0043, AU0045, AU0048, AU004A, AU004L, BA0002, BA0005, BE0001, BE0002, BE0004, BE0006, BE0007, BE0009, BE000A, BE000C, BE000D, BE000E, BE000G, BE000K, BE000L, BE000M, BE000Q, BE000T, BE000U, BE000V, BE000Y, BE0014, BE0015, BE0019, BE001A, BE001B, BG0001, BG0003, BG0005, BG000B, BG000C, BR0002, BR000G, BR000M, BR000T, BR001F, BR001Q, BR001R, BR001T, BR001W, BR002A, CA0007, CA000Q, CA000U, CA000V, CA0012, CA001B, CA001R, CA0026, CA002K, CA002L, CA002Q, CA002R, CA002U, CA002V, CA0031, CA003A, CA003D, CA003E, CH0002, CH0003, CH0005, CZ0004, CZ0008, CZ0009, CZ000A, CZ000B, CZ000E, CZ000G, CZ000J, CZ000K, CZ000L, CZ000M, CZ000U, CZ000W, CZ000X, DE0001, DE0005, DE000B, DE000J, DE000M, DE000Q, DE000S, DE000X, DE000Y, DE0013, DK0001, DK0009, DK000B, DK000D, DK000G, ES0004, ES0005, ES000E, ES000K, ES000T, ES000U, ES000V, ES0013, ES0016, ES0019, ES001J, ES001L, FR0006, FR000A, FR000G, FR000R, FR000Y, FR000Z, FR0011, FR0013, GR0002, GR0004, GR0005, GR0006, GR0007, GR0008, GR0009, HR0002, HR0006, HR0007, HR000D, HR000F, HR000G, HR000H, HR000J, HR000K, HR000M, HR000P, HR000Q, HR000S, HR000V, HR000W, HR000Z, HR0010, HR0015, HR0016, HR001A, HR001D, HR001H, HR001L, HR001N, HR001Q, HR001S, HR001Z, HR0024, HR0025, HR0027, HR002D, HR002F, HR002G, HR002H, HR002J, HR002K, HR002V, HR002W, HR002X, HR002Y, HU0001, HU0002, HU0003, HU0005, HU000A, HU000B, IE0004, IE000H, IE000J, IE000M, IL0002, IL0004, IL0009, IT0001, IT0004, IT0008, KR0001, KR0002, KR0003, KR0004, KR0005, KR0006, KR0007, KR0008, KR0009, KR000A, KR000C, KR000D, KR000E, KR000F, KR000G, KR000H, KR000J, KR000K, KR000L, KR000M, KR000N, KR000P, KR000Q, KR000R, KR000S, KR000Y, KR000Z, KR0010, KR0011, KR0012, KR0013, KR0014, KR0015, KR0016, KR0017, KR0018, KR0019, KR001A, KR001B, KR001C, KR001D, KR001E, KR001F, KR001K, KR001P, KR001U, KR001X, KR001Y, KR0020, KR0021, KR0022, KR0025, KR0026, KR0027, KR0029, KR002A, KR002B, KR002D, KR002E, KR002F, KR002G, KR002H, KR002J, KR002M, KR002N, KR002Q, KR002R, KR002S, KR002T, KR0036, KR0037, KR0039, KR003J, KR003K, KR003M, KR003N, KR003P, KR003Q, KR003R, KR003S, KR003T, KR003U, KR003V, KR003W, KR003X, LU0001, MX000D, NL0001, NL000C, NL000K, NL000M, NL000Q, NL0010, NZ0001, NZ0002, NZ0003, NZ0004, NZ0007, NZ0008, NZ0009, NZ000D, NZ000H, NZ000L, NZ000P, NZ000S, NZ000W, NZ000X, NZ000Y, NZ000Z, NZ0010, NZ0011, NZ0012, NZ0014, NZ0015, NZ0016, NZ0017, NZ0018, NZ0019, NZ001E, NZ001G, NZ001H, NZ001L, NZ001R, NZ001S, NZ001X, NZ001Y, NZ0020, NZ0021, NZ0022, NZ0023, NZ0026, NZ0027, NZ0028, NZ0029, NZ002C, NZ002D, NZ002F, NZ002G, NZ002H, NZ002K, NZ002L, NZ002N, NZ002Q, NZ002R, NZ002S, NZ002T, NZ002U, NZ002V, NZ002W, NZ002X, NZ002Z, NZ0030, NZ0032, NZ0033, NZ0034, NZ0036, NZ0037, NZ0038, NZ003B, NZ003C, NZ003E, NZ003H, NZ003K, NZ003N, NZ003Q, NZ003R, NZ003S, NZ003T, NZ003U, NZ003V, NZ003Y, NZ003Z, NZ0040, NZ0041, NZ0042, NZ0044, NZ0045, NZ0046, NZ0049, NZ004A, NZ004B, NZ004C, NZ004D, NZ004E, NZ004F, NZ004H, NZ004J, NZ004L, NZ004M, NZ004N, NZ004R, NZ004T, NZ004U, NZ004W, NZ004Y, NZ0051, NZ0059, NZ005B, NZ005C, NZ005F, NZ005G, NZ005H, NZ005K, NZ005M, NZ005N, NZ005Q, NZ005R, NZ005U, NZ005Z, NZ0061, NZ0063, NZ0065, NZ0066, NZ0067, NZ0069, NZ006A, NZ006C, NZ006D, NZ006E, NZ006F, NZ006G, NZ007C, PL0005, PL000B, PL000D, PL000G, PT0002, RO0001, RO0002, RO0004, RU0003, RU0004, RU000B, RU000M, RU0012, RU0013, RU0019, SI0001, SI0002, SI0005, SK0003, SK0005, SK0006, UK0001, UK0002, UK0004, UK0006, UK0008, UK0009, UK000D, UK000H, UK000P, UK000S, UK000T, UK000Y, UK000Z, UK001H, UK001L, UK001P, UK001R, UK001S, UK001T, UK001Y, UK001Z, UK0024, UK0025, UK0026, UK002C, UK002F, UK002K, UK002L, UK002T, UK002W, UK002X, UK002Y, UK002Z, UK0031, UK0032, UK0034, UK0035, UK0038, UK003A, UK003B, UK003C, UK003D, UK003G, UK003L, UK003S, UK003U, UK003V, UK003X, UK003Z, UK0041, UK0042, UK0049, UK004B, UK004D, UK004E, UK004F, UK004G, UK004J, UK004M, UK004P, UK004V, UK0056, UK0057, UK005E, UK005G, UK005H, UK005L, UK005M, UK005N, UK005P, UK005R, UK005V, UK0060, UK0061, UK0066, UK0067, UK006C, UK006D, UK006E, UK006G, UK006H, UK006L, UK006P, UK006V, UK006Z, UK0070, UK0078, UK0079, UK007A, UK007B, UK007G, UK007H, UK007L, UK007P, UK007R, UK007U, UK007V, UK007Y, UK007Z, UK0080, UK0081, UK0083, UK0084, UK0087, UK008B, UK008C, UK008D, UK008F, UK008G, UK008T, UK0092, UK0096, UK0098, UK009A, UK009D, UK009F, UK009G, UK009J, UK009L, UK009P, UK009Q, UK009V, UK009W, UK009X, UK00A0, UK00A1, UK00A2, UK00A3, UK00A4, UK00A5, UK00A7, UK00AB, UK00AD, UK00AE, UK00AF, UK00AG, UK00AJ, UK00AK, UK00AL, UK00AM, UK00AN, UK00AP, UK00AT, UK00AU, UK00B0, UK00B1, UK00B2, UK00B5, UK00B7, UK00BA, UK00BE, UK00BF, UK00BJ, UK00BK, UK00BL, UK00BW, UK00C1, UK00C2, UK00C7, UK00CC, UK00CH, UK00CJ, UK00CQ, UK00CS, UK00CT, UK00CU, UK00CV, UK00CZ, UK00DB, UK00DE, UK00DH, UK00DJ, UK00DN, US0001, US0002, US0003, US0004, US0005, US0006, US0007, US0008, US0009, US000A, US000C, US000D, US000E, US000G, US000H, US000J, US000K, US000L, US000M, US000N, US000P, US000R, US000S, US000U, US000V, US001L, US001P, US001Q, US001R, US001V, US0020, US0021, US0022, US0027, US002A, US002M, US002N, US002R, US002X, US002Z, US0030, US0036, US0037, US0039, US003G, US003N, US003P, US003T, US003Y, US004A, US004B, US004C, US004N, US004P, US004Q, US004U, US0050, US0051, US0055, US0057, US005A, US005B, US005C, US005D, US005E, US005H, US005J, US005K, US005Q, US005W, US005X, US005Y, US005Z, US0061, US0062, US0066, US006A, USL001, USL002, USL003, USL004, USL005,

USL006, USL007, USL008, USL009, USL00A, USL00B, USL00C, USL00D, USL00E, USL00F, USL00G, USL00H, USL00J, USL00M, USL00N, USL00P, USL00Q, USL00V, USL00Y, USL00Z, USL011, USL012, USL013, USL014, USL015, USL017, USL018, USL019, USL01A, USL01B, USL01D, USL01E, USV001, USV002, USV003, ZA0002, ZA0007, ZA000A, ZA000D.

References

Drummond J. D. (1981). "A test of comet and meteor shower associations". *Icarus*, **45**, 545–553.

Jopek T. J. (1993). "Remarks on the meteor orbital similarity D-criterion". *Icarus*, **106**, 603–607.

Jopek T. J., Rudawska R. and Pretka-Ziomek H. (2006). "Calculation of the mean orbit of a meteoroid stream". *Monthly Notices of the Royal Astronomical Society*, **371**, 1367–1372.

Moorhead A. V., Clements T. D., Vida D. (2020). "Realistic gravitational focusing of meteoroid streams". *Monthly Notices of the Royal Astronomical Society*, **494**, 2982–2994.

Roggemans P., Vida D., Šegon D., Scott J. M. (2026a). "Meteoroid orbit shower identification method and its application in meteor shower case studies". *eMetN Meteor Journal*, **11**, 189–204.

Roggemans P., Campbell-Burns P., Kalina M., McIntyre M., Scott J. M., Šegon D., Vida D. (2026b). "Global Meteor Network report 2025". *eMetN Meteor Journal*, **11**, 89–129.

Southworth R. B. and Hawkins G. S. (1963). "Statistics of meteor streams". *Smithsonian Contributions to Astrophysics*, **7**, 261–285.

Vida D., Gural P., Brown P., Campbell-Brown M., Wiegert P. (2020a). "Estimating trajectories of meteors: an observational Monte Carlo approach - I. Theory". *Monthly Notices of the Royal Astronomical Society*, **491**, 2688–2705.

Vida D., Gural P., Brown P., Campbell-Brown M., Wiegert P. (2020b). "Estimating trajectories of meteors: an observational Monte Carlo approach - II. Results". *Monthly Notices of the Royal Astronomical Society*, **491**, 3996–4011.

Vida D., Šegon D., Gural P. S., Brown P. G., McIntyre M. J. M., Dijkema T. J., Pavletić L., Kukić P., Mazur M. J., Eschman P., Roggemans P., Merlak A., Zubrović D. (2021). "The Global Meteor Network – Methodology and first results". *Monthly Notices of the Royal Astronomical Society*, **506**, 5046–5074.

New meteor shower in Dorado (M2026-E1)

Damir Šegon[1,2], Denis Vida[3,4], Paul Roggemans[5], James M. Scott[6], Jeff Wood[7]

[1] **Astronomical Society Istra Pula, Park Monte Zaro 2, 52100 Pula, Croatia**

[2] **Višnjan Observatory, Istarska 5, 52463 Višnjan, Croatia**
damir@astro.hr

[3] **Department of Physics and Astronomy, University of Western Ontario, Richmond Street, London, N6A 3K7, Ontario, Canada**

[4] **Institute for Earth and Space Exploration, University of Western Ontario, Perth Drive, London, N6A 5B8, Ontario, Canada**
denis.vida@gmail.com

[5] **Pijnboomstraat 25, 2800 Mechelen, Belgium**

[6] **Department of Geoscience, Aarhus University, Høegh-Guldbergs Gade 2. DK-8000 Aarhus C, Denmark**

[7] **PO Box 162, Willetton, Western Australia 6955, Australia**

A new meteor shower has been detected between the 17th and 22nd of February 2026 from a radiant at R.A. = 69.4° and Decl.= –54.8° in the constellation of Dorado. It has a geocentric velocity of 17.3 km/s and a Jupiter family comet orbit. The new shower has been included in the IAU-MDC working list of meteor showers with the provisional identification M2026-E1.

1 Introduction

A very diffuse radiant concentration appeared near the Southern ecliptic pole at the rear of the Earth where meteoroids must overtake Earth in its orbit around the Sun (about 30 km/s) to produce a meteor. The activity was noticed on 22 February, but monitored before being reported as the radiants appeared very dispersed. The activity was recorded by 175 cameras in Australia and New Zealand in 2026.

Such diffuse radiants prove a challenge to distinguish from the sporadic background. The only way this caught attention was because this part of the sky normally is rather empty. The shower is barely visible on the daily radiant density maps but is well visible on the cumulated monthly plot for February 2026 (*Figure 1*). The shower was reported to the IAU-MDC Working List of Meteor Showers and it has received the provisional identification M2026-E1.

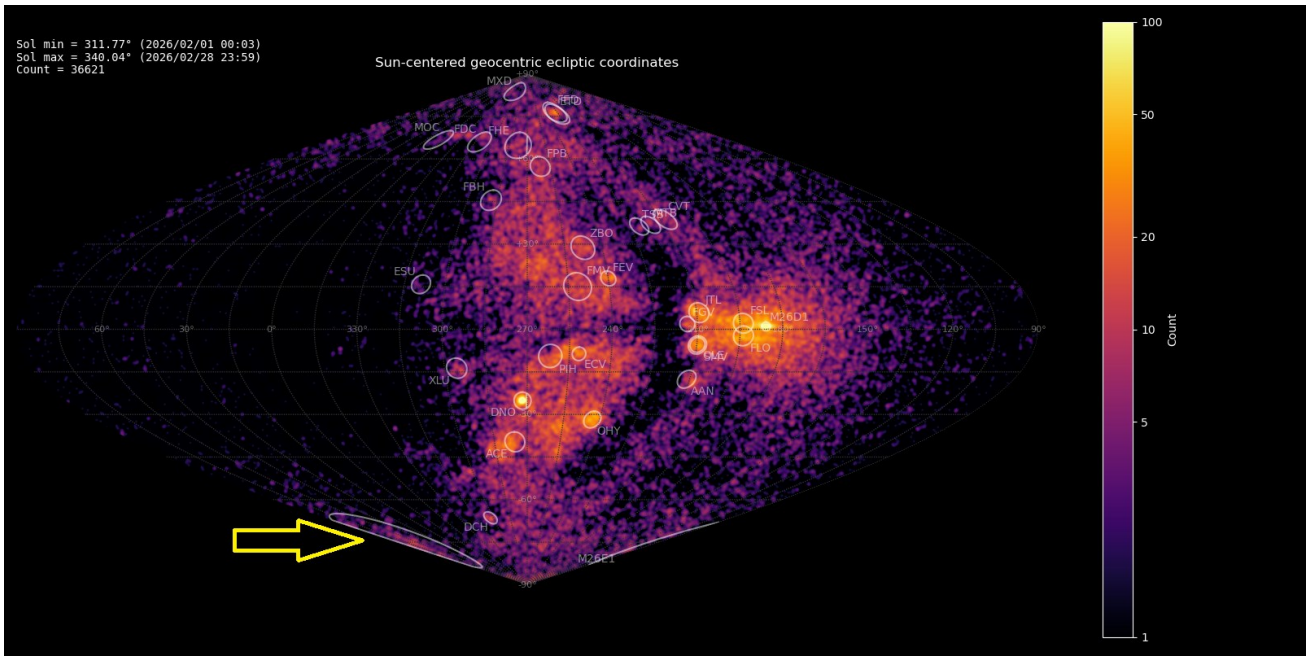

Figure 1 – Radiant density map with 36621 radiants obtained by the Global Meteor Network during February, 2026. The position of the M2026-E1 radiant in Sun-centered geocentric ecliptic coordinates is marked with a yellow arrow.

2 Shower classification based on radiants

The GMN shower association criteria assume that meteors within 1° in solar longitude, within 7.3° in radiant in this case, and within 10% in geocentric velocity of a shower reference location are members of that shower. Further details about the shower association are explained in Moorhead et al. (2020). Using these meteor shower selection criteria, 76 orbits have been identified as M2026-E1 meteors. The final results have been listed in *Table 1*.

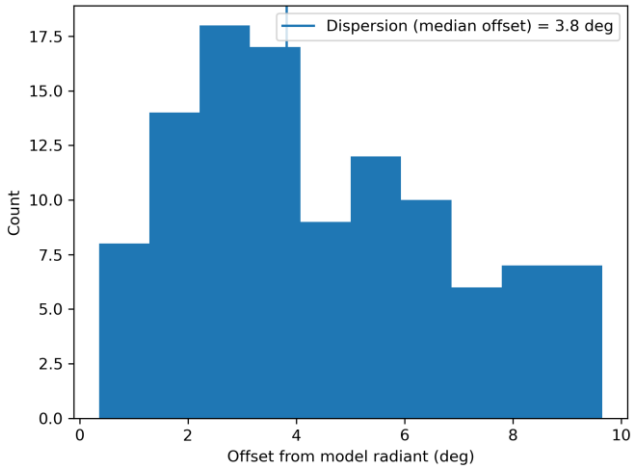

Figure 2 – Dispersion median offset on the radiant position.

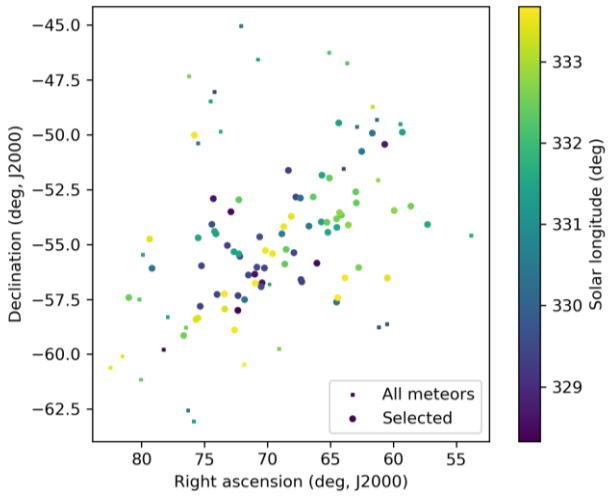

Figure 3 – The radiant distribution during the solar-longitude interval 328° – 334° in equatorial coordinates in 2026.

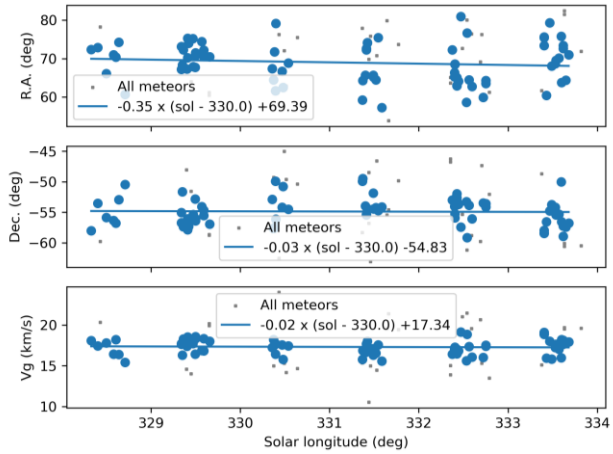

Figure 4 – The radiant drift.

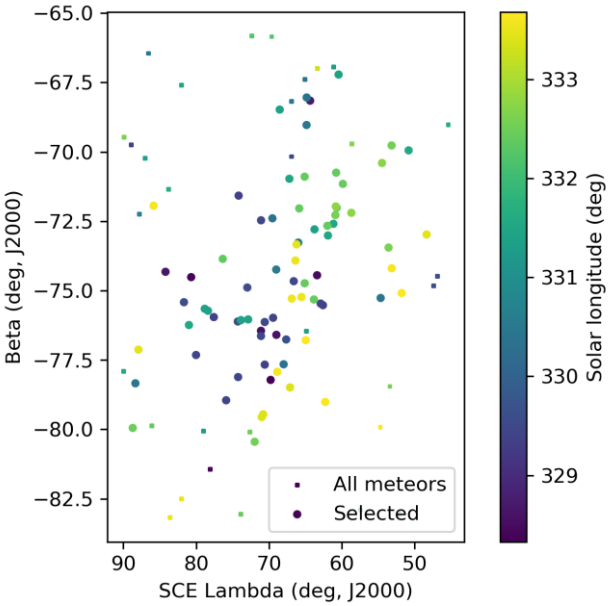

Figure 5 – The radiant distribution during the solar-longitude interval 328° – 334° in Sun-centered geocentric ecliptic coordinates.

3 Shower classification based on orbits

A complete independent meteoroid stream search has been applied for confirmation based upon orbit data obtained between Solar Longitude 322.0° and 339.0° during the years 2019 to 2026. 99772 orbits were available within this time interval and a final mean orbit has been computed by the method of Jopek et al. (2006) for the thresholds $D_{SH} < 0.10$ and $D_D < 0.04$ and $D_J < 0.10$ (Southworth and Hawkins, 1963; Drummond, 1981; Jopek, 1993), based upon the Rayleigh fit in *Figure 6*. The solutions with a mean orbit based upon 244 meteors for 2022–2026 and upon 122 meteors for 2026 are listed in *Table 1*. The method has been described in detail in a separate publication (Roggemans et al., 2026a).

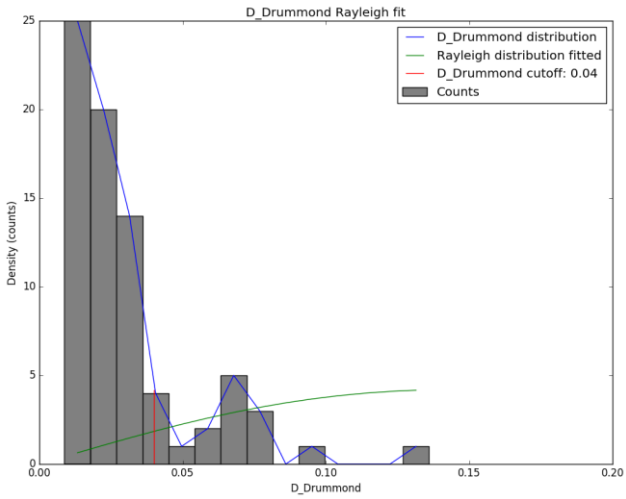

Figure 6 – Rayleigh fit on the Drummond criterion for the 2026 data of M2026-E1.

The radiant area is very diffuse stretched over about 30 degrees in Right Ascension and 15 degrees in Declination (*Figure 7*).

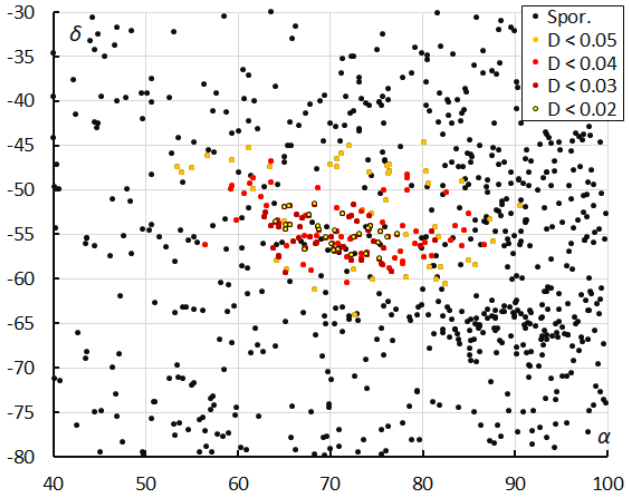

Figure 7 – The radiant distribution during the solar-longitude interval 322° – 339° in equatorial coordinates, color-coded for different threshold values of the combined similarity criteria.

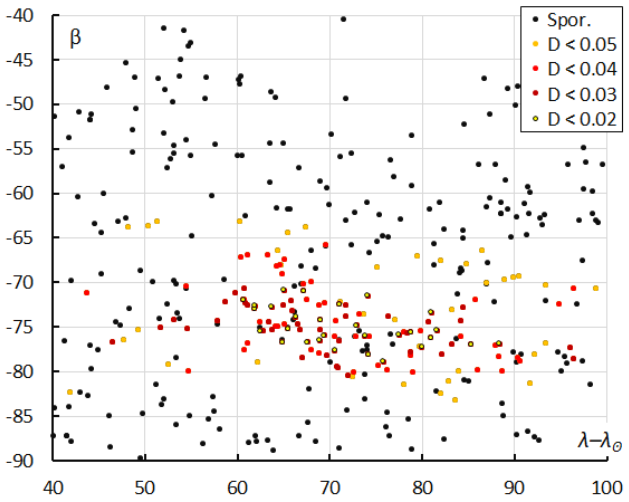

Figure 8 – The radiant distribution during the solar-longitude interval 322° – 339° in Sun-centered geocentric ecliptic coordinates, color-coded for different threshold values of the combined similarity criteria.

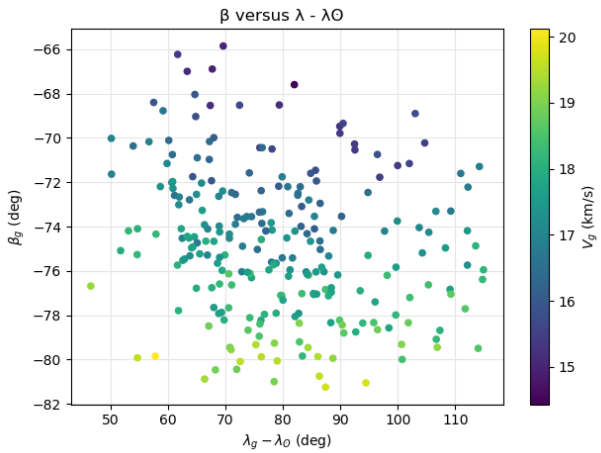

Figure 9 – The radiant distribution during the solar-longitude interval 322° – 339° in Sun-centered geocentric ecliptic coordinates, color-coded for the geocentric velocity.

The Sun-centered geocentric ecliptic coordinates appear dispersed due to the plotting projection near the ecliptic South pole (*Figure 8*). There is a large variation in geocentric velocity with the fastest meteors being those with their radiant close to the ecliptic South pole. The more to the north in the direction of the Antapex, the slower the meteors (*Figure 9*). There is a remarkable strong drift in Sun-centered geocentric ecliptic longitude with $\Delta(\lambda-\lambda_\odot)/\lambda_\odot = -1.61°$ which compensates the usual radiant drift due to the rotation of the Earth around the Sun in Equatorial coordinates and resulting in $\Delta(\alpha)/\lambda_\odot = -0.35°$, which is a negative value and indicates a drift in the opposite direction than normal. This rapid decline in $\lambda-\lambda_\odot$ can be seen in *Figure 10*.

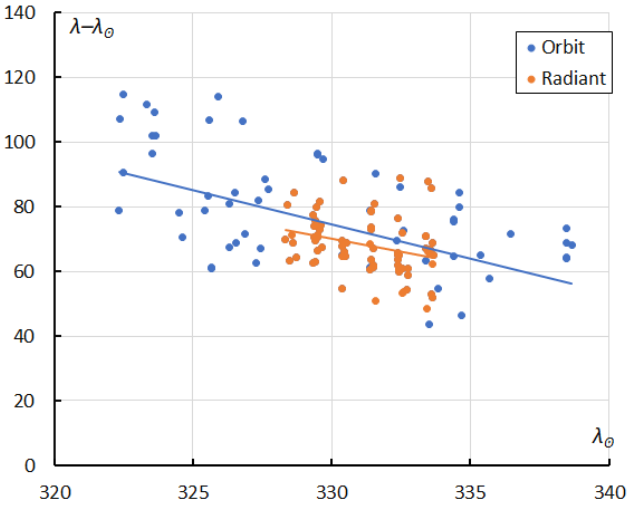

Figure 10 – The Sun-centered geocentric longitude $\lambda-\lambda_\odot$ in function of the Solar Longitude $\lambda_\odot$ for M2026-E1 based upon orbits classification (2026) and radiant classification (2026).

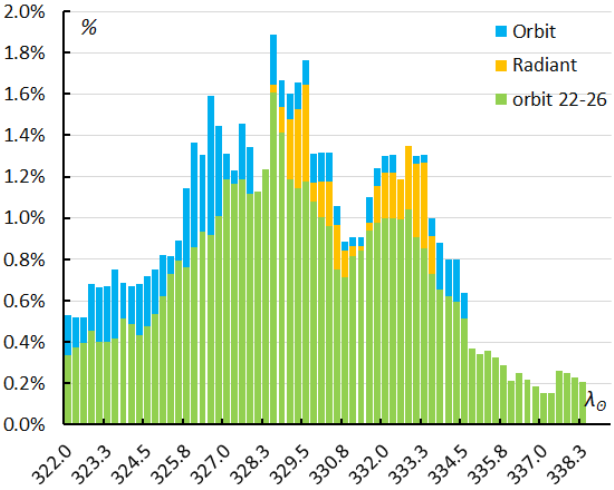

Figure 11 – The percentage of M2026-E1-meteors relative to the total number of meteors at the Southern Hemisphere, for the radiant method 2026 (orange), the orbit classification method 2026 (blue) and orbit classification method 2022–2026 (green).

The radiant-based shower identification covered an activity period in Solar Longitude from 328° to 334° and identified 76 M2026-E1 candidates. The orbit-based shower identification detected 122 possible M2026-E1 orbits between Solar Longitude 322° to 339°. During the common activity period 67 (75%) of the M2026-E1 meteors were detected by both methods, 13 (15%) by the orbit method but not by the radiant method and 9 (10%) by the radiant method but failing to fit the thresholds $D_{SH} < 0.10$ and $D_D < 0.04$ and $D_J < 0.10$ on their orbits.

Plotting the ratio of M2026-E1 meteors relative to the total number of meteors recorded at the Southern hemisphere, counted per two degrees in Solar Longitude, in steps of 0.25° (*Figure 11*), reveals three peaks and two dips in 2026. The radiant method missed the first peak because the activity period was assumed to start from $\lambda_\odot = 328°$. As the 2026 data is solely based upon data from Australia and New Zealand without any input from South America or South Africa, no 24-on-24 coverage is available. Adding the ratio of M2026-E1 activity for the period 2022–2026, the first peak and dip are smoothed out, best rates occurred at $\lambda_\odot = 328.5°$ followed by a dip at $\lambda_\odot = 330.8°$ and a secondary peak at $\lambda_\odot = 332.5°$. The activity ratio in 2026 was slightly higher than in the period 2022–2026.

4 Orbit and parent body

Despite the differences in numbers of possible M2026-E1 meteors between both methods, the final mean orbits and shower parameters are in good agreement (*Table 1)*. The difference in node, argument and longitude of perihelion is due to the longer activity period used for the mean orbit based upon the orbit shower identification.

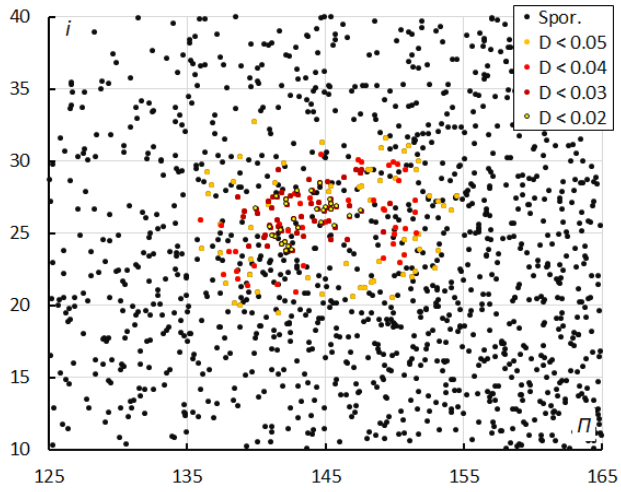

Figure 12 – Inclination i versus the longitude of perihelion Π color-coded for different classes of D-criteria thresholds, for $\lambda_\odot$ between 322°and 339°.

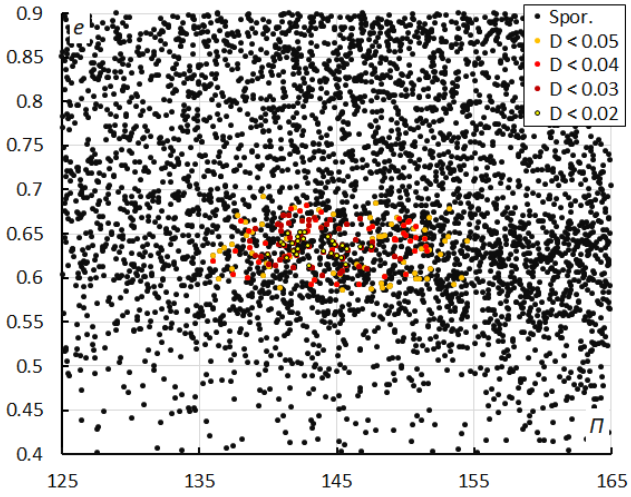

Figure 13 – Eccentricity e versus the longitude of perihelion Π color-coded for different classes of D-criteria thresholds, for $\lambda_\odot$ between 322°and 339°.

Table 1 – Comparing solutions derived by the radiant based method and the orbit based menthod for $D_{SH} < 0.10$ & $D_D < 0.04$ & $D_J < 0.10$, in 2026 and for the years 2022–2026.

	Radiant method 2026	Orbit method 2026	Orbit method 2022–2026
$\lambda_\odot$ (°)	330.0	328.5	328.5
$\lambda_{\odot b}$ (°)	328.0	322.3	322.1
$\lambda_{\odot e}$ (°)	334.0	338.7	339.0
α_g (°)	69.4	71.1	73.4
δ_g (°)	–54.8	–55.0	–54.2
$\Delta\alpha_g$ (°)	–0.35	–0.57	–0.68
$\Delta\delta_g$ (°)	–0.03	+0.06	–0.01
v_g (km/s)	17.3	17.6	17.4
H_b (km)	93.7	93.5	93.6
H_e (km)	83.2	83.2	82.5
H_p (km)	89.3	88.6	87.8
Mag_{Ap}	+0.6	+0.8	+0.5
λ_g (°)	40.05	41.6	48.7
$\lambda_g - \lambda_\odot$ (°)	70.05	70.6	78.1
β_g (°)	–74.6	–75.3	–74.9
a (A.U.)	2.660	2.700	2.697
q (A.U.)	0.984	0.984	0.985
e	0.630	0.635	0.635
i (°)	25.9	26.2	26.0
ω (°)	351.9	353.7	355.4
Ω (°)	151.9	150.3	150.0
Π (°)	143.1	144.0	145.4
T_j	2.96	2.93	2.93
N	76	122	244

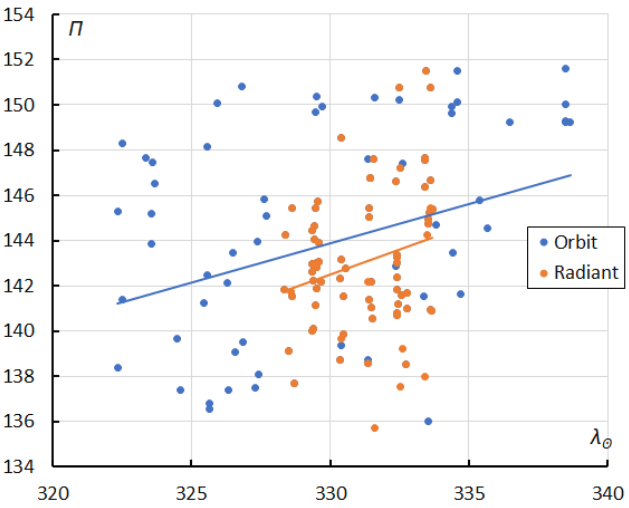

Figure 14 – The evolution of the Longitude of perihelion Π in function of the Solar Longitude $\lambda_\odot$ for the M2026-E1 based upon orbits (2022–2026) and radiant classification (2026).

Looking at the inclination (*Figure 12*) and eccentricity (*Figure 13*) against longitude of perihelion shows there to be a large spread in perihelion longitude. *Figure 14* shows a significant increase in longitude of perihelion during the

activity period. The other Kepler elements remain relatively stable during the activity period.

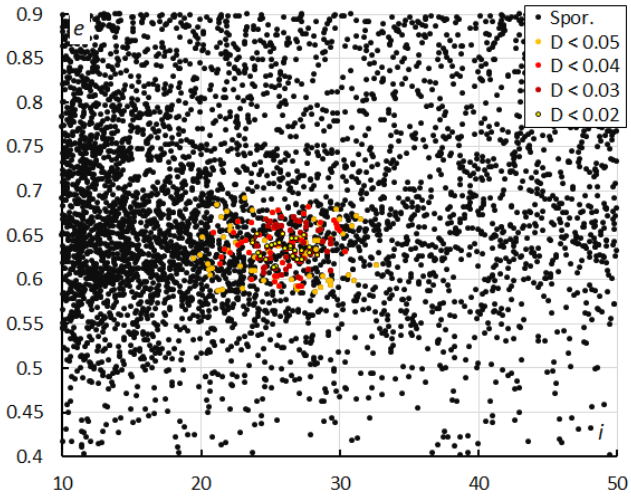

Figure 15 – Eccentricity e versus the inclination i color-coded for different classes of D-criteria thresholds, for $\lambda_\odot$ between 322°and 339°.

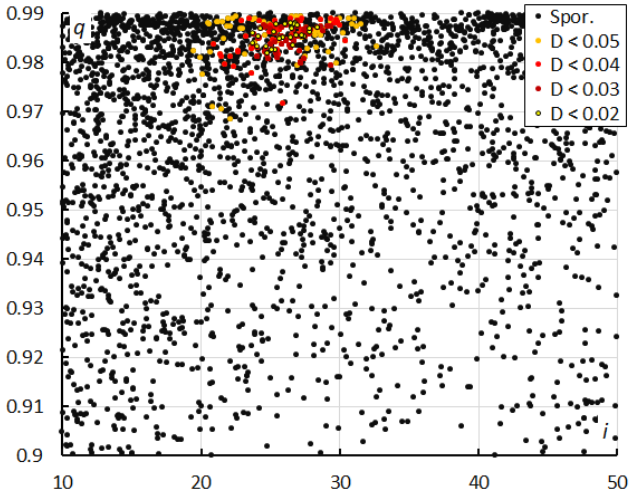

Figure 16 – Perihelion distance q versus the inclination i color-coded for different classes of D-criteria thresholds, for $\lambda_\odot$ between 322°and 339°.

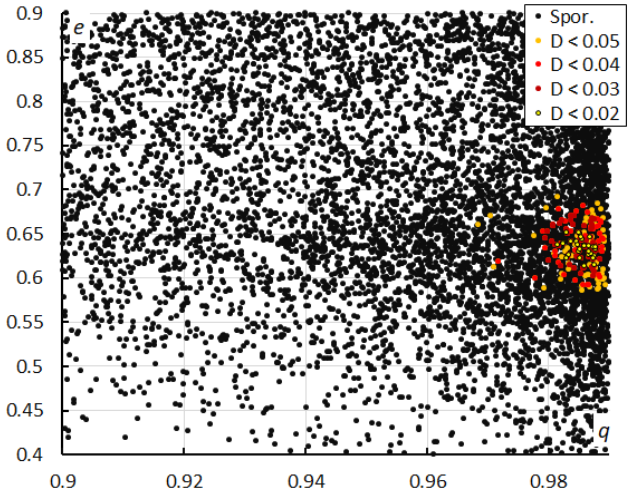

Figure 17 – Eccentricity e versus the perihelion distance q color-coded for different classes of D-criteria thresholds, for $\lambda_\odot$ between 322°and 339°.

The concentration in orbits is best visible in eccentricity e and perihelion distance q (*Figures 15, 16 and 17*).

The M2026-E1 meteoroid stream has a Jupiter-family comet type orbit with a Tisserand value relative to planet Jupiter of T_J = 2.96. The meteoroid stream intersects the Earth orbit at its ascending node (☊) while the descending node (☋) is situated between the asteroid belt and Jupiter (*Figure 18*).

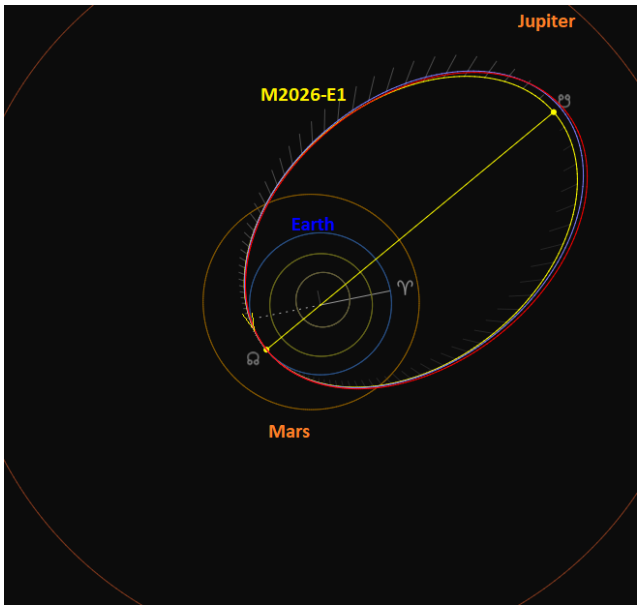

Figure 18 – Comparing the M2026-E1 solution (yellow) obtained by the radiant method with the solutions obtained by the orbit method for 2026 (blue) and 2022–2026 (red). (Plotted with the Orbit visualization app provided by Pető Zsolt).

The number of orbits per year reflects the expansion of GMN in the Southern Hemisphere, although in detail the camera coverage has not changed significantly since 2024. The number of M2026-E1 meteors in 2026 (*Table 2*) was much higher than in previous years. The very diffuse nature of the radiant area explains why it was overlooked in previous years when much less of these meteors were recorded.

Table 2 – The number of M2026-E1 orbits with $D_{SH} < 0.10$ and $D_D < 0.04$ and $D_J < 0.10$ per year during the period 2022–2026.

Year	Number of orbits
2022	2
2023	16
2024	49
2025	55
2026	121
Total	243

A search for possible parent bodies resulted in the top ten candidates listed in *Table 3*. None of the discrimination thresholds is conclusive to confirm any of these objects as a possible parent body. Numeric integrations of the orbital evolution are required to reconstruct the most likely behavior of the stream and its possible parent bodies.

Table 3 – Top ten matches of a search for possible parent bodies with $D_D < 0.085$, based upon the mean orbit derived from the radiant classification method.

Name	D_D
$2010JF_{87}$	0.057
$2017FL_{127}$	0.058
499P/Catalina	0.064
2016DK	0.072
$2017FG_{63}$	0.074
2018DG	0.074
$2025CV_{2}$	0.078
$2025DC_{25}$	0.080
$2016CC_{30}$	0.081
$2025DP_{13}$	0.083

5 Conclusion

A reliable orbit has been established for a newly discovered meteor shower that has a diffuse radiant in the constellation Dorado, and which displayed activity between 11 and 27 February 2026. The large dispersed radiant with slow meteors means the shower was barely detectable, which may account for it not having been discovered in the past. The shower has been added to the IAU-MDC Working List of Meteor Showers and has the temporary assignation M2026-E1.

Acknowledgments

This report is based on the data of the Global Meteor Network (Vida et al., 2020a; 2020b; 2021) which is released under the CC BY 4.0 license[10]. We thank all 927 participants in the Global Meteor Network project for their contribution and perseverance. A list with the names of the volunteers who contribute to GMN has been published in the 2025 annual report (Roggemans et al., 2026). The following 256 cameras contributed to paired meteors used in this study:

AU0002, AU0003, AU0004, AU0006, AU0007, AU0009, AU000A, AU000B, AU000C, AU000D, AU000E, AU000G, AU000L, AU000Q, AU000R, AU000S, AU000T, AU000V, AU000W, AU000X, AU000Y, AU0010, AU001A, AU001B, AU001C, AU001D, AU001E, AU001F, AU001K, AU001L, AU001N, AU001P, AU001Q, AU001R, AU001S, AU001U, AU001V, AU001W, AU001X, AU001Y, AU001Z, AU0029, AU002A, AU002B, AU002C, AU002E, AU0030, AU003C, AU003E, AU003G, AU003H, AU003J, AU0047, AU0048, AU004B, AU004J, AU004K, ES000U, KR0005, KR000A, KR000J, KR000K, KR000L, KR000N, KR001C, KR002E, KR003X, MX0002, MX000E, MX000F, NZ0001, NZ0002, NZ0003, NZ0004, NZ0007, NZ0008, NZ0009, NZ000A, NZ000B, NZ000C, NZ000D, NZ000G, NZ000H, NZ000L, NZ000M, NZ000N, NZ000P, NZ000Q, NZ000S, NZ000T, NZ000W, NZ000X, NZ000Y, NZ000Z, NZ0010, NZ0011, NZ0012, NZ0013, NZ0014, NZ0015, NZ0016, NZ0017, NZ0018, NZ0019, NZ001C, NZ001E, NZ001F, NZ001G, NZ001H, NZ001J, NZ001K, NZ001L, NZ001N, NZ001P, NZ001Q, NZ001R, NZ001S, NZ001V, NZ001W, NZ001X, NZ0020, NZ0022, NZ0023, NZ0024, NZ0025, NZ0026, NZ0027, NZ0029, NZ002B, NZ002C, NZ002D, NZ002E, NZ002F, NZ002G, NZ002H, NZ002J, NZ002K, NZ002L, NZ002M, NZ002N, NZ002P, NZ002Q, NZ002R, NZ002S, NZ002T, NZ002U, NZ002W, NZ002X, NZ002Y, NZ002Z, NZ0030, NZ0032, NZ0033, NZ0034, NZ0035, NZ0036, NZ0037, NZ0038, NZ0039, NZ003A, NZ003B, NZ003C, NZ003E, NZ003F, NZ003H, NZ003K, NZ003N, NZ003R, NZ003T, NZ003U, NZ003V, NZ003W, NZ003X, NZ003Y, NZ003Z, NZ0040, NZ0041, NZ0042, NZ0043, NZ0044, NZ0045, NZ0046, NZ0049, NZ004A, NZ004B, NZ004C, NZ004D, NZ004E, NZ004F, NZ004H, NZ004J, NZ004L, NZ004M, NZ004N, NZ004R, NZ004T, NZ004U, NZ004W, NZ004X, NZ004Y, NZ004Z, NZ0051, NZ0059, NZ005B, NZ005C, NZ005D, NZ005F, NZ005G, NZ005H, NZ005J, NZ005K, NZ005L, NZ005M, NZ005N, NZ005Q, NZ005R, NZ005S, NZ005T, NZ005U, NZ005Y, NZ0063, NZ0065, NZ0066, NZ0067, NZ0068, NZ0069, NZ006A, NZ006C, NZ006D, NZ006E, NZ006F, NZ006G, NZ006K, NZ007B, NZ007C, NZ007D, NZ007F, PT0002, US0006, US0008, US000A, US000C, US000E, US000H, US000M, US0023, US0030, US005C, ZA0002, ZA0007, ZA0008, ZA000A, ZA000C, ZA000D.

References

Drummond J. D. (1981). "A test of comet and meteor shower associations". *Icarus*, **45**, 545–553.

Jopek T. J. (1993). "Remarks on the meteor orbital similarity D-criterion". *Icarus*, **106**, 603–607.

Jopek T. J., Rudawska R. and Pretka-Ziomek H. (2006). "Calculation of the mean orbit of a meteoroid stream". *Monthly Notices of the Royal Astronomical Society*, **371**, 1367–1372.

Moorhead A. V., Clements T. D., Vida D. (2020). "Realistic gravitational focusing of meteoroid streams". *Monthly Notices of the Royal Astronomical Society*, **494**, 2982–2994.

Roggemans P., Vida D., Šegon D., Scott J. M. (2026a). "Meteoroid orbit shower identification method and its application in meteor shower case studies". *eMetN Meteor Journal*, **11**, 189–204.

Roggemans P., Campbell-Burns P., Kalina M., McIntyre M., Scott J. M., Šegon D., Vida D. (2026b). "Global Meteor Network report 2025". *eMetN Meteor Journal*, **11**, 89–129.

Southworth R. B. and Hawkins G. S. (1963). "Statistics of meteor streams". *Smithsonian Contributions to Astrophysics*, **7**, 261–285.

Vida D., Gural P., Brown P., Campbell-Brown M., Wiegert P. (2020a). "Estimating trajectories of meteors: an observational Monte Carlo approach - I. Theory". *Monthly Notices of the Royal Astronomical Society*, **491**, 2688–2705.

[10] https://creativecommons.org/licenses/by/4.0/

Vida D., Gural P., Brown P., Campbell-Brown M., Wiegert P. (2020b). “Estimating trajectories of meteors: an observational Monte Carlo approach - II. Results”. *Monthly Notices of the Royal Astronomical Society*, **491**, 3996–4011.

Vida D., Šegon D., Gural P. S., Brown P. G., McIntyre M. J. M., Dijkema T. J., Pavletić L., Kukić P., Mazur M. J., Eschman P., Roggemans P., Merlak A., Zubrović D. (2021). “The Global Meteor Network – Methodology and first results”. *Monthly Notices of the Royal Astronomical Society*, **506**, 5046–5074.

Delta-Chamaeleontids (DCH#107) confirmed

Paul Roggemans[1], **Denis Vida**[2,3], **Damir Šegon**[4,5], **James M. Scott**[6], **Jeff Wood**[7]

[1] **Pijnboomstraat 25, 2800 Mechelen, Belgium**
Paul.roggemans@gmail.com

[2] **Department of Physics and Astronomy, University of Western Ontario, Richmond Street, London, N6A 3K7, Ontario, Canada**

[3] **Institute for Earth and Space Exploration, University of Western Ontario, Perth Drive, London, N6A 5B8, Ontario, Canada**
denis.vida@gmail.com

[4] **Astronomical Society Istra Pula, Park Monte Zaro 2, 52100 Pula, Croatia**

[5] **Višnjan Observatory, Istarska 5, 52463 Višnjan, Croatia**

[6] **Department of Geoscience, Aarhus University, Høegh-Guldbergs Gade 2. DK-8000 Aarhus C, Denmark**

[7] **PO Box 162, Willetton, Western Australia 6955, Australia**

An activity source identified as the delta-Chamaeleontids has been detected between the 19th and 25th of February 2026 from a radiant at R.A. = 3.9° and Decl.= –87.1°, with a geocentric velocity of 40.8 km/s. This case study confirms the existence of this annual meteor shower and that it fulfils the criteria to be nominated for established status by the IAU-MDC.

1 Introduction

During the delta-Normids outburst on 22–23 February 2026 (*Figure 1*), a weaker activity source caught attention. The shower wasn't included in the list of showers monitored by GMN. The radiant position in equatorial coordinates at Right Ascension 4° and Declination –87° is very close to the Southern Hemisphere pole in the constellation Octans. The activity corresponds to the delta-Chamaeleontids (DCH#107) in the IAU-MDC Working List of Meteor Showers[11]. The name is weird as the star δ-Chamaeleonis is nowhere near this radiant. According to Jenniskens (2023), the shower was first noticed and named based upon Adelaide radar data from December 1968 to June 1969 (Gartrell and Elford, 1975). However, Gartrell and Elford mention a radiant position at R.A. 250° and Decl. –86°, based upon only 4 meteors, located in Octans, but without defining and naming the association of meteors as a shower.

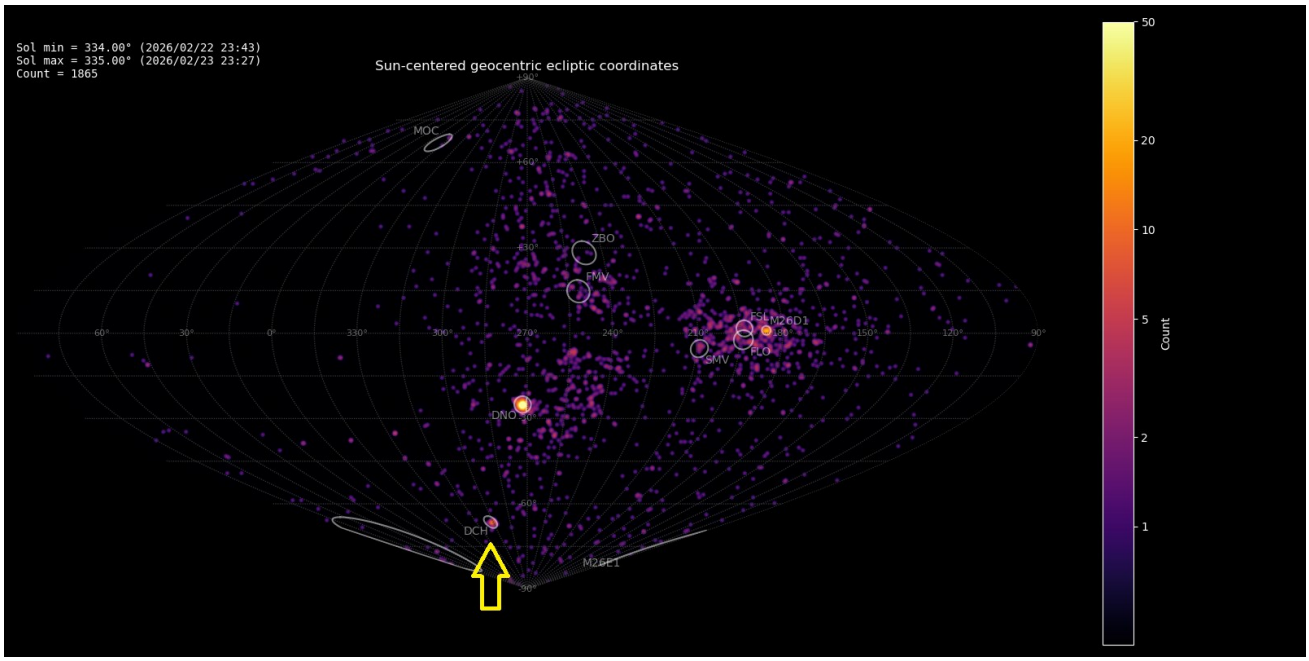

Figure 1 – Radiant density map with 1865 radiants obtained by the Global Meteor Network during 22–23 February, 2026. The position of the delta-Chamaeleontids in Sun-centered geocentric ecliptic coordinates is marked with a yellow arrow.

[11] https://www.ta3.sk/IAUC22DB/MDC2022/Roje/pojedynczy_obiekt.php?lporz=00386&kodstrumienia=00107

This solution is DCH#107.000 in the IAU-MDC list and it was associated by Gartrell and Elford with comet C/1930 D1 Peltier-Schwassmann-Wachmann as likely parent body. The second solution, DCH#107.001, is based upon 47 meteors but differs a lot in velocity and eccentricity and is based upon a very poor D-criterion threshold of $D_{SH} = 0.39$. Given that radar meteoroid orbits at that time had large uncertainties, combined with such a poor discrimination threshold, solution DCH#107.001 should be removed from the IAU-MDC list. Gartrell and Elford nowhere link it to DCH#107.000.

The name Chamaeleontids appears in a later study by Jopek et al. (1999) where the distance function D_N by Valsecchi et al. (1999) was applied on the Adelaide radar data. This solution was based upon 33 radar meteors recorded between 10 and 17 February 1969, listed as DCH#107.002. The radiant was at R.A. 207° and Decl. –78° which is in the constellation Chamaeleon but nowhere near the star delta. The radar observations covered only one week per month and missed the activity period of the shower completely. The activity period, eccentricity and inclination of DCH#107.002 differ a lot from the observed shower in recent times. This solution may refer to another activity or may be even a spurious association. Jopek et al. marked it as probably never identified before, thus not related to the solution published by Gartrell and Elford. This solution may be also considered to be removed from IAU-MDC list.

The name delta-Chamaeleontids first appears in Jenniskens (2006) where the two unrelated solutions from Gartrell and Elford (1975) are combined, although the radiant positions based upon four meteors is in Octans and the radiant based upon 47 meteors was derived with a very poor discrimination threshold and therefore highly uncertain.

2 Shower classification based on radiants

The GMN shower association criteria assume that meteors within 1° in solar longitude, within 2.0° in radiant in this case, and within 10% in geocentric velocity of a shower reference location are members of that shower. Further details about the shower association are explained in Moorhead et al. (2020). Using these meteor shower selection criteria, 60 orbits have been identified as delta-Chamaeleontids recorded in 2025–2026 by 130 GMN cameras installed in Australia, New Zealand and South Africa. Since the shower is only observable from the Southern Hemisphere only data from this part of the world has been used. The final results have been listed in *Table 1*.

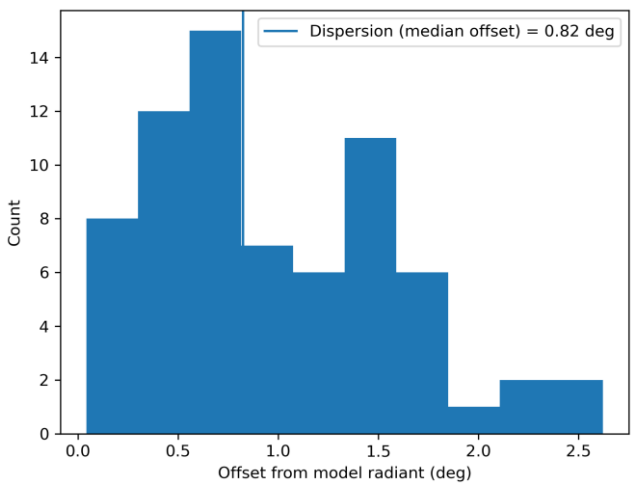

Figure 2 – Dispersion median offset on the radiant position.

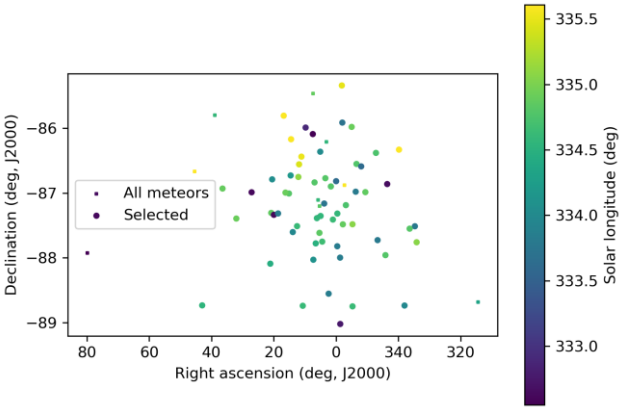

Figure 3 – The radiant distribution during the solar-longitude interval 332.5° – 335.5° in equatorial coordinates.

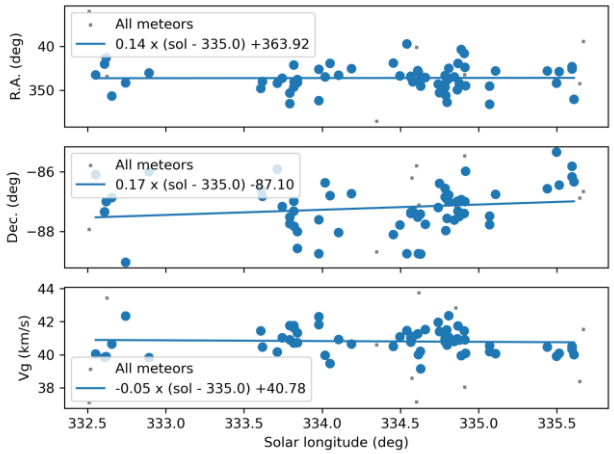

Figure 4 – The radiant drift.

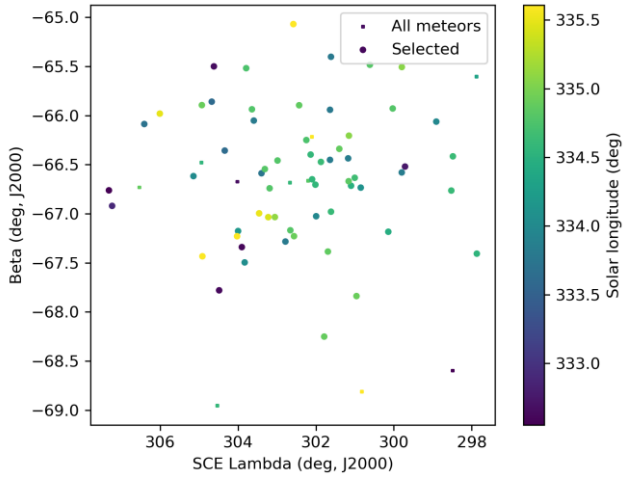

Figure 5 – The radiant distribution during the solar-longitude interval 332.5° – 335.5° in Sun centered geocentric ecliptic coordinates.

3 Shower classification based on orbits

A complete independent meteoroid stream search has been applied for confirmation based upon orbit data obtained between Solar Longitude 330.0° and 338.0° during the years 2019 to 2026. 51612 orbits were available within this time interval and a final mean orbit has been computed by the method of Jopek et al. (2006) for the thresholds $D_{SH} < 0.125$ and $D_D < 0.05$ and $D_J < 0.125$ (Southworth and Hawkins, 1963; Drummond, 1981; Jopek, 1993. No data are available for the Southern Hemisphere before 2022. The results with the mean orbit based upon 83 meteors for 2022–2026 have been listed in *Table 1*. The method has been described in detail in a separate publication (Roggemans et al., 2026a).

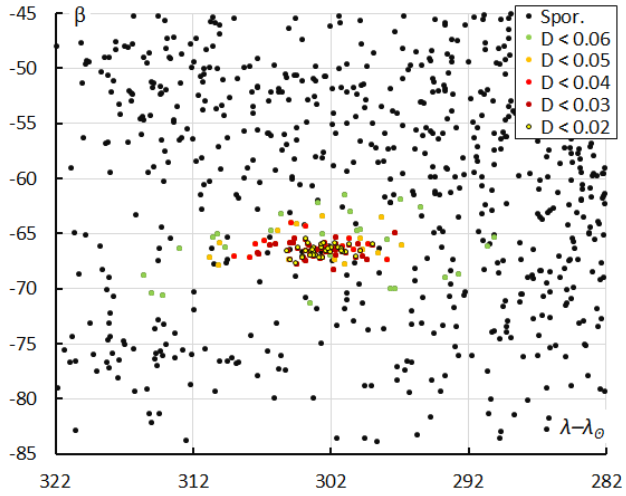

Figure 6 – The radiant distribution during the solar-longitude interval 330° – 338° in Sun-centered geocentric ecliptic coordinates, color-coded for different threshold values of the combined similarity criteria.

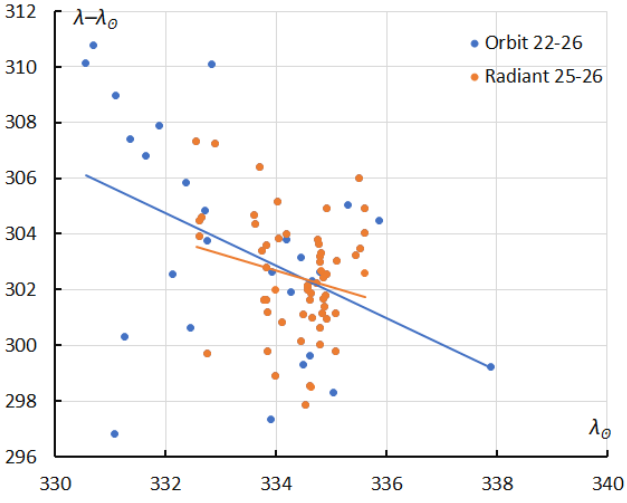

Figure 7 – The Sun-centered geocentric longitude $\lambda–\lambda_\odot$ in function of the Solar Longitude $\lambda_\odot$ for DCH#107 based upon orbits (2022–2026) and radiant classification (2025–2026).

The green dots in *Figure 6* with $D_{SH} < 0.15$ and $D_D < 0.06$ and $D_J < 0.15$ appear rather dispersed and were ignored as outliers. The cutoff for the thresholds on the D criteria was set at $D_{SH} < 0.125$ and $D_D < 0.05$ and $D_J < 0.125$. The Sun-centered ecliptic longitude appears stretched in *Figure 6* due to the radiant drift $\Delta(\lambda–\lambda_\odot)/\Delta\lambda_\odot$ with $–0.59°/\Delta\lambda_\odot$ (*Figure 7*). No drift in ecliptic latitude occurs.

Both methods identified 87 meteors as delta-Chamaeleontids with 56 (or 64%) of them in common, four by the radiant method that fail to fit the $D_{SH} < 0.125$ and $D_D < 0.05$ and $D_J < 0.125$ thresholds, and 27 (or 31%) identified by the orbit method but ignored by the radiant method, 14 of which from years not covered by the radiant method.

The orbit classification method detects a longer activity period than the period assumed for the radiant classification method. Plotting the ratio delta-Chamaeleontids meteors/all meteors, for time intervals of 1.5° in Solar Longitude, plotted every 0.25°, results in a skewed profile with a slow incline followed by a steep decline in activity (*Figure 8*). The orbit method (blue) identified more delta-Chamaeleontids candidates than the radiant method (orange). The best rates occurred at $\lambda_\odot = 334.5°$. The shower activity duration lasts one week from 19 until 26 February making it very unlikely that the 1969 radar data recorded between 10 and 17 February includes any data related to the currently known delta-Chamaeleontids.

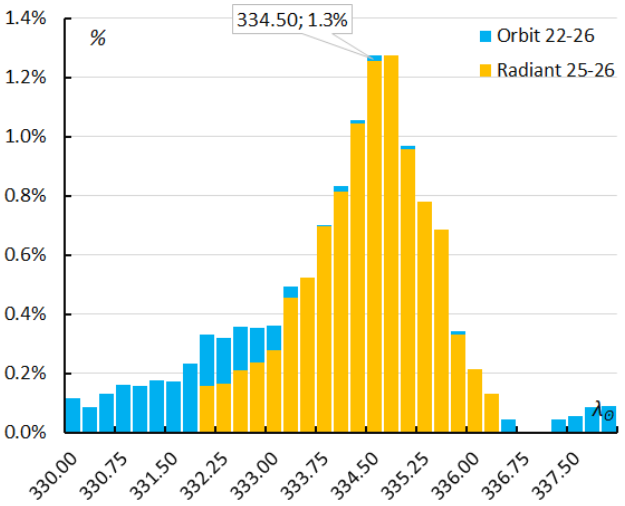

Figure 8 – The percentage of delta-Chamaeleontids relative to the total number of meteors, for the radiant method (2025–2026) and the orbit classification method 2022–2026.

4 Orbit and parent body

The diagram of the inclination i versus the Longitude of Perihelion Π shows a concentration in i, stretched in Π (*Figure 9*). The eccentricity e versus the Longitude of Perihelion Π appears very scattered (*Figure 10*). The spread in Longitude of Perihelion is caused by a steep increase in Longitude of Perihelion during the activity (*Figure 11*), while the spread in eccentricity is caused by the larger uncertainty on this Kepler element with values close to the hyperbolic limit ($e > 1$). This spread in eccentricity appears in the diagrams versus inclination (*Figure 12*) and versus perihelion distance (*Figure 14*). There is a small increase in inclination with $0.3°/\lambda_\odot$ and in perihelion distance with $0.002AU/\lambda_\odot$. The cluster of orbits is best visible in the diagram of the perihelion distance q versus inclination i

(*Figure 13*). The eccentricity remains constant during the activity period.

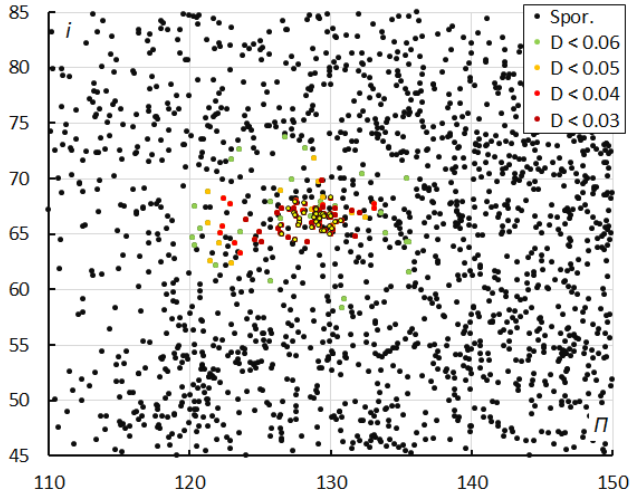

Figure 9 – Inclination *i* versus the longitude of perihelion *Π* color-coded for different classes of D-criteria thresholds, for $\lambda_\odot$ between 330° and 338°. Spor. = sporadics.

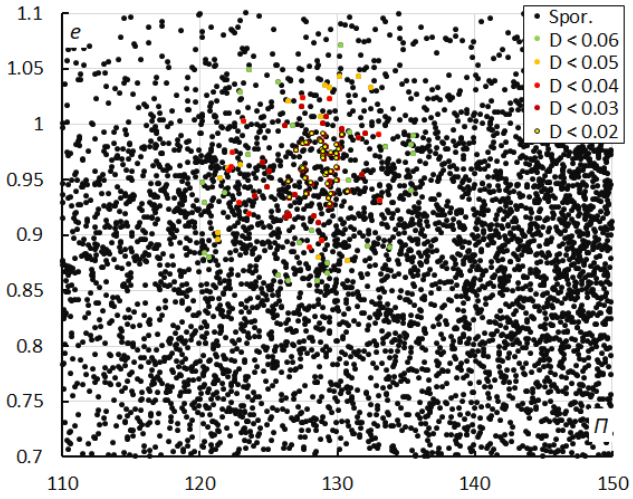

Figure 10 – A diagram of the eccentricity *e* versus the longitude of perihelion *Π* color-coded for different classes of D-criteria thresholds, for $\lambda_\odot$ between 330° and 338°. Spor. = sporadics.

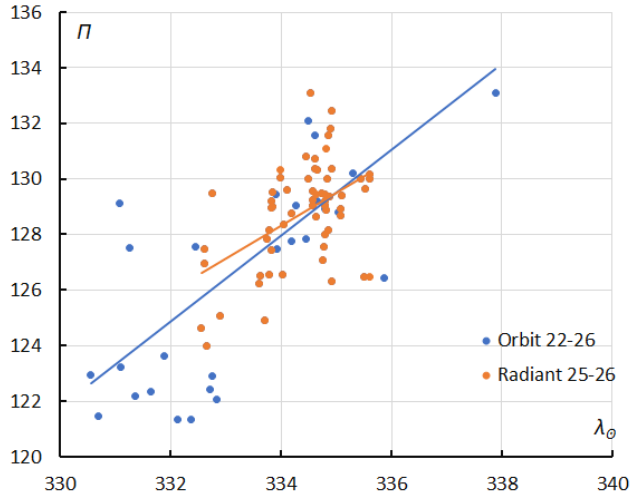

Figure 11 – The evolution of the Longitude of Perihelion *Π* in function of the Solar Longitude $\lambda_\odot$ based upon the radiant method (2025–2026) and upon the orbit method (2022–2026).

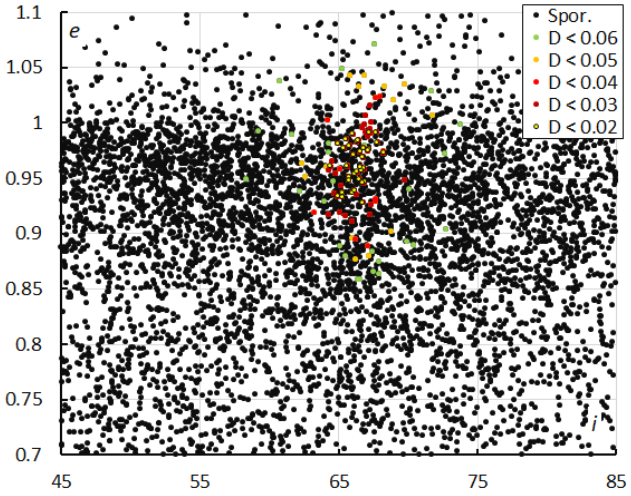

Figure 12 – Eccentricity *e* versus the inclination *i* color-coded for different classes of D-criteria thresholds, for $\lambda_\odot$ between 330° and 338°. Spor. = sporadics.

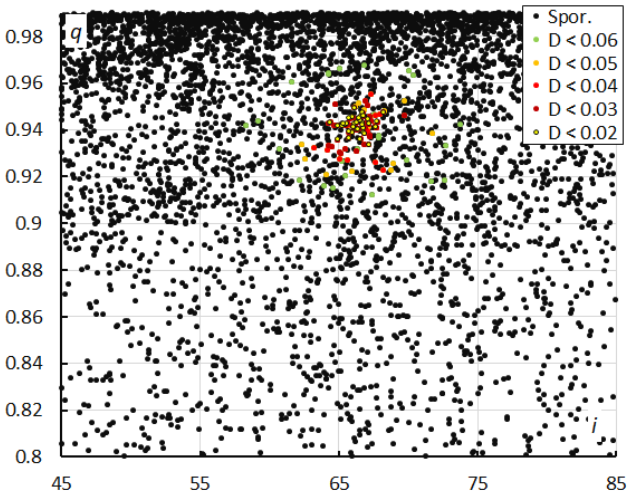

Figure 13 – Perihelion distance *q* versus the inclination *i* color-coded for different classes of D-criteria thresholds, for $\lambda_\odot$ between 330° and 338°. Spor. = sporadics.

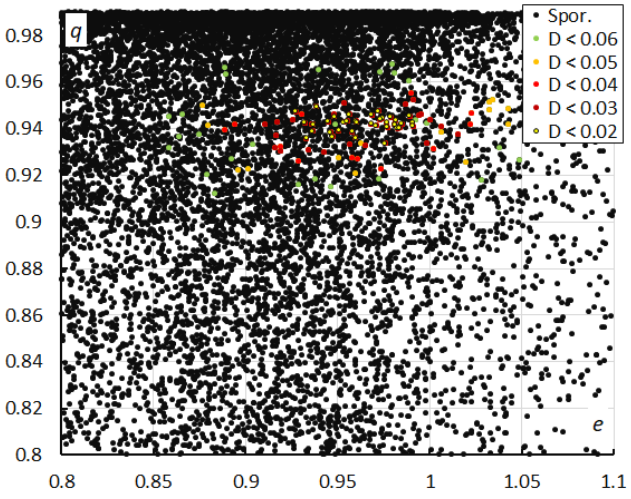

Figure 14 – Perihelion distance *q* versus the eccentricity *e* color-coded for different classes of D-criteria thresholds, for $\lambda_\odot$ between 330° and 338°. Spor. = sporadics.

Table 1 – Comparing solutions obtained by the radiant method for 2025–2026, the orbit method 2022–2026 for $D_D < 0.05$ and $D_D < 0.04$, compared to the solution by Jenniskens (2023).

	Radiant 2025-26	Orbit $D_D < 0.05$	Orbit $D_D < 0.04$	Jenniskens (2023)
$\lambda_\odot$ (°)	334.5	334.5	334.5	334.8
$\lambda_{\odot b}$ (°)	332.0	330.5	331.0	330.0
$\lambda_{\odot e}$ (°)	337.0	337.9	337.9	336.0
α_g (°)	3.9	43.0	36.4	1.8
δ_g (°)	–87.1	–87.0	–87.0	–87.3
$\Delta\alpha_g$ (°)	+0.14	–	–	+7.50
$\Delta\delta_g$ (°)	+0.17	–0.03	+0.01	+0.30
v_g (km/s)	40.8	40.9	40.9	41.3
H_b (km)	106.4	106.1	106.1	108.3
H_e (km)	94.7	94.5	94.2	92.6
H_p (km)	98.7	98.7	98.7	98.0
Mag_{Ap}	–0.6	–0.4	–0.4	+1.9
λ_g (°)	277.1	277.0	277.1	277.0
$\lambda_g - \lambda_\odot$ (°)	302.6	302.6	302.6	302.2
β_g (°)	–66.6	–66.5	–66.5	–66.5
a (A.U.)	23.4	24.7	23.6	58.3
q (A.U.)	0.941	0.939	0.940	0.942
e	0.960	0.962	0.960	0.984
i (°)	66.3	66.4	66.3	66.8
ω (°)	334.4	334.0	334.1	334.9
Ω (°)	154.4	154.0	154.1	154.8
Π (°)	128.8	128.0	128.2	129.2
T_j	0.70	0.69	0.70	0.56
N	60	83	69	16

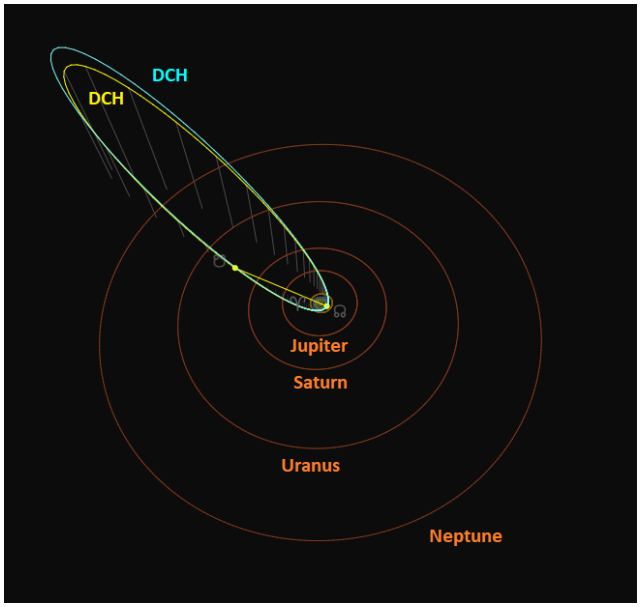

Figure 15 – Comparing the radiant determined delta-Chamaeleontids solution (yellow) with the orbit determined solution (blue). (Plotted with the Orbit visualization app provided by Pető Zsolt).

With a Tisserand value relative to Jupiter of $T_J = 0.70$ the delta-Chamaeleontids are a long-period comet type meteoroid stream steeply inclined to the ecliptic (*Figure 15*). The meteoroids cross the Earth orbit at the ascending node (*Figure 16*). The descending node is situated in the ecliptic plane between the orbits of Saturn and Uranus.

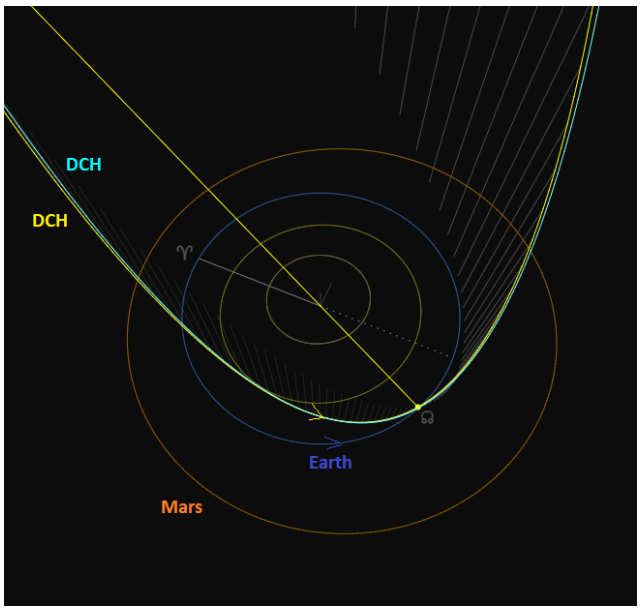

Figure 16 – Comparing the radiant determined delta-Chamaeleontids solution (yellow) with the orbit determined solution (blue), close-up at the inner Solar System. (Plotted with the Orbit visualization app provided by Pető Zsolt).

Table 2– Top ten matches of a search for possible parent bodies with $D_D < 0.25$, based upon the mean orbit derived from the radiant classification method.

Name	D_D
C/574 G1	0.153
C/1976 D1 (Bradfield)	0.162
C/1993 Y1 (McNaught-Russell)	0.177
C/1804 E1 (Pons)	0.179
C/1905 F1 (Giacobini)	0.218
C/1930 D1 (Peltier-Schwassmann-Wachmann)	0.219
C/1240 B1	0.221
(248590) 2006 CS	0.226
C/1931 O1 (Nagata)	0.236
C/1942 EA (Vaisala)	0.244

A search for possible parent bodies did not result in any convincing association. C/1930 D1 (Peltier-Schwassmann-Wachmann), which was proposed as a very likely parent body for some radar meteors by Gartrell and Elford (1975), differs a lot in inclination by 33° and is rather unlikely as a candidate parent body. Either the parent body has yet to be discovered or stream modeling may prove how the stream has been formed and separated from its parent body.

The shower has produces annual activity. The GMN recorded two DCH meteors in 2022, six in 2023, six in 2024, 40 in 2025 and 29 in 2026. The numbers of shower meteors per year reflect the expansion of the GMN network

at the Southern Hemisphere and the weather circumstances during the rather short activity period.

5 Conclusions

This GMN meteoroid orbit data case study confirms the existence of the delta-Chamaeleontids. Our independent solution has been reported to the IAU-MDC, and the shower now fulfils the criteria to be nominated for established status. The new GMN solution has been double checked by using two independent shower identification methods as a two-factor authentication for the validation of the analyses.

Some corrections are required to the IAU-MDC Working List of Meteor Showers for the stream data entry for the delta-Chamaeleontids[12]. The listed solutions under 00107.000, 00107.001 and 00107.002 are based on radar orbit data recorded during 10 and 17 February 1969 which is too far off in time from the current activity period, which is between 19 and 25 February. Moreover, the original paper by Gartrell and Elford (1975) searched among 1667 radar orbits spread over six weeks of which one week in February. Using the Southworth and Hawkins D-criterion to look for similar orbits with two, three or more members, these small groups are listed as simple associations of three or more meteors most of which are nowhere defined as meteor showers by the authors, including the solutions 00107.000 based upon four meteors with a radiant in Octans and 00107.001 based upon 47 meteors but with a far too tolerant D_{SH} = 0.39. Nowhere do Gartrell and Elford claim these associations represent meteor showers, and the name delta-Chamaeleontids is not mentioned anywhere. Given the uncertainties typical for radar orbit data and the small numbers of orbits available, the associations may be regarded as possible spurious combinations. Jopek et al. (1999) used 3675 Adelaide radio meteors, including the 1667 used by Gartrell and Elford in 1975. In that publication the name Chamaeleontids appears based upon 33 meteors but with an activity period of 11 to 17 February. Activity period, eccentricity and inclination differ too much to link this activity to the currently known shower.

The naming of delta-Chamaeleontids appears in Jenniskens (2006) based upon the sources of the unrelated solutions 00107.000 and 00107.001. The naming of meteor showers remains problematic as the actual radiant of the delta-Chamaeleontids is located in the constellation Octans instead of near delta Chamaeleonis, which is based upon incorrect associations in the past. This situation favors the current procedure with a provisional naming until the shower is confirmed for established status.

Acknowledgments

This report is based on the data of the Global Meteor Network (Vida et al., 2020a; 2020b; 2021) which is released under the CC BY 4.0 license[13]. We thank all 927 participants in the Global Meteor Network project for their contribution and perseverance. A list with the names of the volunteers who contribute to GMN has been published in the 2025 annual report (Roggemans et al., 2026b). The following 157 cameras contributed to paired meteors used in this study:

AU0002, AU0003, AU0004, AU0006, AU0007, AU0009, AU000B, AU000D, AU000E, AU000F, AU000G, AU000L, AU000Q, AU000R, AU000S, AU000T, AU000U, AU000V, AU000Z, AU0010, AU001A, AU001B, AU001E, AU001F, AU001K, AU001L, AU001N, AU001P, AU001Q, AU001R, AU001S, AU001U, AU001V, AU001W, AU0029, AU002B, AU002D, AU0030, AU0038, AU003E, AU003G, AU003J, AU0042, AU0047, AU0048, AU004K, AU004L, AU004Q, NZ0001, NZ0002, NZ0003, NZ0004, NZ0007, NZ0009, NZ000B, NZ000G, NZ000L, NZ000P, NZ000Q, NZ000V, NZ000Z, NZ0010, NZ0011, NZ0012, NZ0014, NZ0015, NZ0016, NZ0017, NZ0018, NZ001E, NZ001G, NZ001J, NZ001L, NZ001N, NZ001R, NZ001S, NZ001V, NZ001Z, NZ0022, NZ0023, NZ0024, NZ0025, NZ0026, NZ0027, NZ0028, NZ0029, NZ002C, NZ002D, NZ002E, NZ002F, NZ002H, NZ002L, NZ002N, NZ002P, NZ002Q, NZ002T, NZ002U, NZ002V, NZ002X, NZ002Y, NZ002Z, NZ0030, NZ0033, NZ0034, NZ0035, NZ0036, NZ0037, NZ003B, NZ003C, NZ003E, NZ003H, NZ003K, NZ003N, NZ003Q, NZ003R, NZ003S, NZ003T, NZ003U, NZ003V, NZ003W, NZ003X, NZ003Y, NZ003Z, NZ0041, NZ0042, NZ0046, NZ004B, NZ004H, NZ004J, NZ004M, NZ004R, NZ004U, NZ004W, NZ004X, NZ004Y, NZ004Z, NZ0051, NZ0059, NZ005D, NZ005G, NZ005K, NZ005L, NZ005N, NZ005T, NZ005U, NZ005Z, NZ0067, NZ006C, NZ006E, NZ006F, NZ006G, NZ006K, ZA0006, ZA0007, ZA0008, ZA0009 and ZA000A.

References

Drummond J. D. (1981). “A test of comet and meteor shower associations”. *Icarus*, **45**, 545–553.

Gartrell G., Elford W.G. (1975). “Southern Hemisphere Meteor Stream Determinations”. *Australian Journal of Physics*, **28**, 521–620.

Jenniskens P. (2006). “Meteor showers and their parent comets”. Cambridge University Press. Page 695.

Jenniskens P. (2023). Atlas of Earth’s meteor showers. Elsevier, Cambridge, United states. ISBN 978-0-443-23577-1. Page 535.

Jopek T. J. (1993). “Remarks on the meteor orbital similarity D-criterion”. *Icarus*, **106**, 603–607.

Jopek T. J., Valsecchi G. B., Froeschle Cl. (1999). “Meteor stream identification a new approach. Application to 3675 radio meteors”. In, W. J. Baggaley and V. Porubcan, editors, Meteoroids 1998: Proceedings of the International Conference held at Tatranska Lomnica, Slovakia, August 17-21, 1998.

[12] https://www.ta3.sk/IAUC22DB/MDC2022/Roje/pojedynczy_obiekt.php?lporz=00386&kodstrumienia=00107

[13] https://creativecommons.org/licenses/by/4.0/

Astronomical Institute of the Slovak Academy of Sciences, 307–310.

Jopek T. J., Rudawska R. and Pretka-Ziomek H. (2006). “Calculation of the mean orbit of a meteoroid stream”. *Monthly Notices of the Royal Astronomical Society*, **371**, 1367–1372.

Moorhead A. V., Clements T. D., Vida D. (2020). “Realistic gravitational focusing of meteoroid streams”. *Monthly Notices of the Royal Astronomical Society*, **494**, 2982–2994.

Roggemans P., Vida D., Šegon D., Scott J.M. (2026a). “Meteoroid orbit shower identification”. *eMetN Meteor Journal*, **11**, 189–204.

Roggemans P., Campbell-Burns P., Kalina M., McIntyre M., Scott J. M., Šegon D., Vida D. (2026b). “Global Meteor Network report 2025”. *eMetN Meteor Journal*, **11**, 89–129.

Southworth R. B. and Hawkins G. S. (1963). “Statistics of meteor streams”. *Smithsonian Contributions to Astrophysics*, **7**, 261–285.

Valsecchi G. B., Jopek T. J., Froeschle Cl. (1999). “Meteoroid stream identification: a new approach - I. Theory”. *Monthly Notices of the Royal Astronomical Society*, **304**, 743–750.

Vida D., Gural P., Brown P., Campbell-Brown M., Wiegert P. (2020a). “Estimating trajectories of meteors: an observational Monte Carlo approach - I. Theory”. *Monthly Notices of the Royal Astronomical Society*, **491**, 2688–2705.

Vida D., Gural P., Brown P., Campbell-Brown M., Wiegert P. (2020b). “Estimating trajectories of meteors: an observational Monte Carlo approach - II. Results”. *Monthly Notices of the Royal Astronomical Society*, **491**, 3996–4011.

Vida D., Šegon D., Gural P. S., Brown P. G., McIntyre M. J. M., Dijkema T. J., Pavletić L., Kukić P., Mazur M. J., Eschman P., Roggemans P., Merlak A., Zubrović D. (2021). “The Global Meteor Network – Methodology and first results”. *Monthly Notices of the Royal Astronomical Society*, **506**, 5046–5074.

Delta[1]-Canis Minorids (DCN#1168) confirmed

Paul Roggemans[1], **Denis Vida**[2,3], **Damir Šegon**[4,5], **James M. Scott**[6], **Jeff Wood**[7]

[1] **Pijnboomstraat 25, 2800 Mechelen, Belgium**
Paul.roggemans@gmail.com

[2] **Department of Physics and Astronomy, University of Western Ontario, Richmond Street, London, N6A 3K7, Ontario, Canada**

[3] **Institute for Earth and Space Exploration, University of Western Ontario, Perth Drive, London, N6A 5B8, Ontario, Canada**
denis.vida@gmail.com

[4] **Astronomical Society Istra Pula, Park Monte Zaro 2, 52100 Pula, Croatia**

[5] **Višnjan Observatory, Istarska 5, 52463 Višnjan, Croatia**

[6] **Department of Geoscience, Aarhus University, Høegh-Guldbergs Gade 2. DK-8000 Aarhus C, Denmark**

[7] **PO Box 162, Willetton, Western Australia 6955, Australia**

An activity source identified as the delta[1]-Canis Minorids was detected between the 9th and 19th of January 2025–2026 with a radiant at R.A. = 109.9° and Decl.= +1.1°, and a geocentric velocity of 23.8 km/s. The shower displayed an activity outburst in 2026. This case study confirms the existence of this annual meteor shower and fulfils the criteria in order to be nominated for established status by the IAU-MDC.

1 Introduction

A weak source of activity appeared on the GMN radiant density plots, about 20° south of the anti-helion point, in January 2026. The radiant was identified as the delta[1]-Canis Minorids (DCN#1168). This shower was noticed by Jenniskens (2023) in CAMS data as an annual shower with episodic outbursts in 2015 and 2020. A first solution was reported to the IAU Meteor Data Center (MDC) Working List of Meteor Showers, based upon 105 meteors[14] recorded by CAMS until 2023.

GMN has collected enough data on this weak activity to confirm the existence of this meteor shower that fulfills the IAU-MDC criteria of having its parameters (radiant coordinates, velocity and orbit) determined by independent studies that it can be nominated for established status.

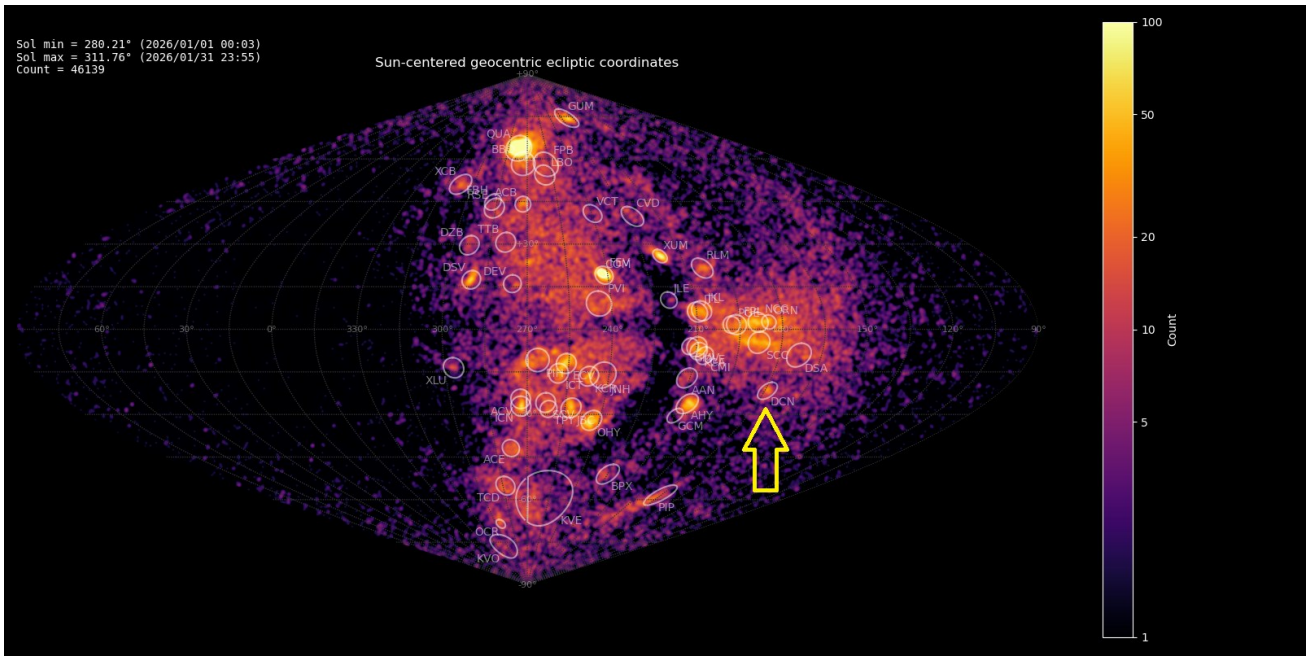

Figure 1 – Radiant density map with 46139 radiants obtained by the Global Meteor Network during January, 2026. The position of the delta[1]-Canis Minorid in Sun-centered geocentric ecliptic coordinates is marked with a yellow arrow.

[14] https://www.ta3.sk/IAUC22DB/MDC2022/Roje/pojedynczy_obiekt.php?lporz=02518&kodstrumienia=01168

2 Shower classification based on radiants

The GMN shower association criteria assume that meteors within 1° in solar longitude, within 2.5° in radiant in this case, and within 10% in geocentric velocity of a shower reference location are members of that shower. Further details about the shower association are explained in Moorhead et al. (2020). Using these meteor shower selection criteria, 108 orbits have been identified as delta[1]-Canis Minorids recorded in 2025–2026 by 243 GMN cameras installed in Austria, Australia, Belgium, Bosnia Herzegovina, Bulgaria, Chile, Croatia, France, Germany, Greece, Hungary, Israel, Italy, New Zealand, Russia, Slovenia, South Korea, United Kingdom, United States and South Africa. The final results have been listed in *Table 2*.

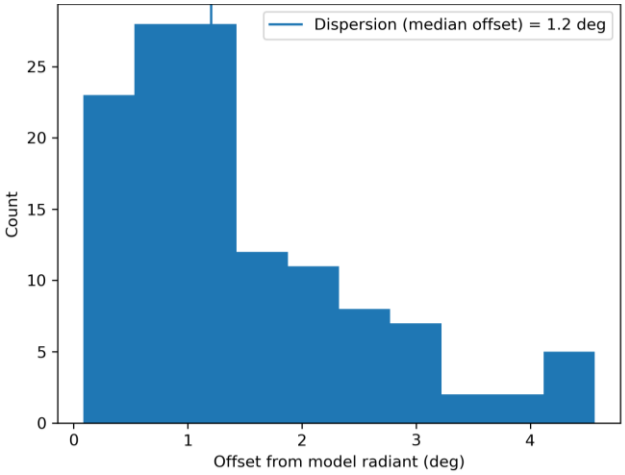

Figure 2 – Dispersion median offset on the radiant position.

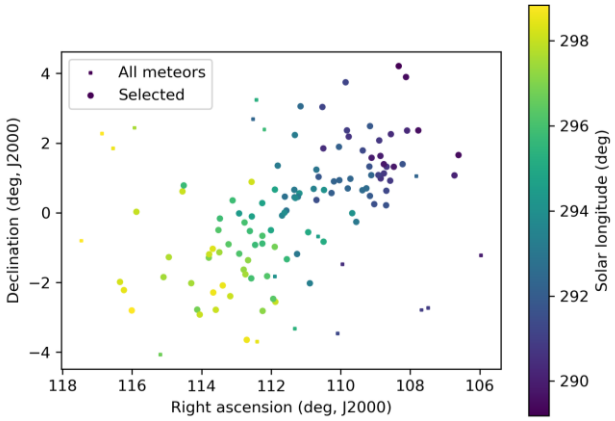

Figure 3 – The radiant distribution during the solar-longitude interval 291.5° – 298.5° in equatorial coordinates.

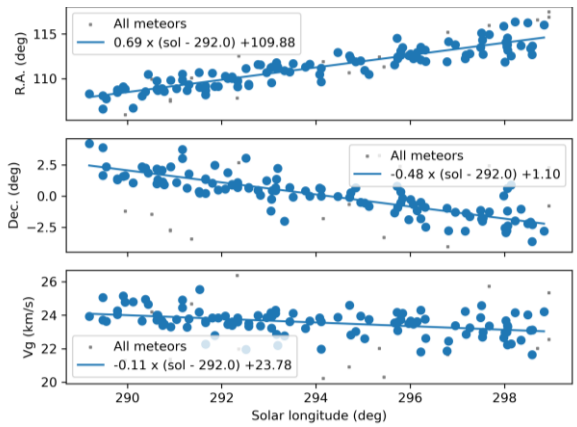

Figure 4 – The radiant drift.

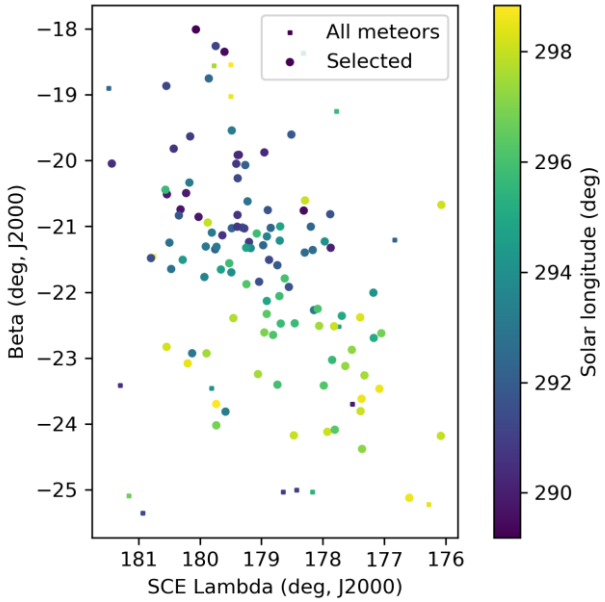

Figure 5 – The radiant distribution during the solar-longitude interval 291.5° – 298.5° in Sun centered geocentric ecliptic coordinates.

3 Shower classification based on orbits

A complete independent meteoroid stream search has been applied for confirmation based upon orbit data obtained between Solar Longitude 282.0° and 303.0° during the years 2019 to 2026. 159494 orbits were available within this time interval and a final mean orbit has been computed by the method of Jopek et al. (2006) for the thresholds according to the Rayleigh fit in *Figure 6*. $D_{SH} < 0.100$ and $D_D < 0.04$ and $D_J < 0.100$ (Southworth and Hawkins, 1963; Drummond, 1981; Jopek, 1993. The results with the mean orbit based upon 234 meteors for 2019–2026 are listed in *Table 2*. The method has been described in detail in a separate publication (Roggemans et al., 2026a).

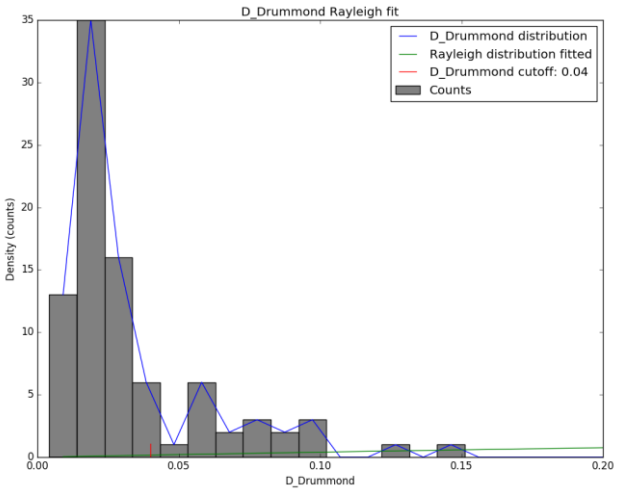

Figure 6 – Rayleigh fit on the Drummond criterion for delta[1]-Canis Minorid, 2026 data.

The radiant plot in equatorial coordinates (*Figure 7*) appears stretched due to the radiant drift caused by the movement of the Earth on its orbit around the Sun. The dense cluster east (left) from DCN are the alpha-Hydrids (AHY#331) an established minor shower. In Sun-centered

ecliptic coordinates the radiant appears more concentrated (*Figure 8*). The orange dots with the threshold class $D_{SH} < 0.125$ and $D_D < 0.05$ and $D_J < 0.125$ appear very dispersed and represent outliers that are difficult to distinguish from the sporadic background. This threshold class appears to be too tolerant for this stream.

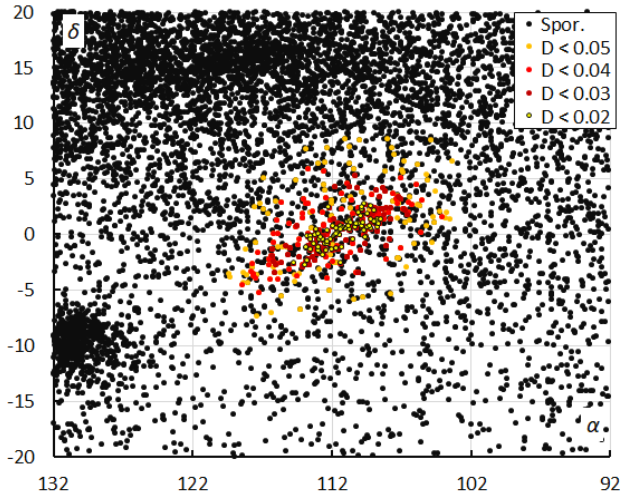

Figure 7 – The radiant distribution during the solar-longitude interval 287° – 300° in equatorial coordinates, color-coded for different threshold values of the combined similarity criteria.

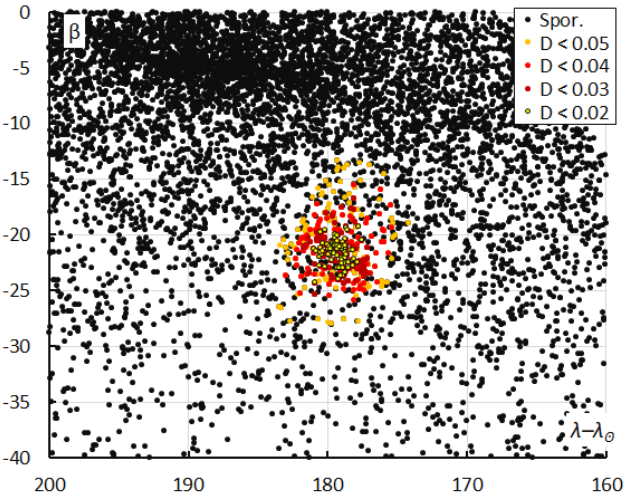

Figure 8 – The radiant distribution during the solar-longitude interval 287° – 300° in Sun-centered geocentric ecliptic coordinates, color-coded for different threshold values of the combined similarity criteria.

Both methods identified 123 DCN-meteors in 2025-2026 during the activity period covered by the radiant method within Solar Longitude 289°–299°. Of these, 99 (76.7%) DCN meteors were identified in common, nine (7%) were identified by the radiant method but failed to fit the orbit similarity threshold, and 15 (12.2%) meteors were identified by the orbit method but not by the radiant method. The orbit method found 100 more DCN-meteors in the years 2019–2024 that were not covered by the radiant method. The orbit method also identified 20 orbits in 2025–2026 beyond the activity period assumed in the radiant method.

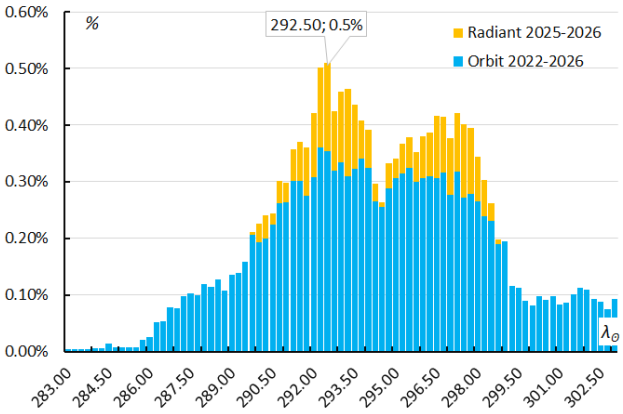

Figure 9 – The percentage of delta[1]-Canis Minorids relative to the total number of meteors, for the radiant method (2025–2026) and the orbit classification method 2019–2026.

The low ratio of DCN-meteors to the overall activity, with 0.5% at best, means that this is a barely detectable meteor shower. The profile shows two peaks separated by a dip (*Figure 9*), with best rates at $\lambda_\odot = 292.5°$. The relative activity was higher for 2025–2026 than for 2019–2026 due to the strong contribution in 2026. The number of shower meteors counted per year reflects the expansion of the GMN, but in recent years the network capacity remained relatively stable. Jenniskens (2023) mentions that outbursts occurred in 2015 and 2020. 2026 brought another outburst as the number of DCN-meteors was significantly higher than previous years (*Table 1*).

Table 1 – Number of delta[1]-Canis Minorid orbits detected by GMN per year.

Year	Orbit method	Radiant method
2019	1	–
2020	13	–
2021	10	–
2022	10	–
2023	17	–
2024	49	–
2025	49	31
2026	85	77

4 Orbit and parent body

The diagram of the inclination *i* versus the Longitude of Perihelion *Π* shows a concentration in *i*, stretched in *Π* (*Figure 10*). The eccentricity e versus the Longitude of Perihelion *Π* also appears stretched in *Π* (*Figure 11*). The spread in Longitude of Perihelion is caused by a steep increase in Longitude of Perihelion during the activity period (*Figure 12*). The background activity is very dense close to the anti-helion (*Figures 13 and 15*). The cluster of DCN orbits is best visible in the diagram perihelion distance versus inclination (*Figure 14*). There is a gradual increase in perihelion distance with 0.004AU/$\lambda_\odot$ (*Figure 16*).

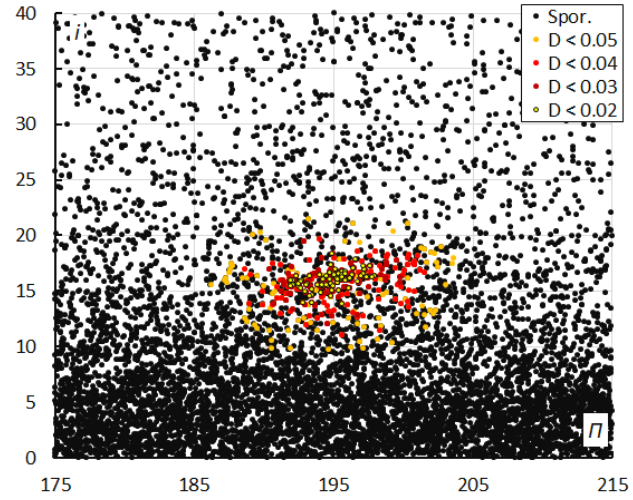

Figure 10 – Inclination i versus the longitude of perihelion Π color-coded for different classes of D-criteria thresholds, for $\lambda_\odot$ between 287° and 300°. Spor. = sporadics.

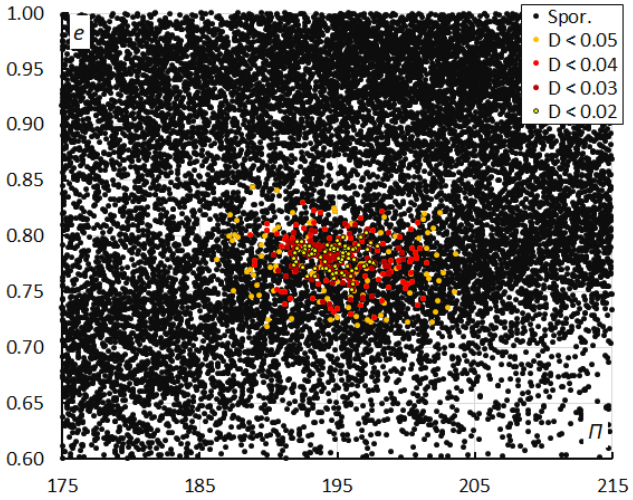

Figure 11 – Eccentricity e versus the longitude of perihelion Π color-coded for different classes of D-criteria thresholds, for $\lambda_\odot$ between 287° and 300°. Spor. = sporadics.

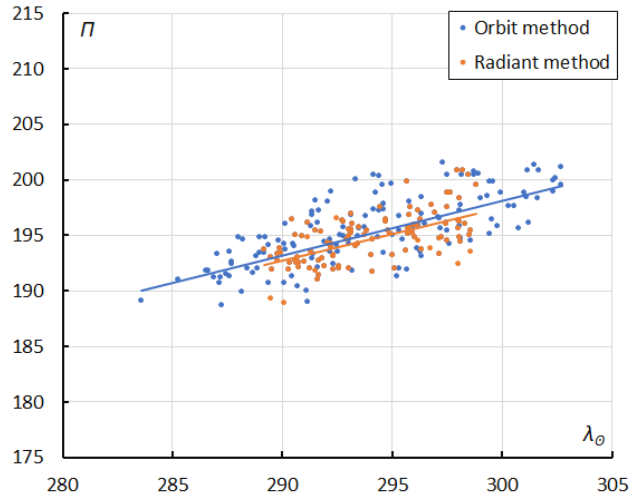

Figure 12 – The evolution of the Longitude of Perihelion Π in function of the Solar Longitude $\lambda_\odot$ based upon the radiant method (2025–2026) and upon the orbit method (2019–2026).

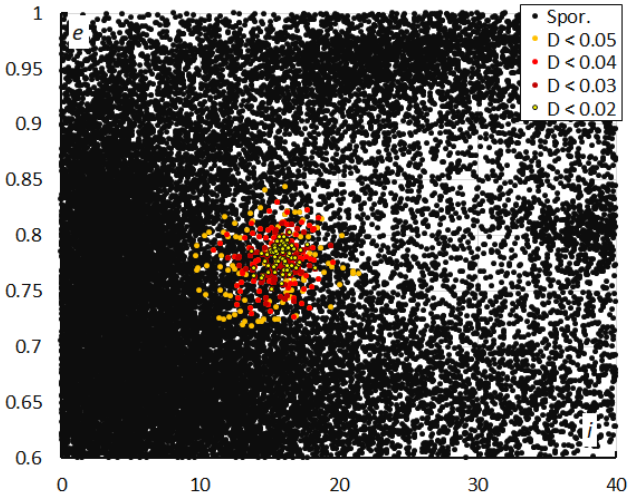

Figure 13 – Eccentricity e versus the inclination i color-coded for different classes of D-criteria thresholds, for $\lambda_\odot$ between 287° and 300°. Spor. = sporadics.

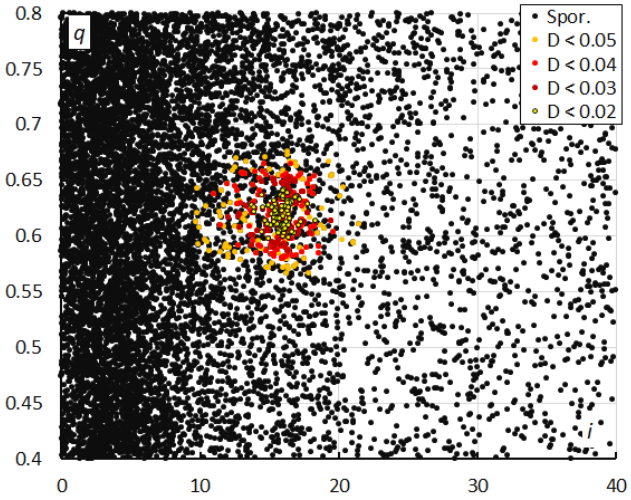

Figure 14 – Perihelion distance q versus the inclination i color-coded for different classes of D-criteria thresholds, for $\lambda_\odot$ between 287° and 300°. Spor. = sporadics.

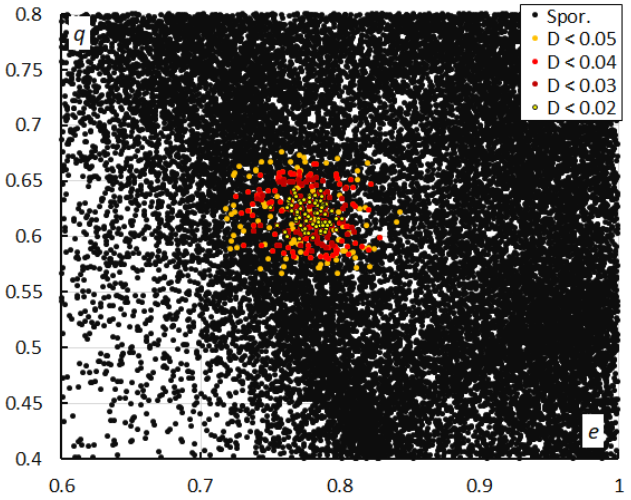

Figure 15 – Perihelion distance q versus the eccentricity e color-coded for different classes of D-criteria thresholds, for $\lambda_\odot$ between 287° and 300°. Spor. = sporadics.

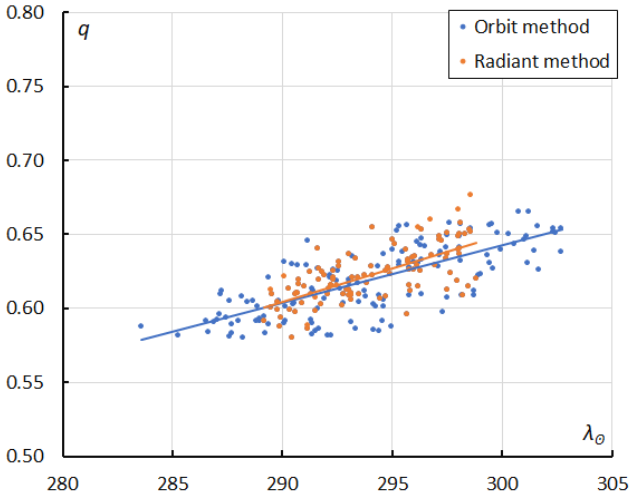

Figure 16 – The evolution of the perihelion distance q in function of the Solar Longitude $\lambda_{\odot}$ based upon the radiant method (2025–2026) and upon the orbit method (2019–2026).

Table 2 – Comparing solutions obtained by the radiant method for 2025–2026, the orbit method 2019–2026 for $D_D < 0.04$ and $D_D < 0.03$, compared to the solution by Jenniskens (2023).

	Radiant 2025–26	Orbit $D_D < 0.04$	Orbit $D_D < 0.03$	Jenniskens (2023)
$\lambda_{\odot}$ (°)	292.5	292.5	292.5	293.2
$\lambda_{\odot b}$ (°)	283.6	283.6	286.5	282.0
$\lambda_{\odot e}$ (°)	302.7	302.7	301.1	303.0
α_g (°)	109.9	111.6	111.3	110.6
δ_g (°)	+1.1	+0.4	+0.3	–0.1
$\Delta\alpha_g$ (°)	+0.69	+0.68	+0.68	+0.56
$\Delta\delta_g$ (°)	–0.48	–0.33	–0.41	–0.45
v_g (km/s)	23.8	23.6	23.6	23.6
H_b (km)	91.6	91.7	91.7	95.0
H_e (km)	78.4	79.6	78.9	77.2
H_p (km)	83.3	83.8	83.5	84.3
Mag_{Ap}	+0.3	+0.5	+0.4	+0.8
λ_g (°)	111.4	113.2	112.9	112.2
$\lambda_g - \lambda_{\odot}$ (°)	179.4	179.2	179.2	179.0
β_g (°)	–20.9	–21.3	–21.5	–22.0
a (A.U.)	2.830	2.78	2.80	2.83
q (A.U.)	0.622	0.619	0.619	0.622
e	0.780	0.778	0.779	0.780
i (°)	15.8	15.7	15.8	16.1
ω (°)	80.6	81.1	81.0	80.5
Ω (°)	114.1	114.1	113.8	113.2
Π (°)	194.7	195.2	194.8	194.0
T_j	2.73	2.76	2.75	2.71
N	108	234	147	132

The Tisserand value relative to Jupiter with $T_J = 2.73$ is typical for a Jupiter-family cometary orbit. This may explain the 2026 outburst, relative to 2024 and 2025, as due to a close pass of the parent body to Jupiter at some unknown time in the past. The meteoroid stream crosses the ecliptic and Earth's orbit at its ascending node (*Figure 16*). The solutions found with the radiant and orbit method are in agreement and confirm the orbit obtained by CAMS (Jenniskens, 2023). A search for candidate parent bodies did not result in any convincing associations (*Table 3*). A value of $D_D = 0.073$ looks acceptable, but this type of orbit requires a better threshold with $D_D < 0.04$ to be a likely parent body.

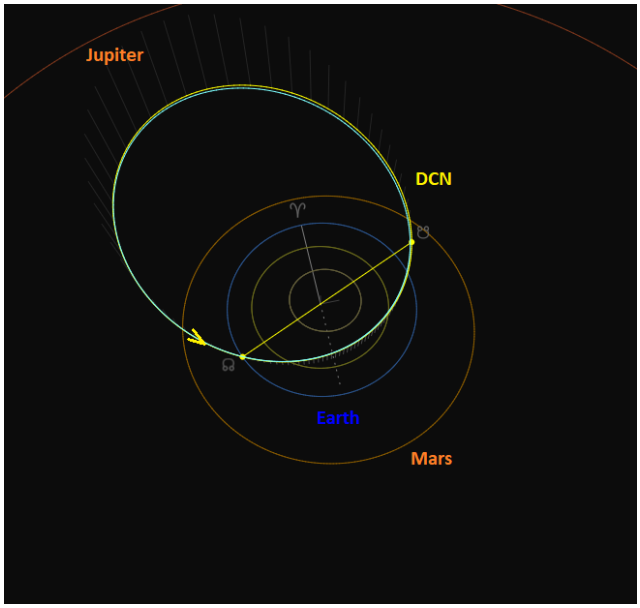

Figure 16 – Comparing the radiant determined delta[1]-Canis Minorids solution (yellow) with the orbit determined solution (blue), close-up at the inner Solar System. (Plotted with the Orbit visualization app provided by Pető Zsolt).

Table 3– Top ten matches of a search for possible parent bodies with $D_D < 0.1$, based upon the mean orbit derived from the radiant classification method.

Name	D_D
2017 NN_6	0.073
2026 AS_3	0.081
2023 YL	0.083
2025 AE_1	0.084
2017 WR_{13}	0.086
2017 BE_3	0.086
2025 XS_1	0.087
2020 YC_3	0.087
2024 XZ_7	0.090
501P/Rankin	0.091

5 Conclusion

This GMN meteoroid orbit data case study confirms the existence of the delta[1]-Canis Minorids. The shower produced an outburst in 2026 and confirms its annual shower status with periodic outbursts. The solution has been double checked by using two independent shower identification methods as a two-factor authentication for the validation of the analyses. Our independent solution has

been reported to the IAU-MDC, and the shower now fulfils the criteria for being upgraded to be nominated for established status.

Acknowledgments

This report is based on the data of the Global Meteor Network (Vida et al., 2020a; 2020b; 2021) which is released under the CC BY 4.0 license[15]. We thank all 927 participants in the Global Meteor Network project for their contribution and perseverance. A list with the names of the volunteers who contribute to GMN has been published in the 2025 annual report (Roggemans et al., 2026b). The following 459 cameras contributed to paired meteors used in this study:

AT0004, AU0002, AU0003, AU0006, AU0007, AU000B, AU000C, AU000D, AU000E, AU000F, AU000G, AU000S, AU000V, AU000W, AU000X, AU000Y, AU000Z, AU0010, AU001A, AU001B, AU001E, AU001F, AU001K, AU001L, AU001N, AU001P, AU001S, AU001W, AU001X, AU001Y, AU001Z, AU0028, AU0029, AU002A, AU002F, AU0030, AU003E, AU003G, AU0046, AU004L, BA0003, BA0005, BE0004, BE0005, BE0008, BE0009, BE000B, BE000C, BE000G, BE000H, BE000K, BE000P, BE000T, BE0010, BE0012, BG0003, BG000K, CA0007, CA0011, CA001J, CA002N, CL0002, CL0003, DE000B, DE000K, DE000S, DE000W, DE000X, DE0016, DE0017, DK0006, ES0007, ES0008, ES000C, ES000Q, ES0016, ES001A, ES001J, FR000F, FR0014, FR0016, GR0006, GR0009, HR0001, HR0006, HR0008, HR000D, HR000K, HR000M, HR000N, HR000P, HR000Q, HR000U, HR000V, HR000W, HR001A, HR001D, HR001N, HR001R, HR001T, HR001X, HR0021, HR0025, HR002D, HR002E, HR002G, HR002H, HR002J, HR002V, HR002W, HR002X, HR002Y, HU0003, HU000B, IL0004, IL0009, IT0001, KR0004, KR0009, KR000B, KR000E, KR000F, KR000H, KR000K, KR000M, KR000N, KR000P, KR000R, KR000Y, KR000Z, KR0010, KR0012, KR0013, KR0019, KR001H, KR0023, KR0024, KR0028, KR0029, KR002C, KR002D, KR002G, KR002S, KR002U, KR002Y, KR002Z, KR0036, KR0039, KR003D, KR003E, KR003G, KR003H, KR003J, KR003N, KR003P, KR003R, KR003U, KR003V, KR003W, MA0001, MA0003, MX000D, NL0001, NL000D, NL000P, NL000R, NL000S, NZ0003, NZ0007, NZ000J, NZ000Q, NZ000Y, NZ000Z, NZ0012, NZ0014, NZ0015, NZ0017, NZ0018, NZ001Q, NZ001V, NZ0023, NZ0029, NZ002H, NZ002K, NZ002L, NZ002N, NZ002R, NZ002T, NZ002U, NZ002V, NZ002X, NZ002Z, NZ0032, NZ0034, NZ0036, NZ0037, NZ0038, NZ003A, NZ003B, NZ003E, NZ003F, NZ003G, NZ003H, NZ003K, NZ003N, NZ003Q, NZ003R, NZ003T, NZ003U, NZ003Y, NZ003Z, NZ0040, NZ0042, NZ0045, NZ0049, NZ004A, NZ004B, NZ004J, NZ004L, NZ004N, NZ004R, NZ004S, NZ004T, NZ004U, NZ0059, NZ005A, NZ005B, NZ005N, NZ0063, PT0002, RU0003, RU0008, RU000B, RU000C, RU000F, RU0019, SI0001, SI0002, UK0001, UK0006, UK000B, UK000F, UK000H, UK000S, UK000W, UK000Y, UK000Z, UK001E, UK001H, UK001K, UK001N, UK001T, UK001W, UK001Z, UK0022, UK0025, UK002J, UK002K, UK002L, UK002Q, UK002W, UK002X, UK002Y, UK002Z, UK0030, UK0031, UK0035, UK003E, UK003F, UK003J, UK003L, UK003M, UK003N, UK003R, UK003T, UK003U, UK003Y, UK003Z, UK0041, UK0042, UK0045, UK0049, UK004B, UK004F, UK004G, UK004M, UK004N, UK004V, UK0050, UK0057, UK005H, UK005J, UK005L, UK005M, UK005P, UK005R, UK005S, UK0067, UK006C, UK006D, UK006H, UK006L, UK006T, UK006V, UK0070, UK0075, UK0077, UK007A, UK007B, UK007G, UK007M, UK007P, UK007Y, UK007Z, UK0081, UK0083, UK0085, UK0088, UK0089, UK008A, UK008B, UK008C, UK008K, UK008S, UK008V, UK0098, UK009P, UK009Q, UK00A1, UK00A2, UK00A3, UK00A6, UK00AA, UK00AB, UK00AJ, UK00AK, UK00AM, UK00AN, UK00AQ, UK00AT, UK00B0, UK00B5, UK00BA, UK00BB, UK00BJ, UK00BK, UK00BW, UK00C1, UK00CA, UK00CC, UK00CH, UK00CV, UK00CZ, UK00DA, UK00DG, UK00DH, UK00DJ, UK00DK, UK00DN, US0001, US0002, US0003, US0004, US0005, US0006, US0007, US0008, US0009, US000A, US000C, US000D, US000E, US000G, US000H, US000J, US000K, US000L, US000M, US000N, US000P, US000R, US000S, US000U, US000V, US001P, US001R, US001U, US0020, US0021, US0022, US0027, US002P, US002Q, US002R, US0030, US0038, US003G, US003N, US003P, US0044, US004C, US004N, US004Q, US004U, US004V, US0054, US0055, US0057, US005B, US005J, US005W, US005X, US005Y, US005Z, US0066, USL001, USL002, USL003, USL004, USL005, USL006, USL007, USL008, USL009, USL00A, USL00B, USL00C, USL00D, USL00E, USL00F, USL00G, USL00K, USL00L, USL00M, USL00P, USL00Q, USL00Y, USL00Z, USL010, USL011, USL012, USL013, USL014, USL015, USL017, USL018, USL019, USL01A, USL01B, USL01D, USL01E, USN004, USV002, USV003, ZA0001, ZA0006, ZA0007, ZA0008 and ZA000C.

References

Drummond J. D. (1981). “A test of comet and meteor shower associations”. *Icarus*, **45**, 545–553.

Jenniskens P. (2023). Atlas of Earth’s meteor showers. Elsevier, Cambridge, United states. ISBN 978-0-443-23577-1. Page 665.

Jopek T. J. (1993). “Remarks on the meteor orbital similarity D-criterion”. *Icarus*, **106**, 603–607.

Jopek T. J., Rudawska R. and Pretka-Ziomek H. (2006). “Calculation of the mean orbit of a meteoroid stream”. *Monthly Notices of the Royal Astronomical Society*, **371**, 1367–1372.

[15] https://creativecommons.org/licenses/by/4.0/

Moorhead A. V., Clements T. D., Vida D. (2020). “Realistic gravitational focusing of meteoroid streams”. *Monthly Notices of the Royal Astronomical Society*, **494**, 2982–2994.

Roggemans P., Vida D., Šegon D., Scott J.M. (2026a). “Meteoroid orbit shower identification”. *eMetN Meteor Journal*, **11**, 189–204.

Roggemans P., Campbell-Burns P., Kalina M., McIntyre M., Scott J. M., Šegon D., Vida D. (2026b). “Global Meteor Network report 2025”. *eMetN Meteor Journal*, **11**, 89–129.

Southworth R. B. and Hawkins G. S. (1963). “Statistics of meteor streams”. *Smithsonian Contributions to Astrophysics*, **7**, 261–285.

Vida D., Gural P., Brown P., Campbell-Brown M., Wiegert P. (2020a). “Estimating trajectories of meteors: an observational Monte Carlo approach - I. Theory”. *Monthly Notices of the Royal Astronomical Society*, **491**, 2688–2705.

Vida D., Gural P., Brown P., Campbell-Brown M., Wiegert P. (2020b). “Estimating trajectories of meteors: an observational Monte Carlo approach - II. Results”. *Monthly Notices of the Royal Astronomical Society*, **491**, 3996–4011.

Vida D., Šegon D., Gural P. S., Brown P. G., McIntyre M. J. M., Dijkema T. J., Pavletić L., Kukić P., Mazur M. J., Eschman P., Roggemans P., Merlak A., Zubrović D. (2021). “The Global Meteor Network – Methodology and first results”. *Monthly Notices of the Royal Astronomical Society*, **506**, 5046–5074.

Xi^2-Lupids (XLU#1100) confirmed

Paul Roggemans[1], **Denis Vida**[2,3], **Damir Šegon**[4,5], **James M. Scott**[6], **Jeff Wood**[7]

[1] **Pijnboomstraat 25, 2800 Mechelen, Belgium**
Paul.roggemans@gmail.com

[2] **Department of Physics and Astronomy, University of Western Ontario, Richmond Street, London, N6A 3K7, Ontario, Canada**

[3] **Institute for Earth and Space Exploration, University of Western Ontario, Perth Drive, London, N6A 5B8, Ontario, Canada**
denis.vida@gmail.com

[4] **Astronomical Society Istra Pula, Park Monte Zaro 2, 52100 Pula, Croatia**

[5] **Višnjan Observatory, Istarska 5, 52463 Višnjan, Croatia**

[6] **Department of Geoscience, Aarhus University, Høegh-Guldbergs Gade 2. DK-8000 Aarhus C, Denmark**

[7] **PO Box 162, Willetton, Western Australia 6955, Australia**

An activity source identified as the xi^2-Lupids was detected between the 27^h of January and the 7th of February 2024–2026. It has a radiant at R.A. = 244.9° and Decl.= –35.2°, and a geocentric velocity of 64.9 km/s. The shower is the twin of the July Pegasids (JPE#175) with C/1979 Y_1 (Bradfield) and the great Comet of 1771 (C/1771 A_1) as parent body. This case study confirms the existence of this annual meteor shower that fulfils the criteria in order to be nominated for established status by the IAU-MDC.

1 Introduction

A weak activity source was spotted on the GMN radiant density maps in late January and early February 2026. The radiant was identified as the xi^2-Lupids (XLU#1100). This shower was noticed by Jenniskens (2023) in CAMS data recorded in 2020–2021. A first solution was reported to the IAU Meteor Data Center (MDC) Working List of Meteor Showers, based upon 28 meteors[16] recorded by CAMS.

GMN has collected sufficient data to confirm and improve characterization of this weak minor shower. The results are presented and discussed in this case study.

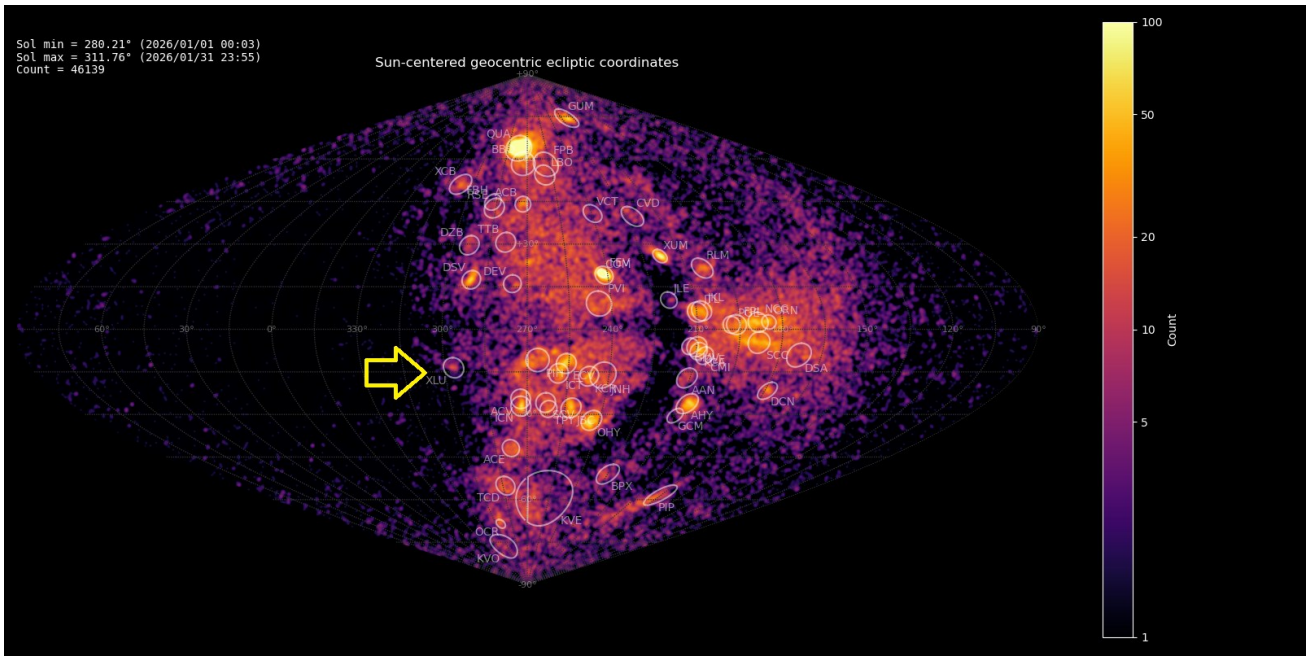

Figure 1 – Radiant density map with 46139 radiants obtained by the Global Meteor Network during January, 2026. The position of the xi^2-Lupids in Sun-centered geocentric ecliptic coordinates is marked with a yellow arrow.

[16] https://www.ta3.sk/IAUC22DB/MDC2022/Roje/pojedynczy_obiekt.php?lporz=02449&kodstrumienia=01100

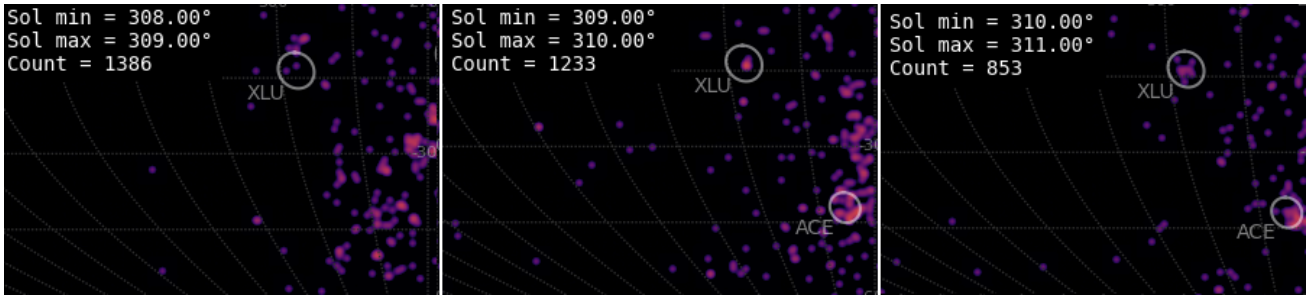

Figure 2 – The weak footprint of the xi^2-Lupids during three consecutive nights.

2 Shower classification based on radiants

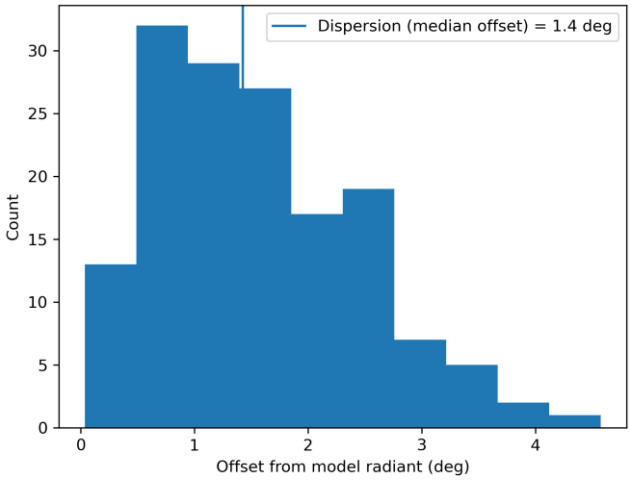

Figure 3 – Dispersion median offset on the radiant position.

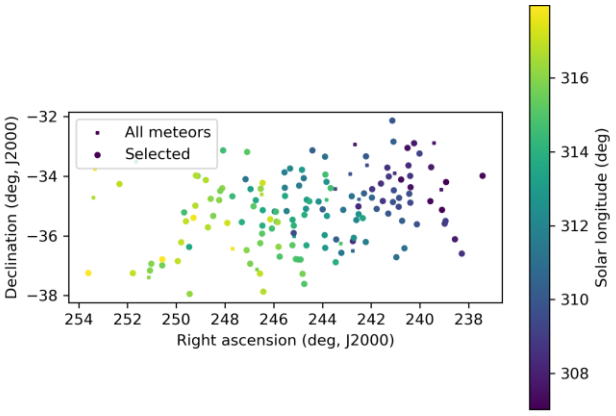

Figure 4 – The radiant distribution during the solar-longitude interval 307.5° – 317.0° in equatorial coordinates.

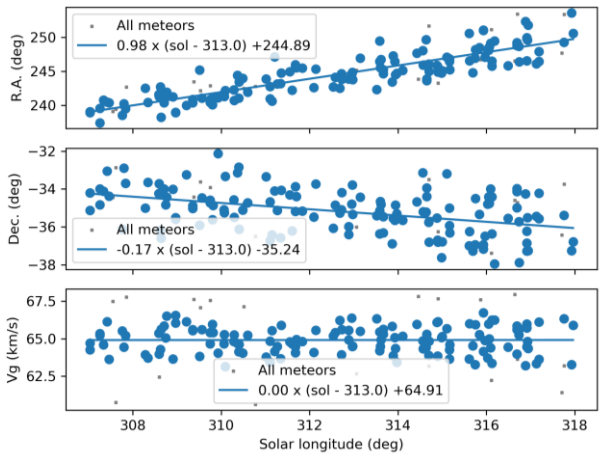

Figure 5 – The radiant drift.

The GMN shower association criteria assume that meteors within 1° in solar longitude, within 3.5° in radiant in this case, and within 10% in geocentric velocity of a shower reference location are members of that shower. Further details about the shower association are explained in Moorhead et al. (2020). Using these meteor shower selection criteria, 133 orbits have been identified as xi^2-Lupids recorded in 2024–2026 by 205 GMN cameras installed in Australia, Brazil, Bulgaria, Greece, Mexico, New Zealand, Russia, United States and South Africa. The final results have been listed in *Table 2*.

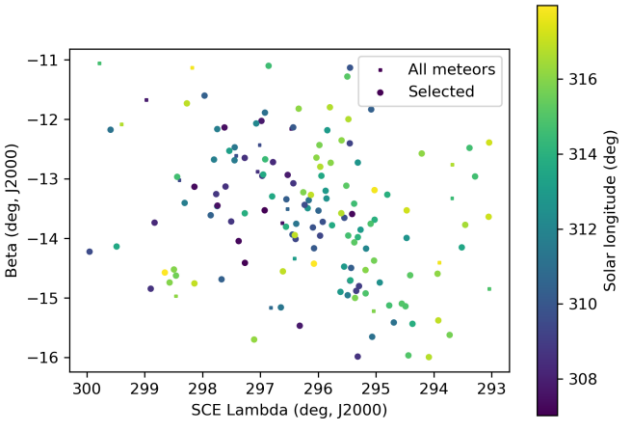

Figure 6 – The radiant distribution during the solar-longitude interval 307.5° – 317.0° in Sun centered geocentric ecliptic coordinates.

3 Shower classification based on orbits

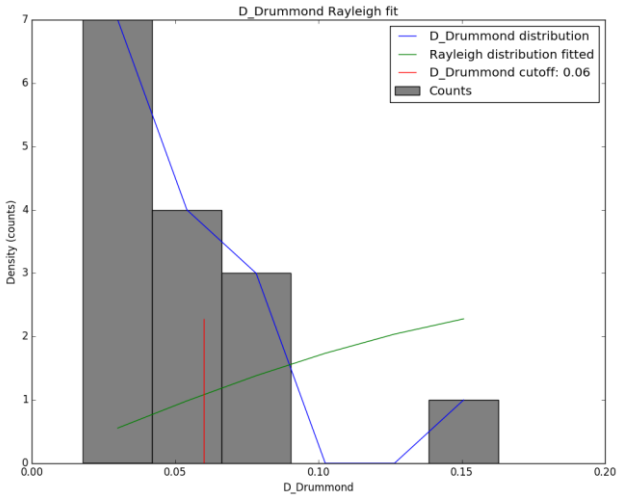

Figure 7 – Rayleigh fit on the Drummond criterion for xi^2-Lupids, 2026 data.

A complete independent meteoroid stream search has been applied to orbit data obtained between Solar Longitude 291.0° and 318.0° during the years 2019 to 2026. 168670 orbits were available within this time interval and a final mean orbit has been computed by the method of Jopek et al. (2006) for the thresholds according to the Rayleigh fit in *Figure 7*, $D_{SH} < 0.15$ and $D_D < 0.06$ and $D_J < 0.15$ (Southworth and Hawkins, 1963; Drummond, 1981; Jopek, 1993. The results and mean orbit based upon 122 meteors for 2022–2026 are listed in *Table 2*. The method has been described in detail in a separate publication (Roggemans et al., 2026a).

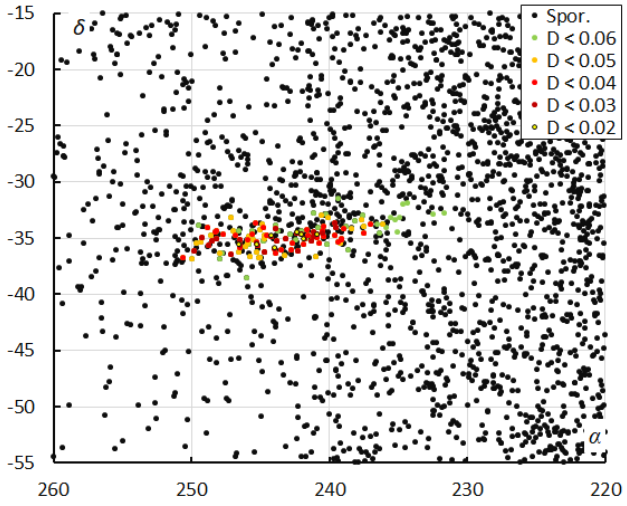

Figure 8 – The radiant distribution during the solar-longitude interval 304° – 318° in equatorial coordinates, color-coded for different threshold values of the combined similarity criteria.

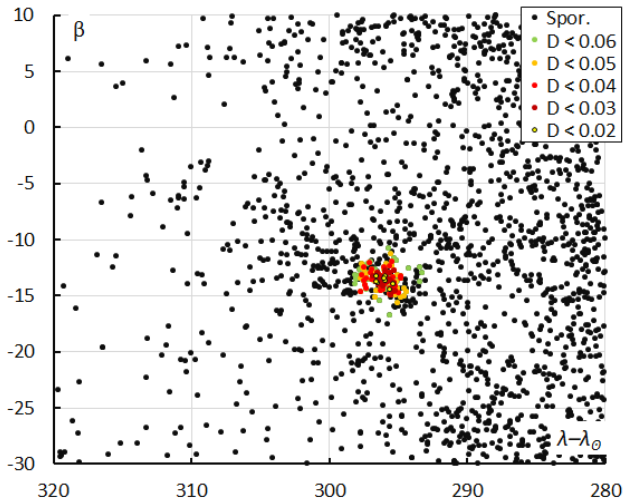

Figure 9 – The radiant distribution during the solar-longitude interval 304° – 318° in Sun-centered geocentric ecliptic coordinates, color-coded for different threshold values of the combined similarity criteria.

During 2024–2026 and within the activity period for Solar Longitude 307°–318°, both methods recorded 134 candidate xi^2-Lupids. Of these, 86 (64%) were identified in common, 47 (35%) were detected by the radiant method but failed to fit the orbit similarity thresholds, and one (1%) was detected by the orbit method but ignored by the radiant method. In this case, the radiant method turns out to be more tolerant than the orbit method. *Figure 8* shows an elongated radiant, stretched due to the radiant drift caused by the Earth on its orbit around the Sun. In Sun-centered ecliptic coordinates the radiant appears as a compact cluster (*Figure 9*) but surrounded by a concentration of non-shower radiants that failed to fit the D-criteria thresholds but which fulfill the radiant position and velocity filter of the radiant method.

The ratio shower/non-shower results in an activity profile with a broad plateau activity without any clear peak (*Figure 10*). The relative activity in the past three years covered by the radiant method was slightly stronger than the activity detected by the orbit method during 2021–2026. Jenniskens (2023) gives as activity period Solar Longitude 291°–318°, but no trace of activity was detected by GMN before $\lambda_\odot = 301°$. The orbit method detected XLU-orbits one week earlier than the radiant method and the profile suggests that the activity may last until past $\lambda_\odot = 318°$, which was the end of the studied time interval.

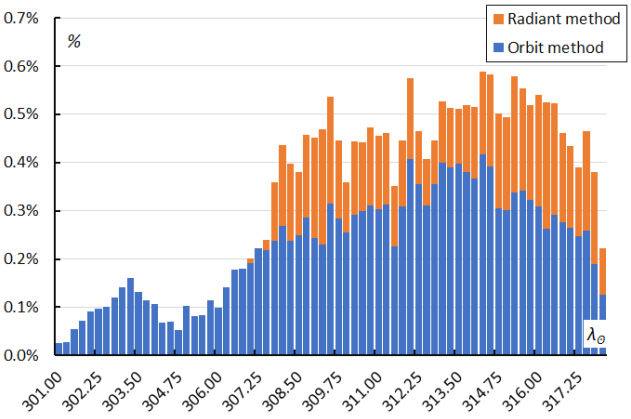

Figure 10 – The percentage of xi^2-Lupids relative to the total number of meteors, for the radiant method (2024–2026) and the orbit classification method 2023–2026.

Table 1 – Number of xi^2-Lupid orbits detected by GMN per year.

Year	Orbit method	Radiant method
2021	1	–
2022	3	–
2023	16	–
2024	31	44
2025	42	55
2026	29	34

4 Orbit and parent body

The diagram of the inclination i versus the Longitude of Perihelion Π shows a concentration in i, stretched in Π (*Figure 11*). The eccentricity e versus the Longitude of Perihelion Π appears scattered (*Figure 12*). The spread in Longitude of Perihelion is caused by a steep increase in Longitude of Perihelion during the activity period (*Figure 16*). The perihelion distance q increases (*Figure 17*), eccentricity e decreases (*Figure 18*) and inclination i remains stable (*Figure 19*) during the activity period. The

cluster of XLU orbits is best visible in the diagram perihelion distance versus inclination (*Figure 14*).

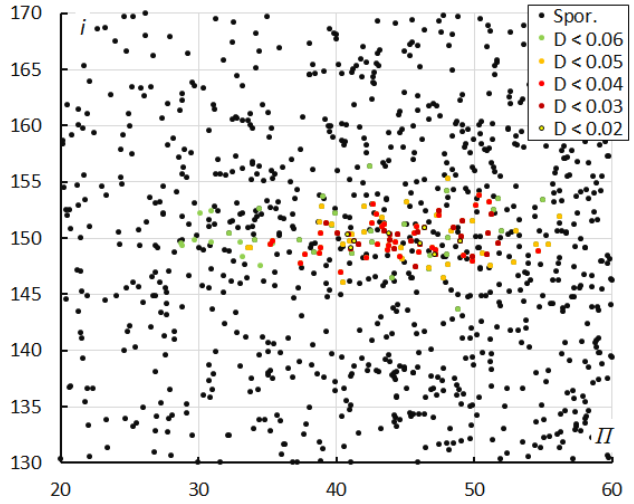

Figure 11 – Inclination i versus the Longitude of Perihelion Π color-coded for different classes of D-criteria thresholds, for $\lambda_\odot$ between 304° and 318°. Spor. = sporadics.

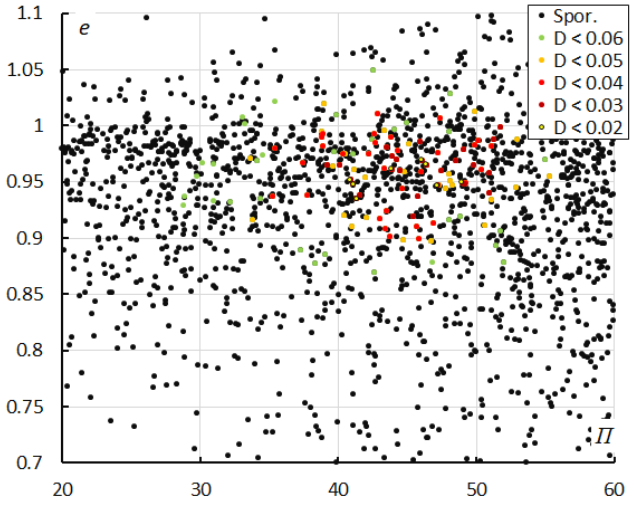

Figure 12 – Eccentricity e versus the Longitude of Perihelion Π color-coded for different classes of D-criteria thresholds, for $\lambda_\odot$ between 304° and 318°. Spor. = sporadics.

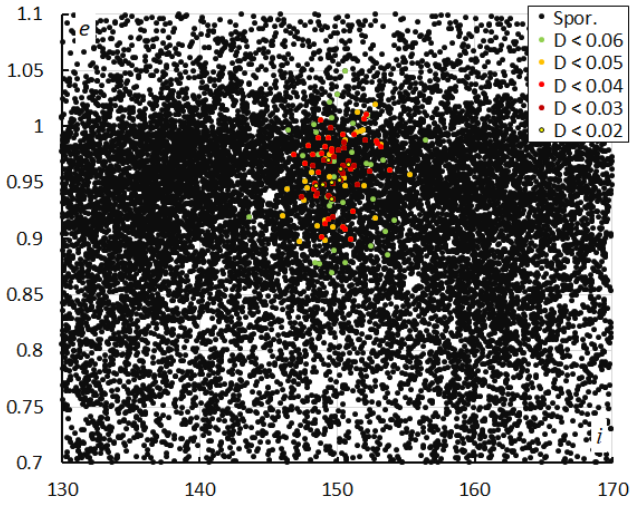

Figure 13 – Eccentricity e versus the inclination i color-coded for different classes of D-criteria thresholds, for $\lambda_\odot$ between 304° and 318°. Spor. = sporadics.

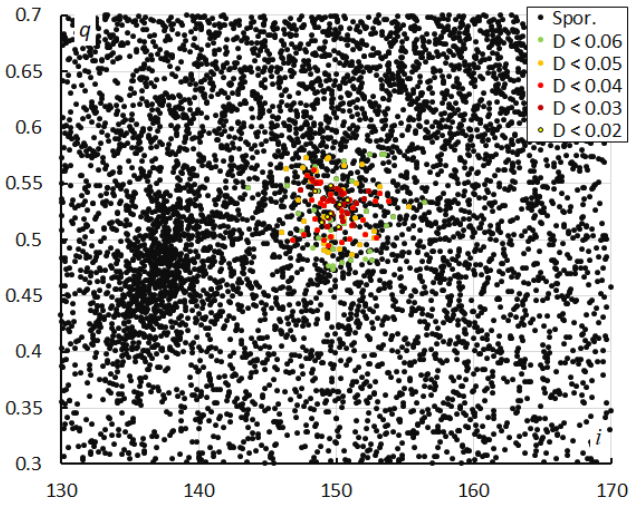

Figure 14 – Perihelion distance q versus the inclination i color-coded for different classes of D-criteria thresholds, for $\lambda_\odot$ between 304° and 318°. Spor. = sporadics.

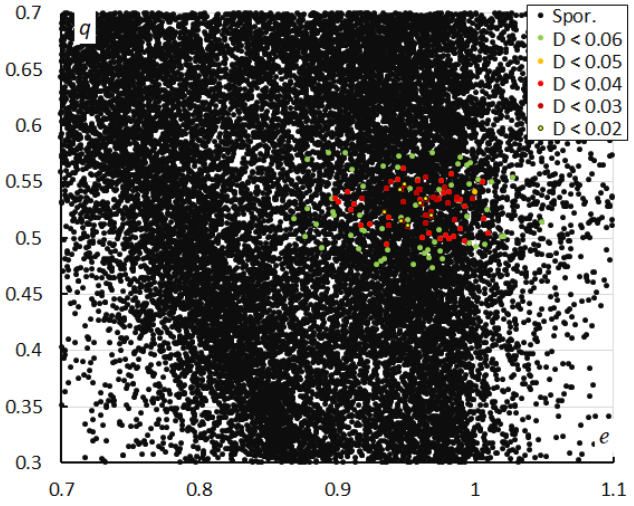

Figure 15 – Perihelion distance q versus the eccentricity e color-coded for different classes of D-criteria thresholds, for $\lambda_\odot$ between 304° and 318°. Spor. = sporadics.

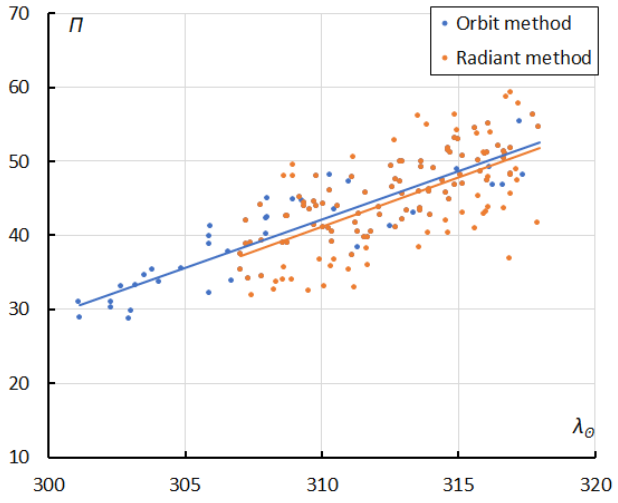

Figure 16 – The evolution of the Longitude of Perihelion Π in function of the Solar Longitude $\lambda_\odot$ based upon the radiant method (2024–2026) and upon the orbit method (2021–2026).

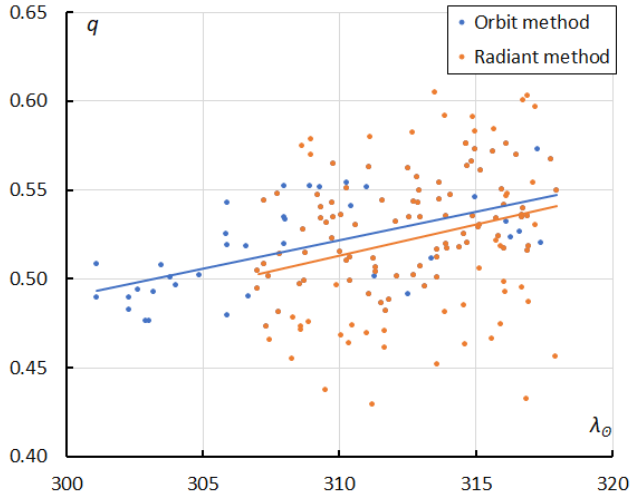

Figure 17 – The evolution of the perihelion distance q in function of the Solar Longitude $\lambda_\odot$ based upon the radiant method (2024–2026) and upon the orbit method (2021–2026).

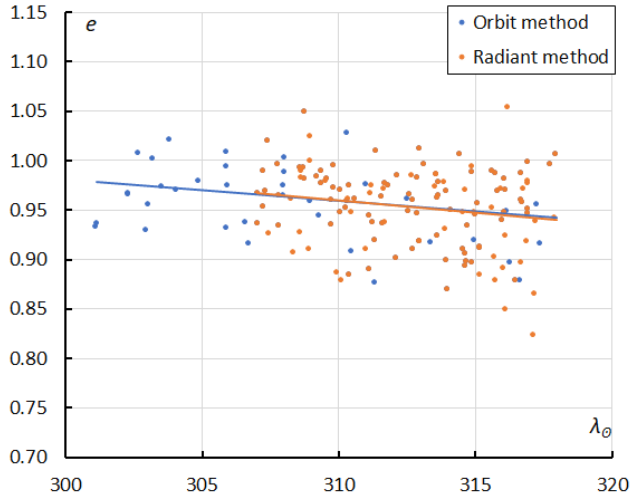

Figure 18 – The evolution of the eccentricity e in function of the Solar Longitude $\lambda_\odot$ based upon the radiant method (2024–2026) and upon the orbit method (2021–2026).

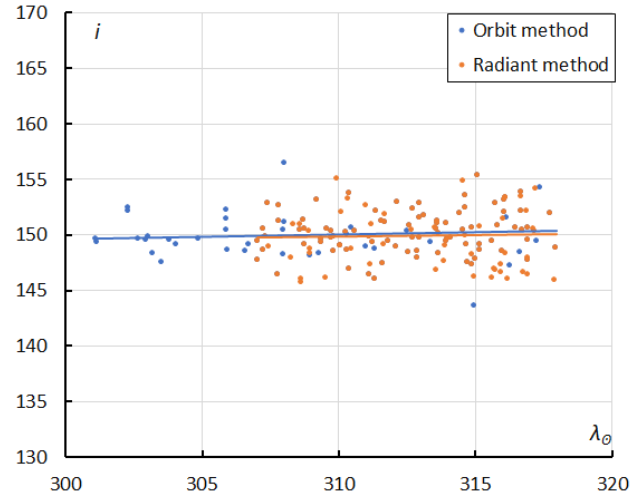

Figure 19 – The evolution of the inclination i in function of the Solar Longitude $\lambda_\odot$ based upon the radiant method (2024–2026) and upon the orbit method (2021–2026).

The Tisserand value relative to Jupiter with $T_J = -0.25$ is typical for a long-period cometary orbit (*Figure 20*). The meteoroid stream crosses the ecliptic and Earth's orbit on a retrograde orbit ($i > 90°$) at its ascending node (*Figure 21*).

Table 2 – Comparing solutions obtained by the radiant method for 2024–2026, the orbit method 2021–2026 for $D_D < 0.06$ and $D_D < 0.05$, compared to the solution by Jenniskens (2023).

	Radiant 2024–26	Orbit $D_D < 0.06$	Orbit $D_D < 0.05$	Jenniskens (2023)
$\lambda_\odot$ (°)	311.5	311.5	312.6	307
$\lambda_{\odot b}$ (°)	301.0	301.1	304.0	291
$\lambda_{\odot e}$ (°)	318.0	318.0	318.0	318
α_g (°)	244.9	243.2	244.3	238.0
δ_g (°)	–35.2	–34.8	–35.1	–34.0
$\Delta\alpha_g$ (°)	+0.98	+0.98	+1.00	+0.90
$\Delta\delta_g$ (°)	–0.17	–0.17	–0.14	–0.26
v_g (km/s)	64.9	65.1	65.2	65.4
H_b (km)	110.8	111.0	111.0	112.5
H_e (km)	98.6	99.0	98.8	98.0
H_p (km)	103.9	104.0	104.0	101.8
Mag_{Ap}	–0.7	–0.6	–0.6	+1.3
λ_g (°)	249.1	247.8	248.6	243.2
$\lambda_g - \lambda_\odot$ (°)	296.1	296.0	296.0	296.6
β_g (°)	–13.6	–13.6	–13.7	–13.5
a (A.U.)	10.2	11.4	12.3	28.8
q (A.U.)	0.522	0.524	0.528	0.522
e	0.949	0.954	0.957	0.982
i (°)	149.9	150.1	150.0	150.2
ω (°)	272.2	272.6	273.0	272.7
Ω (°)	132.8	131.2	132.1	126.6
Π (°)	45.0	43.8	45.1	37.6
T_j	–0.25	–0.31	–0.35	–0.57
N	133	122	88	106

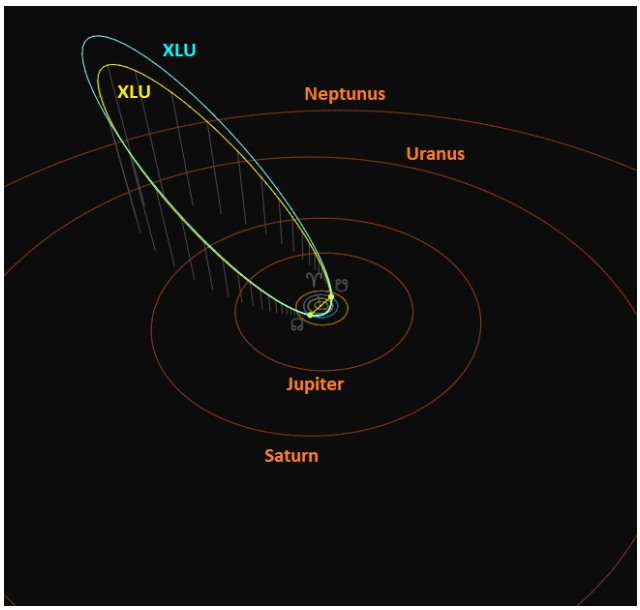

Figure 20 – Comparing the radiant determined xi²-Lupids solution (yellow) with the orbit determined solution (blue). (Plotted with the Orbit visualization app provided by Pető Zsolt).

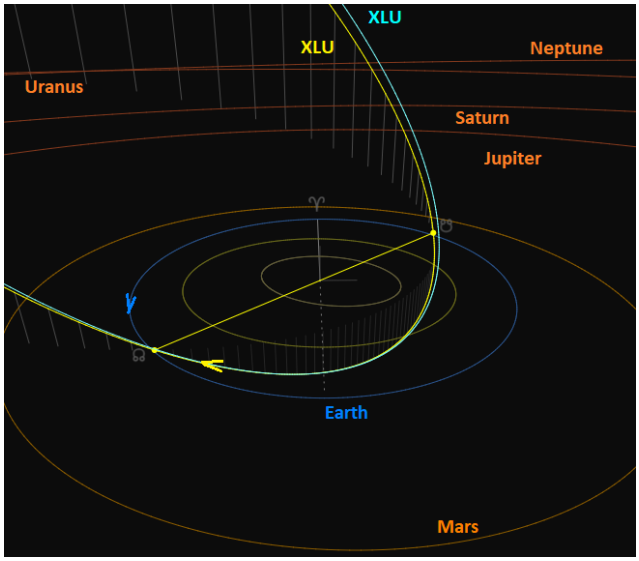

Figure 21 – Comparing the radiant determined xi²-Lupids solution (yellow) with the orbit determined solution (blue), close-up at the inner Solar System. (Plotted with the Orbit visualization app provided by Pető Zsolt).

Table 3– Top ten matches of a search for possible parent bodies with $D_D < 0.3$, based upon the mean orbit derived from the radiant classification method.

Name	D_D
C/1771 A1 (Great comet)	0.073
C/1979 Y1 (Bradfield)	0.106
C/1590 E1	0.122
C/1992 J2 (Bradfield)	0.123
C/1995 Q1 (Bradfield)	0.198
C/2015 G2 (MASTER)	0.212
C/1976 E1 (Bradfield)	0.227
C/1896 C1 (Perrine-Lamp)	0.257
C/1822 K1 (Pons)	0.263
C/1864 R1 (Donati)	0.278

Table 4 – The orbital elements of the xi²-Lupids, the two possible parent bodies, C/1771 A_1, C/1979 Y_1 and the twin shower July Pegasids (Jenniskens, 2023) with the D-criteria relative to XLU.

	XLU #1100N	C/1771 A_1	C/1979 Y_1	JPE #175 (CAMS)
q	0.522	0.528	0.545	0.559
e	0.949	1.000	0.988	0.968
i	149.9	148.56	148.6	149.2
ω	272.2	260.4	257.6	265.4
Ω	132.8	111.9	103.2	113.1
Π	45.0	12.3	0.8	18.5
D_D		0.073	0.106	0.085
D_{SH}		0.21	0.33	0.25

The solutions found with the radiant and orbit method (*Table 2*) are in agreement and confirm the orbit obtained by CAMS (Jenniskens, 2023). *Figure 21* reveals that the ascending node is also close to the Earth orbit. Such a situation makes it very likely that the Earth encounters the same dust twice as a twin shower.

The twin of the xi²-Lupids is likely to be the July Pegasids (JPE#175)[17], an established shower that displays a much stronger activity than the xi²-Lupids. Holman and Jenniskens (2013) have shown that the July Pegasids are related to the Great Comet of 1771 (C/1771 A_1) as well as the comet C/1979 Y_1 Bradfield identified earlier by Ueda (2012). Both may be the same comet or remnants of a larger body that broke up at the formation of the related meteoroid streams. Hajduková and Neslušan (2017), modelled the dust trails produced by comet C/1979 Y_1 (Bradfield) and linked this to the observed July Pegasids. The xi²-Lupids are very likely related to the filament F2 in this model, but the shower was unknown at the time of the publication of the model in 2017.

Although the thresholds for the Drumond criterion with $D_D = 0.085$ looks like a favorable degree of similarity, the Southworth and Hawkins criterion is less convincing with $D_{SH} = 0.25$. The XLU-orbit and the JPE-orbit differ significantly in node and longitude of perihelion. The low activity level without a clear peak activity and the scatter on the Kepler elements indicate that the Earth crosses the outliers of the meteoroid stream at the ascending node. The xi²-Lupids are a barely detectable footprint of this dust while Earth encounters the denser part of the stream at the descending node which is responsible for the much better activity levels of the July Pegasids. *Table 4* lists the Kepler elements and the D_D and D_{SH} criteria thresholds relative to the XLU-orbit.

5 Conclusion

This GMN meteoroid orbit data case study confirms the existence of the xi²-Lupids. The activity period starts at $\lambda_O = 301°$, ten days later than previously assumed. The activity last longer than $\lambda_O = 318°$. The solution has been checked by using two independent shower identification methods as a two-factor authentication for the validation of the analysis. The xi²-Lupids appear to be the twin shower of the July Pegasids, encountered at the descending node of the meteoroid stream. This shower has been associated with C/1771 A_1 (Great comet) and C/1979 Y_1 (Bradfield) which may be remnants of a larger object that created the meteoroid stream during a major break up. Further adjusted modelling may reveal the past evolution of this dust stream. Our independent solution has been reported to the IAU-MDC, and the shower now fulfils the criteria for being upgraded to be nominated for established status.

Acknowledgments

This report is based on the data of the Global Meteor Network (Vida et al., 2020a; 2020b; 2021) which is released under the CC BY 4.0 license[18]. We thank all 927

[17] https://www.ta3.sk/IAUC22DB/MDC2022/Roje/pojedynczy_obiekt.php?lporz=00579&kodstrumienia=00175

[18] https://creativecommons.org/licenses/by/4.0/

participants in the Global Meteor Network project for their contribution and perseverance. A list with the names of the volunteers who contribute to GMN has been published in the 2025 annual report (Roggemans et al., 2026b). The following 459 cameras contributed to paired meteors used in this study: AU0002, AU0003, AU0004, AU0006, AU0007, AU0009, AU000A, AU000B, AU000C, AU000D, AU000E, AU000F, AU000G, AU000J, AU000R, AU000U, AU000V, AU000W, AU000X, AU000Y, AU0010, AU0011, AU001A, AU001B, AU001C, AU001E, AU001F, AU001G, AU001K, AU001L, AU001N, AU001P, AU001Q, AU001R, AU001S, AU001U, AU001W, AU001X, AU001Y, AU001Z, AU0028, AU0029, AU002A, AU002B, AU002C, AU002E, AU002F, AU0030, AU0031, AU0036, AU0038, AU003C, AU003E, AU003F, AU003H, AU003J, AU0040, AU0042, AU0047, AU0048, BG000K, BR000F, BR000G, BR0015, BR001M, BR001T, BR001U, CA002K, CA002U, CA0035, GR0008, HR0025, HR002G, KR000D, KR000J, KR000P, KR000S, KR0010, KR001B, KR001C, KR002K, KR002S, KR003M, KR003T, MX000D, NZ0001, NZ0002, NZ0003, NZ0004, NZ0007, NZ0009, NZ000A, NZ000B, NZ000D, NZ000F, NZ000H, NZ000K, NZ000M, NZ000N, NZ000Q, NZ000R, NZ000S, NZ000T, NZ000U, NZ000V, NZ000Y, NZ000Z, NZ0011, NZ0012, NZ0014, NZ0015, NZ0016, NZ0017, NZ0018, NZ001A, NZ001C, NZ001E, NZ001G, NZ001L, NZ001N, NZ001Q, NZ001R, NZ001S, NZ001V, NZ001Y, NZ001Z, NZ0020, NZ0022, NZ0023, NZ0024, NZ0026, NZ0027, NZ0028, NZ0029, NZ002B, NZ002D, NZ002E, NZ002F, NZ002G, NZ002H, NZ002K, NZ002L, NZ002N, NZ002P, NZ002R, NZ002S, NZ002T, NZ002U, NZ002W, NZ002X, NZ002Y, NZ002Z, NZ0030, NZ0032, NZ0033, NZ0034, NZ0035, NZ0036, NZ0037, NZ0038, NZ0039, NZ003A, NZ003B, NZ003C, NZ003E, NZ003F, NZ003H, NZ003K, NZ003L, NZ003M, NZ003R, NZ003S, NZ003T, NZ003U, NZ003V, NZ003W, NZ003X, NZ003Y, NZ003Z, NZ0040, NZ0041, NZ0045, NZ0046, NZ0049, NZ004A, NZ004B, NZ004C, NZ004D, NZ004H, NZ004J, NZ004N, NZ004R, NZ004U, NZ004V, NZ004W, NZ004Y, NZ004Z, NZ0051, NZ0059, NZ005F, NZ005G, NZ005K, NZ005N, NZ005R, NZ0063, NZ0065, NZ006C, RU0003, RU000M, RU0019, US0002, US0003, US0004, US0005, US0009, US000A, US000C, US000D, US000E, US000G, US000H, US000J, US000K, US000L, US000M, US000N, US000R, US001R, US0021, US0030, US004C, US004P, US005A, US005B, US0066, USL003, USL004, USL007, USL008, USL009, USL00A, USL00B, USL00C, USL00F, USL00H, USL00K, USL00L, USL00M, USL014, USL016, USL018, USL01C, USL01D, ZA0001, ZA0006, ZA0007, ZA0008, ZA000C and ZA000F.

References

Drummond J. D. (1981). “A test of comet and meteor shower associations”. *Icarus*, **45**, 545–553.

Hajduková M., Neslušan L. (2017). “Regular and transitory showers of comet C/1979 Y1 (Bradfield)”. *Astronomy & Astrophysics*, **605**, id.A36.

Holman D., Jenniskens P. (2013). “Discovery of the Upsilon Andromedids (UAN, IAU #507)”. *WGN, Journal of the International Meteor Organization*, **41**, 43–47.

Jenniskens P. (2023). Atlas of Earth’s meteor showers. Elsevier, Cambridge, United states. ISBN 978-0-443-23577-1. Page 529.

Jopek T. J. (1993). “Remarks on the meteor orbital similarity D-criterion”. *Icarus*, **106**, 603–607.

Jopek T. J., Rudawska R. and Pretka-Ziomek H. (2006). “Calculation of the mean orbit of a meteoroid stream”. *Monthly Notices of the Royal Astronomical Society*, **371**, 1367–1372.

Moorhead A. V., Clements T. D., Vida D. (2020). “Realistic gravitational focusing of meteoroid streams”. *Monthly Notices of the Royal Astronomical Society*, **494**, 2982–2994.

Roggemans P., Vida D., Šegon D., Scott J.M. (2026a). “Meteoroid orbit shower identification”. *eMetN Meteor Journal*, **11**, 189–204.

Roggemans P., Campbell-Burns P., Kalina M., McIntyre M., Scott J. M., Šegon D., Vida D. (2026b). “Global Meteor Network report 2025”. *eMetN Meteor Journal*, **11**, 89–129.

Southworth R. B. and Hawkins G. S. (1963). “Statistics of meteor streams”. *Smithsonian Contributions to Astrophysics*, **7**, 261–285.

Ueda M. (2012). “Orbits of the July Pegasid meteors observed during 2008 to 2011”. *WGN, Journal of the International Meteor Organization*, **40**, 59–64.

Vida D., Gural P., Brown P., Campbell-Brown M., Wiegert P. (2020a). “Estimating trajectories of meteors: an observational Monte Carlo approach - I. Theory”. *Monthly Notices of the Royal Astronomical Society*, **491**, 2688–2705.

Vida D., Gural P., Brown P., Campbell-Brown M., Wiegert P. (2020b). “Estimating trajectories of meteors: an observational Monte Carlo approach - II. Results”. *Monthly Notices of the Royal Astronomical Society*, **491**, 3996–4011.

Vida D., Šegon D., Gural P. S., Brown P. G., McIntyre M. J. M., Dijkema T. J., Pavletić L., Kukić P., Mazur M. J., Eschman P., Roggemans P., Merlak A., Zubrović D. (2021). “The Global Meteor Network – Methodology and first results”. *Monthly Notices of the Royal Astronomical Society*, **506**, 5046–5074.

Kappa-Velids (KVE#784) confirmed

Paul Roggemans[1], **Denis Vida**[2,3], **Damir Šegon**[4,5], **James M. Scott**[6], **Jeff Wood**[7]

[1] **Pijnboomstraat 25, 2800 Mechelen, Belgium**
Paul.roggemans@gmail.com

[2] **Department of Physics and Astronomy, University of Western Ontario, Richmond Street, London, N6A 3K7, Ontario, Canada**

[3] **Institute for Earth and Space Exploration, University of Western Ontario, Perth Drive, London, N6A 5B8, Ontario, Canada**
denis.vida@gmail.com

[4] **Astronomical Society Istra Pula, Park Monte Zaro 2, 52100 Pula, Croatia**

[5] **Višnjan Observatory, Istarska 5, 52463 Višnjan, Croatia**

[6] **Department of Geoscience, Aarhus University, Høegh-Guldbergs Gade 2. DK-8000 Aarhus C, Denmark**

[7] **PO Box 162, Willetton, Western Australia 6955, Australia**

An activity source with a large diffuse radiant at R.A. = 142° and Decl.= –52°, and a geocentric velocity of 42.0 km/s, identified as the kappa-Velids, was detected between the 19th of December 2025 and 2nd of January 2026. The shower has been detected since 2020 by the GMN. This case study confirms the existence of this annual meteor shower, meaning that it is now recognized by multiple independent methods and this fulfills the criteria required to be nominated for established status by the IAU-MDC.

1 Introduction

During the monitoring of the outburst of the Volantids in 2025–2026 (Roggemans et al., 2026a) a diffuse but nevertheless relative strong activity source was detected. The shower is identified as the kappa-Velids (KVE-784)[19], and was visible as a very bright spot on the radiant density map for December 2025 (*Figure 1*). The kappa-Velids radiate from a very dispersed radiant, almost 20° in diameter, with a very changeable appearance during the activity period. *Figure 2* shows these changes day-by-day in close-up.

The shower was first noticed by Pokorny at al. (2017) in meteor radar data collected in 2012–2015 by SAAMER (Southern Argentine Agile Meteor Radar). Jenniskens (2023) suggested that CAMS low light camera data show that the kappa-Velids consists of several showers.

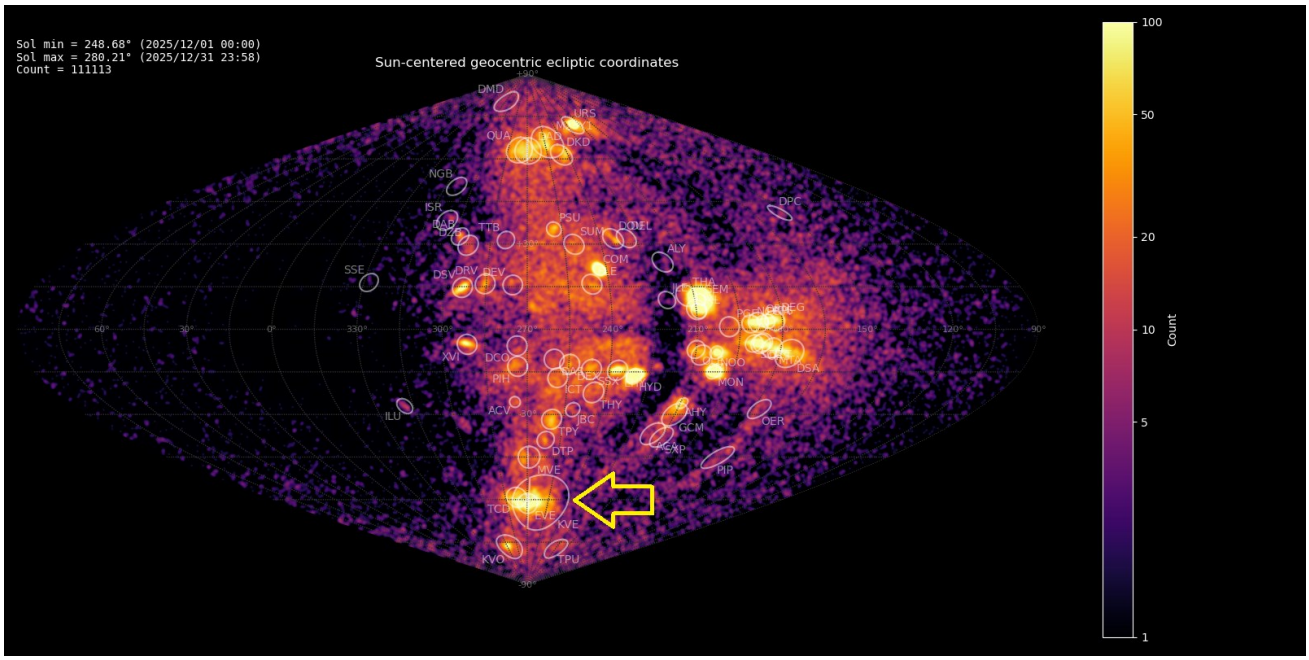

Figure 1 – Radiant density map with 111113 radiants obtained by the Global Meteor Network during December, 2025. The position of the kappa-Velids in Sun-centered geocentric ecliptic coordinates is marked with a yellow arrow.

[19] https://www.ta3.sk/IAUC22DB/MDC2022/Roje/pojedynczy_obiekt.php?lporz=01997&kodstrumienia=00784

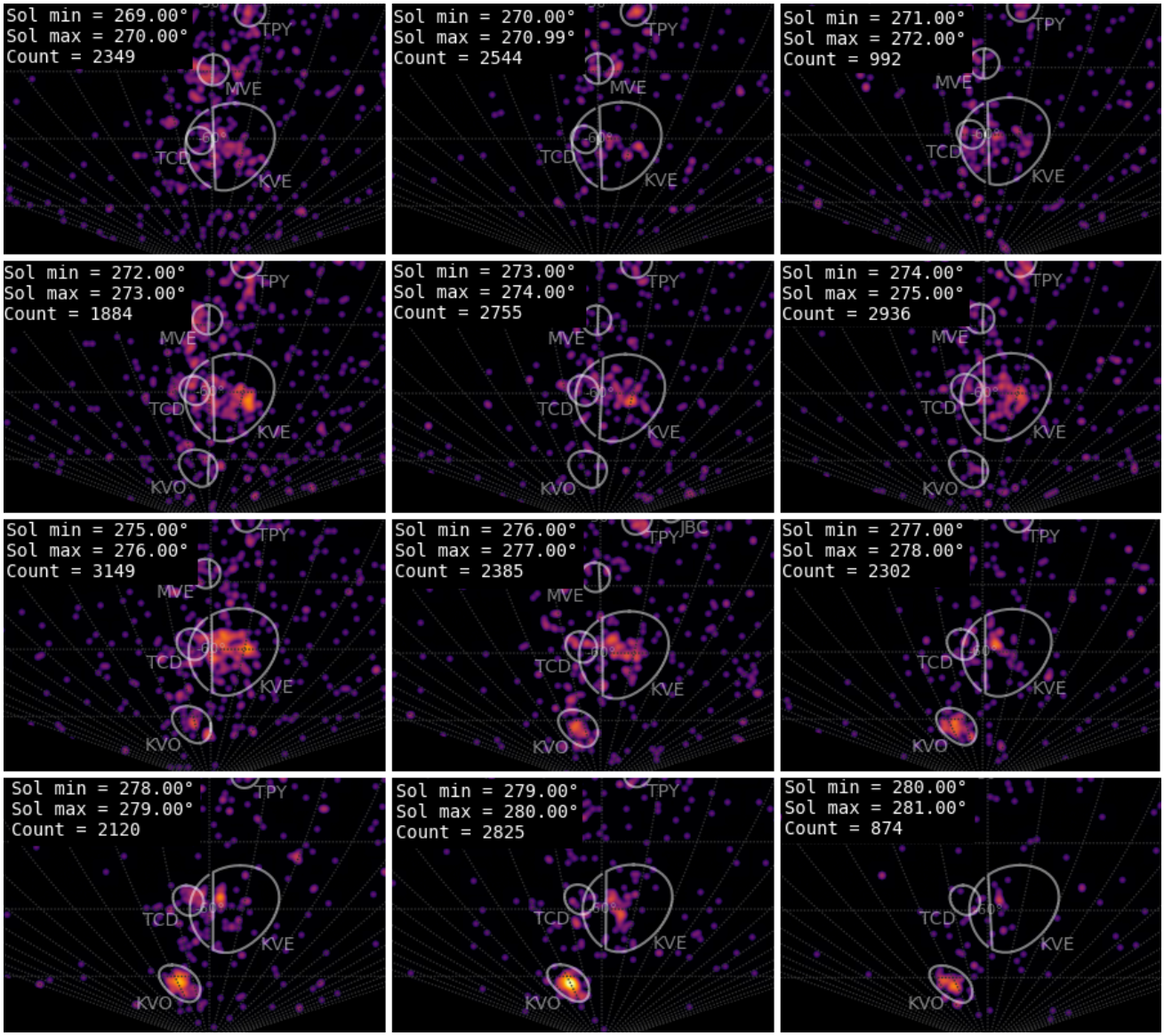

Figure 2 – Day by day changes in the appearance of the kappa-Velids radiant for the solar longitudes between 269° and 281°.

2 Shower classification based on radiants

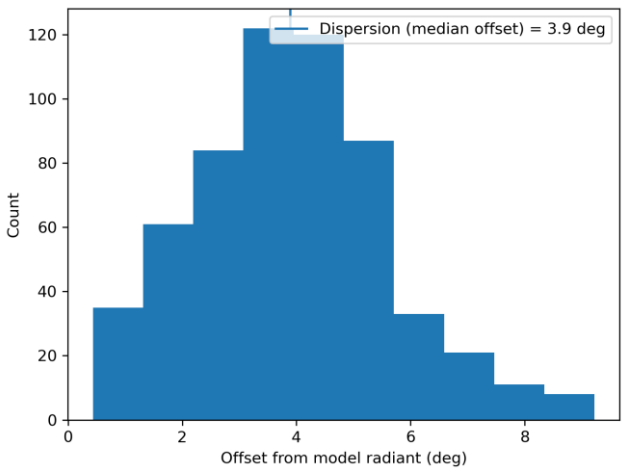

Figure 3 – Dispersion median offset on the radiant position.

The GMN shower association criteria assume that meteors within 1° in solar longitude, within 8.8° in radiant in this case, and within 10% in geocentric velocity of a shower reference location are members of that shower. Further details about the shower association are explained in Moorhead et al. (2020). Using these meteor shower selection criteria, 386 orbits have been identified as kappa-Velids recorded in 2025–2026 by 235 GMN cameras installed in Australia, Brazil, New Zealand, United States and South Africa. The final results have been listed in *Table 1*.

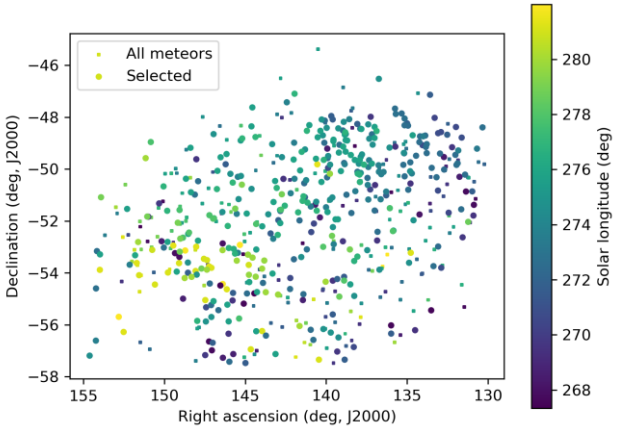

Figure 4 – The radiant distribution during the solar-longitude interval 267.5° – 281.5° in equatorial coordinates.

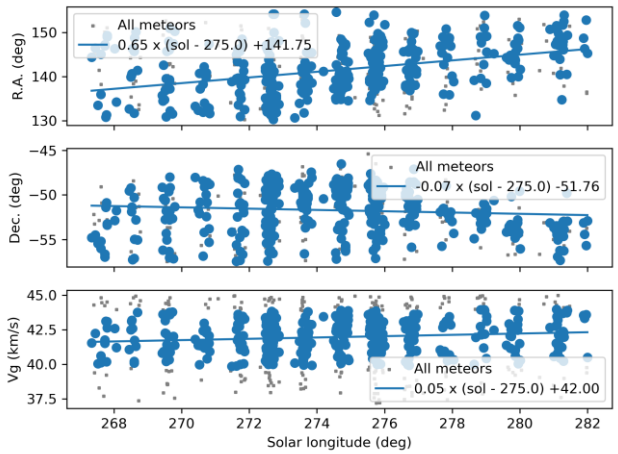

Figure 5 – The radiant drift.

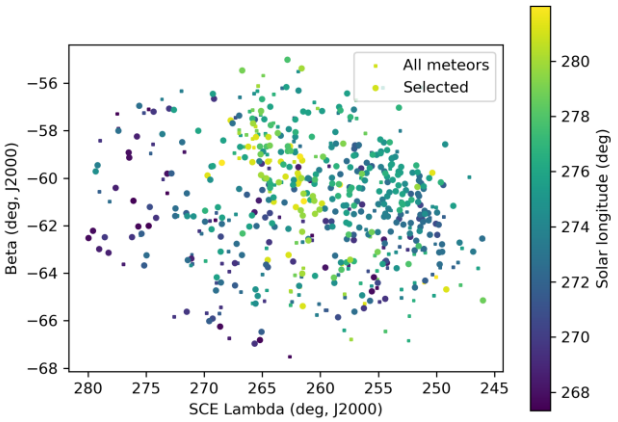

Figure 6 – The radiant distribution during the solar-longitude interval 267.5° – 281.5° in Sun centered geocentric ecliptic coordinates.

3 Shower classification based on orbits

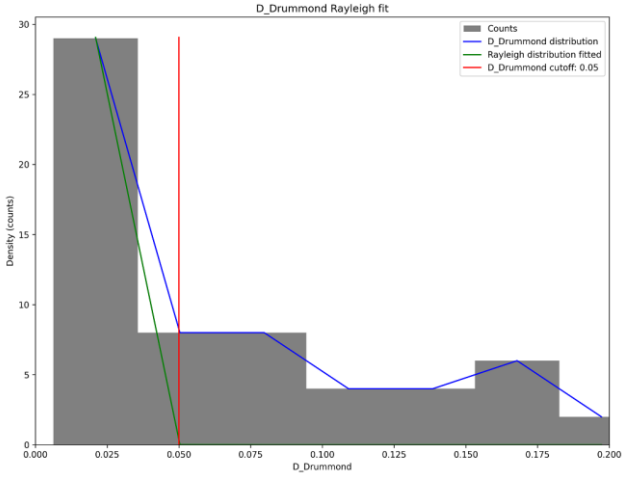

Figure 7 – Rayleigh fit on the Drummond criterion for kappa-Velids, 2025 data.

A complete independent meteoroid stream search has been applied for confirmation based upon orbit data obtained between solar longitude 260.0° and 286.0° during the years 2019 to 2026. 316002 orbits were available within this time interval and a final mean orbit has been computed by the method of Jopek et al. (2006) for the thresholds according to the Rayleigh fit in *Figure 7* with $D_{SH} < 0.125$ and $D_D < 0.05$ and $D_J < 0.125$ (Southworth and Hawkins, 1963; Drummond, 1981; Jopek, 1993. The results with the mean orbit based upon 326 meteors for 2020–2026 are listed in *Table 1*. The method has been described in detail in a separate publication (Roggemans et al., 2026a).

The radiant plot in equatorial coordinates (*Figure 8*) shows that the chosen similarity criteria fail to identify most of the likely kappa-Velids in the large cluster of radiant points. This means that the spread on the orbital elements is too large to represent the shower with a single mean orbit. Choosing more tolerant threshold values like $D_{SH} < 0.2$ and $D_D < 0.08$ and $D_J < 0.2$ (green dots in *Figure 8*) still fail to cover the large cluster of radiants and risk contaminating the selection with sporadic orbits.

The concentration above the KVE-radiant is caused by the mu-Velids (MVE#318) with a much higher eccentricity and retrograde orbit. Just right from the KVE-radiant are the e-Velids (EVE#746) which have their activity mainly before the kappa-Velids and a lower inclination orbit. Meteor shower activity is often a puzzle that requires detective work to distinguish between different activities.

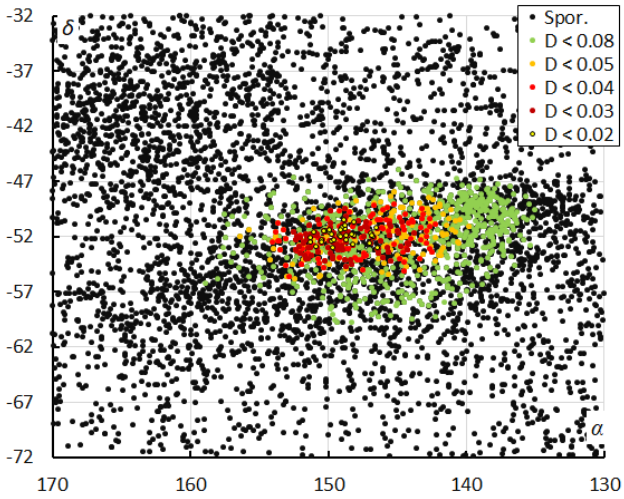

Figure 8 – The radiant distribution during the solar-longitude interval 260° – 286° in equatorial coordinates, color-coded for different threshold values of the combined similarity criteria.

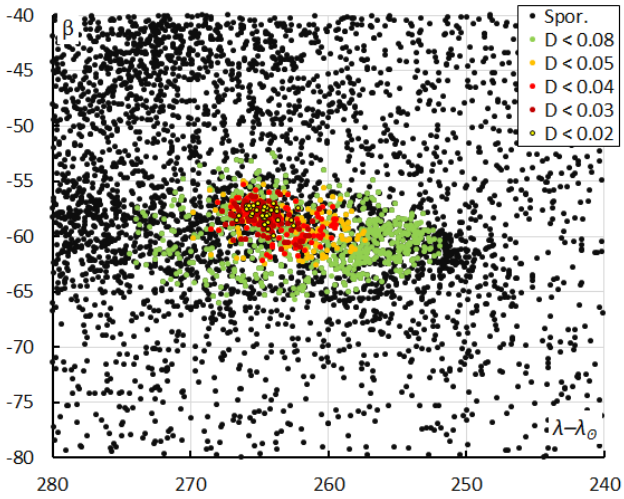

Figure 9 – The radiant distribution during the solar-longitude interval 260° – 286° in Sun-centered geocentric ecliptic coordinates, color-coded for different threshold values of the combined similarity criteria.

The Sun-centered ecliptic coordinates eliminate the radiant drift caused by the Earth moving on its orbit around the Sun (*Figure 9*), but also here the selected threshold to separate the kappa-Velids from the background fails to fit the entire shower. To the left from the KVE-radiant we see a cluster formed by the e-Velids and theta-Carinids (TCD#785) both with radiant, velocity and orbits that are hard to distinguish from the kappa-Velids. The cluster around $\lambda - \lambda_\odot = 270°$ and $\beta = -45°$ are the mu-Velids with a much faster velocity of $v_g = 56$ km/s.

The orbit shower association method is not suitable for very diffuse showers with a large spread on the Kepler elements of the shower meteors. The orbit method will only identify a specific population of the particles in the stream according to their orbit similarity. The ratio of kappa-Velids relative to the overall activity reaches over 7% and should be notable by dedicated visual observers. *Figure 10* shows the difference in activity profile between the recommended threshold class $D_{SH} < 0.125$ and $D_D < 0.05$ and $D_J < 0.125$ to exclude sporadic contamination (orange) and the more tolerant class with $D_{SH} < 0.2$ and $D_D < 0.08$ and $D_J < 0.2$ (green). Here the straightforward radiant classification method (red) appears to be the best compromise to cover the large diffuse radiant, despite sporadic contamination. No activity was detected before $\lambda_\odot = 266.5°$, and the best rates occurred at $\lambda_\odot = 275.0°$. The activity profile appears as a symmetric bell- shaped profile.

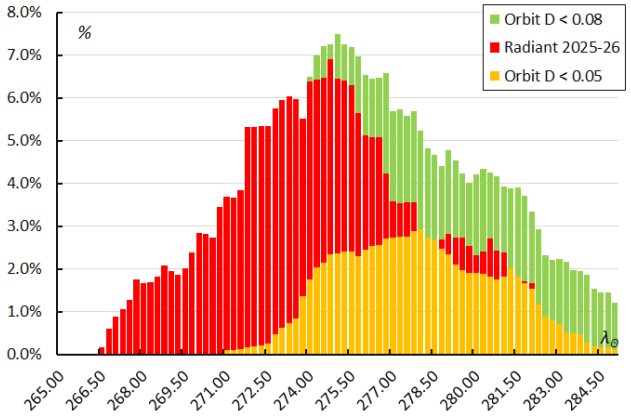

Figure 10 – The percentage of kappa-Velids relative to the total number of meteors, for the radiant method (2025–2026) and the orbit classification method 2020–2026.

4 Orbit and parent body

The diagram of the inclination i versus the Longitude of Perihelion Π shows a concentration in i, stretched in Π (*Figure 11*). The dense concentration at $\Pi = 90°–100°$ and $i = 65°–75°$ consists mainly of Quadrantids, December alpha-Draconids and M2025-Y1 related to the December kappa-Draconids. The eccentricity e versus the Longitude of Perihelion Π also appears stretched in Π (*Figure 11*). The spread in Longitude of Perihelion is caused by an increase in Longitude of Perihelion during the activity period (*Figure 13*). There is also a subtle increase in inclination (*Figure 16*). The other Kepler elements remain stable during the activity period. The meteoroid population is very dense in this range of eccentricities and perihelion distances (*Figures 15 and 17*). The cluster of KVE-orbits is best visible in the diagram inclination versus Longitude of Perihelion (*Figure 11*).

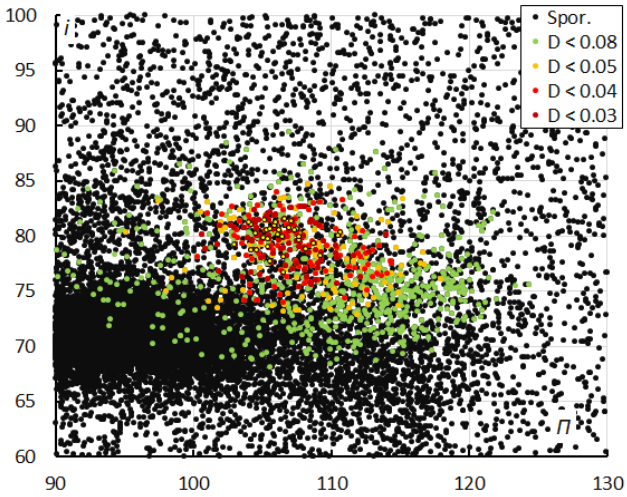

Figure 11 – Inclination i versus the longitude of perihelion Π color-coded for different classes of D-criteria thresholds, for $\lambda_\odot$ between 260° and 286°. Spor. = sporadics.

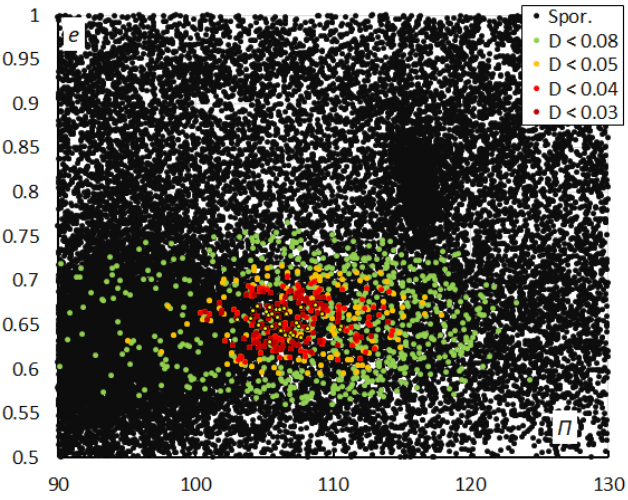

Figure 12 – Eccentricity e versus the Longitude of Perihelion Π color-coded for different classes of D-criteria thresholds, for $\lambda_\odot$ between 260° and 286°. Spor. = sporadics.

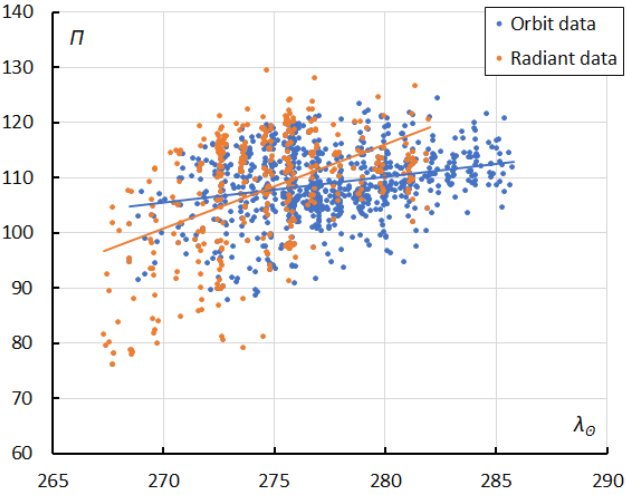

Figure 13 – The evolution of the Longitude of Perihelion Π in function of the solar longitude $\lambda_\odot$ based upon the radiant method (2025–2026) and upon the orbit method (2020–2026).

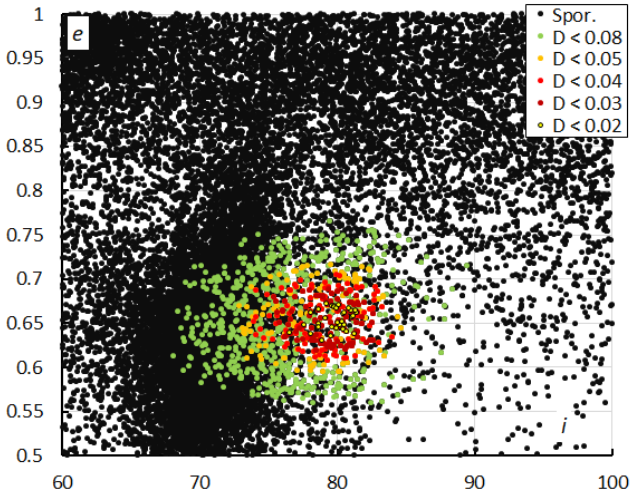

Figure 14 – Eccentricity e versus the inclination i color-coded for different classes of D-criteria thresholds, for $\lambda_\odot$ between 260° and 286°. Spor. = sporadics.

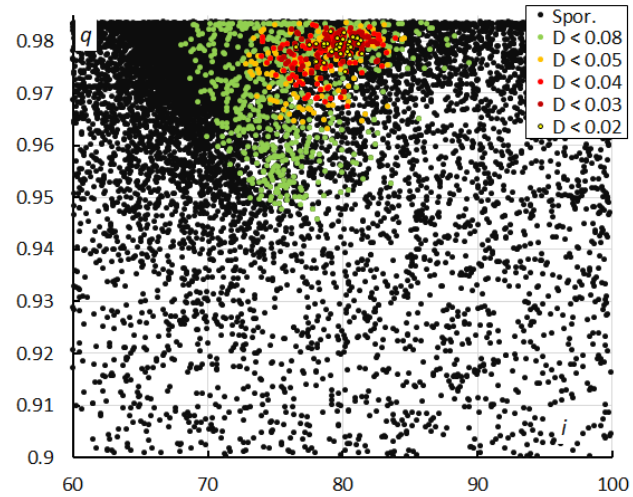

Figure 15 – Perihelion distance q versus the inclination i color-coded for different classes of D-criteria thresholds, for $\lambda_\odot$ between 260° and 286°. Spor. = sporadics.

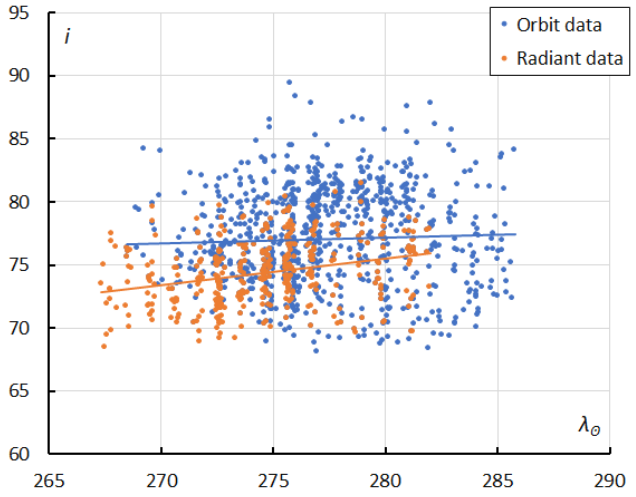

Figure 16 – The evolution of the inclination i in function of the solar longitude $\lambda_\odot$ based upon the radiant method (2025–2026) and upon the orbit method (2020–2026).

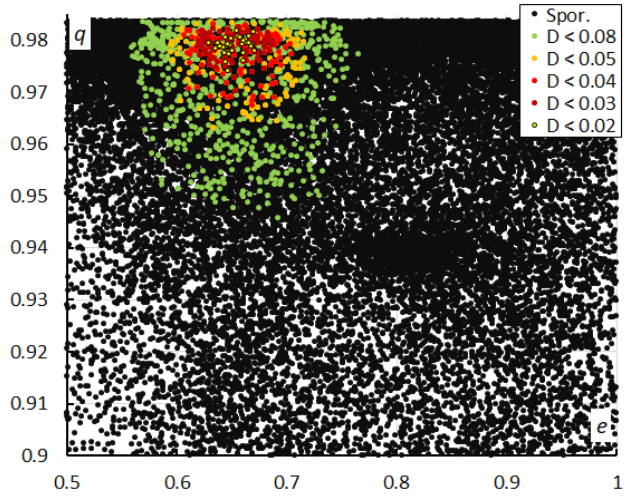

Figure 17 – Perihelion distance q versus the eccentricity e color-coded for different classes of D-criteria thresholds, for $\lambda_\odot$ between 260° and 286°. Spor. = sporadics.

Table 1 – Comparing solutions obtained by the radiant method for 2025–2026, the orbit method 2020–2026 for $D_D < 0.08$ and $D_D < 0.05$, compared to the solution by Jenniskens (2023).

	Radiant 2025–26	Orbit $D_D < 0.08$	Orbit $D_D < 0.05$	Jenniskens (2023)
$\lambda_\odot$ (°)	275.0	276.8	277.6	278.2
$\lambda_{\odot b}$ (°)	267.0	268.0	271.8	270.0
$\lambda_{\odot e}$ (°)	282.0	286.0	284.2	285.0
α_g (°)	141.8	145.4	148.3	146.9
δ_g (°)	–51.8	–51.9	–52.1	–52.7
$\Delta\alpha_g$ (°)	+0.65	+0.82	0.85	+0.89
$\Delta\delta_g$ (°)	–0.07	–0.45	–0.41	–0.36
v_g (km/s)	42.0	43.3	44.3	44.4
H_b (km)	98.3	99.1	99.3	100.4
H_e (km)	88.0	88.3	88.5	87.4
H_p (km)	92.3	92.7	92.8	92.3
Mag_{Ap}	–0.3	–0.4	–0.4	+1.4
λ_g (°)	175.3	179.8	181.6	181.4
$\lambda_g - \lambda_\odot$ (°)	260.3	262.4	264.1	263.2
β_g (°)	–60.8	–59.5	–58.5	–59.7
a (A.U.)	2.577	2.759	2.81	3.24
q (A.U.)	0.968	0.968	0.974	0.978
e	0.624	0.649	0.654	0.699
i (°)	74.3	77.0	78.8	78.1
ω (°)	13.4	11.6	9.8	9.4
Ω (°)	94.6	97.3	97.9	98.2
Π (°)	107.9	108.9	107.7	107.9
T_j	2.32	2.14	2.08	1.93
N	386	933	326	748

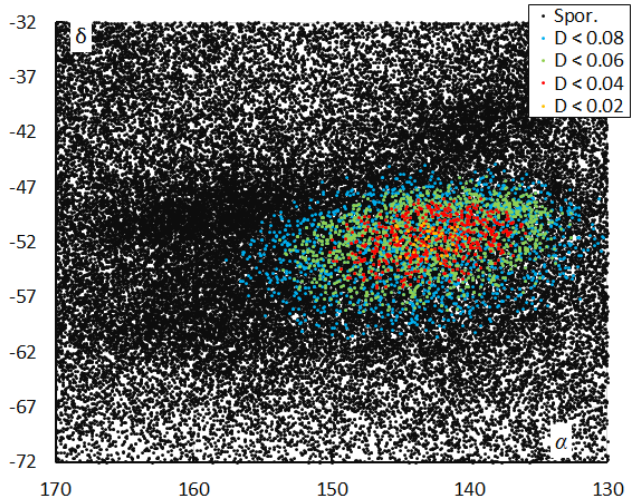

Figure 18 – The radiant distribution during the solar-longitude interval 271° – 286° in equatorial coordinates, color-coded for different threshold values of the combined similarity criteria (SAAMER 2020–2023).

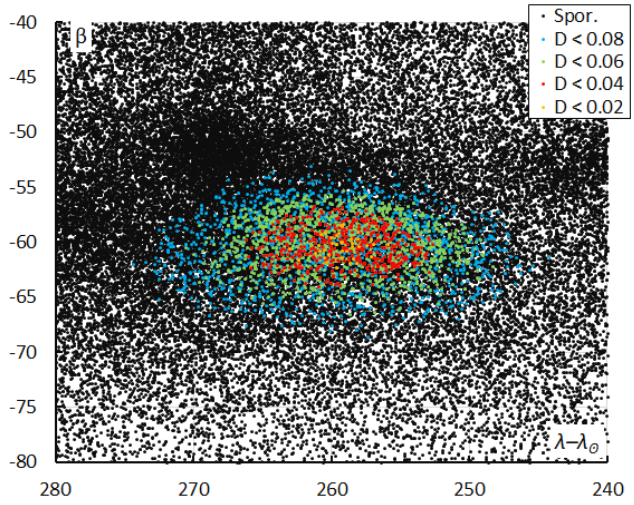

Figure 19 – The radiant distribution during the solar-longitude interval 271° – 286° in Sun-centered geocentric ecliptic coordinates, color-coded for different threshold values of the combined similarity criteria (SAAMER 2020–2023).

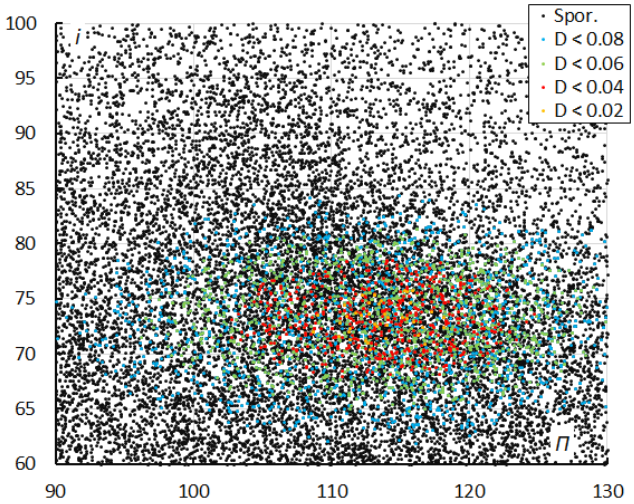

Figure 20 – Inclination i versus the Longitude of Perihelion Π color-coded for different classes of D-criteria thresholds, for $\lambda_\odot$ between 271° and 286°. Spor. = sporadics (SAAMER 2020–2023).

Table 2 – Comparing solutions of the original discovery on SAAMER 2012–2015 radar data, the solution for 2020–2023 SAAMER radar data using the orbit method for $D_D < 0.08$ and $D_D < 0.06$, compared to the solution by Greaves (2026).

	Radar 2012–15	Radar $D_D < 0.08$	Radar $D_D < 0.06$	Greaves (2026)
$\lambda_\odot$ (°)	276.0	277.1	276.8	276.0
$\lambda_{\odot b}$ (°)	272.0	271.6	271.6	272.1
$\lambda_{\odot e}$ (°)	286.0	286.1	286.1	280.3
α_g (°)	141.1	143.1	143.0	140.8
δ_g (°)	–51.0	–51.7	–51.5	–50.8
$\Delta\alpha_g$ (°)	+1.24	+0.82	+0.87	–
$\Delta\delta_g$ (°)	–0.48	–0.49	–0.46	–
v_g (km/s)	40.5	40.4	40.5	–
H_p (km)	–	92.6	92.8	–
λ_g (°)	173.77	177.1	176.5	173.2
$\lambda_g - \lambda_\odot$ (°)	257.77	259.5	259.3	257.2
β_g (°)	–60.48	–60.2	–60.2	–60.4
a (A.U.)	2.08	1.96	1.98	2.05
q (A.U.)	0.965	0.962	0.962	0.963
e	0.536	0.510	0.513	0.531
i (°)	72.9	73.1	73.1	72.9
ω (°)	19.1	16.1	16.1	19.63
Ω (°)	96.0	97.3	97.3	95.77
Π (°)	115.1	113.5	113.5	115.4
T_j	2.82	2.96	2.94	2.85
N	806	3143	1730	500

The same analysis applied to orbit data obtained from low light video cameras has been applied on the 2020-2023 SAAMER radar data. 477108 radar meteor orbits were extracted between solar longitudes 271° and 286°. The radar data represent a different dust population with much smaller sized particles that correspond to a limiting magnitude of +9 for SAAMER against +5 for low light video cameras. The radiant density maps in equatorial coordinates (*Figure 18*) and in Sun-centered ecliptic coordinates (*Figure 19*) differ a lot from the visual equivalents in *Figures 8 and 9*. The diagram with the inclination versus Longitude of Perihelion (*Figure 20*) shows the concentration of the KVE-orbits, but the other shower concentrations that are visible in the visual range (*Figure 11*) are barely visible.

The mean orbits have been calculated for 3143 SAAMER orbits that fulfill the D-criteria thresholds $D_{SH} < 0.2$ and $D_D < 0.08$ and $D_J < 0.2$, and 1730 orbits for the thresholds $D_{SH} < 0.15$ and $D_D < 0.06$ and $D_J < 0.15$. The results are compared to the original discovery data of the kappa-Velids and another solution derived by Greaves (2026) based upon the same SAAMER dataset of 2020–2023 (*Table 2*). The four solutions based upon radar data are in good agreement and differ mainly in geocentric velocity and the Kepler elements that strongly depend upon the velocity. The lower

velocity results in a shorter semi-major axis, lower eccentricity and lower inclination.

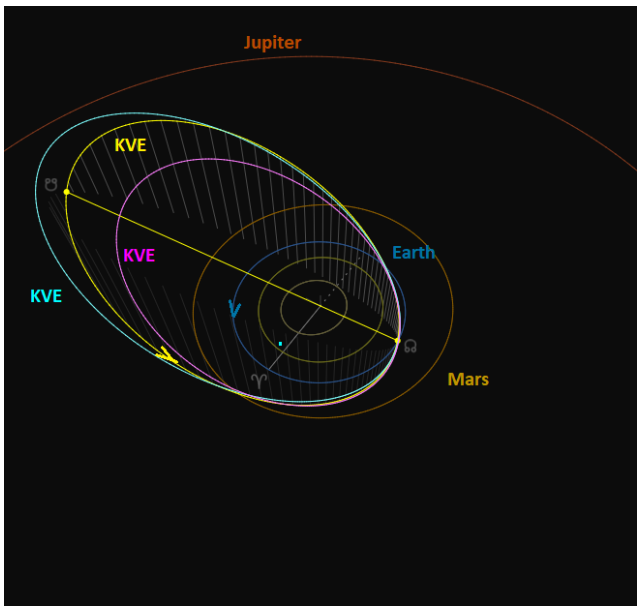

Figure 21 – Comparing the radiant determined kappa-Velids solution (yellow) with the orbit determined solution (blue) and the radar based mean orbit (pink). (Plotted with the Orbit visualization app provided by Pető Zsolt).

The Tisserand value T_J classifies the kappa-Velids as a Jupiter-family comet type stream. The meteoroids encounter the Earth from deep south of the ecliptic at the ascending node (*Figure 21*). The orbit similarity shower classification method filtered slower meteors out as the orbits failed to fit the D-criteria, resulting in a higher velocity selection, longer semi-major axis, larger eccentricity and higher inclination (blue orbit in *Figure 21*) This solution compares best to the CAMS solution. The radiant classification picks more meteors as kappa-Velids and includes many slightly slower meteors as shower members (yellow orbit). The radar-based solution (pink) is situated far inside the low light camera solutions. This is due to the mass-sorting effect as smaller particles with lower energy suffer more from solar radiation and lose angular momentum so that these slowly spiral to the Sun. This is known as the Poynting-Robertson Effect. The older the meteoroid stream, the stronger this mass sorting effect becomes. This, and the very diffuse structure of the kappa-Velids, indicates that this is an old stream.

A search for a possible parent body did not reveal any plausible candidate (*Table 3*)

The number of orbits per year reflects the growth of GMN in the Southern hemisphere from 2020 to 2024 (*Table 4*). The SAAMER radar data runs from 31 December 2019 till 2 January 2023. There is no indication for any episodic activity.

The annual activity should be strong enough to be noticed by visual observers. Naked eye observations picked the diffuse nature of this activity. One center of reasonably strong activity was identified from approximately 20 through to 30 December (267°–277° in solar longitude) with an apparent radiant around RA 135 ± 10°, Decl. –47 ± 7°, at maximum which was on 25 or 26 December ($\lambda_\odot = 274°$) uncorrected visual rates were 3 to 4 meteors per hour. This radiant area activity was first observed by Williams in 1886 and later by most of the Southern Hemisphere observers thereafter. The shower was well monitored between 1971 and 1986 by M. Clark, D. Skelsey, M. Buhagiar and WAMS/NAPOMS.

A second activity was observed from about 29 December to 15 January (277° to 295° in solar longitude) with a broad maximum of 5 to 7 per hour from 6 to 8 January. The radiant position at maximum was RA 125 ± 10° and Decl. –47 ± 7°). This activity differs in radiant position and activity period from the kappa-Velids.

Table 3– Top ten matches of a search for possible parent bodies with $D_D < 0.25$, based upon the mean orbit derived from the radiant classification method.

Name	D_D
2017 YN_3	0.152
2023 GZ_1	0.213
2014 UF_{206}	0.213
2020 WS_5	0.219
2009 HV_{58}	0.226
2018 XQ_3	0.229
(523967) 1998 YR_{11}	0.235
2022 WC_{12}	0.235
2024 VW_3	0.241
2024 XB_4	0.242

Table 4 – Number of kappa-Velid orbits detected by GMN and SAAMER per year.

Year	GMN $D_D < 0.08$	GMN $D_D < 0.05$	SAAMER $D_D < 0.08$	SAAMER $D_D < 0.06$
2019	–	–	60	31
2020	2	2	1109	590
2021	23	11	994	541
2022	79	23	966	564
2023	44	12	14	4
2024	386	131	–	–
2025	365	133	–	–
2026	34	14	–	–

5 Conclusions

This GMN meteoroid orbit data case study confirms the existence of the kappa-Velids. The solution has been checked by using two independent shower identification methods as a two-factor authentication for the validation of the analysis. The diffuse nature of this meteoroid stream with a very large radiant area and large spread on the orbital parameters proves to be a challenge to distinguish the kappa-Velids from the sporadic background by using the radiant classification method. The orbit classification

method based upon D-criteria identifies only a portion of the actual number of kappa-Velids as the spread on the Kepler elements in the shower is too large to fulfill these orbital similarity criteria. The solutions are a trade-off between rejecting as many sporadics as possible and the selection of a statistical relevant number of kappa-Velids to approach a representative mean orbit.

Since the shower was first discovered based upon radar data from SAAMER, an attempt was made to compare the results based upon low-light video camera data with limiting magnitude +5 and the radar data with limiting magnitude +9 which consists of a different population in mass. The radar data yield a much shorter orbit far inside the orbit derived from GMN data. Physically this can be explained as the result of smaller dust particles spiraling towards the Sun caused the Poynting-Robertson effect. This indicates that this dust stream is probably very old and already heavily perturbed and dispersed.

The IAU-MDC Working List of Meteor showers list all solutions derived from different observing techniques. To some extend this is like comparing apples with oranges as each solution strongly depends upon the activity period covered, the mass range that has been observed and the shower classification methodology that has been used. The GMN solutions are based upon the computed mean orbit while other researchers use average or median values of the Kepler elements, which can result in a calculated orbit that does not cross the Earth orbit.

Our independent solutions based upon SAAMER and GMN data have been reported to the IAU-MDC, and the shower now fulfils the criteria for being upgraded to be nominated for established status.

Acknowledgments

This report is based on the data of the Global Meteor Network (Vida et al., 2020a; 2020b; 2021) which is released under the CC BY 4.0 license[20]. We thank all 927 participants in the Global Meteor Network project for their contribution and perseverance. A list with the names of the volunteers who contribute to GMN has been published in the 2025 annual report (Roggemans et al., 2026b). The following 317 cameras contributed to paired meteors used in this study:

AU0001, AU0002, AU0003, AU0004, AU0006, AU0007, AU0009, AU000A, AU000B, AU000C, AU000D, AU000E, AU000F, AU000G, AU000H, AU000J, AU000K, AU000L, AU000Q, AU000R, AU000S, AU000T, AU000U, AU000V, AU000W, AU000X, AU000Y, AU000Z, AU0010, AU001A, AU001B, AU001C, AU001D, AU001E, AU001F, AU001K, AU001L, AU001N, AU001P, AU001Q, AU001R, AU001S, AU001U, AU001V, AU001W, AU001X, AU001Y, AU001Z, AU0028, AU0029, AU002A, AU002B, AU002C, AU002D, AU002E, AU002F, AU0030, AU003C, AU003E, AU003G, AU003H, AU003J, AU0040, AU0041, AU0042, AU0043, AU0046, AU0047, AU0048, AU004A, AU004B, AU004H, AU004J, AU004K, AU004L, AU004M, AU004Q, AU004R, BR0001, BR0002, BR0003, BR000A, BR000F, BR000G, BR000J, BR000Q, BR000T, BR0013, BR0015, BR001F, BR001Q, BR001T, BR001U, BR001W, BR001Z, BR002A, BR002B, BR002C, ES0002, ES0003, KR0004, KR0010, KR0015, MX0001, MX0002, MX0003, MX0006, MX000B, MX000E, MX000F, NZ0001, NZ0002, NZ0003, NZ0004, NZ0006, NZ0007, NZ0008, NZ0009, NZ000B, NZ000D, NZ000F, NZ000G, NZ000H, NZ000J, NZ000K, NZ000M, NZ000N, NZ000P, NZ000Q, NZ000S, NZ000T, NZ000U, NZ000V, NZ000W, NZ000X, NZ000Y, NZ000Z, NZ0010, NZ0011, NZ0012, NZ0013, NZ0014, NZ0015, NZ0016, NZ0017, NZ0018, NZ0019, NZ001A, NZ001C, NZ001E, NZ001F, NZ001G, NZ001H, NZ001J, NZ001L, NZ001N, NZ001P, NZ001Q, NZ001R, NZ001S, NZ001V, NZ001W, NZ001X, NZ001Y, NZ001Z, NZ0020, NZ0021, NZ0022, NZ0023, NZ0024, NZ0025, NZ0026, NZ0027, NZ0028, NZ0029, NZ002C, NZ002D, NZ002E, NZ002F, NZ002G, NZ002H, NZ002J, NZ002K, NZ002L, NZ002M, NZ002N, NZ002P, NZ002Q, NZ002R, NZ002S, NZ002T, NZ002U, NZ002V, NZ002W, NZ002X, NZ002Y, NZ002Z, NZ0030, NZ0032, NZ0033, NZ0034, NZ0035, NZ0036, NZ0037, NZ0038, NZ0039, NZ003A, NZ003B, NZ003C, NZ003E, NZ003F, NZ003G, NZ003H, NZ003K, NZ003N, NZ003Q, NZ003R, NZ003S, NZ003T, NZ003U, NZ003V, NZ003W, NZ003X, NZ003Y, NZ003Z, NZ0040, NZ0041, NZ0042, NZ0044, NZ0045, NZ0046, NZ0049, NZ004A, NZ004B, NZ004C, NZ004D, NZ004E, NZ004H, NZ004J, NZ004L, NZ004M, NZ004N, NZ004R, NZ004S, NZ004T, NZ004U, NZ004V, NZ004W, NZ004X, NZ004Y, NZ004Z, NZ0051, NZ0059, NZ005A, NZ005B, NZ005C, NZ005D, NZ005E, NZ005F, NZ005G, NZ005H, NZ005J, NZ005K, NZ005L, NZ005M, NZ005N, NZ005Q, NZ005R, NZ005S, NZ005T, NZ005U, NZ005Y, NZ005Z, NZ0061, NZ0063, NZ0065, NZ0066, NZ0067, NZ0068, NZ0069, NZ006F, NZ006G, NZ006K, US0004, US0005, US000A, US000C, US000G, US000H, US000L, US000P, US000S, US000U, US000V, US001Q, US001R, US0021, US002W, US002X, US002Y, US004Q, US005D, US005F, US0061, USL001, USL002, USL005, USL008, USL00B, USL00E, USL00M, USL00P, USL00X, USL011, USL012, USL013, USL016, USL01A, USL01D, ZA0001, ZA0002, ZA0006, ZA0007, ZA0008, ZA000C, ZA000F and ZA000G.

References

Drummond J. D. (1981). “A test of comet and meteor shower associations”. *Icarus*, **45**, 545–553.

Greaves J. (2026). “Independent confirmation of meteor shower candidates from the Southern Argentine Agile Meteor Radar”. *eMetN Meteor Journal*, **11**, 151–153.

[20] https://creativecommons.org/licenses/by/4.0/

Jenniskens P. (2023). Atlas of Earth's meteor showers. Elsevier, Cambridge, United states. ISBN 978-0-443-23577-1. Page 511.

Jopek T. J. (1993). "Remarks on the meteor orbital similarity D-criterion". *Icarus*, **106**, 603–607.

Jopek T. J., Rudawska R. and Pretka-Ziomek H. (2006). "Calculation of the mean orbit of a meteoroid stream". *Monthly Notices of the Royal Astronomical Society*, **371**, 1367–1372.

Moorhead A. V., Clements T. D., Vida D. (2020). "Realistic gravitational focusing of meteoroid streams". *Monthly Notices of the Royal Astronomical Society*, **494**, 2982–2994.

Pokorný P., Janches D., Brown P. G., Hormaechea J. L. (2017). "An orbital meteoroid stream survey using the Southern Argentina Agile MEteor Radar (SAAMER) based on a wavelet approach". *Icarus*, **290**, 162–182.

Roggemans P., Vida D., Šegon D., Scott J.M., Wood J. (2026a). "2025 outburst of the Volantids (VOL#758)". *eMetN Meteor Journal*, **11**, 135–141.

Roggemans P., Vida D., Šegon D., Scott J.M. (2026b). "Meteoroid orbit shower identification". *eMetN Meteor Journal*, **11**, 189–204.

Roggemans P., Campbell-Burns P., Kalina M., McIntyre M., Scott J. M., Šegon D., Vida D. (2026c). "Global Meteor Network report 2025". *eMetN Meteor Journal*, **11**, 89–129.

Southworth R. B. and Hawkins G. S. (1963). "Statistics of meteor streams". *Smithsonian Contributions to Astrophysics*, **7**, 261–285.

Vida D., Gural P., Brown P., Campbell-Brown M., Wiegert P. (2020a). "Estimating trajectories of meteors: an observational Monte Carlo approach - I. Theory". *Monthly Notices of the Royal Astronomical Society*, **491**, 2688–2705.

Vida D., Gural P., Brown P., Campbell-Brown M., Wiegert P. (2020b). "Estimating trajectories of meteors: an observational Monte Carlo approach - II. Results". *Monthly Notices of the Royal Astronomical Society*, **491**, 3996–4011.

Vida D., Šegon D., Gural P. S., Brown P. G., McIntyre M. J. M., Dijkema T. J., Pavletić L., Kukić P., Mazur M. J., Eschman P., Roggemans P., Merlak A., Zubrović D. (2021). "The Global Meteor Network – Methodology and first results". *Monthly Notices of the Royal Astronomical Society*, **506**, 5046–5074.

Delta-Normids (DNO#915) outburst in 2026

Paul Roggemans[1], **Denis Vida**[2,3], **Damir Šegon**[4,5], **James M. Scott**[6], **Jeff Wood**[7]

[1] **Pijnboomstraat 25, 2800 Mechelen, Belgium**
Paul.roggemans@gmail.com

[2] **Department of Physics and Astronomy, University of Western Ontario, Richmond Street, London, N6A 3K7, Ontario, Canada**

[3] **Institute for Earth and Space Exploration, University of Western Ontario, Perth Drive, London, N6A 5B8, Ontario, Canada**
denis.vida@gmail.com

[4] **Astronomical Society Istra Pula, Park Monte Zaro 2, 52100 Pula, Croatia**

[5] **Višnjan Observatory, Istarska 5, 52463 Višnjan, Croatia**

[6] **Department of Geoscience, Aarhus University, Høegh-Guldbergs Gade 2. DK-8000 Aarhus C, Denmark**

[7] **PO Box 162, Willetton, Western Australia 6955, Australia**

A sharp short-duration outburst was recorded during 22–23 February, 2026 from a radiant at R.A. = 238.5° and Decl.= –46.0°, with a geocentric velocity of 66.7 km/s. The shower is identified as the delta-Normids, and Comet C/1861 Y1 (Tuttle) could be the parent body. This case study confirms the existence of this annual meteor shower that fulfils the criteria for it to be nominated as having an established status by the IAU-MDC.

1 Introduction

Between 22–23 February, 2026, a bright spot revealed a strong outburst of a minor shower on the GMN radiant density maps (*Figure 1*). The activity was identified as the delta-Normids (DNO-915)[21] and the outburst reported to the astronomical community (Vida et al., 2026). A more in-depth case study was made based upon GMN orbit data collected for this shower since 2020.

The delta-Normids were discovered by CAMS (Jenniskens, 2023). A possible connection with the gamma-Normids (GMO-118) is unlikely since this shower appears later in time according to visual observers.

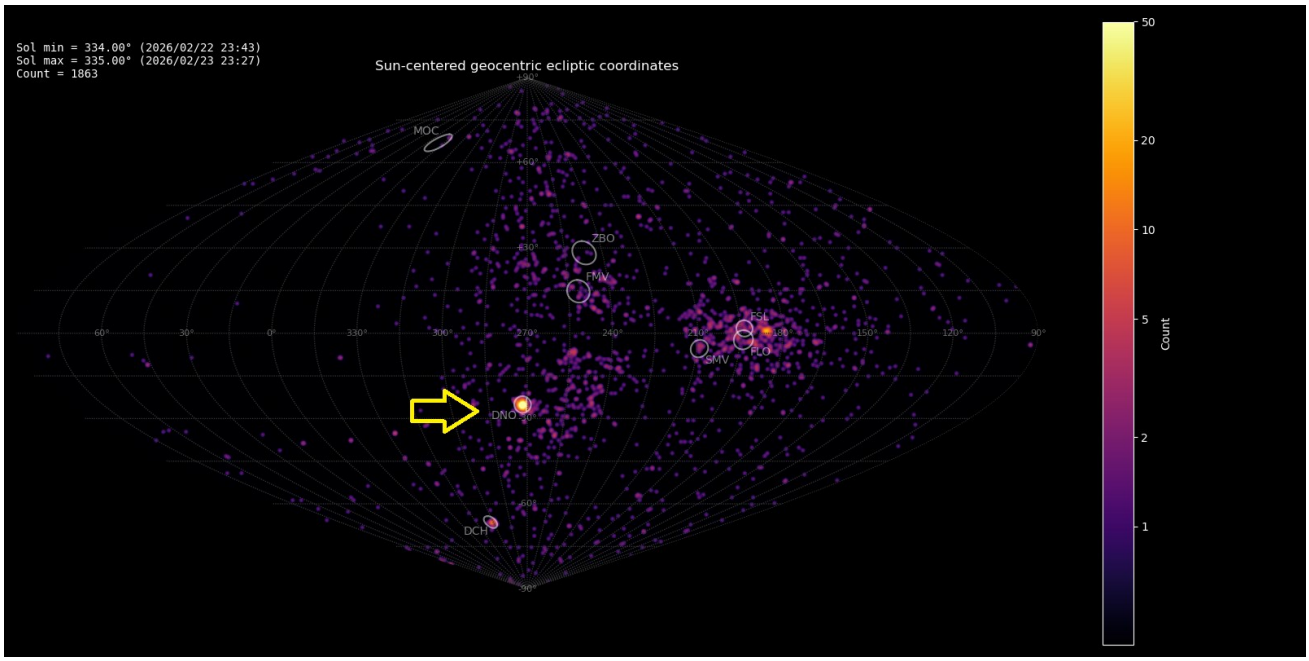

Figure 1 – Radiant density map with 1863 radiants obtained by the Global Meteor Network during 22–23 February, 2026. The position of the delta-Normids in Sun-centered geocentric ecliptic coordinates is marked with a yellow arrow.

[21] https://www.ta3.sk/IAUC22DB/MDC2022/Roje/pojedynczy_obiekt.php?lporz=02243&kodstrumienia=00915

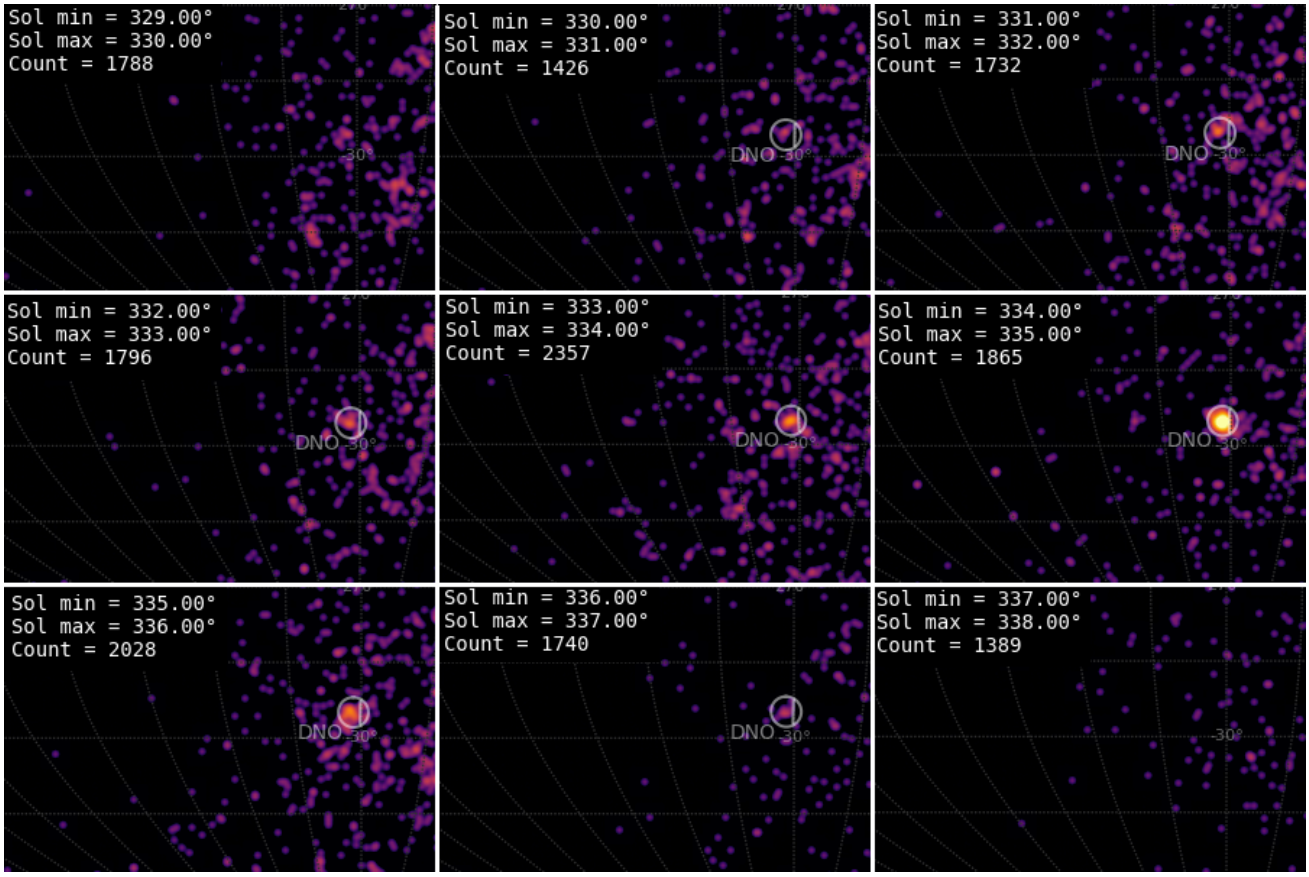

Figure 2 – The appearance of the delta-Normids during consecutive nights, the outburst appeared at $\lambda_\odot = 334.7°$.

2 Shower classification based on radiants

The GMN shower association criteria assume that meteors within 1° in solar longitude, within 1.4° of a common radiant, and within 10% in geocentric velocity of a shower reference location are members of that shower. Further details about the shower association are explained in Moorhead et al. (2020). Using these meteor shower selection criteria, 281 orbits have been identified as delta-Normids recorded in 2026 by 213 GMN cameras installed in Australia, Brazil, New Zealand, South-Korea, United States and South Africa. The final results have been listed in *Table 2*.

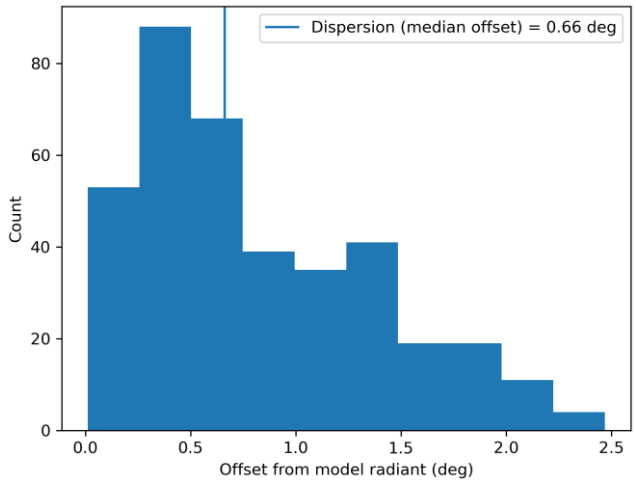

Figure 3 – Dispersion median offset on the radiant position.

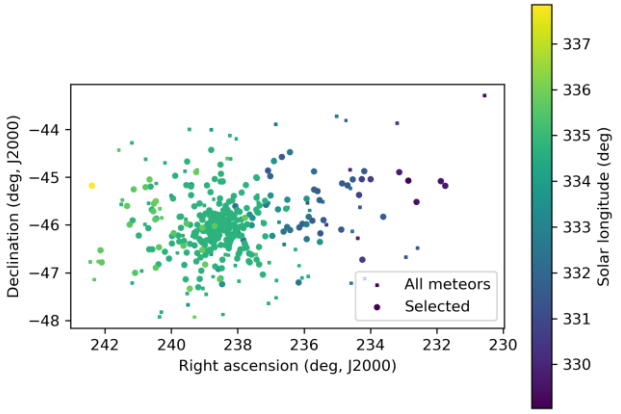

Figure 4 – The radiant distribution during the solar-longitude interval 329° – 338° in equatorial coordinates.

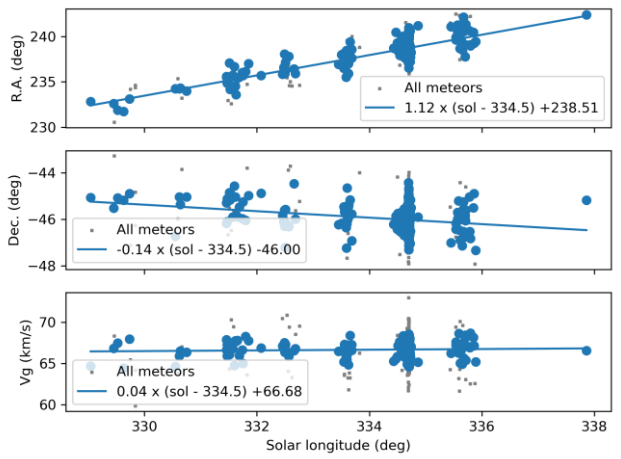

Figure 5 – The radiant drift.

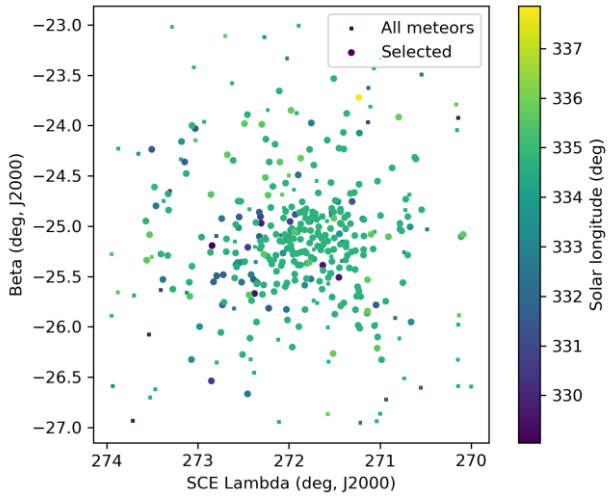

Figure 6 – The radiant distribution during the solar-longitude interval 329° – 338° in Sun centered geocentric ecliptic coordinates.

3 Shower classification based on orbits

A complete independent meteoroid stream search has been applied to orbit data obtained between solar longitude 320.0° and 360.0° during the years 2019 to 2026. 249194 orbits were available within this time interval and a final mean orbit has been computed by the method of Jopek et al. (2006) for the thresholds according to the Rayleigh fit in *Figure 7*, $D_{SH} < 0.125$ and $D_D < 0.05$ and $D_J < 0.125$ (Southworth and Hawkins, 1963; Drummond, 1981; Jopek, 1993. The results and mean orbit based upon 437 meteors for 2020–2026 are listed in *Table 2*. The method has been described in detail in a separate publication (Roggemans et al., 2026a).

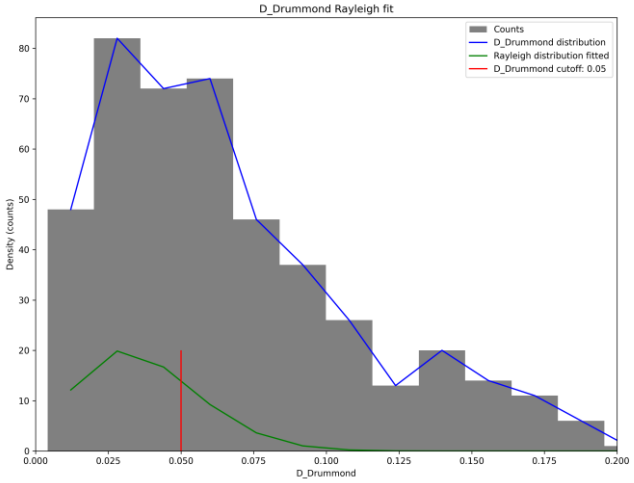

Figure 7 – Rayleigh fit on the Drummond criterion for delta-Normids, 2026 data.

Both methods identified 332 delta-Normids in 2026, 190 (57.2%) in common. The radiant classification method counted 92 (27.7%) delta-Normids that failed to fit the orbit thresholds with $D_{SH} < 0.125$ and $D_D < 0.05$ and $D_J < 0.125$. The orbit classification method identified 50 (15.1%) delta-Normids that were missed by the radiant identification method, 25 of these were recorded before or after the activity period used in the radiant method. The radiant method measured a small dispersion on the radiant with 0.66° and a radius of 1.4° was used to define the radiant size which is a compact radiant. For so many meteors with these narrow radiant criteria to fail to fit the D-criteria thresholds could indicate that these thresholds were too strict. However, statistically both selections are representative for the shower and the derived orbital parameters are in very good agreement (*Table 2*).

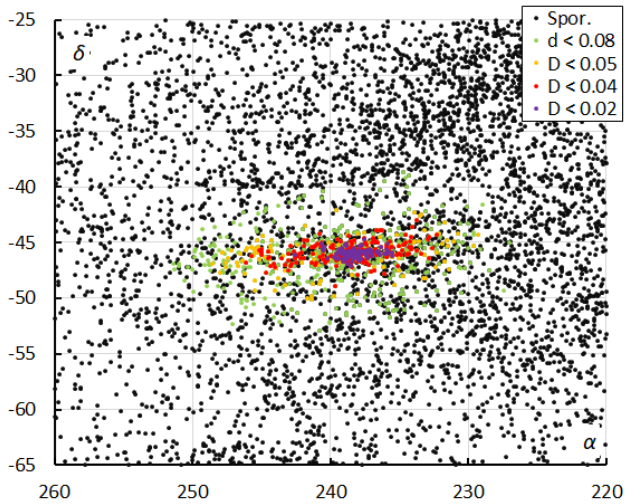

Figure 8 – The radiant distribution during the solar-longitude interval 327° – 339° in equatorial coordinates, color-coded for different threshold values of the combined similarity criteria. Spor. = sporadics.

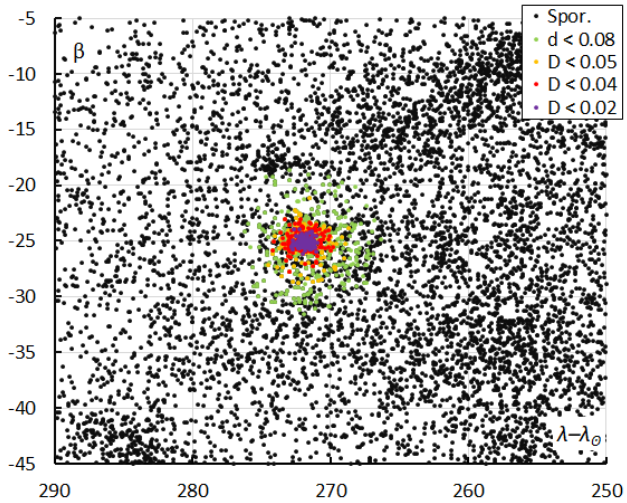

Figure 9 – The radiant distribution during the solar-longitude interval 327° – 339° in Sun-centered geocentric ecliptic coordinates, color-coded for different threshold values of the combined similarity criteria.

For the graph with the ratio delta-Normids/total-activity, only observations south of 30° in latitude were counted and the 2026 data has been processed separately from the 2020–2025 activity (*Figure 10*). The annual activity 2020–2025 barely reaches 2% of the total meteor activity with a first maximum between solar longitude 334° and 335°, and a second maximum around $\lambda_\odot = 339°$. In 2026 a sharp outburst occurred at the first maximum, at $\lambda_\odot = 334.7°$. No delta-Normids activity was detected before $\lambda_\odot = 326.4°$ and nothing after $\lambda_\odot = 344.1°$. The extended activity to

$\lambda_\odot = 360°$ given by Jenniskens (2023) was unable to be confirmed.

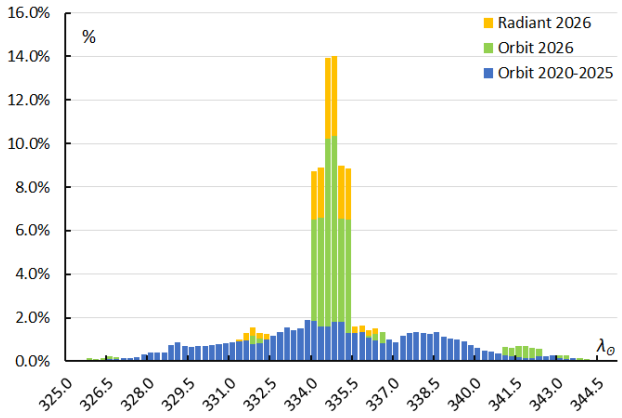

Figure 10 – The percentage of delta-Normids relative to the total number of meteors, for the radiant method (2026, orange) and the orbit classification method 2020–2025 (blue) and 2026 (green).

The profile in *Figure 10* gives the ratios counted per 1.5° (~36 hours) in solar longitude in steps of 0.25° (~6 hours). The large interval of 1.5° smooths fluctuations in the activity caused by unequal coverage at the southern hemisphere. Any sharp, sort duration peak is flattened in this graph. Compared to previous years, the delta-Normids produced an exceptional strong activity in 2026 (*Table 1*) when most meteors appeared in a short interval.

The main peak lasted about 45 minutes, with the majority of meteors appearing within 10 mins. Using 30 minutes time bins, the ZHR was around 70. It's hard to tell what the peak ZHR was during that short period as the time-area product was small, but it could have easily been greater than 100 during those 10 minutes. The meteor flux has been plotted based upon 30 minutes time bins (Vida et al., 2022). The result is shown in *Figure 11*.

Such short duration outbursts can be easily missed and this may explain why no earlier delta-Normid outbursts are know from the past. Daylight time or cloudy weather may have interfered in past years. The peak activity in 2026 was recorded by New Zealand and Australia based cameras where GMN has an excellent coverage. Future observations may reveal if the delta-Normids are an episodic shower and if the shower brings more surprises.

Table 1 – Number of delta-Normids orbits detected by GMN per year.

Year	Orbit method	Radiant method
2020	1	–
2021	2	
2022	2	–
2023	27	–
2024	48	–
2025	116	–
2026	241	281

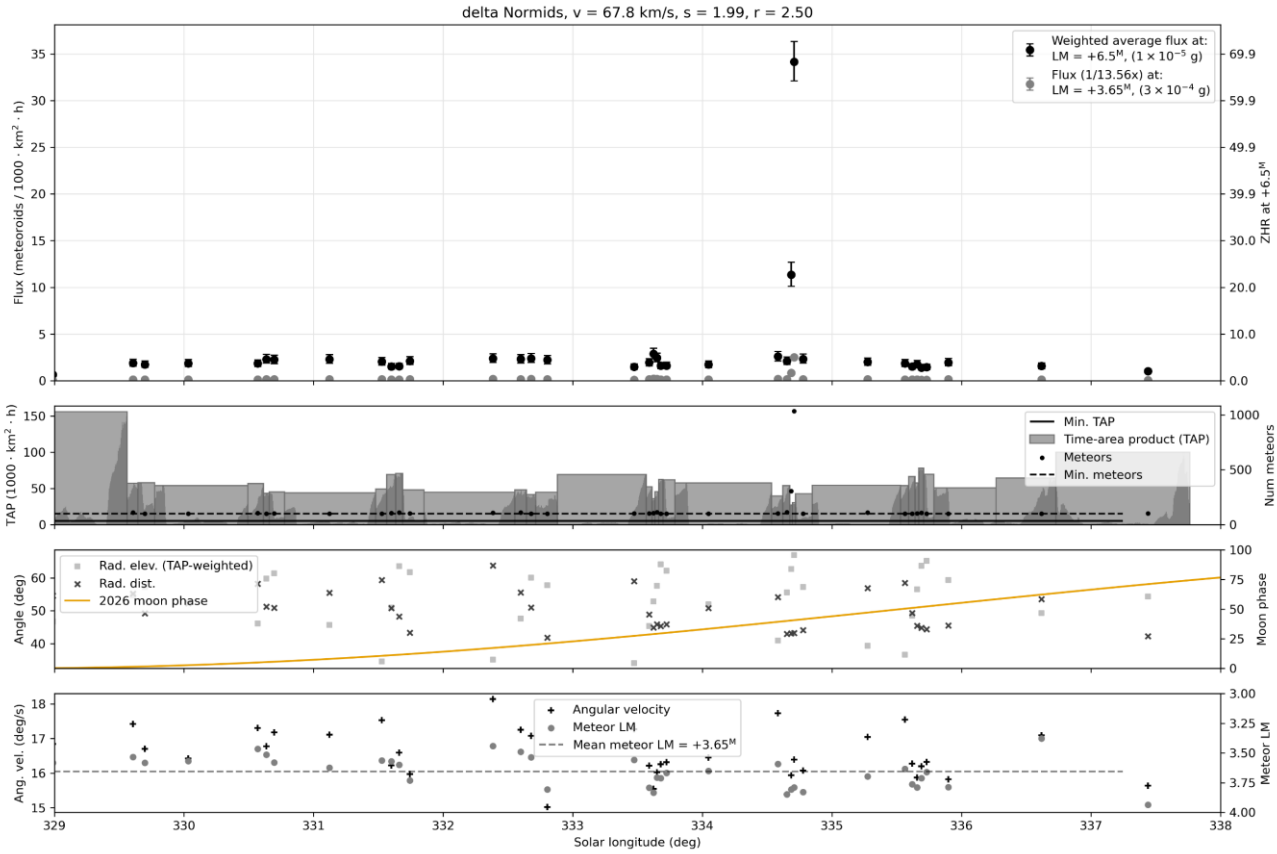

Figure 11 – The meteor flux and Zenithal Hourly Rate (ZHR) for the delta-Normids in 2026.

4 Orbit and parent body

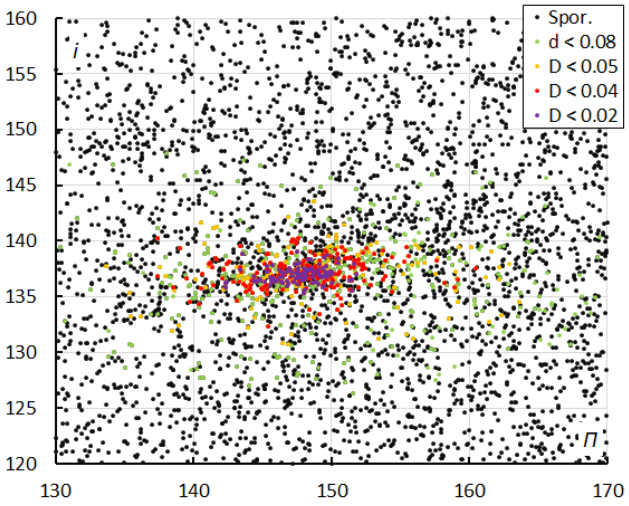

Figure 12 – Inclination i versus the Longitude of Perihelion Π color-coded for different classes of D-criteria thresholds, for $\lambda_\odot$ between 327° and 339°. Spor. = sporadics.

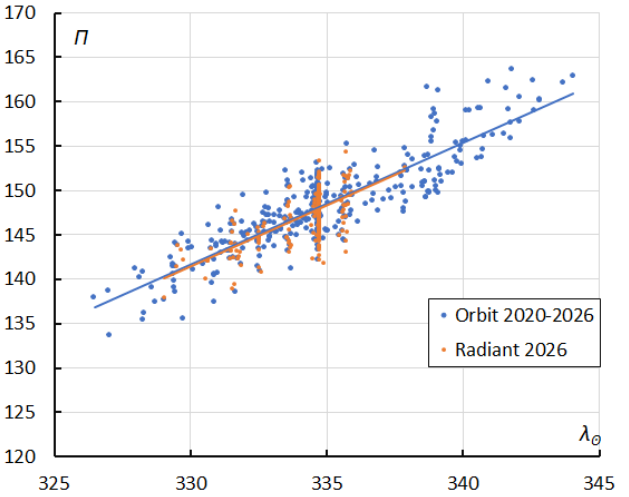

Figure 13 – The evolution of the Longitude of Perihelion Π in function of the Solar Longitude $\lambda_\odot$ based upon the radiant method (2026) and upon the orbit method (2020–2026).

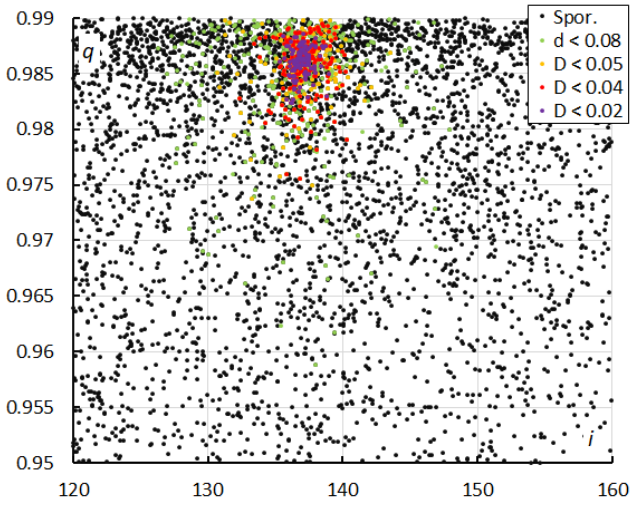

Figure 14 – Perihelion distance q versus the inclination i color-coded for different classes of D-criteria thresholds, for $\lambda_\odot$ between 327° and 339°. Spor. = sporadics.

The diagram of the inclination i versus the Longitude of Perihelion Π shows a concentration in i, stretched in Π (*Figure 12*). The spread in Longitude of Perihelion is caused by a steep increase in Longitude of Perihelion during the activity period:

$$\Pi = 1.36(\lambda_\odot - 334.7) + 148.13$$

Both methods confirm this trend (*Figure 13*). The other Kepler elements remain stable during the activity period. The cluster of DNO orbits is best visible in the diagram perihelion distance versus inclination (*Figure 14*).

Table 2 – A comparison of solutions obtained by the radiant method for 2026, the orbit method for 2020–2026 and $D_D < 0.05$ and the solution by Jenniskens (2023).

	Radiant 2026	Orbit $D_D < 0.05$	Jenniskens (2023)
$\lambda_\odot$ (°)	334.7	334.7	338.7
$\lambda_{\odot b}$ (°)	329.0	326.4	324
$\lambda_{\odot e}$ (°)	337.9	344.1	356
α_g (°)	238.5	238.5	245.5
δ_g (°)	–46.0	–46.0	–46.1
$\Delta\alpha_g$ (°)	+1.12	+1.12	+1.26
$\Delta\delta_g$ (°)	–0.14	–0.13	–0.04
v_g (km/s)	66.7	67.0	67.5
H_b (km)	113.6	114.0	114.1
H_e (km)	97.7	98.3	99.1
H_p (km)	103.6	104.0	104.4
Mag_{Ap}	–1.8	–1.6	+1.5
λ_g (°)	246.4	246.4	250.5
$\lambda_g - \lambda_\odot$ (°)	271.9	271.9	271.8
β_g (°)	–25.1	–25.1	–24.5
a (A.U.)	12.4	17.1	35.7
q (A.U.)	0.985	0.985	0.987
e	0.921	0.942	0.972
i (°)	136.9	137.1	138.3
ω (°)	353.1	353.4	353.7
Ω (°)	154.3	154.8	158.7
Π (°)	147.4	148.2	152.7
T_j	–0.46	–0.58	–0.78
N	281	437	354

The Tisserand value relative to Jupiter with $T_J = -0.46$ is typical for a long-period cometary orbit. The meteoroid stream crosses the ecliptic and Earth's orbit on a retrograde orbit ($i > 90°$) at its ascending node (*Figure 16*). The descending node crosses the ecliptic near the orbit of Neptune (*Figure 15*). A search for a possible parent body did not result in a solid match but comet C/1861 Y1 (Tuttle) could be a plausible candidate. The Drummond criterion with $D_D = 0.13$ is too weak (*Table 3*) but this may be due to this being a poorly observed comet on a parabolic orbit. The most striking resemblance is the retrograde orbit with $i = 138°$. The perihelion distance at 0.839AU, the node at 147.04° and even the eccentricity with $e = 1$ do not differ

too much from the delta-Normids orbit. The largest discrepancy is in the Longitude of Perihelion with Π =118.6° for the comet against 147.4° for the shower. Perhaps this is related to the steep increase in Π during the shower activity period?

Table 3– Top ten matches of a search for possible parent bodies with $D_D < 0.3$, based upon the mean orbit derived from the radiant classification method.

Name	D_D
C/1861 Y1 (Tuttle)	0.130
C/1940 S1 (Okabayasi-Honda)	0.157
C/1893 U1 (Brooks)	0.197
C/2018 Y1 (Iwamoto)	0.199
C/2015 X8 (NEOWISE)	0.201
C/1926 B1 (Blathwayt)	0.209
C/1718 B1	0.211
C/2023 X1 (Leonard)	0.24
C/1340 F1	0.242
C/1760 A1 (Great comet)	0.254

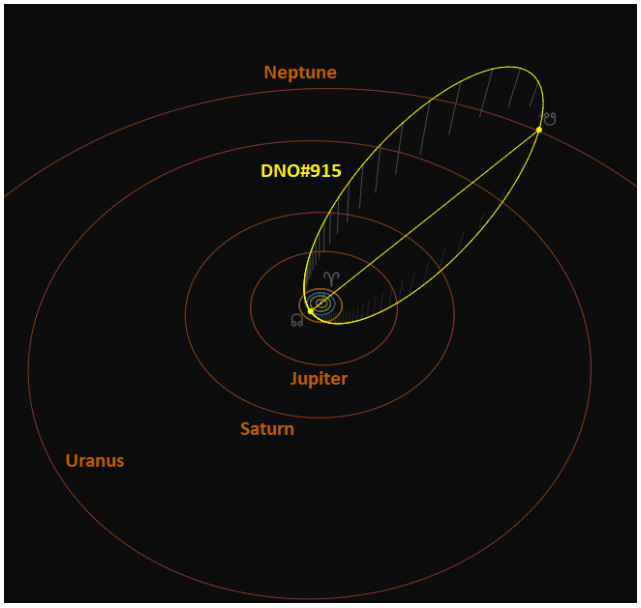

Figure 15 – The orbit determined delta-Normids solution (yellow) in the Solar System. (Plotted with the Orbit visualization app provided by Pető Zsolt).

5 Conclusion

The 2026 outburst of the delta-Normids allowed a detailed analysis of this shower and confirms the discover made by the CAMS network in 2023. Comet C/1861 Y1 (Tuttle) may be the parent body. The maximum activity level in 2026 occurred during a short time interval of 10 minutes. Based upon 30 minutes time bin the maximum ZHR was about 70. Our independent solution has been reported to the IAU-MDC, and the shower now fulfils the criteria for being nominated for established status.

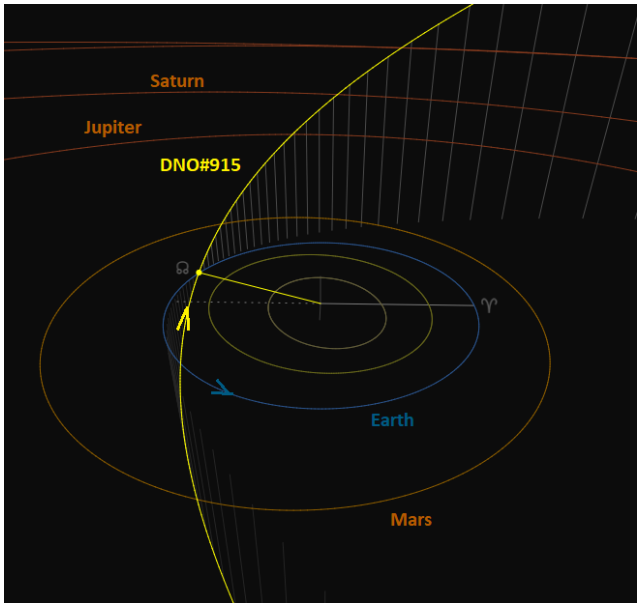

Figure 16 – The orbit determined delta-Normids solution (yellow) in the inner Solar System. (Plotted with the Orbit visualization app provided by Pető Zsolt).

Acknowledgments

This report is based on the data of the Global Meteor Network (Vida et al., 2020a; 2020b; 2021) which is released under the CC BY 4.0 license[22]. We thank all 927 participants in the Global Meteor Network project for their contribution and perseverance. A list with the names of the volunteers who contribute to GMN has been published in the 2025 annual report (Roggemans et al., 2026b). The following 353 cameras contributed to paired meteors used in this study: AU0002, AU0003, AU0004, AU0006, AU0007, AU0009, AU000A, AU000B, AU000C, AU000D, AU000E, AU000F, AU000G, AU000L, AU000Q, AU000R, AU000S, AU000U, AU000V, AU000W, AU000X, AU000Y, AU000Z, AU0010, AU0011, AU001A, AU001B, AU001C, AU001D, AU001E, AU001F, AU001K, AU001L, AU001N, AU001P, AU001Q, AU001R, AU001S, AU001T, AU001U, AU001V, AU001W, AU001X, AU001Y, AU001Z, AU0028, AU0029, AU002A, AU002B, AU002C, AU002E, AU002F, AU0030, AU0034, AU0038, AU003E, AU003G, AU003J, AU0042, AU0044, AU0045, AU0047, AU0048, AU004B, AU004K, AU004L, AU004M, AU004Q, BR000A, BR000G, BR000Q, BR000S, BR001F, BR001M, BR001R, BR001T, BR001U, BR001W, BR0029, BR002A, ES0002, ES0003, GR0006, GR0009, KR0002, KR0008, KR000A, KR000B, KR000C, KR000K, KR000L, KR0015, KR001A, KR001D, KR0024, KR0029, KR002E, KR002G, KR002K, KR002P, KR002Q, KR003Q, MX0001, MX0003, MX0007, MX0009, MX000F, NZ0003, NZ0004, NZ0007, NZ0008, NZ0009, NZ000A, NZ000B, NZ000C, NZ000D, NZ000G, NZ000H, NZ000L, NZ000M, NZ000N, NZ000P, NZ000Q, NZ000R, NZ000S, NZ000T, NZ000U, NZ000V, NZ000W, NZ000X, NZ000Y, NZ000Z, NZ0010, NZ0011, NZ0012, NZ0013, NZ0014, NZ0015, NZ0016, NZ0017, NZ0018, NZ0019, NZ001A, NZ001C, NZ001E, NZ001G, NZ001H,

[22] https://creativecommons.org/licenses/by/4.0/

NZ001J, NZ001K, NZ001L, NZ001N, NZ001P, NZ001Q, NZ001R, NZ001S, NZ001V, NZ001W, NZ001X, NZ001Y, NZ001Z, NZ0020, NZ0021, NZ0022, NZ0023, NZ0024, NZ0025, NZ0026, NZ0027, NZ0028, NZ0029, NZ002B, NZ002C, NZ002D, NZ002E, NZ002F, NZ002G, NZ002H, NZ002J, NZ002K, NZ002L, NZ002M, NZ002N, NZ002P, NZ002Q, NZ002R, NZ002S, NZ002T, NZ002U, NZ002V, NZ002W, NZ002X, NZ002Y, NZ002Z, NZ0030, NZ0032, NZ0033, NZ0034, NZ0035, NZ0036, NZ0037, NZ0038, NZ0039, NZ003A, NZ003B, NZ003C, NZ003E, NZ003G, NZ003H, NZ003K, NZ003L, NZ003M, NZ003N, NZ003Q, NZ003R, NZ003S, NZ003T, NZ003U, NZ003V, NZ003W, NZ003X, NZ003Y, NZ003Z, NZ0040, NZ0041, NZ0042, NZ0043, NZ0044, NZ0045, NZ0046, NZ0049, NZ004A, NZ004B, NZ004C, NZ004D, NZ004E, NZ004F, NZ004H, NZ004J, NZ004L, NZ004M, NZ004N, NZ004R, NZ004S, NZ004T, NZ004U, NZ004W, NZ004X, NZ004Y, NZ004Z, NZ0051, NZ0059, NZ005A, NZ005B, NZ005C, NZ005D, NZ005F, NZ005G, NZ005H, NZ005J, NZ005K, NZ005L, NZ005M, NZ005N, NZ005Q, NZ005S, NZ005T, NZ005U, NZ005Y, NZ005Z, NZ0061, NZ0063, NZ0065, NZ0066, NZ0067, NZ0068, NZ0069, NZ006A, NZ006B, NZ006C, NZ006E, NZ006F, NZ006G, NZ006H, NZ006J, NZ006K, NZ007C, NZ007E, US0002, US0003, US0004, US0005, US0007, US0008, US0009, US000A, US000C, US000E, US000G, US000J, US000K, US000L, US000M, US000R, US000S, US000V, US001E, US001Q, US001R, US0022, US0027, US002Y, US0035, US003M, US003P, US003R, US004C, US005A, US005B, US005C, US005Q, US005X, US005Y, US0062, USL003, USL004, USL005, USL00A, USL00C, USL00F, USL00G, USL00J, USL00L, USL00M, USL00N, USL00Q, USL00Z, USL011, USL012, USL013, USL016, USL017, USL01A, USL01B, USL01C, USL01D, USV003, ZA0001, ZA0006, ZA0007, ZA0008, ZA0009, ZA000C and ZA000F.

References

Drummond J. D. (1981). “A test of comet and meteor shower associations”. *Icarus*, **45**, 545–553.

Jenniskens P. (2023). Atlas of Earth’s meteor showers. Elsevier, Cambridge, United states. ISBN 978-0-443-23577-1. Page 537.

Jopek T. J. (1993). “Remarks on the meteor orbital similarity D-criterion”. *Icarus*, **106**, 603–607.

Jopek T. J., Rudawska R. and Pretka-Ziomek H. (2006). “Calculation of the mean orbit of a meteoroid stream”. *Monthly Notices of the Royal Astronomical Society*, **371**, 1367–1372.

Moorhead A. V., Clements T. D., Vida D. (2020). “Realistic gravitational focusing of meteoroid streams”. *Monthly Notices of the Royal Astronomical Society*, **494**, 2982–2994.

Roggemans P., Vida D., Šegon D., Scott J.M. (2026a). “Meteoroid orbit shower identification”. *eMetN Meteor Journal*, **11**, 189–204.

Roggemans P., Campbell-Burns P., Kalina M., McIntyre M., Scott J. M., Šegon D., Vida D. (2026b). “Global Meteor Network report 2025”. *eMetN Meteor Journal*, **11**, 89–129.

Southworth R. B. and Hawkins G. S. (1963). “Statistics of meteor streams”. *Smithsonian Contributions to Astrophysics*, **7**, 261–285.

Vida D., Gural P., Brown P., Campbell-Brown M., Wiegert P. (2020a). “Estimating trajectories of meteors: an observational Monte Carlo approach - I. Theory”. *Monthly Notices of the Royal Astronomical Society*, **491**, 2688–2705.

Vida D., Gural P., Brown P., Campbell-Brown M., Wiegert P. (2020b). “Estimating trajectories of meteors: an observational Monte Carlo approach - II. Results”. *Monthly Notices of the Royal Astronomical Society*, **491**, 3996–4011.

Vida D., Šegon D., Gural P. S., Brown P. G., McIntyre M. J. M., Dijkema T. J., Pavletić L., Kukić P., Mazur M. J., Eschman P., Roggemans P., Merlak A., Zubrović D. (2021). “The Global Meteor Network – Methodology and first results”. *Monthly Notices of the Royal Astronomical Society*, **506**, 5046–5074.

Vida D., Blaauw Erskine R. C., Brown P. G., Kambulow J., Campbell-Brown M., Mazur M. J. (2022). “Computing optical meteor flux using global meteor network data”. *Monthly Notices of the Royal Astronomical Society*, **515**, 2322–2339.

Vida D., Šegon D., Roggemans P., Wood J., Scott J., Cooke W.J., Vriezelaar A. (2026). “Delta Normid meteors 2026”. CBET 5666, 2026 February 24, D. W. E. Green, editor.

The Southern delta-Aquariids 2000–2025

Koen Miskotte

Dutch Meteor Society
k.miskotte@upcmail.nl

A case study is presented on the variation in activity of the Southern delta-Aquariids. The activity was stable during the period 2000–2022, but 2025 shows significantly lower activity. Years with possible outbursts are 1977, 2003, 2022 and 2025.

1 Introduction

Besides the well-known Perseid maximum around August 12th, late July is also a good time to observe meteors. On top of the existing Perseid activity, many minor meteor showers are active: the Capricornids, the Aquariids complex, the gamma-Draconids, and the Pisces Austrinids. Sporadic activity also increases significantly throughout July. All of this combined often results in high meteor activity. Most of the activity at the end of July comes from the Southern delta-Aquariids (SDA). The SDAs are medium-speed meteors that are usually faint, although an occasional fireball is possible. DMS observers have often undertaken visual expeditions to better understand the meteor shower. The first good DMS data came from the first international expedition in 1984 in Puimichel, southern France. But especially the later expeditions to La Palma in 2008 (van Leuteren, 2008; Johannink et al., 2008a; 2008b) and Namibia in 2011 (van Leuteren, 2011; Johannink and Miskotte, 2011; 2012) yielded a wealth of visual data. Since those expeditions, the SDAs have been regularly observed from southern locations, resulting in analyses of the SDAs based on IMO data. In 2025, the author conducted a study with two objectives: is there a trend in annual SDA activity and does the meteor shower sometimes show increased activity?

2 A bit of SDA history

The first possible SDA observations were made in August 1858–1883 by E. Heiss and G. Neumayer (Heiss and Schmidt, 1867; Kronk, 2014). It is possible that there is a mix-up here with the Antihelion radiant and the Northern and Southern iota-Aquariids and Northern delta-Aquariids. In the following years, more observers reported meteors originating from roughly the radiant position of the SDAs. One of these observers was the well-known meteor observer William Denning.

It wasn't until the 1950s that the SDAs were officially recognized as a meteor shower. Radar data (McKinley) provided some more information about the radiant and heliocentric velocity, and the photographic Harvard Meteor Project 1952–1954 (2000 meteors for which orbital elements could be calculated) showed a clear radiant drift and the discovery of the northern branch linked to the SDA. This was due to perturbations from the planet Jupiter. B.A. Lindblad concluded from the Harvard Meteor Project that the SDAs are active between July 21 and August 8 (Lindblad, 1971), while the northern branch is active between August 5 and 25. Meanwhile, we know from CAMS data, among other sources, that the SDAs are already active from July 15 to August 30, with a maximum on July 29 ($\lambda_\odot = 126.5°$). The parent body may be comet 96P Machholz (Jenniskens, 2023).

3 Analysis method

When analyzing the observational data from different years, it became apparent that there are sometimes large differences in the ZHR values found between observers active in Northern or Southern Europe. The problem may lie in the radiant height of the shower and/or the transparency and brightness of the sky.

Table 1 shows the maximum radiant height on July 29th at a specific location. It also indicates how long the radiant remains above the 25-degree limit. The 25-degree limit is the minimum radiant height used by the author for ZHR analyses. For this reason, the author decided to limit the geographical limit to use only observations made south of 46° N.

Table 1 – Overview of several SDA observation locations. Column 5 shows the number of hours the SDA radiant is above 25 degrees elevation. Column 7 shows the maximum number of observable SDAs, the latter column also depends on the C_p of an observer.

Location	Lat. (°)	Long. (°)	Max. radiant height (°)	Time with radiant >25°	Max lm	Max number of SDA
Netherlands	52	5	21	~	6.5	~5
Provence (FR)	44	6	30	3	6.7	~10
Crete (GR)	35	25	35	4.3	6.7	~20
La Palma (SP)	28	–17	45	5	6.8	~30
Namibia	–23	17	82	8.5	7.0	~40

Next, the IMO database was consulted for SDA data from the period 2000–2025. *Table 2* was compiled from this data.

Table 2 – Overview of available SDA data in the IMO database.

Year	N° SDA	Moon	N° of Obs.	With >50 SDA	Used
2000	2034	no	155	6	
2001	819	no	110	4	
2002	311	yes	84	0	
2003	1035	no	76	4	y
2004	272	partial	61	0	
2005	465	yes	70	1	
2006	1341	no	76	10	
2007	1121	partial	109	1	
2008	4062	no	114	12	y
2009	2040	partial	109	11	
2010	1483	yes	130	4	
2011	5077	no	86	7	y
2012	1050	partial	112	1	
2013	1597	yes	114	6	
2014	1411	no	98	3	y
2015	1143	yes	140	2	
2016	2434	partial	133	16	
2017	1532	no	73	6	y
2018	1213	yes	116	5	
2019	1488	no	93	6	y
2020	763	partial	64	6	
2021	681	yes	72	4	
2022	1130	no	46	8	y
2023	281	partial	28	2	
2024	308	yes	34	0	
2025	825	no	25	7	y

To determine which years can be used and which cannot, we looked at moonlight during the maximum period; years with abundant or partial moonlight were excluded. I also looked at how many observers observed more than 50 SDAs per year. These are observers who observed more than two nights, for which a good C_p is often available. This information also provides additional insight into the choice of a particular year. Using only the number of observed SDAs as a benchmark is not an option here, because if we look at 2016, for example, we see that 2434 SDAs were observed. There were 133 active observers, but there was abundant moonlight during the SDA maximum. Most SDAs that year were seen after July 29th. Perhaps also because there had been considerable writing about the possible increased Perseid activity on the night of August 11–12, 2016, which resulted in many observers also seeing a considerable number of SDAs.

Furthermore, the data were subject to the usual requirements:

- Minimum radiant height: 25 degrees.
- A reliable C_p for the observer must be known.
- The individual observer must have observed a relatively large number of SDAs.
- A weighted average ZHR was always determined over a day. In practice, this is usually between 20^h and 11^h UT (Europe and America). Australian data was sometimes also used.
- Hourly counts were used for *Figures 1 through 6*.
- A fixed population index *r* of 2.7 was used.
- The ZHR formula is:

$$ZHR = \frac{n \cdot r^{6.5-lm}}{(\sin h)^{\gamma} \cdot C_p \cdot T_{eff}}$$

To compare the graphs, the 2011 SDA ZHR graph was used as a basis. This is because a group of observers in Namibia collected a large amount of data with a large number of SDAs, high radiant positions, and excellent Bortle scale 1 observing conditions (Johannink and Miskotte, 2011; 2012). There is, however, some difference compared to the earlier analysis of the 2011 data. At that time, the radiant height correction γ was set at 1.4, while it is now 1.0. Therefore, all years were recalculated with $\gamma = 1.0$. The population index *r* was fixed at 2.70. This results in slightly lower ZHRs in 2003, 2008, and 2011 than what was calculated then.

Table 3 – Overview of numbers of SDAs, periods and observers used for this analysis.

Year	N° of SDA	N° of periods	N° of Obs.
2003	311	28	1
2008	1592	90	5
2011	3512	272	4
2014	516	96	5
2017	813	96	8
2019	817	133	9
2022	454	77	6
2025	573	118	12

4 The annual SDA comparisons

2003–2011

Although the 2003 data is only a fraction of the 2011 data, the agreements are good. The possible outburst of July 28–29, 2003 (see next section), occurred near $\lambda_{\odot} = 125.5°$. That ZHR point is indeed slightly elevated compared to 2011. But it is small, yet explainable. The ZHR before and after the observed increased activity was actually somewhat on the low side of what is expected for this period; see also *Figure 7* in the next chapter. In other words, the increased activity is therefore barely reflected in the average ZHR for that night (*Figure 1*).

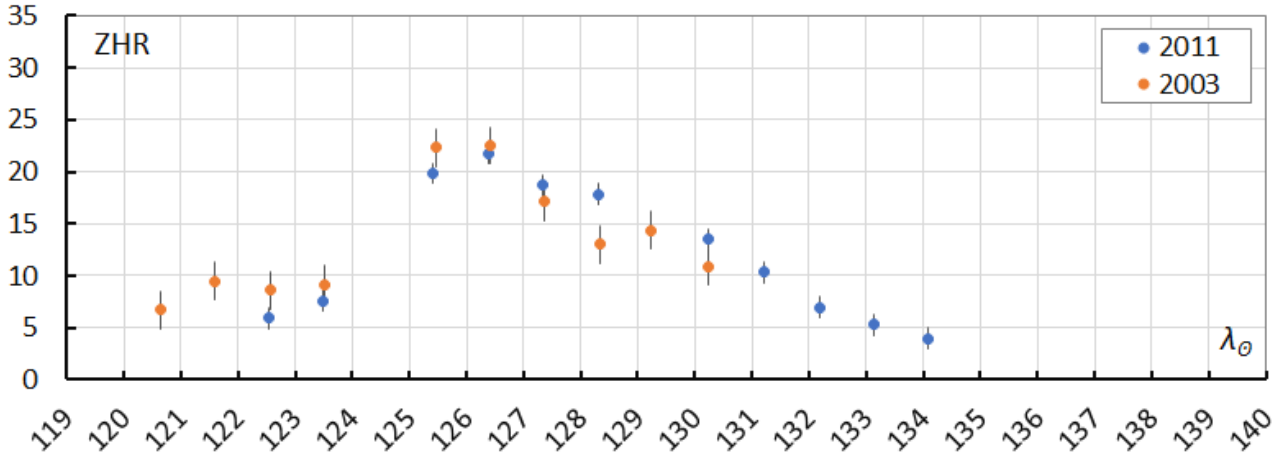

Figure 1 – Comparison of the ZHR of the Southern delta-Aquariids in 2003 and 2011.

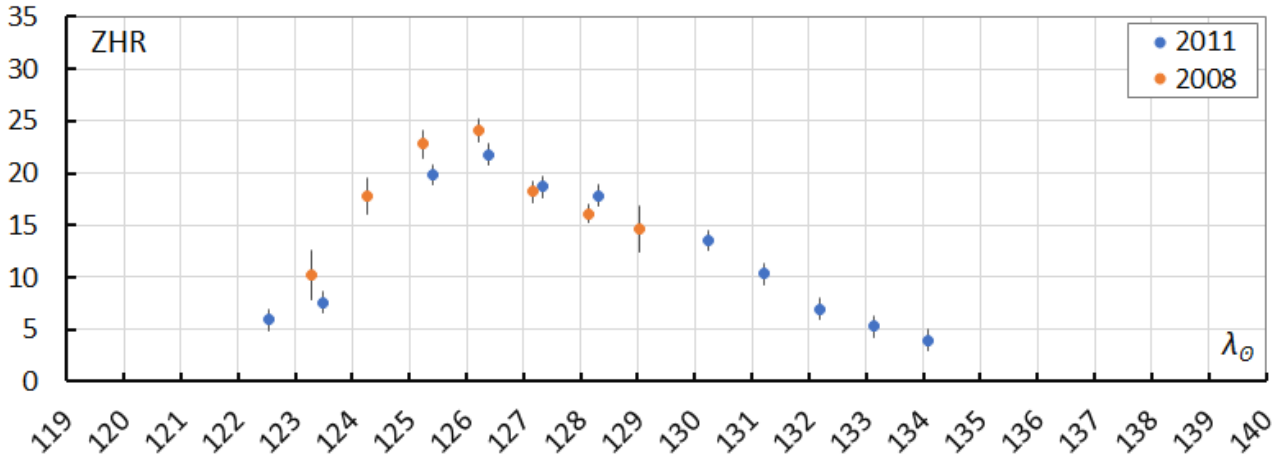

Figure 2 – Comparison of the ZHR of the Southern delta-Aquariids in 2008 and 2011.

2008–2011

As indicated in Johannink and Miskotte (2011), both ZHR and population index *r* graphs were very similar. These are therefore the best SDA data sets from after 2000. In both ZHR graphs, a rapid increase of the ZHR towards the maximum and a slower decline after the maximum are visible (*Figure 2*).

2014–2011

A striking feature of this combination is that the upward trend is quite similar, but the downward trend is much lower than in 2011 (*Figure 3*). Two possibilities: perhaps this is due to the very limited data available during this period (July 31st to August 2nd). Or it is simply a fact. Thomas Weiland observed from Crete in 2014 and obtained similar results as in 2011 (Weiland, 2016).

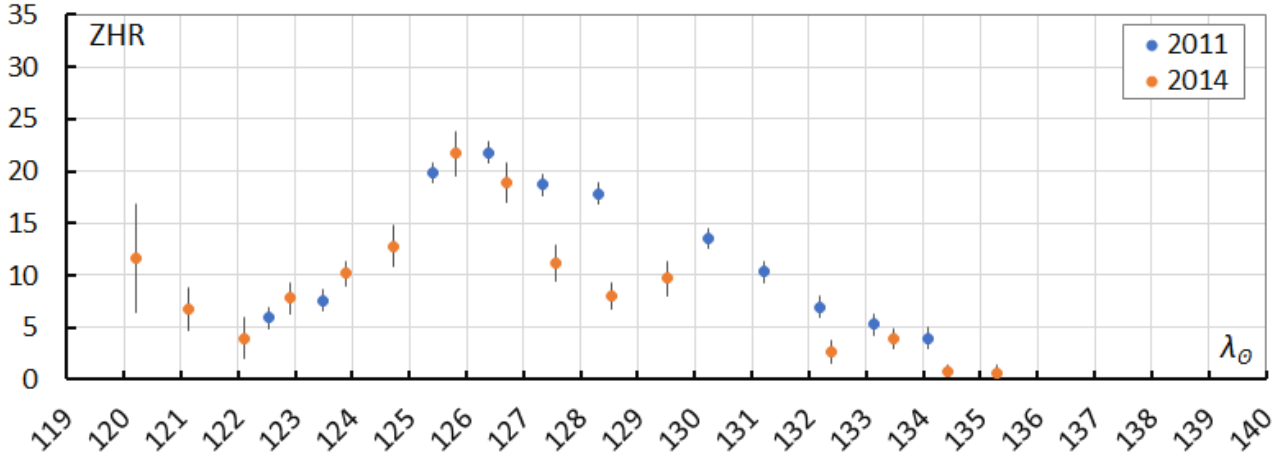

Figure 3 – Comparison of the ZHR of the Southern delta-Aquariids in 2011 and 2014.

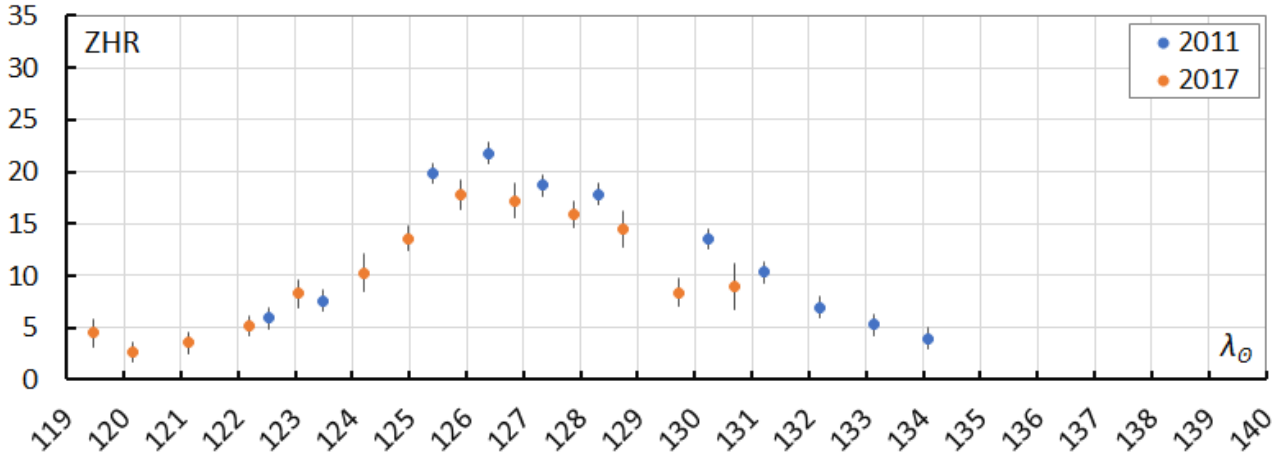

Figure 4 – Comparison of the ZHR of the Southern delta-Aquariids in 2011 and 2017.

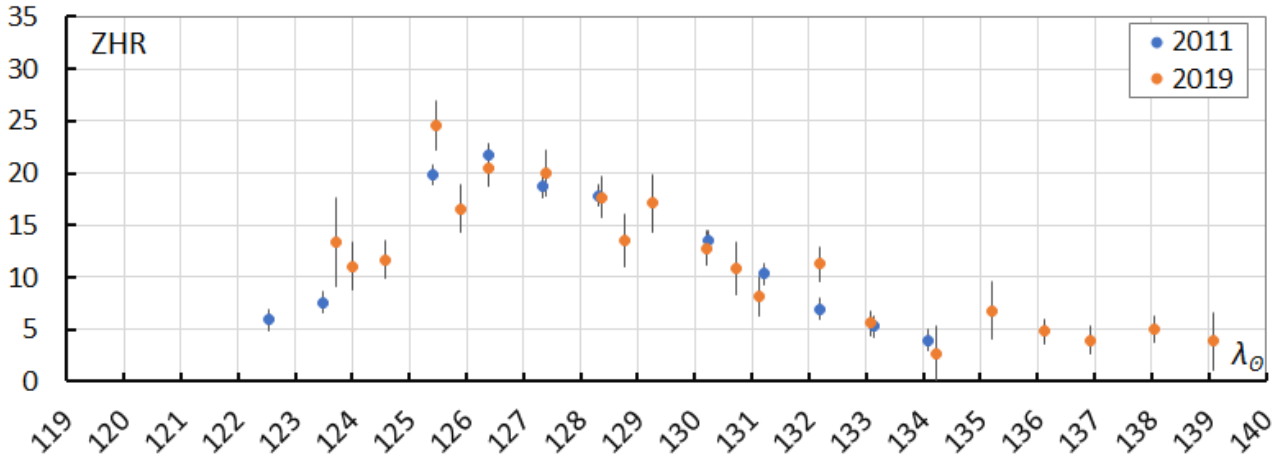

Figure 5 – Comparison of the ZHR of the Southern delta-Aquariids in 2011 and 2019.

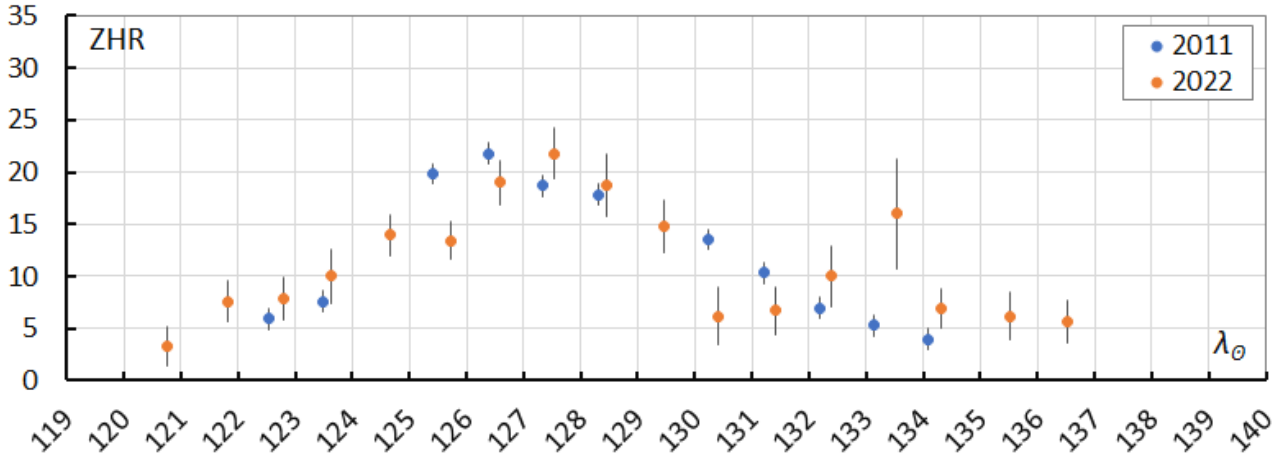

Figure 6 – Comparison of the ZHR of the Southern delta-Aquariids in 2011 and 2022.

2017–2011

The entire 2017 graph follows the 2011 pattern fairly closely, but is slightly lower across the board (*Figure 4*).

2019–2011

The 2019 graph also follows the 2011 pattern nicely: sometimes slightly lower ZHR, sometimes slightly higher (Figure 5).

2022–2011

The 2022 graph also shows a somewhat erratic pattern compared to 2011 (*Figure 6*). A striking feature is the ZHR of 16 ± 5 at $\lambda_\odot = 133.5°$ (August 6, 2022, 7.4^h UT). This data comes from an experienced observer, but with a relatively low radiant height. Comparing the graph with video data from the Global Meteor Network on the SDA-activity in 2022 (see *Figure 8* in the next chapter), there is no evidence of increased activity. Furthermore, it is notable that the maximum ZHR in 2022 ($\lambda_\odot = 127.5°$) falls later than what I find in previous years. This ZHR point is most likely due to increased SDA activity, more on this in the next section.

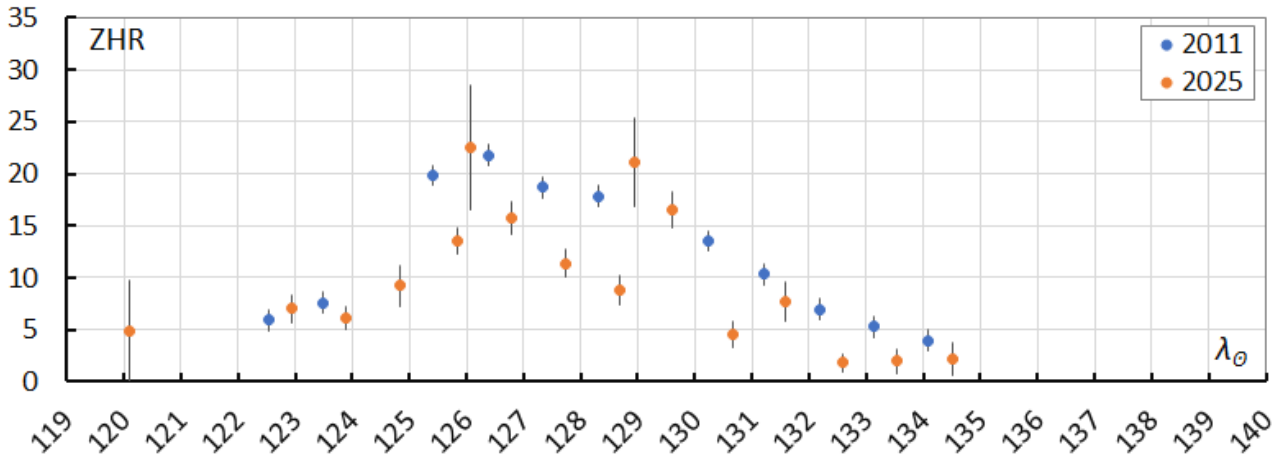

Figure 7 – Comparison of the ZHR of the Southern delta-Aquariids in 2011 and 2025.

2025–2011

Two things stand out when comparing 2025 with 2011. Almost the entire 2025 graph is 30 to 40% lower in activity than in 2011 (*Figure 7*). Before this analysis began, Thomas Weiland, observing from Crete, reported seeing roughly 30% fewer SDAs compared to previous observations from that location. What is higher than the 2011 graph are the two points at $\lambda_\odot = 129.0°$ and $\lambda_\odot = 129.6°$. These may also indicate increased SDA activity. This will be discussed in the next section.

5 Discussion of SDA activity between 2000 and 2025

Generally, we can say that the activity remains relatively consistent annually. Looking closely at the ZHR in recent years, it is noted that the declining activity sometimes lags slightly behind compared to 2008–2011. This, combined with the much lower activity in 2025, could lead to the conclusion that we're in a downward trend with the SDAs. However, there are nuances.

Clearly, 2025 is a less active SDA year. The other years are only slightly lower than 2011. The deviations sometimes overlap or are close together. The difference could also be caused by weak SDAs that are less noticeable in locations other than La Palma and Namibia (both Bortle 1 locations). This is because the skies in Namibia and La Palma are very transparent, even at much lower altitudes.

Using the correction $\gamma = 1.0$ for the radiant height instead of $\gamma = 1.4$ also produces lower ZHRs at lower radiant altitudes below 40 degrees. At 40 degrees, this is approximately 20 percent, and below that, it increases to 100% at 10 degrees. Above 40 degrees, the differences are small and within the error margins.

All of this is a good reason to go out and look for the SDAs again. It might also be useful to extend this research to the period before 2000 (IMO). The author still has a very small portion of the DMS visual paper archive, which contains numerous SDA observations from the Western Australian Meteor Section (WAMS) from 1977-1991. Unfortunately, only the SDA observations from 1977 are missing.

6 Possible SDA outbursts

While searching for possible increased SDA activity, the on-the-fly curves on the IMO website were also examined. Occasionally, something "suspicious" was found this way, but often it wasn't an outburst. An example is the 2014 On-The-Fly diagram. At solar longitude 127.703° (July 29, 2014, 04^h UT), we see a ZHR of 37 ± 10. The accompanying table shows that this value is based on only 12 SDAs. Looking at the observation in question, it was made with a limiting magnitude of 5.88 (just at the limit the author always sets for analysis) and a cloud cover factor of $F = 1.13$. This, combined with a low radiant, can produce such high values.

Date: July 28–29, 1977

In the book "Meteor Showers. An Annotated Catalogue Second Edition" written by Gary Kronk (2014), on page 148, the following is written about the Southern delta-Aquariids: "*Section director J. Wood said a maximum ZHR of about 42 was observed on July 29, 1977, with an overall observed duration from July 23 to August 14*".

Unfortunately, the data is no longer available via J. Wood or G. Kronk. Furthermore, the Moon was nearly full on July 29, 1977. Observers observing under moonlight conditions often tend to underestimate the limiting magnitude, resulting in too high ZHR's. On the other hand, Australia still has very dark and very dry locations, and the Moon will have less of a negative influence on the limiting magnitude. To investigate whether overlap in solar longitude could be found during potentially increased activity in more recent years, the following research was conducted.

The (winter) night of July 28–29, 1977, in Western Australia lasted approximately from 11^h to 22^h UT. *Table 4* shows the data for this night.

Assuming that observers will primarily observe at high radiant altitudes, observations will not have occurred until after 14^h UT, and perhaps even later due to the Moon. Observations will have been in a northeasterly to southeasterly direction. After that time, the Moon moved rapidly toward the western horizon. Based on these

assumptions, the high ZHR of 42 would have been observed somewhere between $\lambda_\odot$ = 126.664° and 126.942° (*Table 4*). This is the period when the SDA radiant rises above 30 degrees and extends until dawn. It is further unknown whether the ZHR of 42 was the average ZHR or a peak value. Unfortunately, besides counts, there are no descriptions of the observed brightnesses of the shower.

Table 4 – Situation of the night of July 28–29, 1977, in Western Australia with a 95% illuminated Moon.

Date	Time UT	$\lambda_\odot$ (°)	Radiant elevation	Moon height
29/07/1977	11.50	126.544	–8	34
29/07/1977	12.50	126.584	4	47
29/07/1977	13.50	126.624	17	59
29/07/1977	14.50	126.664	30	69
29/07/1977	15.50	126.703	42	74
29/07/1977	16.50	126.743	55	69
29/07/1977	17.50	126.783	66	59
29/07/1977	18.50	126.823	73	47
29/07/1977	19.50	126.863	71	34
29/07/1977	20.50	126.902	62	22
29/07/1977	21.50	126.942	50	10

Table 5 – Data from the author from the night of July 28–29, 2003.

Date	Period UT		*Tm*	*Teff*	*Lm*	SDA
	Start	End	UT	(*h*)		
28/07/2003	18:52	20:03	19.46	1.18	6.6	0
28/07/2003	20:06	21:05	20.59	0.98	6.7	7
28/07/2003	21:07	22:18	21.71	1.18	6.7	8
28/07/2003	22:24	23:36	23.00	1.20	6.7	14
28/07/2003	23:40	00:52	0.27	1.20	6.7	36
29/07/2003	00:54	02:01	1.46	1.12	6.6	18

July 28–29, 2003

In 2003 the author stayed at a small holiday park near Ferma, on the south coast of Crete, from July 20th to August 3rd. Observations were possible there for 10 nights (Miskotte, 2004). During the night of July 28th on 29th, the sky was crystal clear and very transparent. After 23^h30^m UT, the SDA activity increased, shortly turning into a spectacular display. Many SDAs were observed in a short period. For example, between 23^h40^m and 00^h52^m UT, 36 SDAs were observed (*Table 5*). These are numbers only observed during a normal maximum in Namibia or La Palma. In 2011, observations were again possible from Namibia around the same Solar Longitude, but no increased activity was observed (Johannink and Miskotte, 2011; 2012).

Several observers were active around the same time. Unfortunately, they didn't observe enhanced activity like the author. The reasons for this are very low limiting magnitudes and/or too far northern geographic positions. However, one observer, Roberto Haver, a well-known meteor observer from Italy, did meet the requirements[23].

Unfortunately, he didn't observe the number of SDAs as seen by the author. There is no explanation for this discrepancy. His observational data shows that he plotted the meteors. This takes over fifteen minutes of his observation data per hour. Perhaps this affects the ZHR because the author observed sometimes within seconds more SDAs. Unfortunately, there is no information from the observer in question about the observational direction or the sky's transparency. The latter certainly affects the visibility of the usually faint SDAs. A ZHR calculation based on the author's observations with an assumed population index r = 2.7, C_p = 1.2 and radiant height correction of 1 (instead of 1.4 from the old analysis) results in a maximum on 29 July 2003 at 00^h36^m UT with a ZHR 35 ± 10. See *Figure 8* and *Table 6* for further details.

Table 6 – ZHR of the Southern delta-Aquariids during the night of 28–29 July 2003.

Date	T_m	T_{eff}	Rad h.	$\lambda_\odot$ (°)	ZHR
28	22.15	0.30	26.2	125.377	10.3 ± 7.3
28	22.65	0.48	30.3	125.397	11.3 ± 5.7
28	23.19	0.58	34.0	125.419	19.0 ± 6.3
28	23.75	0.43	37.0	125.441	29.1 ± 8.8
29	0.23	0.45	38.6	125.460	29.2 ± 8.4
29	0.63	0.37	39.4	125.476	34.9 ± 10.1
29	1.00	0.48	39.5	125.491	32.2 ± 8.9
29	1.68	0.69	38.2	125.518	13.7 ± 5.2

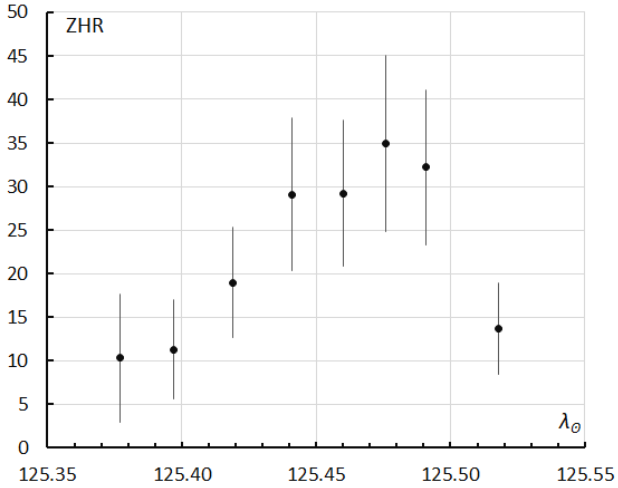

Figure 8 – The ZHR graph of the SDAs during the night of July 28–29, 2003 by Koen Miskotte, Ferma, Crete.

July, 30, 2022

While entering data from 2022, the author came across this remarkable observation by Terrence Ross[24], a prolific visual meteor observer from Texas, USA.

[23] https://www.imo.net/members/imo_vmdb/view?session_id=16221

[24] https://www.imo.net/members/imo_vmdb/view?session_id=84234

At first glance, nothing unusual seems to have happened, but looking at the actual time periods reveals unusual activity. The author contacted the observer, who was able to provide him with all basic data with shorter counting periods. The ZHR calculations were based on half-hourly counts taken every fifteen minutes. The *r*-value was chosen as 2.7 based on the totals in *Table 8*. This resulted in *Table 7* and *Figure 9*.

This very interesting observation can be interpreted as a broad 2.5-hour enhanced activity with a dip in the middle, or two outbursts in a row. The calculated maximum ZHR of 75 ± 17 is very high by SDA standards. The magnitude distribution is also striking; see *Table 8*. Unfortunately, no other observers were active during the observation to confirm this high SDA activity.

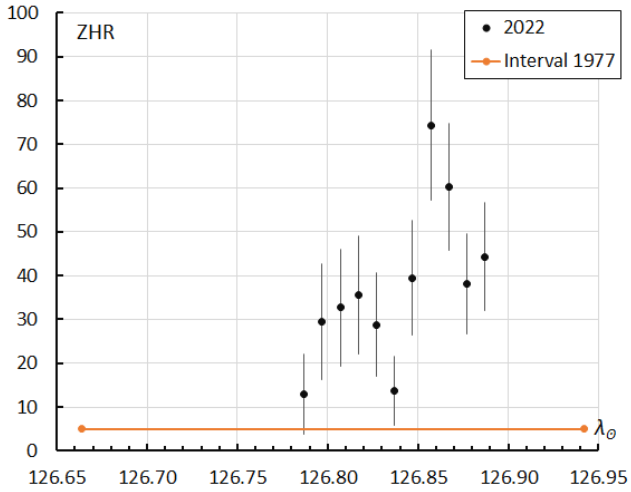

Figure 9 – The ZHR of the SDAs as observed by Terrence Ross on July 30, 2022.

Table 7 – The ZHR of the SDAs on July 30, 2022 as observed by Terrence Ross, Texas, US.

Year	Month	Day	T_m UT	T_{eff}	*Lm*	SDA	Rad h.	$\lambda_\odot$	ZHR
2022	7	30	6.28	0.46	6.29	2	24.6	126.787	12.9 ± 9.1
2022	7	30	6.53	0.46	6.29	5	27.1	126.797	29.4 ± 13.2
2022	7	30	6.78	0.46	6.29	6	29.5	126.807	32.7 ± 13.3
2022	7	30	7.03	0.46	6.29	7	31.7	126.817	35.6 ± 13.5
2022	7	30	7.28	0.46	6.29	6	33.9	126.827	28.8 ± 11.8
2022	7	30	7.53	0.46	6.29	3	35.8	126.837	13.7 ± 7.9
2022	7	30	7.78	0.46	6.29	9	37.6	126.847	39.5 ± 13.2
2022	7	30	8.03	0.46	6.37	19	39.2	126.857	74.4 ± 17.1
2022	7	30	8.28	0.46	6.44	17	40.6	126.867	60.3 ± 14.6
2022	7	30	8.53	0.46	6.44	11	41.7	126.877	38.1 ± 11.5
2022	7	30	8.78	0.46	6.44	13	42.6	126.887	44.3 ± 12.3

Table 8 – Magnitude distribution of SDAs on July 30, 2022, as observed by Terrence Ross. For the entire series of magnitude distributions, *r*[–2;+5] was 2.60 ± 0.28 and *r*[–1;+5] was 2.88 ± 0.29.

Start	End		–2	–1	0	+1	+2	+3	+4	+5	Lm	mean Mag.
30/07/2022 04:47	30/07/2022 06:39	SDA					7	5	2		6.3	2.64
30/07/2022 06:40	30/07/2022 07:52	SDA				2	4	1	4	3	6.3	3.14
30/07/2022 07:53	30/07/2022 08:14	SDA		1	1	1	3	2	4	2	6.3	2.71
30/07/2022 08:15	30/07/2022 08:46	SDA				1	6	5	2	1	6.4	2.73
30/07/2022 08:47	30/07/2022 09:00	SDA	1		1		2	3			6.4	1.57

The numbers per interval are too small to calculate a population index *r*, but *Table 8* already shows that the number of bright meteors increased during the outburst, while the number of faint meteors decreased. This is also reflected somewhat in the average magnitude. Since this is a recent observation, the author was able to search for confirmation via the GMN network. *Figure 10* is the graph from the GMN website, compiled from simultaneously recorded SDAs.

A striking feature is an extra peak above the broad peak at Solar Longitude 127°. This coincides exactly with the peak of the visual curve. You can't directly compare the graphs, of course, because the underlying data is completely different. However, the fact that both observation techniques find a peak in activity at the same time is striking. This confirms the visual peak. Also interesting is the fact that this high activity occurred in the same time window as on July 29, 1977, in Australia (see the orange horizontal line in *Figure 9*).

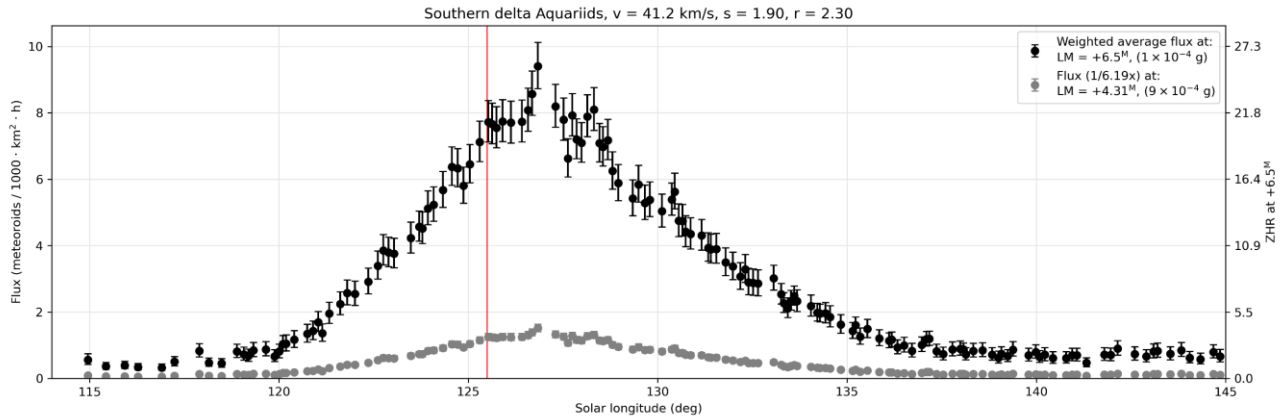

Figure 10 – ZHR/flux curve of the GMN network[25] of the SDAs from 2022 (Vida et al., 2022).

August 1–2, 2025

Another interesting observation last year: a late, possible outburst on the night of August 1–2, 2025. The possible outburst was observed from Israel by observers Anna Levin, Eini Shlomi, and Ella Ratz. They were at exactly the same location and all looked in the same direction. The results from these three observers are summarized in *Figure 11*. This was done using 20-minute counts, with the ZHR calculated every ten minutes using an assumed population index *r* of 2.70. An average ZHR was then calculated for all individual ZHRs.

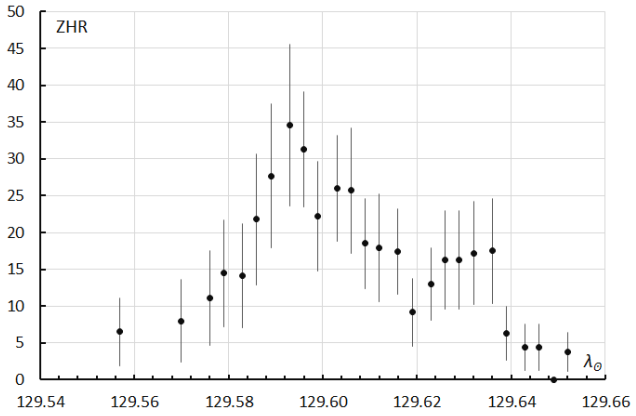

Figure 11 – ZHR profile of the SDAs during the night of August 15, 2025 based only on Israelian observations.

With a maximum ZHR of 35 ± 11 at 23^h10^m UT ($\lambda_\odot = 129.593°$), there was considerable activity. However, there was a problem. At the same time, another observer was active: Thomas Weiland, observing from Crete, Greece. His observation was not yet available on the IMO website when the first ZHR curve was generated. At the time the Israeli observers saw the outburst, Weiland observed relatively normal activity. However, right at the end of his session, he saw the ZHR surge to 20. Unfortunately, the Israeli observers had stopped by then.

Weiland's data were added, resulting in *Figure 12*. Instead of using overlapping data as in *Figure 11*, the average ZHR was determined every fifteen minutes. Interestingly, two peaks are now visible, with a ZHR of 13 near $\lambda_\odot = 129.60°$ and a ZHR 20 near 129.68°. This is slightly higher than what you would normally expect at this Solar Longitude.

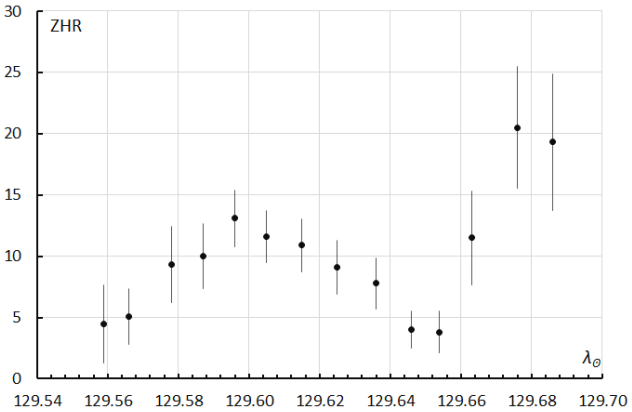

Figure 12 – ZHR profile of the SDAs during the night of 1–2 August 2025, Anna Levin, Eini Shlomi, Ella Ratz and Thomas Weiland.

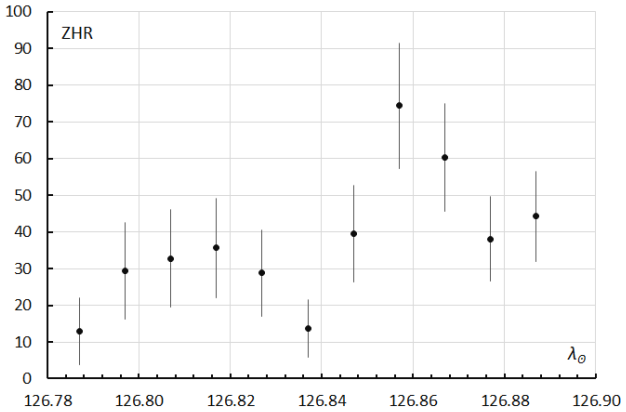

Figure 13 – ZHR distribution for the night of 30 July 2022, as observed by Terrence Ross. Compare to *Figure 12*.

So, the question is, is this increased SDA activity? Comparison with the video ZHR curve from the GMN video network indicates a peak in activity around $\lambda_\odot = 129.5°$ during this night with a ZHR of 17 (*Figure 14*).

[25] https://globalmeteornetwork.org/flux/plots/

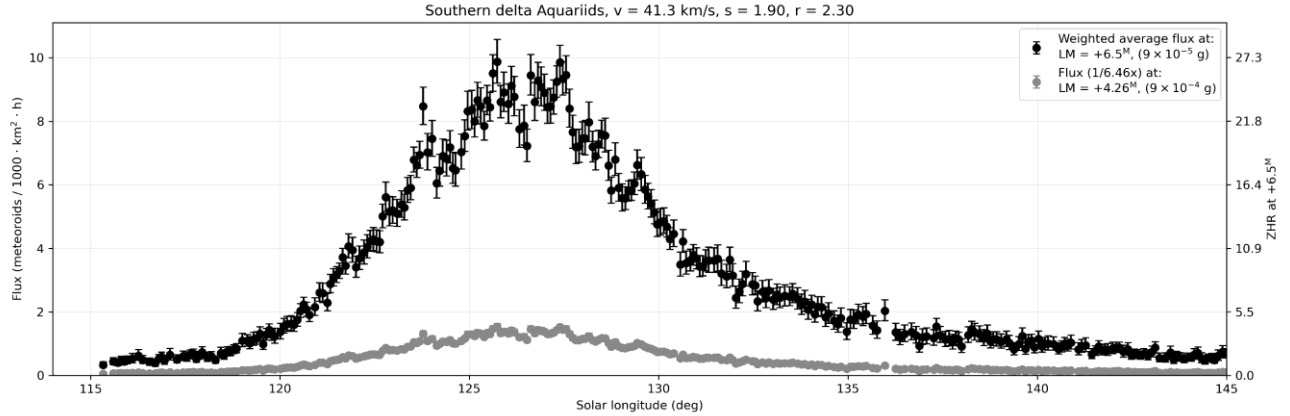

Figure 14 – ZHR of the SDAs in 2025 based on GMN multi-station video data (Vida et al, 2022). Note the subpeak around Solar Longitude 129.0°.

Figure 15 – The Israelian meteor observers in 2025: from left to right Omri Katz, Noga Karni, Anna Levin, Shlomi Eini, Ella Ratz and Ido Braun. It is thanks to groups and individual observers that visual analyses with useful results can still be made. This article is therefore a tribute to the visual meteor observer. Visual meteor observations are the most demanding but also the most satisfying observation method. Watching meteors live under a brilliant clear sky is so much fun!

Again, these are two completely different observation techniques. But the fact that both techniques find a peak around the same time is interesting.

Another striking detail: if we look at the progression of the graphs in *Figure 12* (2025) and *Figure 13* (2022), they show a similarity: a weak peak followed by a dip and a higher peak. The width of both graphs also corresponds quite well, with about 0.11° in 2025 (starting from ZHR 10) and 0.12° (but possibly a bit longer) in 2022. The Solar Longitude at which both phenomena occurred is quite different. The author has no further explanation for this.

7 Conclusions

The SDA meteor shower appears to remain stable over the period 2000–2022, but 2025 shows significantly lower activity. Looking at 2017, 2019, and 2022, there could have been also a slight downward trend, but this is more likely due to the differences in observational locations and the chosen correction for the radiant height. Furthermore, the SDAs appears to occasionally show increased activity (or strong subpeaks). The 2022 outburst stands out with high ZHR values. The 2003 outburst is unconfirmed, and 2025 could also have been a subpeak. A surprising similarity is that the peaks from 2022 and 2025 are actually double peaks. It is also clear that geographically southern locations provide a good indication of SDA activity. Observations made from more northern locations often show significant differences compared to observations made from southern locations.

Acknowledgments

I am sincerely grateful to all observers who have ever observed SDAs for their contributions. The list is too long to publish. However, I would like to acknowledge the observers who traveled specifically for this meteor shower or with whom I exchanged ideas about the results: *Jürgen Rendtel, Anna Levin, Thomas Weiland, Kai Frode Gaarder, Terrence Ross, Peter van Leuteren, Klaas Jobse, Carl Johannink, Michel Vandeputte, Felix Bettonvil, Casper ter Kuile*, and *Pierre Martin*.

Figure 16 – Composite image of the Milky Way taken at the Hakos Observatory in Namibia by the author in July 2011. The photo was taken with a Canon 40D, a Canon EF 15 mm F 2.8 lens mounted on an AstroTrac tracking mount. Three Capricornids and two Southern delta-Aquariids can be seen.

References

Heis E., Schmidt J. F. J. (1867). "On Meteors in the Southern Hemisphere". Mannheim: J. Schneider, page 15.

Jenniskens P. (2023). Atlas of Earth's Meteor Showers, Elsevier, page 71.

Johannink C., Miskotte K., Jobse K. (2008a). "Resultaten van de Aquariiden-campagne op La Palma juli 2008." *Radiant*, **30**, 98–107.

Johannink C., Miskotte K., Jobse K., Vandeputte M., van Leuteren P. (2008b). "Results of the Aquariid expedition to La Palma, July 2008". *WGN, Journal of the International Meteor Organization*, **36**, 139–146.

Johannink C., Miskotte K. (2011). "Resultaten van de Aquariiden-campagne in Namibië juli 2011". *Radiant*, **33**, 103–107.

Johannink C., Miskotte K. (2012). "Results for the Aquariid-expedition to Namibia, July 2011". *WGN,*

Journal of the International Meteor Organization, **40**, 65–68.

Kronk G. (2014). Meteor Showers. An Annotated Catalog Second edition. Springer, page142.

Lindblad B.A. (1971). "A computerized stream search among 2401 photographic meteor orbits". *Smitsonian Contriubutions to Astrophysics*, **12**, 14–24.

Miskotte K. (2001). "Meteoren waarnemen vanaf Chios eiland". *Radiant*, **23**, 80–83.

Miskotte K. (2004). "(Meteoren) waarnemen op Kreta". *Zenit*, **31**, 375–376.

Van Leuteren P. (2008). "De Zuidelijke delta-Aquariiden vanuit La Palma". *Radiant*, **30**, 86–97.

Van Leuteren P. (2011). "Namibië, land van natuurlijke duisternis". *Radiant*, **33**, 87–98.

Vida D., Blaauw Erskine R. C., Brown P. G., Kambulow J., Campbell-Brown M., Mazur M. J. (2022). "Computing optical meteor flux using global meteor network data". *Monthly Notices of the Royal Astronomical Society*, **515**, 2322–2339.

Weiland T. (2016). "2014 Southern δ-Aquariid observing campaign - carried out from Crete". *Proceedings of the International Meteor Conference*, Egmond, the Netherlands, 2-5 June 2016, Eds.: Roggemans, A.; Roggemans, P., ISBN 978-2-87355-030-1, pages 338–340.

February 2026 CARMELO report

Mariasole Maglione[1], **Lorenzo Barbieri**[2]

[1] **GAV, Gruppo Astrofili Vicentini, Italy**
mariasole@astrofilivicentini.it

[2] **CARMELO network and AAB: Associazione Astrofili Bolognesi, Italy**
carmelometeor@gmail.com

The CARMELO network (Cheap Amateur Radio Meteor Echoes LOgger) is a collaboration of SDR radio receivers aimed at detecting meteor echoes. This report presents the data for February 2026.

1 Introduction

February is one of the least active months in terms of meteor showers, with no particularly significant showers occurring. We therefore took the opportunity to qualitatively analyze the diurnal variation in the number of meteors intercepted by Earth.

2 Methods

The CARMELO network consists of SDR radio receivers. In them, a microprocessor (Raspberry) performs three functions simultaneously:

- By driving a dongle, it tunes the frequency on which the transmitter transmits and tunes like a radio, samples the radio signal and through the FFT (Fast Fourier Transform) measures frequency and received power.
- By analyzing the received data for each packet, it detects meteor echoes and discards false positives and interference.
- It compiles a file containing the event log and sends it to a server.

The data are all generated by the same standard, and are therefore homogeneous and comparable. A single receiver can be assembled with a few devices whose total current cost is about 210 euros.

To participate in the network read the instructions on this page[26].

3 February data

In the plots that follow, all available at this page[27], the abscissae represent time, which is expressed in UT (Universal Time) or in solar longitude (Solar Long), and the ordinates represent the hourly rate, calculated as the total number of events recorded by the network in an hour divided by the number of operating receivers.

In *Figure 1*, the trend of signals detected by the receivers for the month of February.

4 The diurnal variation of meteors

One of the most obvious effects in meteor observations is the diurnal variation in the frequency of recorded events. The number of meteors observed is not constant throughout the day, but shows a systematic trend with a maximum around 6 a.m. and a minimum around 6 p.m.

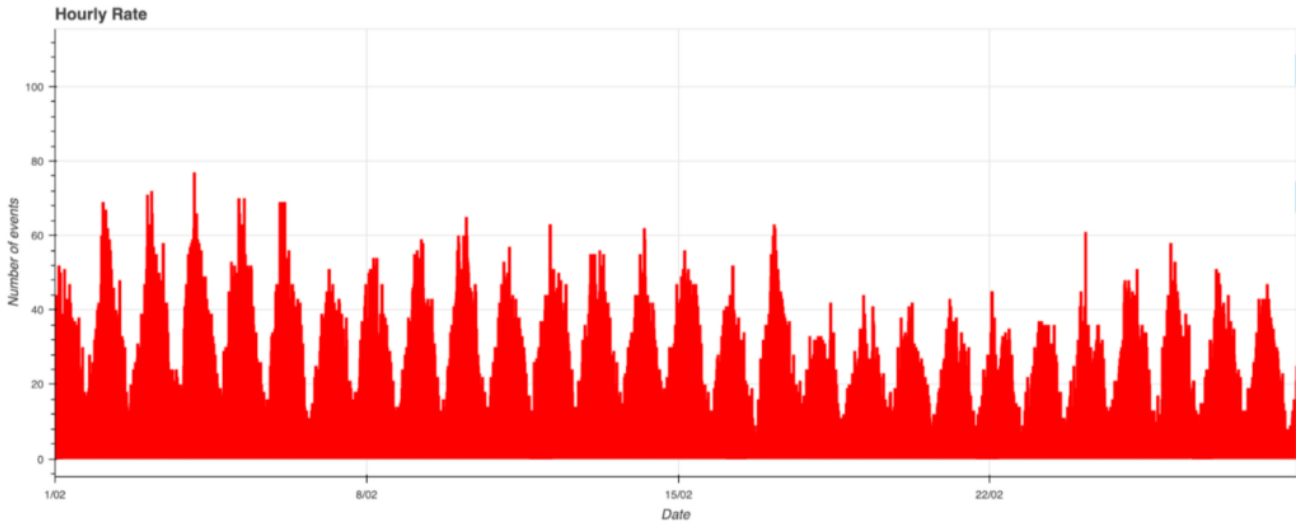

Figure 1 – February 2026 data trend.

[26] http://www.astrofiliabologna.it/about_carmelo

[27] http://www.astrofiliabologna.it/graficocarmelohr

The daily variation in meteor frequency is a direct consequence of the Earth's motion through space. This effect was first explained in 1867 by Giovanni Virginio Schiaparelli (1867) in his work on the astronomical theory of shooting stars. At that time, it was not yet universally accepted that meteors were a cosmic phenomenon: many astronomers believed them to be atmospheric events. With an extraordinary combination of observations and geometric reasoning, Schiaparelli demonstrated instead that they are bodies coming from space and that their apparent distribution in the sky depends on the motion of the Earth.

In his study, he showed how the number of meteors observed depends on the direction in which the Earth moves in space, identifying a fundamental point in the sky: the apex of the Earth's motion. The apex is the point in the sky toward which the Earth moves in its orbit around the Sun. In other words, it represents the "frontal" direction of the Earth's orbital motion.

As the Earth travels along its orbit at approximately 29 km/s, it continuously passes through interplanetary space, encountering dust particles and small cometary debris. These particles, upon entering the Earth's atmosphere, produce meteors.

The phenomenon of daily variation in the frequency of recorded events can be understood with a simple analogy:

- An aircraft flying at high-speed intercepts objects approaching head-on more easily;
- It will be much more difficult for it to be hit by objects approaching from behind, because these must be faster than the aircraft itself in order to catch up with it.

The same applies to Earth:

- In front, in the direction of the apex, we intercept meteors of all speeds;
- Behind, in the opposite direction (antapex), we can only intercept those that are faster than Earth.

Due to the Earth's rotation, the direction of the apex changes continuously relative to the horizon of an observer on the Earth's surface. Schiaparelli demonstrated that the frequency of intercepted meteors depends on the height of the apex above the horizon. When the apex is high in the sky, the Earth intercepts a greater number of meteoroids; when it is below the horizon, the frequency decreases.

In his work, he derived a mathematical relationship that describes precisely this periodic variation in the observed frequency. In particular, he showed that the maximum occurs when the apex culminates in the observer's sky, which happens at around six in the morning, while the minimum occurs at around six in the evening (Schiaparelli, 1867).

It is therefore a true daily sine wave, determined exclusively by the geometry of the Earth's motion:

- At around 6 a.m., the observer is facing the direction of the Earth's motion: that is, looking towards the apex. In this case, the Earth "sweeps" the space in front of it and intercepts the maximum number of meteoroids.
- At around 6 p.m., the observer is on the opposite side of the Earth from the direction of orbital motion: they are therefore looking towards the antapex. In this configuration, only the fastest meteors are intercepted.
- At midnight and midday, the observer is in an intermediate position and the number of meteors observed is average.

This behavior is illustrated in the diagram in *Figure 2*.

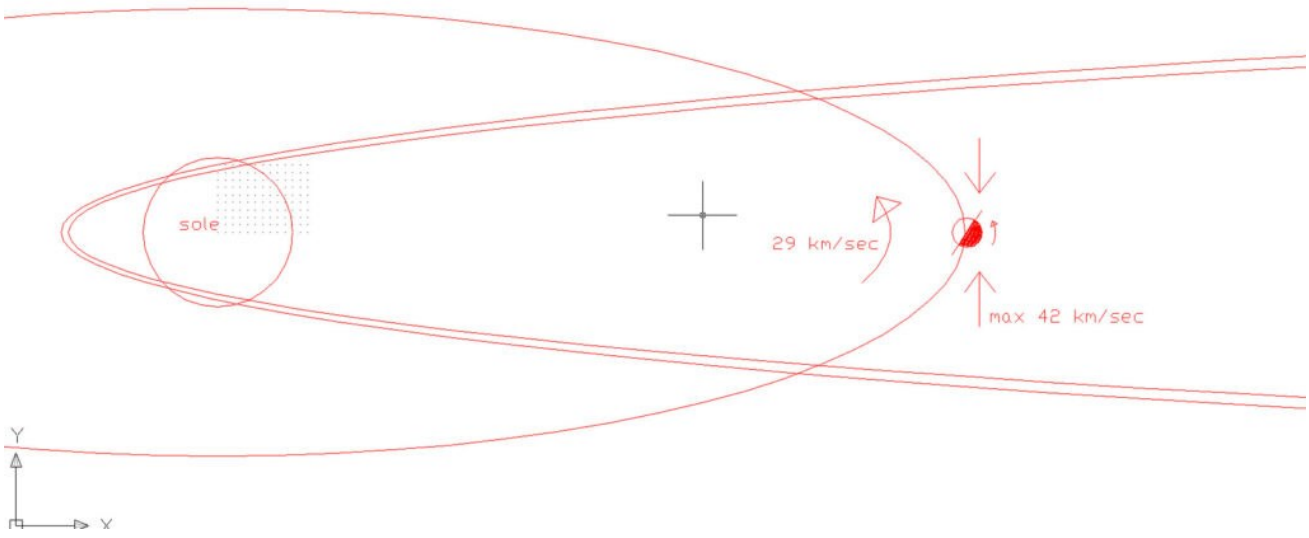

Figure 2 – Schematic view of the Earth's orbit around the Sun, with its inclined axis of rotation, and the direction of the apex and antapex.

Modern radio observations of meteors allow these theoretical predictions to be verified with great precision. The Hourly Rate (HR) graph obtained from the CARMELO network (in *Figure 3*) clearly shows a wave pattern with a period of 24 hours.

The number of meteors recorded peaks in the morning, around 6 a.m. local time, and drops to a minimum in the evening, around 6 p.m. This pattern corresponds exactly to the theoretical prediction made by Schiaparelli over a century and a half ago.

However, the meteor frequency graph is not the only interesting piece of data. The second graph (also in *Figure 3*) shows the average power of the radio signals from the detected meteors. Since the energy of the meteor event depends on the mass and speed squared of the meteoroid, this parameter can be considered a good indication of the average speed of the observed meteors.

What can be observed in the CARMELO data is:

- When the number of meteors is at its maximum (in the morning), the average power is lower;
- When the number of meteors is at its minimum (in the evening), the average power is higher.

The two graphs are therefore in counterphase. This behavior is perfectly consistent with the theory:

- In the morning, looking towards the apex, we observe meteors of all speeds: both slow and fast;
- In the evening, looking towards the antapex, we can only intercept those faster than the Earth, i.e., the most energetic ones.

Consequently, even though the total number of meteors decreases, the average speed of the observed events increases, producing an increase in the average power detected.

The comparison between the two graphs therefore provides clear observational verification of the theory proposed by Schiaparelli in 1867. The daily variation in the frequency of meteors and the opposite variation in their average energy are both direct consequences of the geometry of the Earth's motion in space.

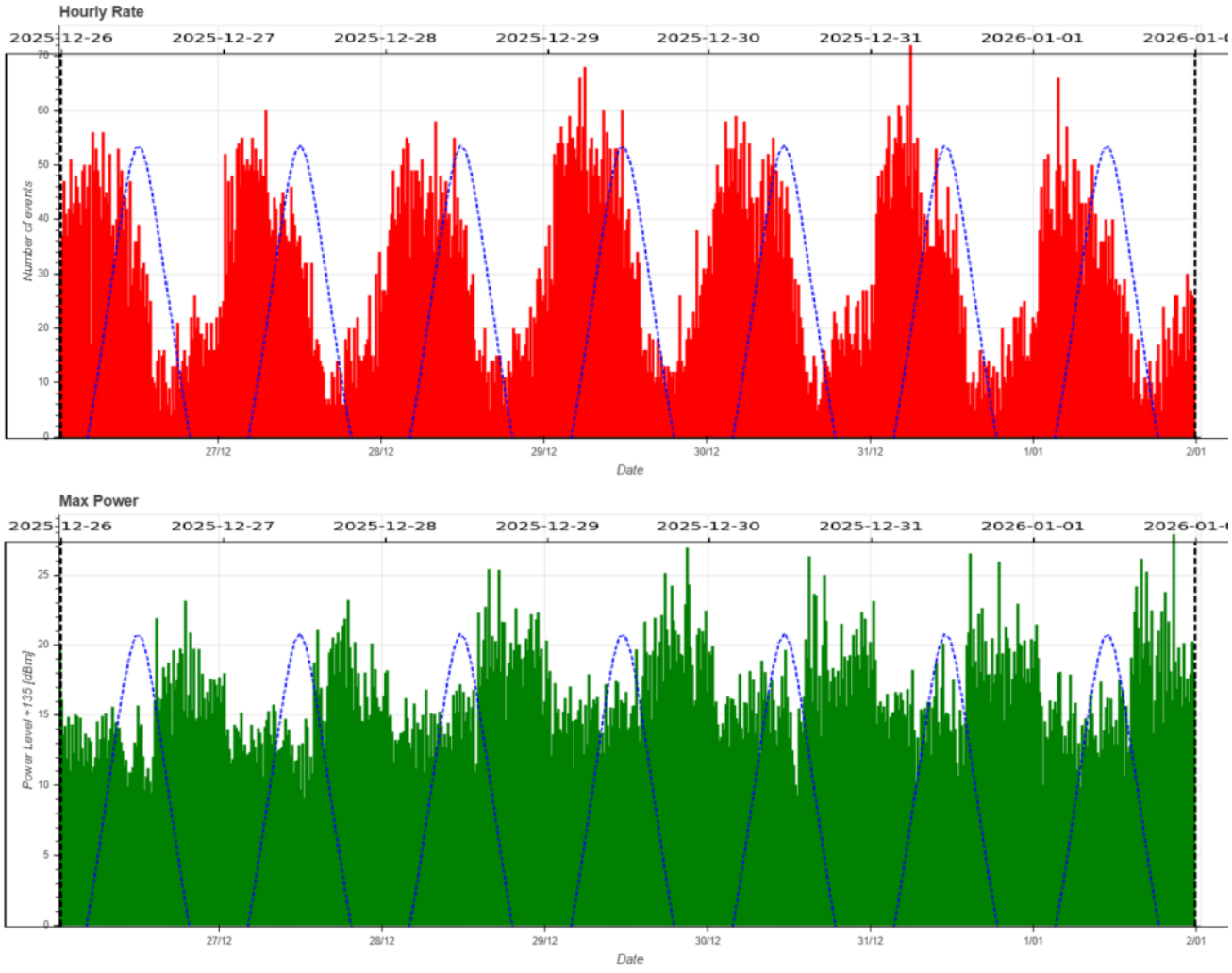

Figure 3 – Hourly Rate and average power of events recorded by the CARMELO network between the end of December 2025 and the beginning of January 2026.

It is fascinating to observe how a theoretical argument developed with little observational data in the 19th century is now precisely confirmed by the automatic and continuous observations of a radio network such as CARMELO.

5 The CARMELO network

The network currently consists of 16 receivers located in Italy, the UK, Switzerland and the USA. The European receivers are tuned to the Graves radar station frequency in France, which is 143.050 MHz. Participating in the network are:

- Lorenzo Barbieri, Budrio (BO) ITA;
- Associazione Astrofili Bolognesi, Bologna ITA;
- Associazione Astrofili Bolognesi, Medelana (BO) ITA;
- Paolo Fontana, Castenaso (BO) ITA;
- Paolo Fontana, Belluno (BL) ITA;
- Associazione Astrofili Pisani, Orciatico (PI) ITA;
- Gruppo Astrofili Persicetani, San Giovanni in Persiceto (BO) ITA;
- Roberto Nesci, Foligno (PG) ITA;
- MarSEC, Marana di Crespadoro (VI) ITA;
- Gruppo Astrofili Vicentini, Arcugnano (VI) ITA;
- Associazione Ravennate Astrofili Rheyta, Ravenna (RA) ITA;
- Mike German a Hayfield, Derbyshire UK;
- Mike Otte, Pearl City, Illinois USA.
- Yuri Malagutti, Comano (TI) CH.
- Leslie Fry, Trawscoed Ceredigion, Wales UK
- Brian Coleman, Redenham Observatory, Andover, England UK

The authors' hope is that the network can expand both quantitatively and geographically, thus allowing the production of better-quality data.

References

Schiaparelli Giovanni V. (1867). Teoria astronomica delle stelle cadenti. Stamperia reale Firenze.

March 2026 CARMELO report

Mariasole Maglione[1], Lorenzo Barbieri[2], Gaetano Brando[2], Silvana Sarto[2], Giovanni Furlato[3] and William Rivato[3]

[1] **CARMELO network andGAV: Gruppo Astrofili Vicentini, Italy**
mariasole@astrofilivicentini.it

[2] **CARMELO network and AAB: Associazione Astrofili Bolognesi, Italy**
carmelometeor@gmail.com

[3] **CARMELO network and MarSEC, Italy**

The CARMELO network (Cheap Amateur Radio Meteor Echoes LOgger) is a collaboration of SDR radio receivers aimed at detecting meteor echoes. This report presents the data for March 2026.

1 Introduction

Like February, March is also a quiet month for meteor showers, and, as expected, it did not feature any particularly notable showers. For this reason, we took the opportunity to delve deeper into the topic of meteor velocities in relation to the Earth's position during its rotation.

2 Methods

The CARMELO network consists of SDR radio receivers. In them, a microprocessor (Raspberry) performs three functions simultaneously:

- By driving a dongle, it tunes the frequency on which the transmitter transmits and tunes like a radio, samples the radio signal and through the FFT (Fast Fourier Transform) measures frequency and received power.
- By analyzing the received data for each packet, it detects meteor echoes and discards false positives and interference.
- It compiles a file containing the event log and sends it to a server.

The data are all generated by the same standard, and are therefore homogeneous and comparable. A single receiver can be assembled with a few devices whose total current cost is about 210 euros.

To participate in the network read the instructions on this page[28].

3 March data

In the plots that follow, all available at this page[29], the abscissae represent time, which is expressed in UT (Universal Time) or in solar longitude (Solar Long), and the ordinates represent the hourly rate, calculated as the total number of events recorded by the network in an hour divided by the number of operating receivers. The time resolution is 15 minutes.

In *Figure 1*, the trend of signals detected by the receivers for the month of March.

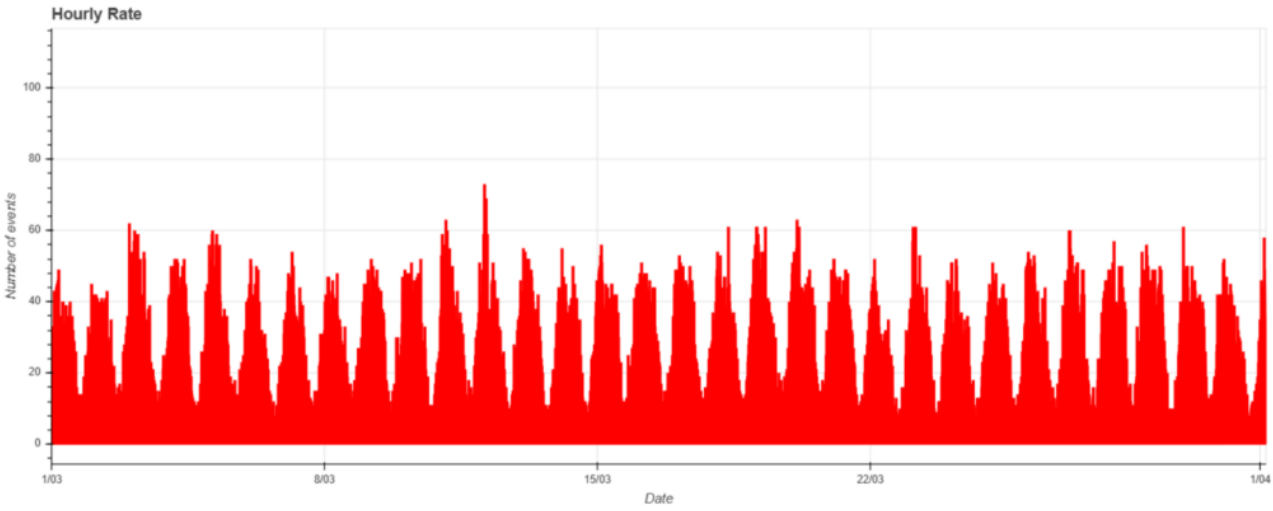

Figure 1 – March 2026 data trend.

[28] http://www.astrofiliabologna.it/about_carmelo

[29] http://www.astrofiliabologna.it/graficocarmelohr

4 Analysis of radio echo profiles and meteor velocities

In the previous report (Maglione and Barbieri, 2026), we analyzed the variation in the average velocity of meteors throughout the day using statistics on radio power recorded by the CARMELo network. In that analysis, we observed how the graph of the average echo power – which is partly determined by the kinetic energy of the meteoroids – shows an opposite trend (out-of-phase) compared to the graph of the number of events, providing an indication of how speeds vary as a function of local time.

This month, we're approaching the same topic from a different angle, no longer using a measurement such as power, but instead analyzing the profile of radio echoes – specifically, the signal's rise time.

As is well known, the radar echo of a meteor is produced by the ionization of the atmosphere along the meteoroid's trajectory. The passage of the particle generates a plasma cylinder consisting of free ion-electron pairs. The reflection of the radio signal off this ionized cylinder occurs according to the laws of specular reflection of electromagnetic waves: the angle of incidence equals the angle of reflection.

A fundamental consequence of this geometry is that the observed echo originates essentially from a single point along the meteoroid's trajectory, known as the "point of specular reflection" or "point of closest approach" *P*. This is the point at which the total path of the signal (from the transmitter to the ionized cylinder and from there to the receiver) is as short as possible.

As a first approximation, therefore, the entire observational phenomenon can be described by considering only a region around this point.

Let us now consider a segment of the meteor's trajectory centered at point *P* (see *Figure 2*). As we move away from *P*, the optical path length of the signal increases progressively, thereby increasing the signal delay and altering the phase of the received wave. The points at which this phase delay reaches $\lambda/4$ define the so-called "first Fresnel zone", which represents the effective region of constructive interference of the reflected signal.

The characteristic length of this region, in the case of backscatter observations, is given by (Belkovich and Wislez, 2006):

$$L = \sqrt{2d\lambda} \quad (1)$$

where:

- d is the distance between the transmitter and the meteor;
- λ is the wavelength of the transmitted and reflected radio signal.

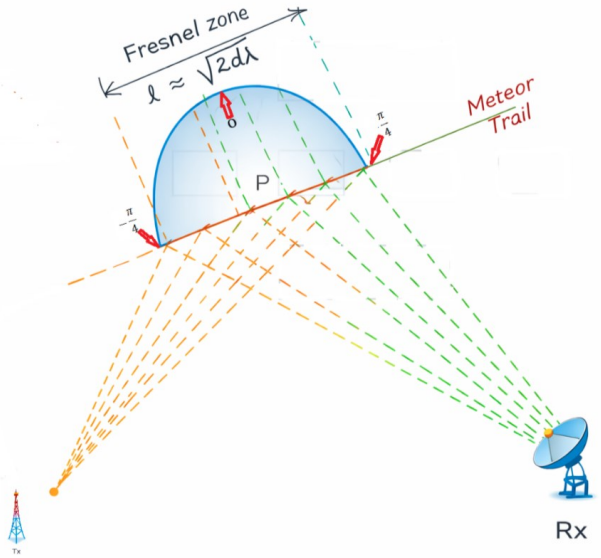

Figure 2 – Schematic representation of a Fresnel zone.

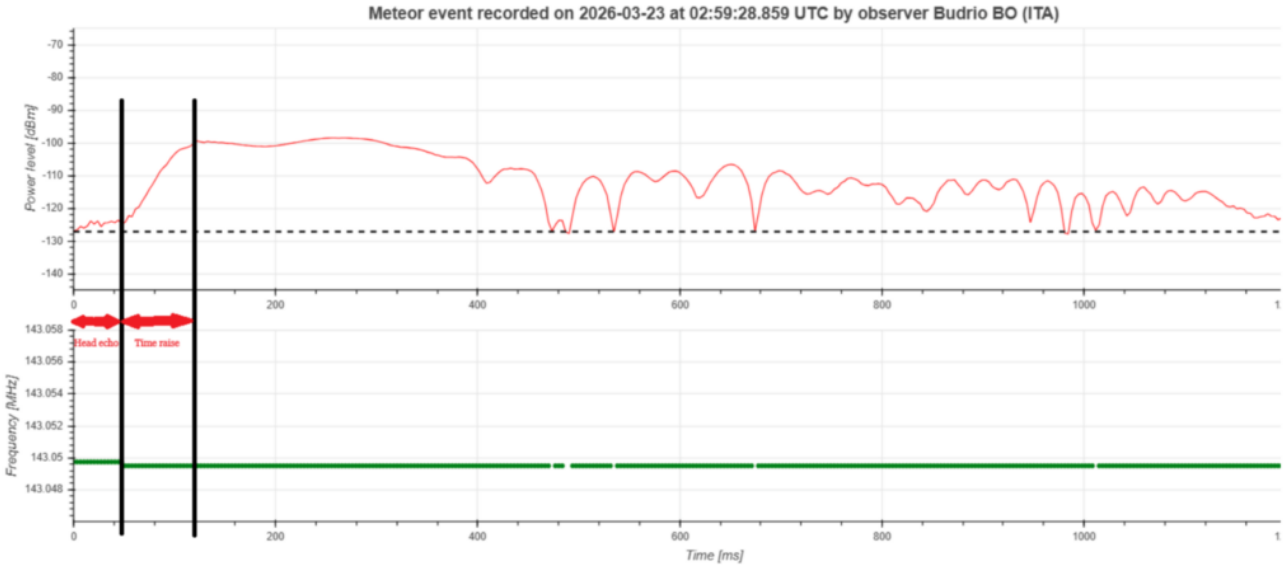

Figure 3 – Evaluation of the rise time on the signal profile of a radio meteor.

As the meteoroid passes through the first Fresnel zone, it progressively generates ionization, causing the signal to rise from zero to the maximum observed echo. The time taken for this passage is referred to as the rise time (the time it takes for the signal to rise).

Assuming, as a first approximation, that the meteoroid moves in a uniform straight line, this time is related to the length L and the velocity v by an equation of the form (2):

$$t = \frac{L}{v} \qquad (2)$$

It follows that:

- Faster meteors have a shorter rise time;
- Slower meteors have a longer rise time.

In the previous bulletin (Maglione and Barbieri, 2026), we explained how the speed at which meteors enter Earth's atmosphere depends on the combination of their speed in interplanetary space and Earth's orbital speed. In particular, meteors observed around 6 a.m. (local time) have velocities resulting from the sum of their speed in space (in the Solar System reference frame) and that of Earth, since the observer is facing the direction of Earth's orbital motion. Conversely, around 6 p.m. (local time), meteors have velocities resulting from the difference between their own velocity and that of Earth, since the observer is looking in the direction opposite to Earth's orbital motion.

Based on what we have just discussed, we therefore expect that:

- In the morning, the rise time will be shorter on average;
- In the evening, the rise time will be longer on average.

Of course, sporadic meteors arrive from random directions and at different intrinsic velocities. However, with a sufficiently large sample size, the statistical effects related to the geometry of Earth's motion should become apparent.

To verify this prediction, we analyzed a database of events recorded by the CARMELo network over a period of more than one month, between January and February 2026.

To minimize the influence of meteor showers and focus on sporadic meteors:

- The first few days of January, dominated by the Quadrantids, were excluded;
- Only events with a signal-to-noise ratio greater than 20 dB were selected, in order to determine the echo's temporal profile with greater precision;
- The data were divided into two groups:
    - Events recorded during the two hours around 6 a.m. local time.
    - Events recorded during the two hours around 6 p.m. local time.

A total of 405 meteors were observed in the morning and 262 in the evening. The rise time distributions obtained for the two time intervals are shown in *Figure 4* and *Figure 5*.

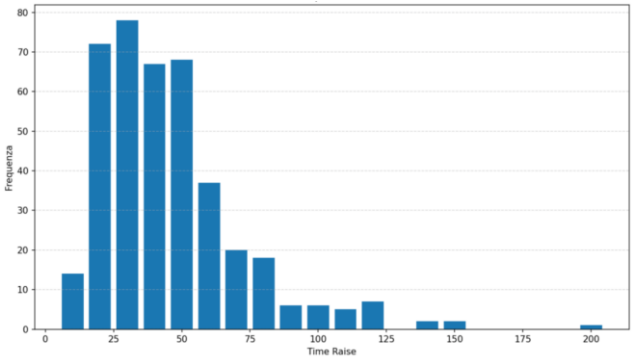

Figure 4 – Distribution of rise times around 6 a.m. local time.

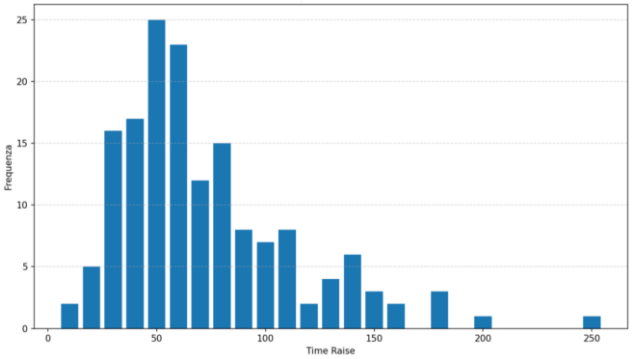

Figure 5 – Distribution of rise times around 6 p.m. local time.

The analysis clearly shows that:

- The morning distribution is skewed toward shorter rise times;
- The evening distribution shows a higher proportion of longer rise times.

This analysis confirms, using a completely independent approach, the results obtained in the previous bulletin:

- The average speed of the observed meteors varies throughout the day;
- This variation is a direct consequence of the geometry of the Earth's motion.

We can also attempt to verify whether the order of magnitude of the rise time measured by CARMELo is consistent with the velocities of the meteors. To this end, we use (1) to estimate the dimensions of the first Fresnel zone. We consider the equation valid also for a forward-scatter system and apply it to the Graves–Italy geometry, taking into account the frequency of the Graves transmitter.

Let us therefore assume that $d = 600000$ and $\lambda = 2$ (meters): from (1) we obtain a Fresnel zone length L of approximately 1500 meters.

Applying (2) for a time rise of 30 ms – such as those predominant in the morning – we find a value slightly above 50000 m/s, a value that is nearly halved for rise times of 50 ms, such as those predominant in the evening. These values are perfectly consistent with the order of magnitude of meteor velocities relative to Earth, which, as we know, range from 16 to 72 km/s.

This demonstrates that the CARMELo network does not merely count events, but is capable of deriving physical information about meteors by analyzing the shape of radio echoes in detail. The fact that a time-dependent parameter such as the rise time – which is directly linked to the meteoroid's velocity – exhibits the theoretically predicted trend provides further observational confirmation of the dynamics of meteor impacts.

5 The CARMELO network

The network currently consists of 15 receivers located in Italy, the UK, Switzerland and the USA. The European receivers are tuned to the Graves radar station frequency in France, which is 143.050 MHz. Participating in the network are:

- Lorenzo Barbieri, Budrio (BO) ITA;
- Associazione Astrofili Bolognesi, Bologna ITA;
- Associazione Astrofili Bolognesi, Medelana (BO) ITA;
- Paolo Fontana, Castenaso (BO) ITA;
- Associazione Astrofili Pisani, Orciatico (PI) ITA;
- Gruppo Astrofili Persicetani, San Giovanni in Persiceto (BO) ITA;
- Roberto Nesci, Foligno (PG) ITA;
- MarSEC, Marana di Crespadoro (VI) ITA;
- Gruppo Astrofili Vicentini, Arcugnano (VI) ITA;
- Associazione Ravennate Astrofili Rheyta, Ravenna (RA) ITA;
- Mike German a Hayfield, Derbyshire UK;
- Mike Otte, Pearl City, Illinois USA.
- Yuri Malagutti, Comano (TI) CH.
- Leslie Fry, Trawscoed Ceredigion, Wales UK
- Brian Coleman, Redenham Observatory, Andover, England UK

The authors' hope is that the network can expand both quantitatively and geographically, thus allowing the production of better-quality data.

References

Belkovich O.I., Wislez J.M. (2006). "The physics of backscattering of radio waves from ionized meteor trails". *Proceedings of radio meteor school 2005*, 27–33.

Maglione M., Barbieri L. (2026). "Bollettino delle radiometeore di febbraio 2026".

Radio meteors February 2026

Felix Verbelen

Vereniging voor Sterrenkunde & Volkssterrenwacht MIRA, Grimbergen, Belgium
felix.verbelen@gmail.com

An overview of the radio observations during February is given.

1 Introduction

The graphs show both the daily totals (*Figure 1 and 2*) and the hourly numbers (*Figure 3 and 4*) of "all" reflections counted automatically, and of manually counted "overdense" reflections, overdense reflections longer than 10 seconds and longer than 1 minute, as observed here at Kampenhout (BE) on the frequency of our VVS-beacon (49.99 MHz) during the month of February 2026.

The hourly numbers, for echoes shorter than 1 minute, are weighted averages derived from:

$$N(h) = \frac{n(h-1)}{4} + \frac{n(h)}{2} + \frac{n(h+1)}{4}$$

Local interference and unidentified noise remained weak, and no lightning activity was recorded.

As anticipated, meteor activity remained low without significant peaks, except for a marginal increase around February 10-11 and February 19.

Activity spiked briefly on a few other days for at most a few hours; however, the lack of sufficient measurable head reflections prevented the clear identification of any specific showers.

This month, only two reflections exceeding one minute were recorded. A selection of some notable or strong reflections is shown in *Figures 5 to 14*. Many more are available upon request.

In addition to the usual graphs, you will also find the raw counts in cvs-format[30] from which the graphs are derived. The table contains the following columns: day of the month, hour of the day, day + decimals, solar longitude (epoch J2000), counts of "all" reflections, overdense reflections, reflections longer than 10 seconds and reflections longer than 1 minute, the numbers being the observed reflections of the past hour.

[30] https://www.emeteornews.net/wp-content/uploads/2026/03/202602_49990_FV_rawcounts.csv

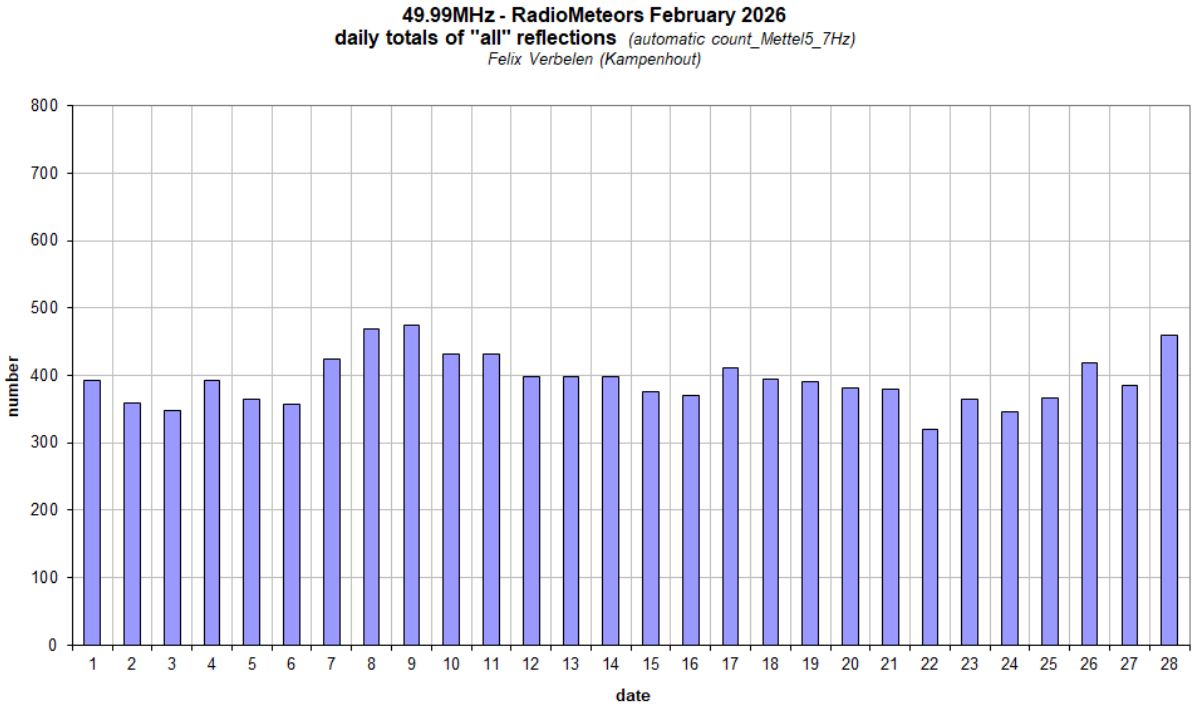

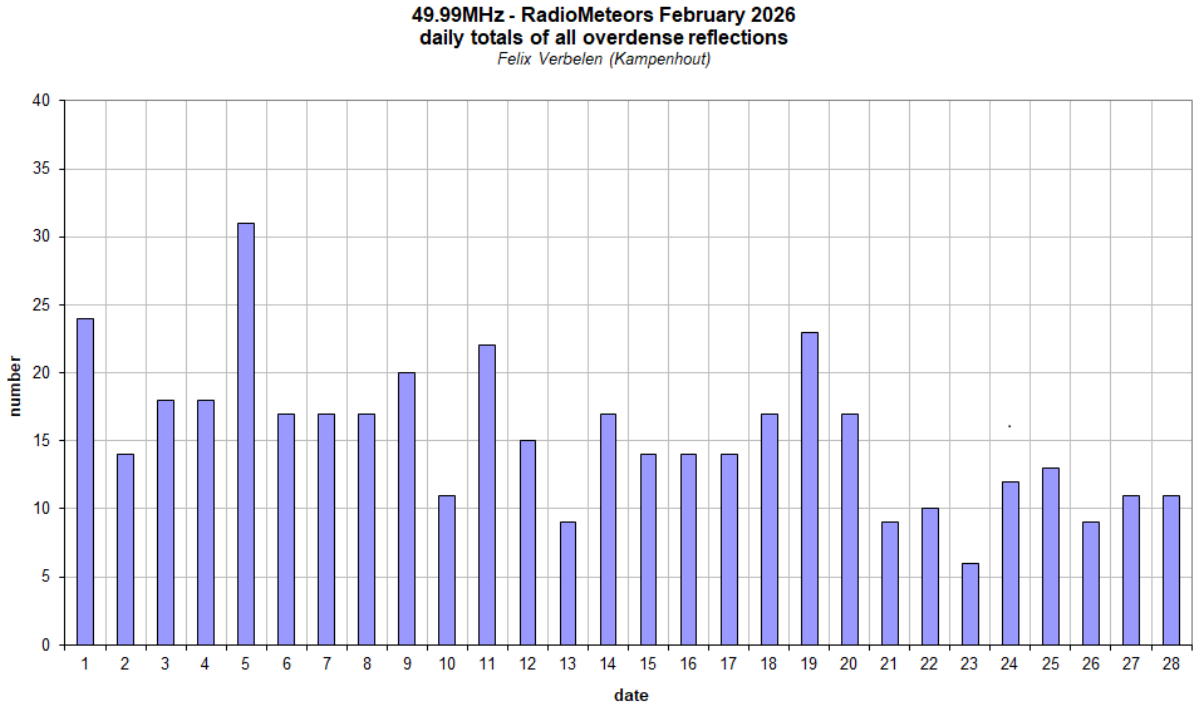

Figure 1 – The daily totals of "all" reflections counted automatically, and of manually counted "overdense" reflections, as observed here at Kampenhout (BE) on the frequency of our VVS-beacon (49.99 MHz) during February 2026.

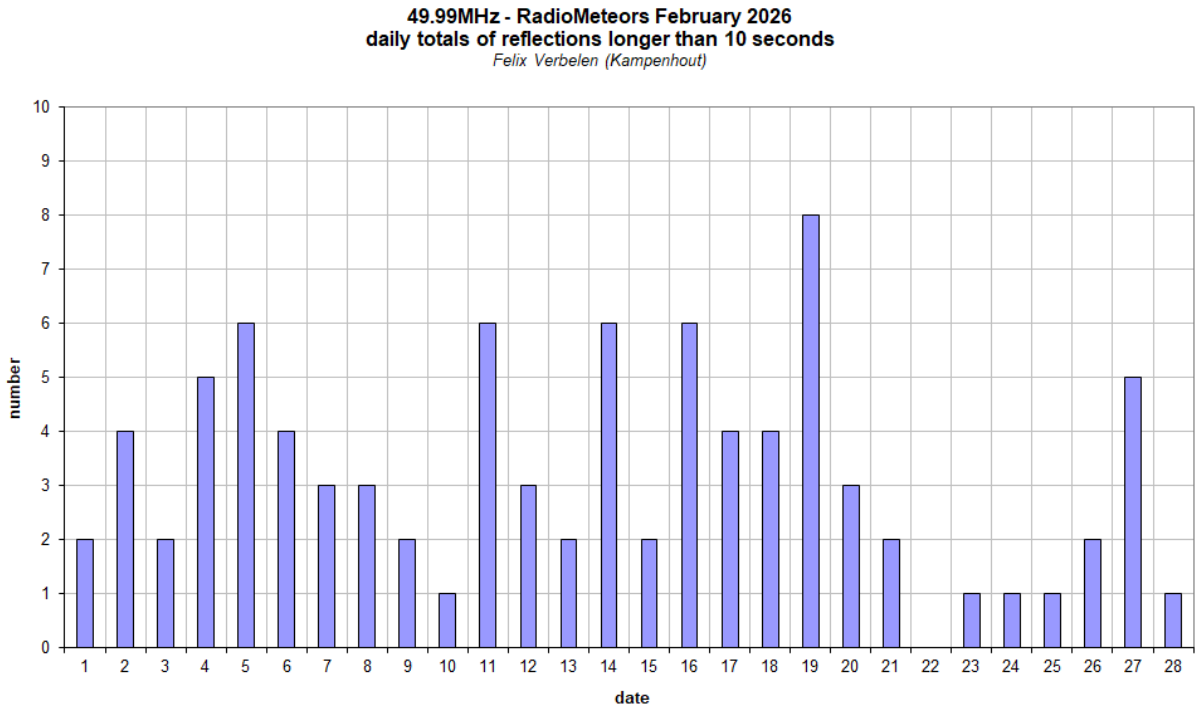

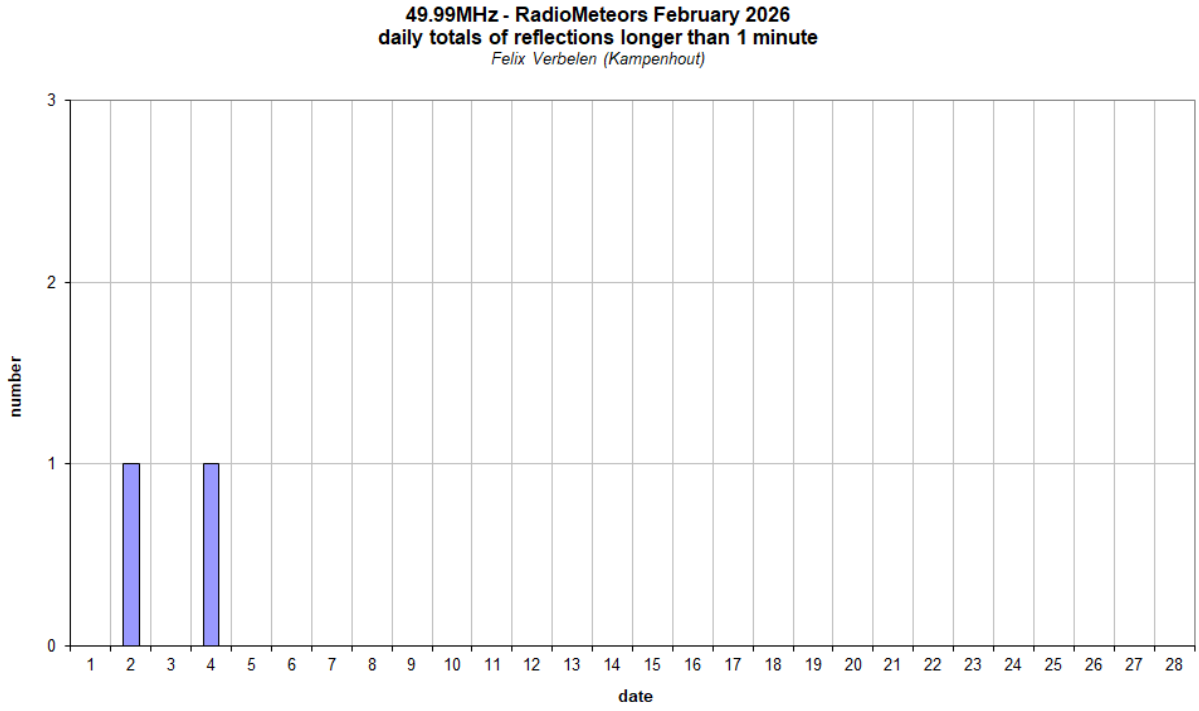

Figure 2 – The daily totals of overdense reflections longer than 10 seconds and longer than 1 minute, as observed here at Kampenhout (BE) on the frequency of our VVS-beacon (49.99 MHz) during February 2026.

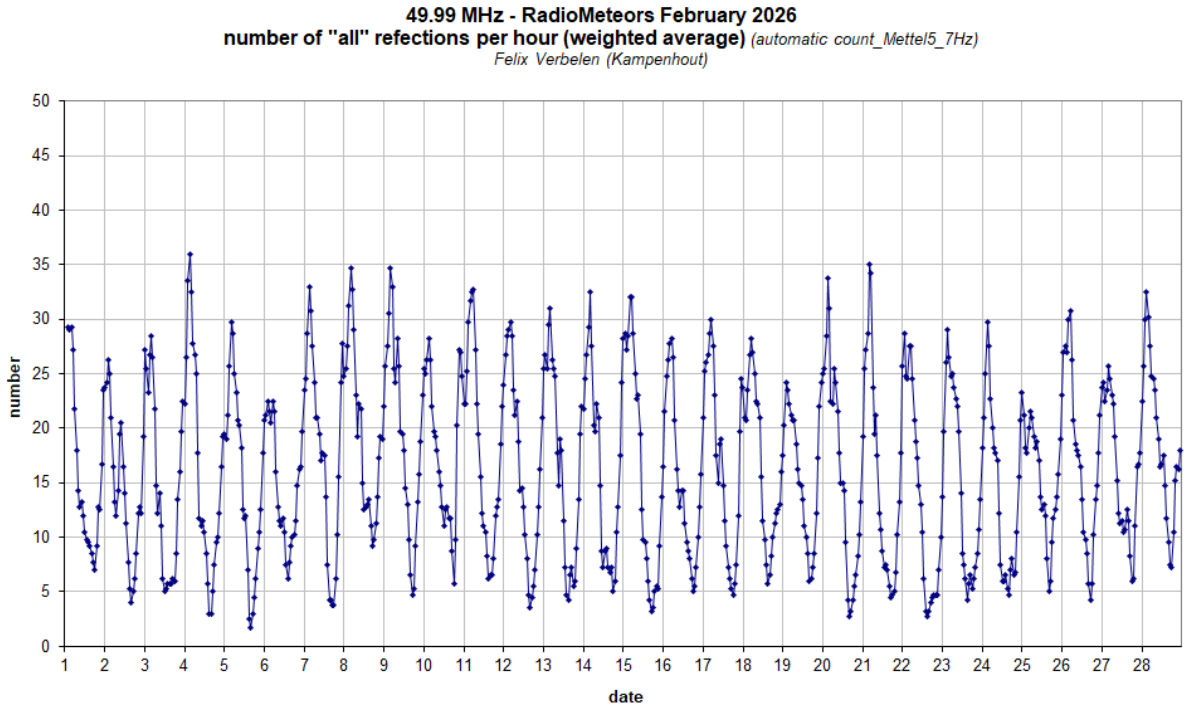

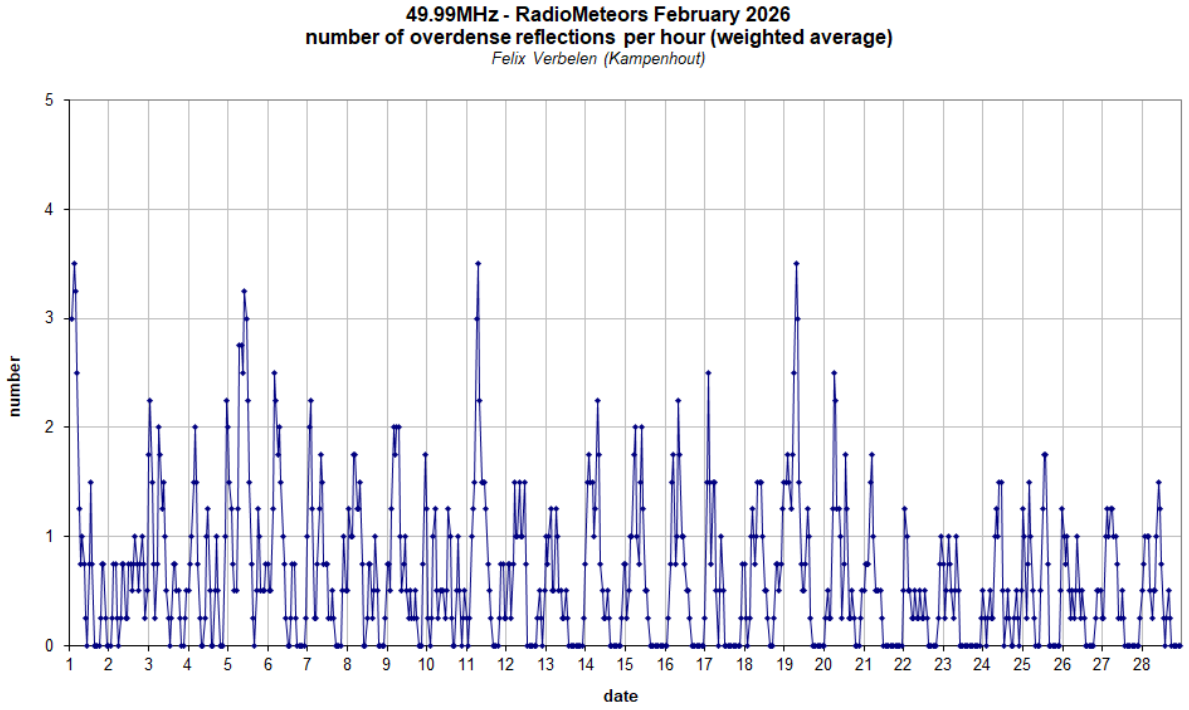

Figure 3 – The hourly numbers of "all" reflections counted automatically, and of manually counted "overdense" reflections, as observed here at Kampenhout (BE) on the frequency of our VVS-beacon (49.99 MHz) during February 2026.

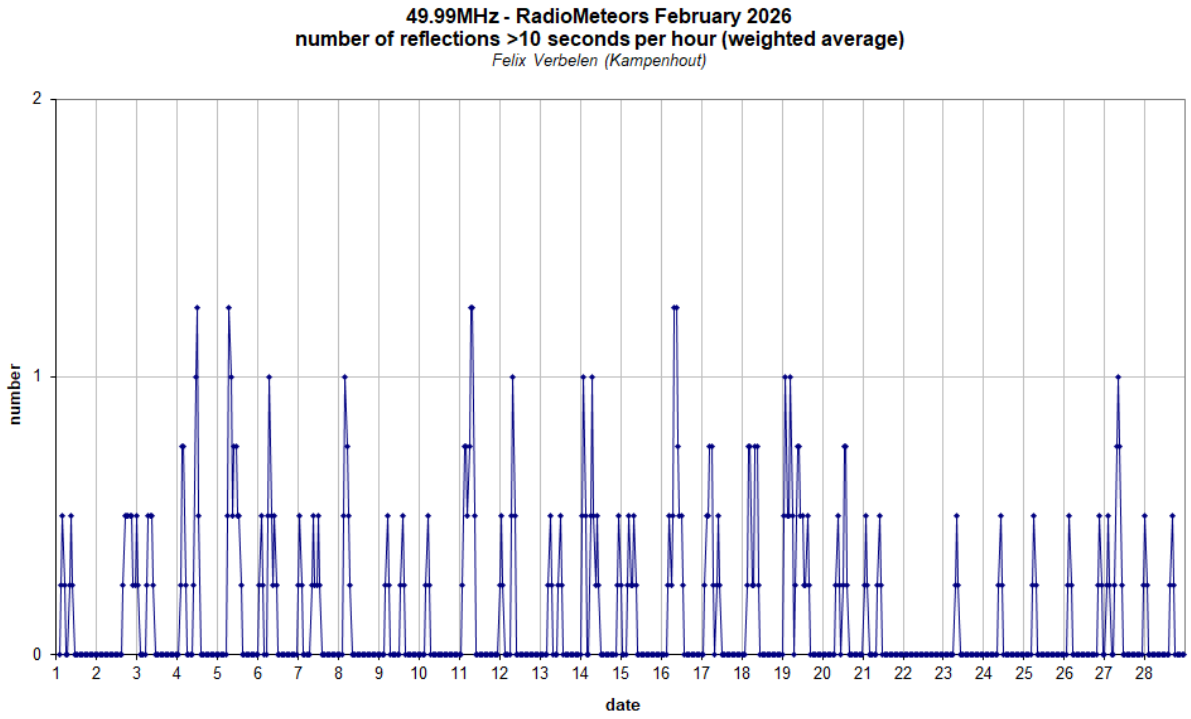

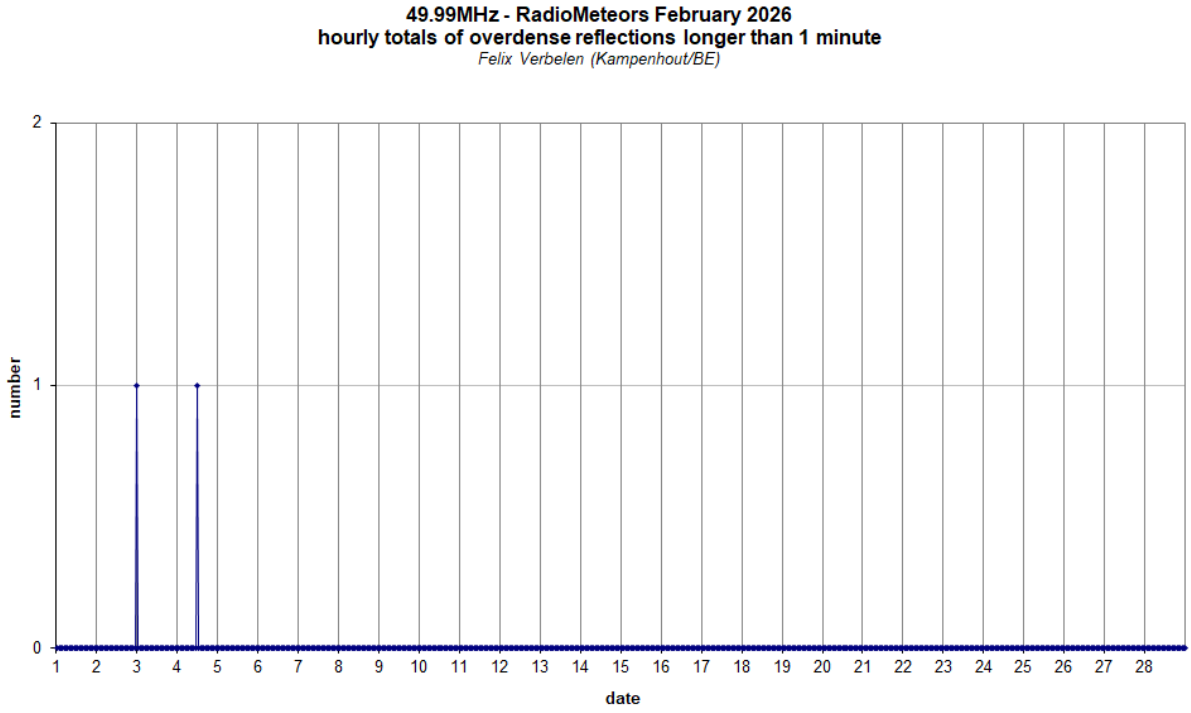

Figure 4 – The hourly numbers of overdense reflections longer than 10 seconds and longer than 1 minute, as observed here at Kampenhout (BE) on the frequency of our VVS-beacon (49.99 MHz) during February 2026.

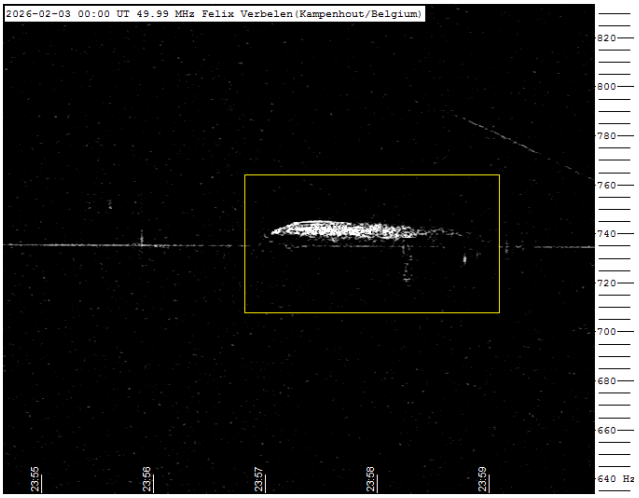

Figure 5 – Meteor echo February 03, 00^h00^m UT.

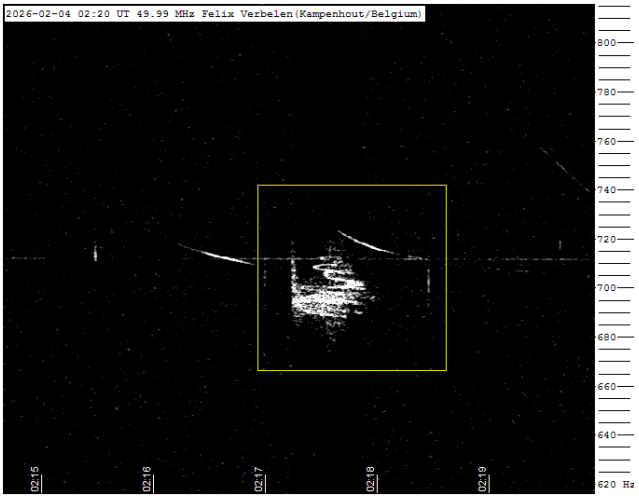

Figure 6 – Meteor echo February 04, 02^h20^m UT.

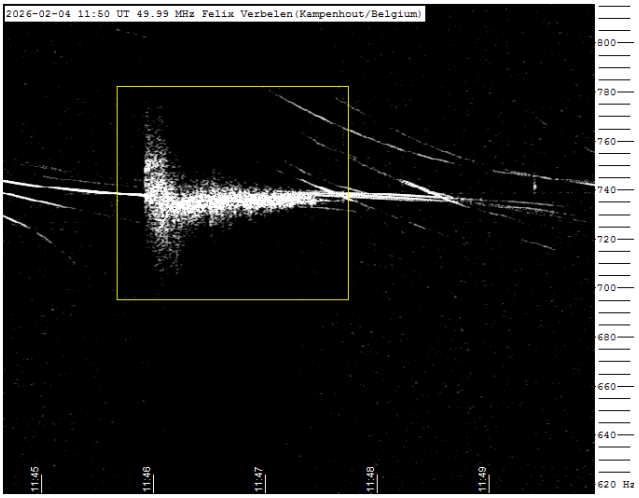

Figure 7 – Meteor echo February 04, 11^h50^m UT.

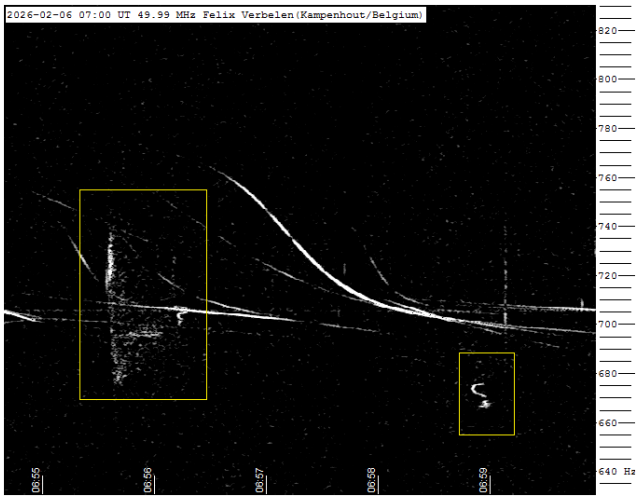

Figure 8 – Meteor echo February 06, 07^h00^m UT.

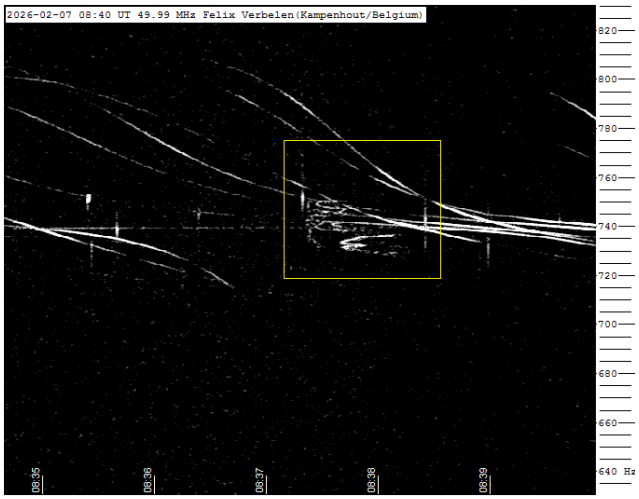

Figure 9 – Meteor echo February 07, 08^h40^m UT.

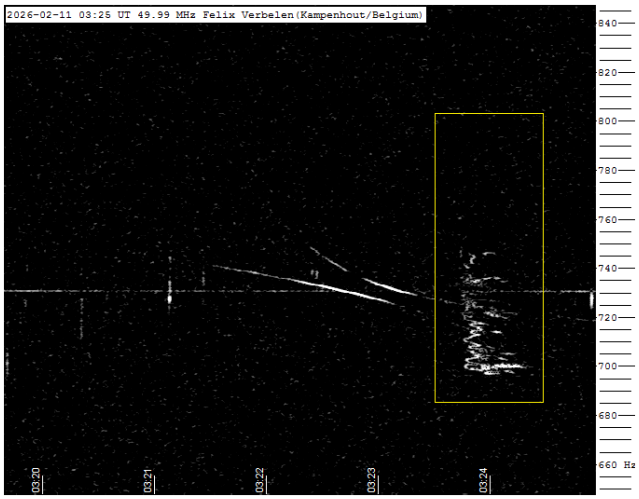

Figure 10 – Meteor echo February 11, 03^h25^m UT.

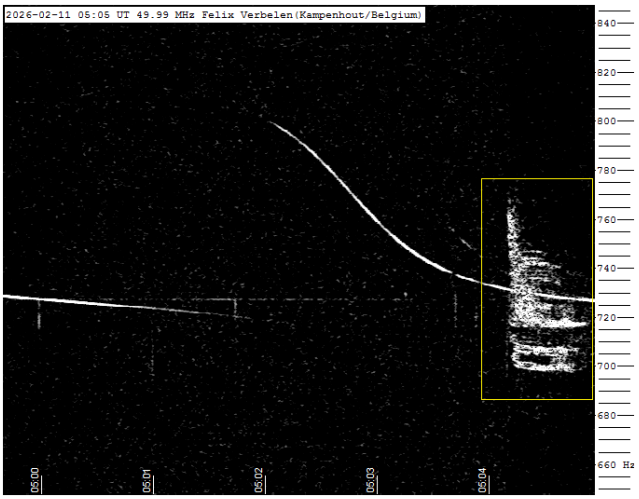

Figure 11 – Meteor echo February 11, 05^{h}05^{m} UT.

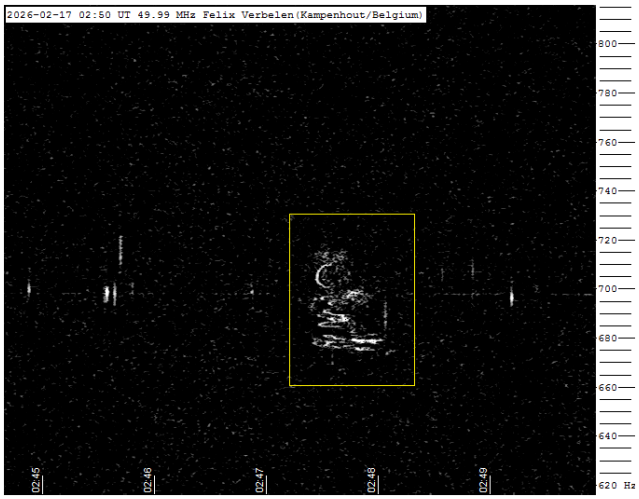

Figure 13 – Meteor echo February 17, 02^{h}50^{m} UT.

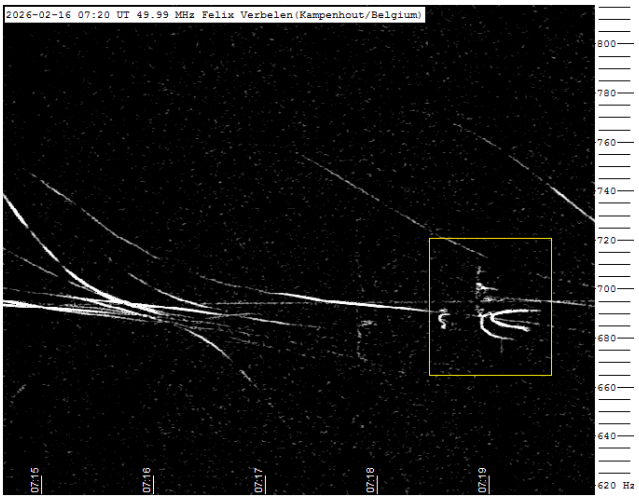

Figure 12 – Meteor echo February 16, 07^{h}20^{m} UT.

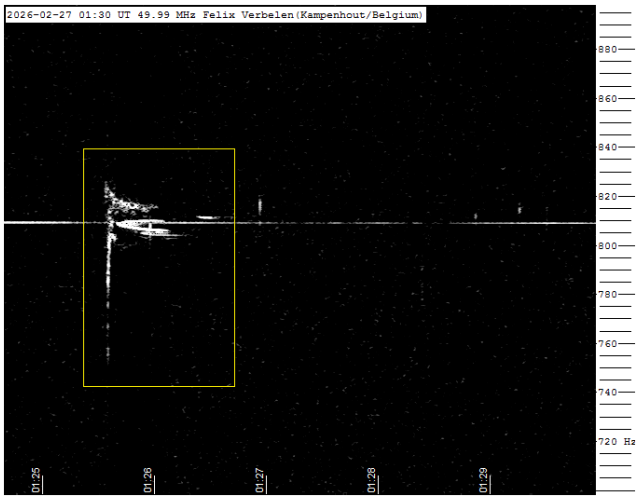

Figure 14 – Meteor echo February 27, 01^{h}30^{m} UT.

Radio meteors March 2026

Felix Verbelen

Vereniging voor Sterrenkunde & Volkssterrenwacht MIRA, Grimbergen, Belgium
felix.verbelen@gmail.com

An overview of the radio observations during March is given.

1 Introduction

The graphs show both the daily totals (*Figure 1 and 2*) and the hourly numbers (*Figure 3 and 4*) of "all" reflections counted automatically, and of manually counted "overdense" reflections, overdense reflections longer than 10 seconds and longer than 1 minute, as observed here at Kampenhout (BE) on the frequency of our VVS-beacon (49.99 MHz) during the month of March 2026.

The hourly numbers, for echoes shorter than 1 minute, are weighted averages derived from:

$$N(h) = \frac{n(h-1)}{4} + \frac{n(h)}{2} + \frac{n(h+1)}{4}$$

Local interference and unidentified noise remained very limited, and no significant lightning activity was recorded. However, there were several fairly strong solar flares, such as on March 16 between 12^h00^m and 13^h00^m UT (*Figure 5*).

As expected, meteor activity remained very low this month. However, the daily counts of overdense reflections showed a clear structure, with peaks on March 6 and March 21. Due to the low number of registrations, caution is advised when interpreting the results, and further research is required.

Only on March 14 was a reflection of approximately 1 minute recorded. A selection of some notable or strong reflections is shown in *Figures 6 to 12*. Many more are available upon request.

In addition to the usual graphs, you will also find the raw counts in cvs-format[31] from which the graphs are derived. The table contains the following columns: day of the month, hour of the day, day + decimals, solar longitude (epoch J2000), counts of "all" reflections, overdense reflections, reflections longer than 10 seconds and reflections longer than 1 minute, the numbers being the observed reflections of the past hour.

[31] https://www.emeteornews.net/wp-content/uploads/2026/04/202603_49990_FV_rawcounts.csv

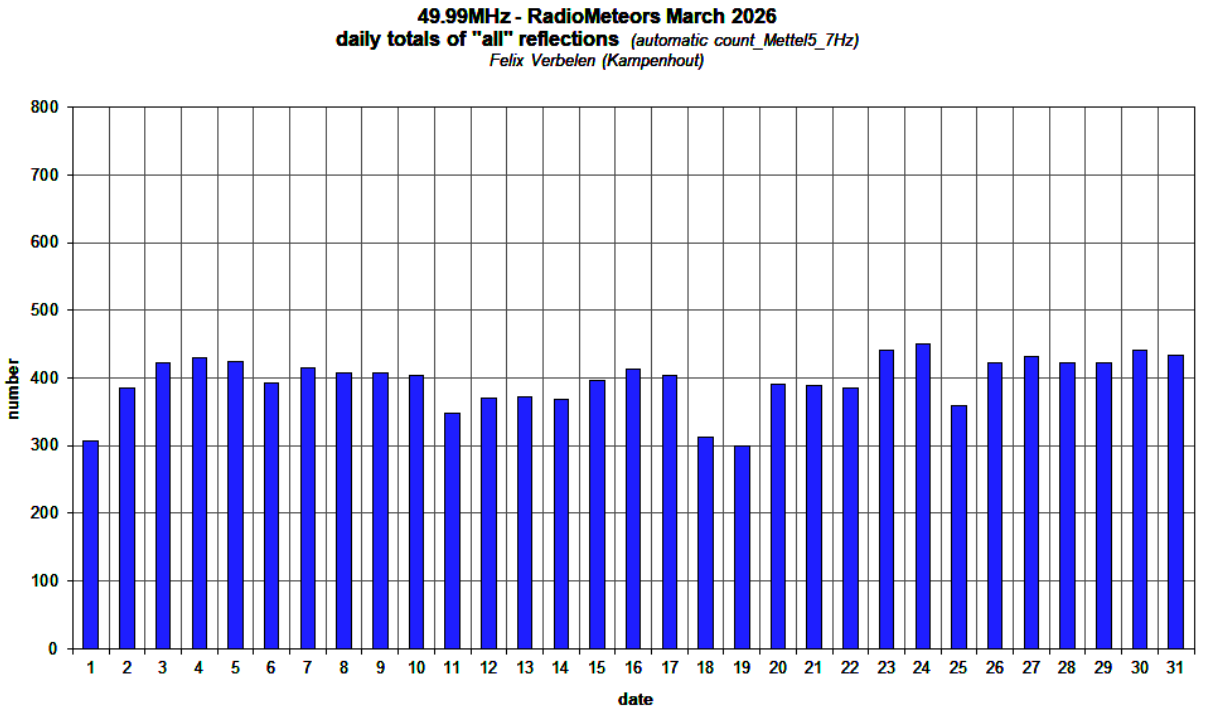

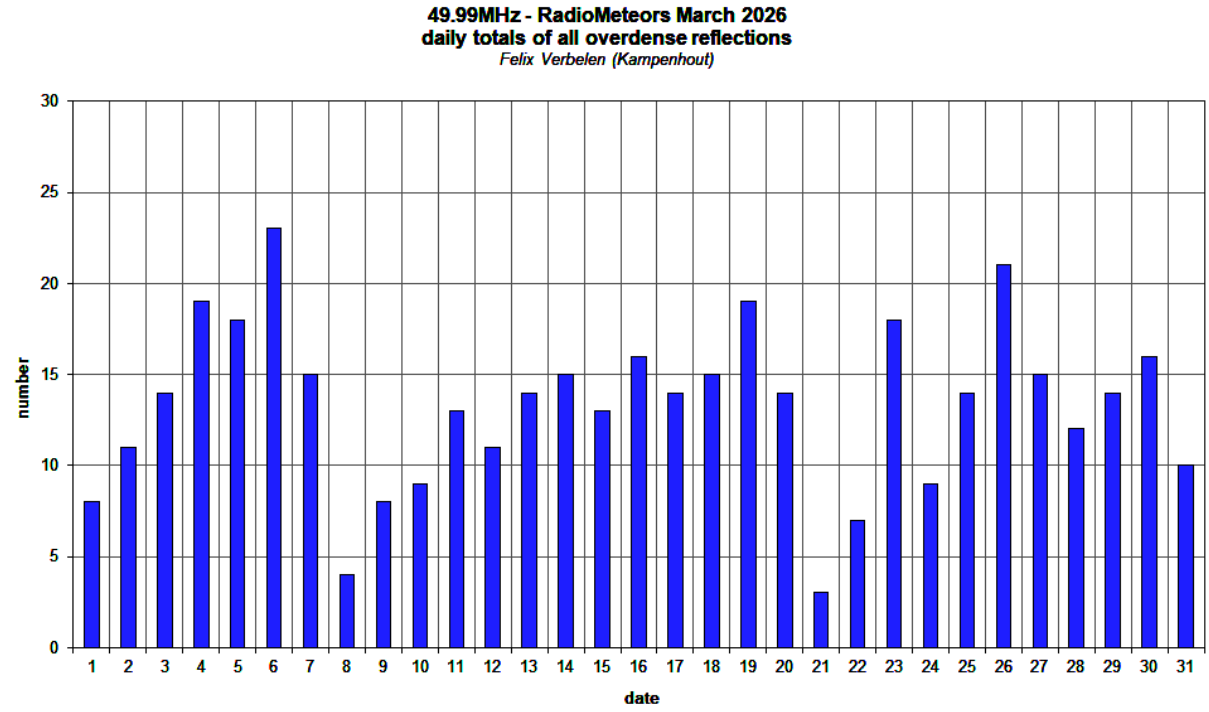

Figure 1 – The daily totals of "all" reflections counted automatically, and of manually counted "overdense" reflections, as observed here at Kampenhout (BE) on the frequency of our VVS-beacon (49.99 MHz) during March 2026.

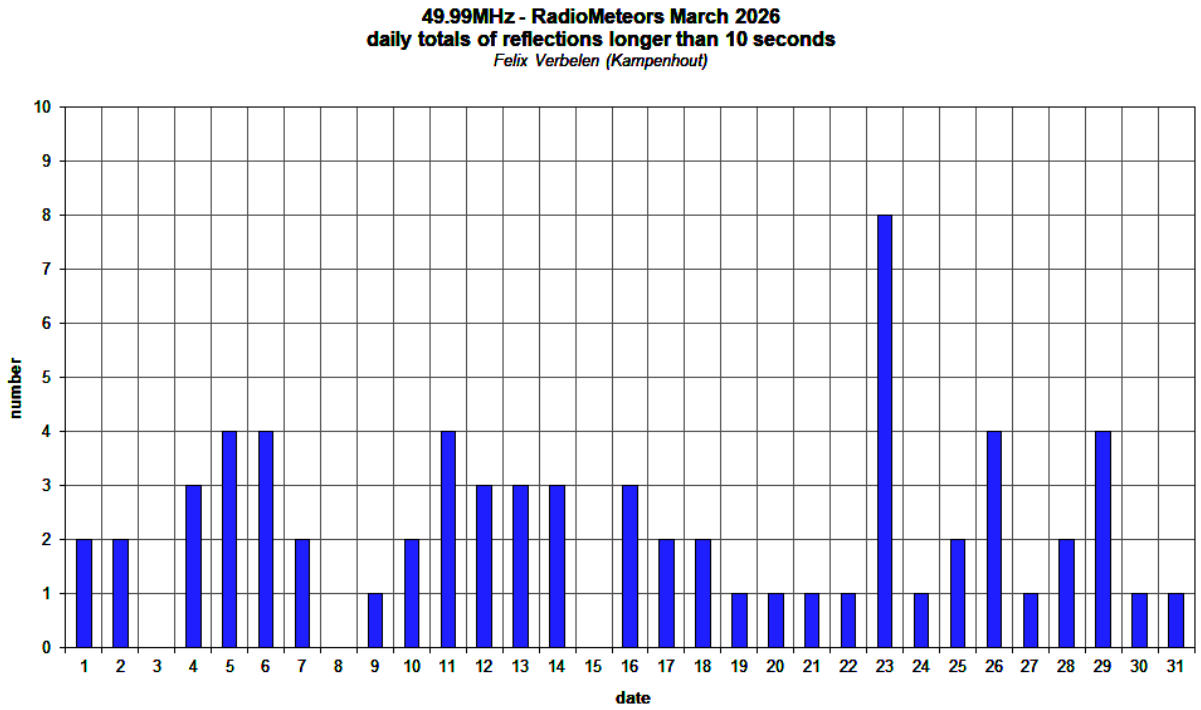

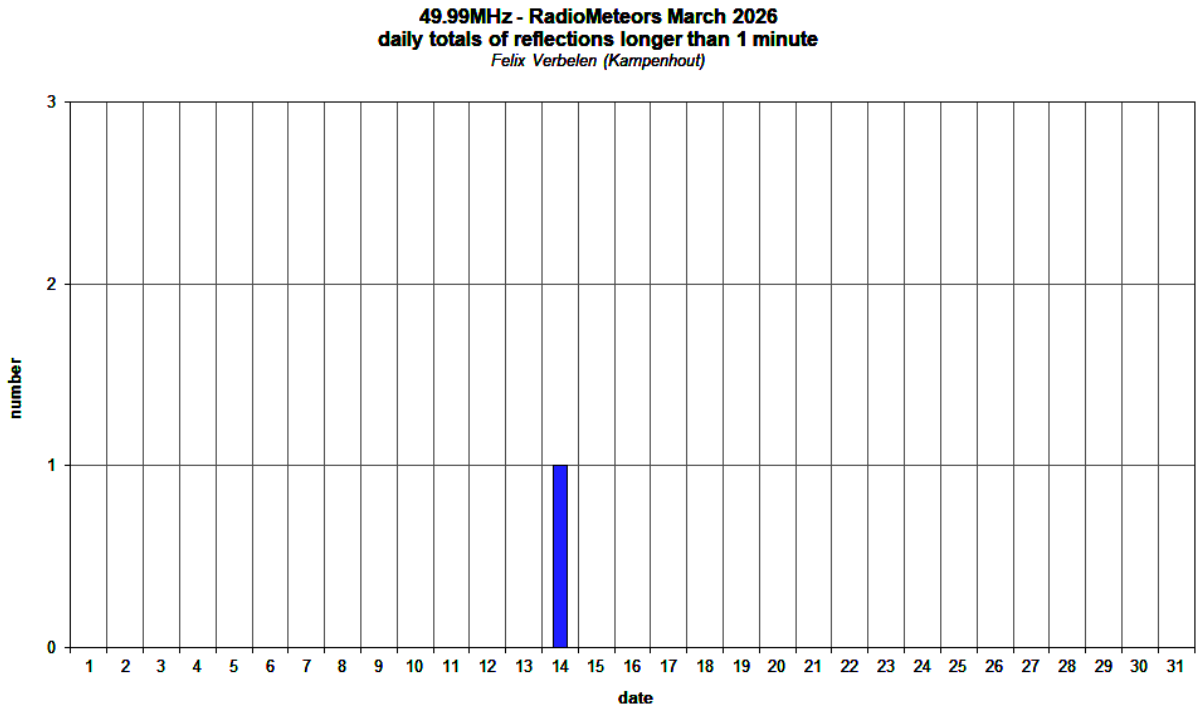

Figure 2 – The daily totals of overdense reflections longer than 10 seconds and longer than 1 minute, as observed here at Kampenhout (BE) on the frequency of our VVS-beacon (49.99 MHz) during March 2026.

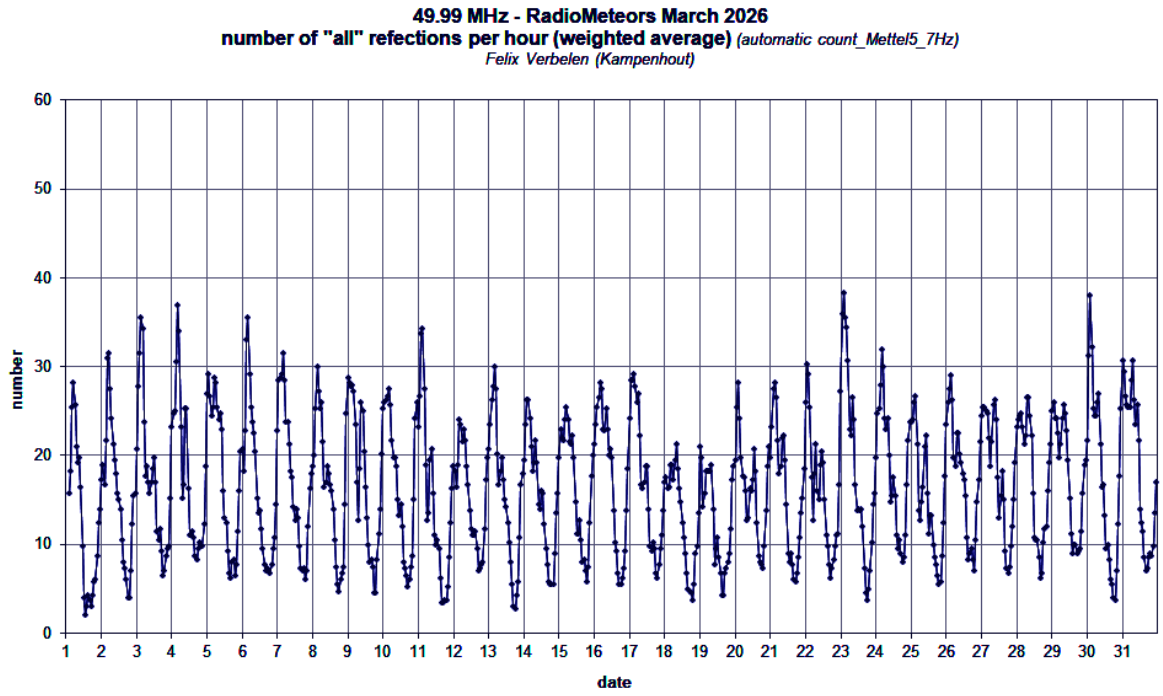

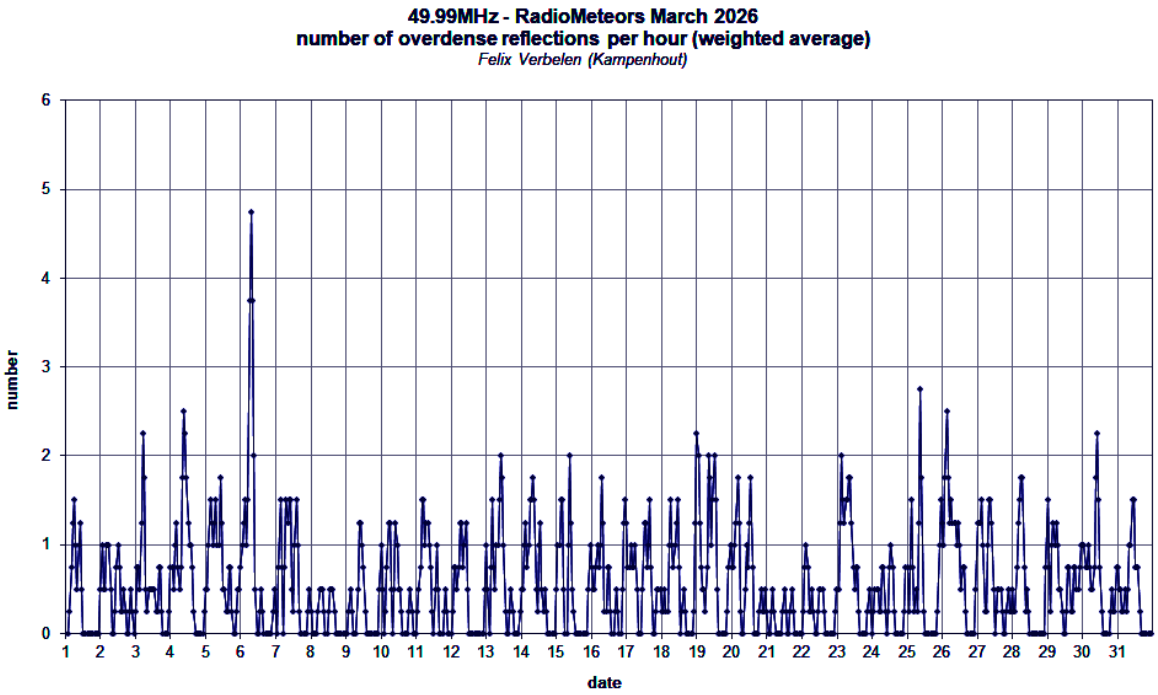

Figure 3 – The hourly numbers of "all" reflections counted automatically, and of manually counted "overdense" reflections, as observed here at Kampenhout (BE) on the frequency of our VVS-beacon (49.99 MHz) during March 2026.

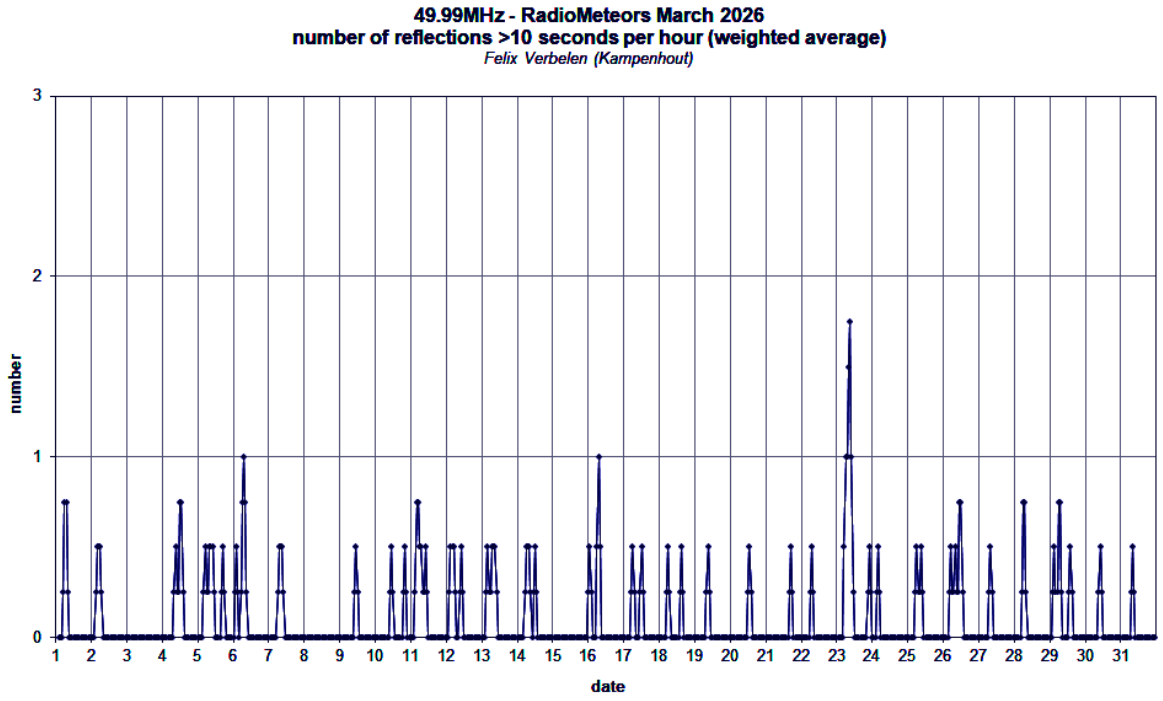

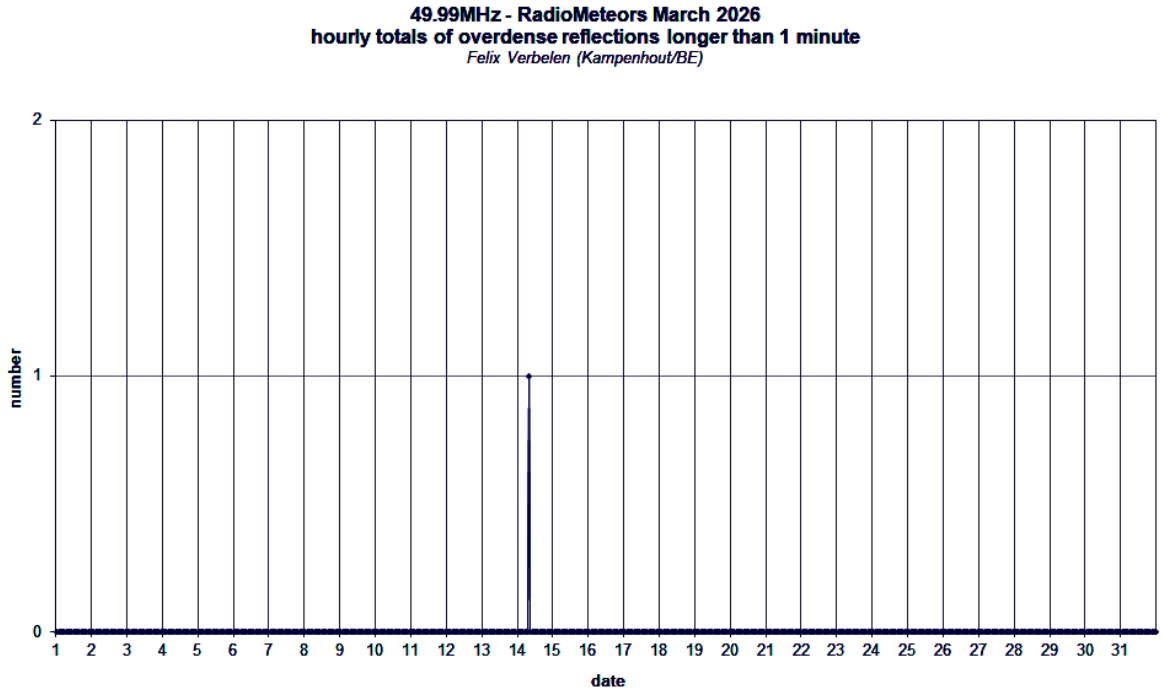

Figure 4 – The hourly numbers of overdense reflections longer than 10 seconds and longer than 1 minute, as observed here at Kampenhout (BE) on the frequency of our VVS-beacon (49.99 MHz) during March 2026.

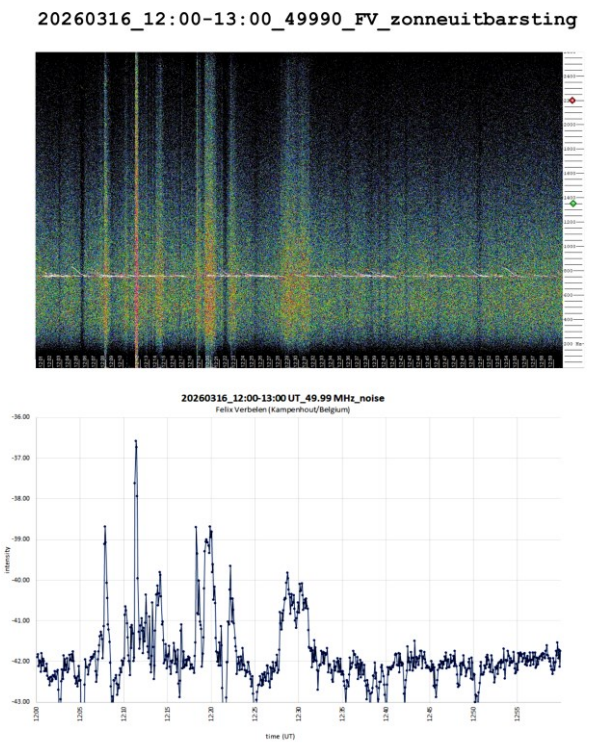

Figure 5 – strong solar flares, such as on March 16 between 12^h00^m and 13^h00^m UT.

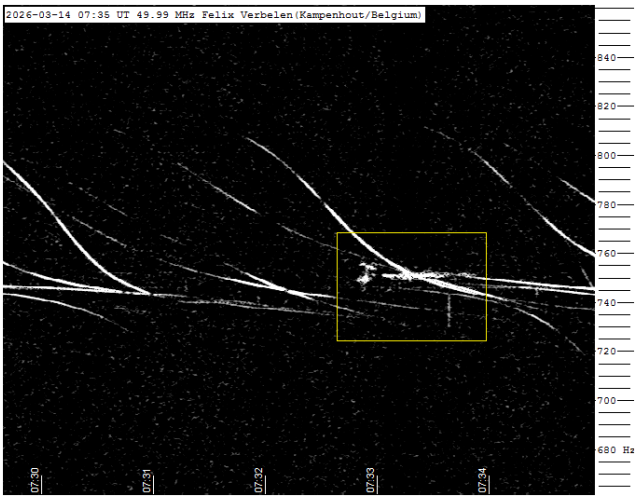

Figure 6 – Meteor echo March 14, 07^h35^m UT.

Figure 7 – Meteor echo March 16, 06^h20^m UT.

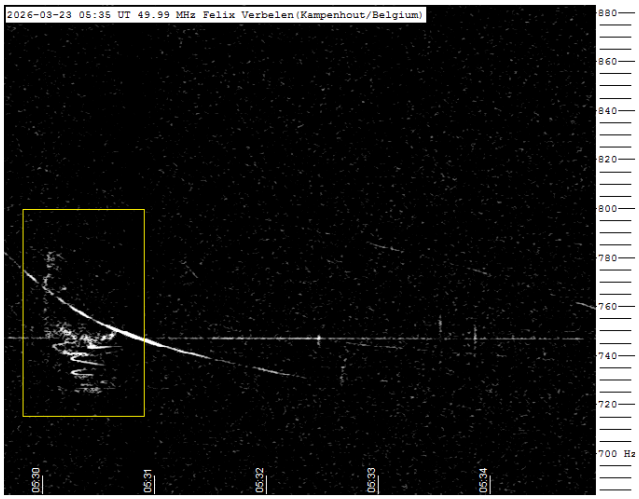

Figure 8 – Meteor echo March 23, 05^h35^m UT.

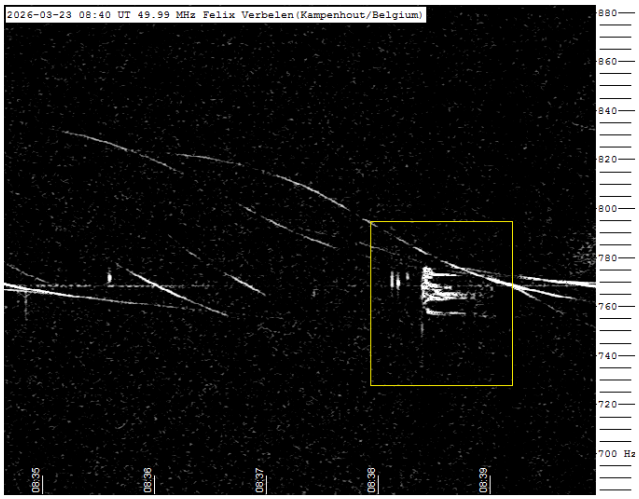

Figure 9 – Meteor echo March 23, 08^h40^m UT.

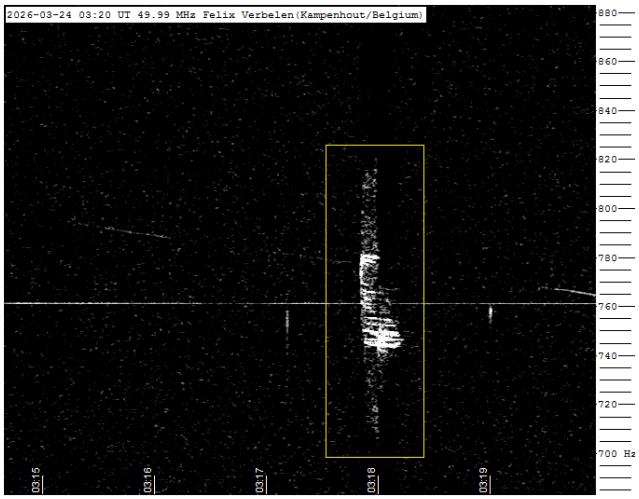

Figure 10 – Meteor echo March 24, 03^h20^m UT.

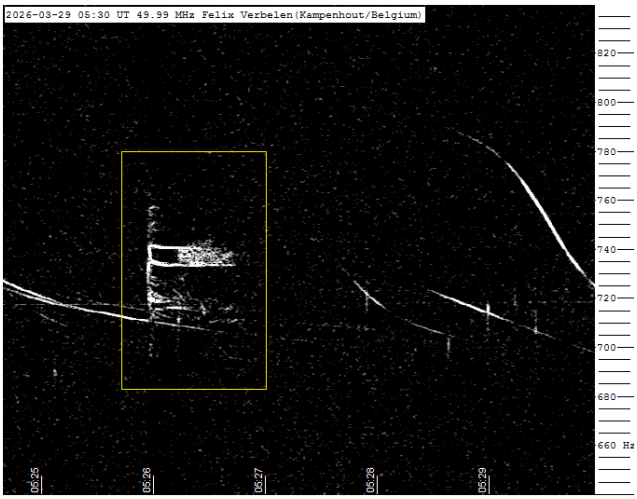

Figure 11 – Meteor echo March 29, 05^{h}30^{m} UT.

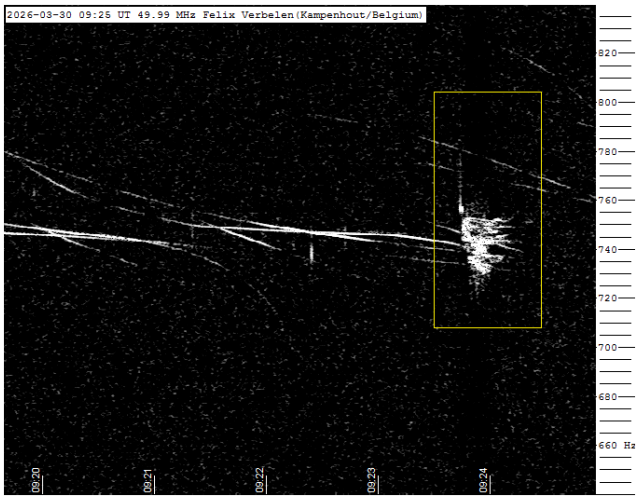

Figure 12 – Meteor echo March 30, 09^{h}25^{m} UT.

eMetN METEOR JOURNAL

Since 2016 the mission of eMetN Meteor Journal is to offer meteor news to a global audience and to provide a swift exchange of information in all fields of active amateur meteor work. eMetN Meteor Journal is freely available without any fees. eMetN Meteor Journal is independent from any country, society, observatory or institute. Articles are abstracted and archived with ADS Abstract Service: https://ui.adsabs.harvard.edu/search/q=eMetN

You are welcome to contribute to eMetN Meteor Journal on a regular or casual basis, if you wish to. Anyone can become an author or editor, for more info read: https://www.emeteornews.net/writing-content-for-emeteornews/

Articles for eMetN Meteor Journal should be submitted to: paul.roggemans@gmail.com

Contact: info@emeteornews.net

Contributors:

- Barbieri L.
- Brando G.
- Campbell-Burns P.
- Furlato G.
- Maglione M.
- Miskotte K.
- Rivato W.
- Roggemans P.
- Sarto S.
- Scott J.M.
- Šegon D.
- Verbelen F.
- Vida D.
- Wood J.

Online publication https://www.emeteornews.net and https://www.emetn.net
ISSN 3041-4261, publisher: Paul Roggemans, Pijnboomstraat 25, 2800 Mechelen, Belgium